UNCLASSIFIED

AD NUMBER
AD477394
NEW LIMITATION CHANGE
TO Approved for public release, distribution unlimited
FROM Distribution authorized to U.S. Gov't. agencies only; Administrative/Operational Use; 30 SEP 1965. Other requests shall be referred to AIr Force Ballistic Systems Division, Attn: BSDYV, Norton AFB, CA.
AUTHORITY
SAMSO USAF ltr, 18 Nov 1977

768227

HARDLING TECHNOLOGY STUDIES

RESPONSE OF REENTRY VEHICLE-TYPE SHELLS TO BLAST LOADS

by
H.E.LINDBERG, D. L. ANDERSON.
R. D. FIRTH, and L. V. PARKER
STANFORD RESEARCH INSTITUTE®

Prepared by
SRI Under LMSC Subcontract No. 24-14517
for
Ballistic Systems Division
Norton Air Force Base, California 92409
Contract No. AF 04(694)-655

Lockheed

MISSILES & SPACE COMPANY

A GROUP DIVISION OF LOCKHEED AIRCRAFT CORPORATION

SUNNYVALE, CALIFORNIA

AVAILABILITY NOTICE

Copies of this document are available at the Defense Documentation Center, Alexandria, Va. to qualified users. In addition to security requirements which apply to this document and must be met, each transmitter outside the Department of Defense must have prior approval of the Air Force Ballistic Systems Division, BSDYV, Norton A. F. B., California.

NOTICE OF AVAILABILITY

Copies of this document are available to U.S. Military Agencies from the Defense Documentation Center, Alexandria, Va. In addition to the security requirements which apply to this document and must be met, each transmittal outside the Department of Defense must have prior approval of the Air Force Ballistic Systems Division, BSYDV, Norton Air Force Base, California 92409.



In reply refer to: LMSC/581512

18 February 1966 51-40/102

Subject:

Notice of Availability for HARTS Final Report,

Contract No. AF 04(694)-655

To:

Distribution

Reference:

(1) LMSC/581410, Letter of Transmittal for LMSC/B130200, Volumes IV-A, IV-B, and IV-C, dated 9 February 1966.

Enclosure:

(a) Sticker: Notice of Availability

1. Please insert Enclosure (a) on the back of the front cover of LMSC/Bl30200, Volumes IV-B and IV-C of the HARTS Final Report.

2. This reflects a clarification of the Availability Notice.

TEA 1. B-369 2 ?0 1. C-477394

LOCKHEED MISSILES & SPACE COMPANY

Bu Maja

B. W. Marsh, Program Manager Advanced Reentry Technology Program,

51-40

BWM: jb

cc: BSYDV, Captain N. Azzarita, Norton AFB, California

California

A GROUP DIVISION OF LOCKHEED AIRCRAFT CORPORATION

HARDENING TECHNOLOGY STUDIES

RESPONSE OF REENTRY VEHICLE-TYPE SHELLS TO BLAST LOADS

by
H.E.LINDBERG, D. L. ANDERSON,
R. D. FIRTH, and L. V. PARKER
STANFORD RESEARCH INSTITUTE

Prepared by
SRI Under LMSC Subcontract No. 24-14517
for
Ballistic Systems Division
Norton Air Force Base, California 92409
Contract No. AF 04(694)-655



MISSILES & SPACE COMPANY

A GROUP DIVISION OF LOCKHEED AIRCRAFT CORPORATION
SUNNYVALE, CALIFORNIA

FOREWORD

The response of re-entry vehicle-type shells (relatively thick-walled) to loads of very short duration--produced by X rays or other means--has been under investigation since about 1958 and response has been well established in terms of the pressures experienced on the vehicle surface. Similarly, extensive information has been reported on the response of launch vehicle and aircraft-type shells (relatively thin-walled) to blast loads. However, very little data are available on the response of re-entry vehicle-type shells to blast loads, and the data that are available are summarized in terms of explosive charge size and distance-to-target rather than in terms of the pressures actually experienced on the structure surface.

In the work reported here the response of re-entry vehicle-type shells to blast loads is investigated and is described in terms of surface loads on the vehicle. The investigation is part of the Air Force Hardening Technology Studies (HARTS) and was performed by Stanford Research Institute for the Ballistics Systems Division under subcontract to Lockheed Missiles and Space Company.

Extensive data on both surface pressures and structural response of cylindrical and conical shells are presented. Peak pressure and impulse are identified as the important load characteristics which determine structural response and critical loads are presented in these terms. A theoretical description of dynamic buckling of cylindrical shells subjected to transient surface pressures is given to explain observed modes of failure and to predict critical loads for buckling over a wide range of load and structural parameters.

The shells investigated fall into four groups: (1) simple metal shells of aluminum and magnesium alloys, (2) stiffened metal shells (ring-stiffened, foam-filled, and sandwich), (3) simple covered shells, with cover materials ranging from brittle (Plexiglas) to fibrous

(Micarta, tape-wound refrasil and carbon phenolic) to very flexible (solid noeprene rubber), and (4) stiffened covered shells. In all, about 650 shell experiments were performed. Long duration blast pressures to cause severe damage ranged from 20 psi for the thinnest uncovered shells to about 2000 psi for covered shells with thick-walled subshells. Experiments were also performed with higher pressure pulses of intermediate duration so that critical curves for no damage and severe damage could be established for loads covering the entire range from very short X-ray type loads to very long blast-type loads. The theoretical investigation also covers the entire range of load durations.

ACKNOWLEDGMENTS

In addition to the great number of models made and experiments performed, the shock tubes and all of the equipment for holding the models, applying preloads, measuring pressures, calibrating the gages, and filtering pressure gage output were designed and built specifically for this program. This task was performed in the short period of 10 months by a monumental effort from the staff of the Poulter Laboratories, directed by Dr. Marjorie W. Evans. It is a pleasure to thank all of those who participated and to single out those whose contributions were indispensable to the completion of the program.

The authors are indebted to Leonard Dary, who made the detailed designs for all of the mechanical hardware, and to John Busma, under whose supervision the hardware and models were built. Invaluable assistance in carrying out the experiments was provided by Kennard Nelson, Philip Wilson, Ronald Homestead, and George Cartwright, who also conceived and executed essential improvements in the shock tubes. The electronic portions of all the pressure and strain gage experiments were performed by Richard Ray and James Hufman. The extensive photography and cataloging of the models and fixtures was undertaken by James Engle. Experiments with oxyacetylene explosive spheres were designed and performed by Bradley Reese. Finally, typing of the manuscript by Nancy Hall and supervision of the art work by Marlene Adams is gratefully acknowledged.

Program direction was provided by Captain James M. Gafney of Ballistic Systems Division, by Dr. W. T. Barry, Dr. F. A. Field, and R. Mortenson of Aerospace Corporation, and by B. W. Marsh, Dr. J. H. Klumpp and L. Brick of Lockheed Missiles and Space Company. To these men the authors are grateful for perceptive direction and cooperation throughout the program.

Singular thanks must be reserved for Dr. George R. Abrahamson, the instigator of it all, who helped formulate the program, provided unwavering council throughout, and crystalized the manuscript into final form.

CONTENTS

FOREWORD	ii
ACKNOWLEDGMENTS	v
LIST OF ILLUSTRATIONS	хi
LIST OF TABLES	хх
1. INTRODUCTION	1
1.1 Background,	1 2
1.3 Characterization of Critical Loads	3 7
1.5 Organization of the Report	9
2, SUMMARY	11
2.1 Blast Pressure Measurements	11 14 17 20
2.5 Concluding Remarks	22
MENTS	23
3.1 Ceneral Remarks	23 25 38 42
4. DETAILED DATA SUMMARY OF SHELL RESPONSE EXPERIMENTS	65
4.1 Model Serial Numbers and Descriptions	65 68 68

CONTENTS (Continued)

5.	RESP	PONSE OF SIMPLE METAL SHETLS	95
	5.1	General Remarks on Dynamic Buckling Theories for Simple Shells	95
	5.2	Experiments to Determine Critical Pressure-	
	5.3	Impulse Curves for Buckling	102
	5.5	Effects of Parameter Changes on Blast Buckling	118
6.	RESP	PONSE OF SIMPLE COVERED SHELLS	133
	6. 1	Failure Modes and Load-Damage Sensitivity	133
	6.2	Critical Pressure-Impulse Curves	146
	6.3	Comparison of Critical Loads for Various	
		Subshell Materials	155
	6.4	Shells with Tape-Wound Covers	157
7.	RESF	PONSE OF COMPLEX SHELLS	167
	7.1	Ribbed Shells	167
	7.2	Foam-Filled Shells	174
	7.3	Sandwich Shells	174
	7.4	Comparison of Critical Quasi-Static Pressures	
		for Stiffened and Unstiffened Shells	182
8.	THE	ORY -DYNAMIC BUCKLING OF CYLINDRICAL	
	SHEL	LLS	195
	8.1	Introduction	195
	8.2	Idealized Models	197
	8.3	Equations of Motion	200
	8.4	Character of the Solutions	212
	8.5	Buckling Criteria	219
	8.6	Critical Pressure-Impulse Curves for Buckling	225
	8.7	Derivation of an Approximate Expression for I	235
	8.8	Strain-Reversal Model	238
9		NSIENT OBSERVATIONS OF SHELL RESPONSE	0.40
	FROI	M BLAST LOADS	249
	9.1	Framing Camera Experiments	249
	9.2	Framing Camera Experiments	259
	0.3	Concluding Romanka	265

CONTENTS (Concluded)

Appendix A	INSTRUMENTATION FOR PRESSURE MEASUREMENTS	67
Appendix B	MODEL SUPPORT FIXTURES	77
Appendix C	THEORY OF EXPLOSIVELY DRIVEN SHOCK TUBES	37
Appendix D	CHRONOLOGICAL SHOT LISTS	27
REFERENCES	3	2 1

ILLUSTRATIONS

1.1	Comparison of Buckling of Cylindrical Shells with Fixed Ends by an Impulsive Load of Cosine Distribution (left) and of Uniform Distribution (right). Cylinders are 3 inches in diameter made of 6061-			
	T6 aluminum with $L/D = 1$, $a/h = 24$. Peak impulse = 10^4 taps for both cylinders (1 tap = 1 dyne-sec/cm ²).		•	3
1, 2	Comparison of Buckling from a Quasi-Static Blast Load and from a Static Load. Cylinders are as in Fig. 1.1		•	4
1.3	Comparison of Loads Required to Produce the Same Maximum Displacement of a Linear Oscillator. P is half the static load required to produce the given displacement and I_O is the ideal impulse to produce the given displacement	•	•	6
1.4	Comparison of Loads Required to Produce the Same Maximum Displacement of a One-Degree-of-Freedom Rigid-Plastic Model. Pois the static yield load and Io is the ideal impulse required to produce the given displacement	•	•	6
2.1	Pressures and Impulses from High Explosive Spheres and Shock Tubes (measured on a 6-inch-diameter cylinder at a gage facing a lateral blast)	•	•	13
2,2	Typical Buckling Patterns in Thin Cylindrical Shells Subjected to Lateral Blast Loads of Various Durations	•	•	14
2.3	Critical Curves for Buckling of 6061-T6 Aluminum Shells with D = 6 Inches, L/D = 1, and Various a/h .	•		16
2.4	Typical Failure of Covered Shells from Blast Loads .			18
2.5	Critical Pressure-Impulse Curves for Buckling or Cracking of Covered Shells (6061-T6 aluminum subshells, L/D = 1, a/h = 61)	•	•	20
3.1	General Arrangement of Spherical HE Shots (a) locating cylindrical test models using a dummy sphere (b) adjusting height and angular orientation of models (c) charge in place with four models and stands · · ·	•	•	26

3, 2	Pressures on a 6-inch-diameter Cylinder 4 feet from a 0.5-pound C2 Sphere (sweep rate 200 µsec/cm, all traces; triggers staggered for ease in reading) 27
3.3	Measured Pressures on a 6-inch-diameter Cylinder vs. Distance from a 0.5-pound Sphere
3.4	Pressure Distribution over Front Face of Cylinder (smoothed data from 0.5-pound charge, Fig. 3.3) 31
3.5	Incident (side-on) Pressure and Impulse from Pento- lite Spheres
3,6	Reflected (flat-wall) Pressure and Impulse from Pentolite Spheres
3.7	Pressures on a 6-inch-diameter Cylinder 6 feet from a 4-pound C2 Sphere (sweep rate 100 µsec/cm, all traces, filtered @ 96 kc)
3.8	Semi-log Plot of Pressure Pulse
3.9	Pressure and Impulse on a 6-inch-diameter Cylinder from HE Spheres
3.10	General Arrangement for a 70-inch-diameter Oxyacetylene Gas Sphere
3.11	Incident Pressure Pulse at 24 inches from the Surface of a 35-inch-diameter Oxyacetylene Sphere
3.12	Incident Pressure and Impulse from a 35-inch-diameter Oxyacetylene Sphere
3. 13	Comparison of Diffracted Pressure-Impulse on a 6-inch-diameter Cylinder from Gas and High Explosive Spheres
3.14	Layout of Shock Tubes
3.15	Overall View of 4-foot and 2-foot Shock Tubes 45
3.16	Loading Sequence for Full-Length Shots in 2-foot

3.17	Flat Charges for Short Pulses
3.18	Loading Sequence for the 4-foot Shock Tube 48
3.19	Pressure Pulses at $\theta = 0^{\circ}$ and $\theta = 22.5^{\circ}$ on a Cylindrical Model in the 2-foot Shock Tube at 20 Fect (sweep rate 1 msec/cm)
3.20	Pressure Pulses at $\theta = 0^{\circ}$ and $\theta = 22.5^{\circ}$ on a 9° Conical Model in the 2-foot Shock Tube at 20 Feet (sweep rate 1 msec/cm)
3.21	Pressure Pulses at $\alpha = 2.0$ Around a Cylindrical Model in the 2-foot Shock Tube at 20 Feet (sweep rate 1 msec/cm)
3.22	Peak Pressure vs. α for Various Angles on a 6-inch-diameter Cylinder in the 2-foot Tube at 20 Feet 55
3.23	Peak Pressure vs. Angle for Various Charge Ratios in the 2-foot Tube at 20 Feet (smoothed data from Fig. 3.22)
3.24	Comparison of Observed Pressure Distribution with Simple Analytic Expressions
3.25	Pressure Pulses on a 6-inch-diameter Cylinder for Various Charge Ratios in the 2-foot Tube at 10 Feet (sweep rate 500 µsec/cm except for i)
3.26	Pressure-Impulse from the 2-foot and 4-foot Shock Tubes
3,27	Pressure Pulses on a 6-inch-diameter Cylinder in the 2-foot Tube at 2 Feet (sweep rate 100 µsec/cm) 62
3.28	Pressure Pulses on a 6-inch-diameter Cylinder in the 4-foot Tube at 30 Feet (sweep rate 2 msec/cm) 64
4.1	Schematic of Shell Critical Curves and Blast Technique Cross-Curves
5.1	Ideal Impulse Io and Static Pressure Po to Produce Buckling in 6061-T6 Aluminum Shells

5.2	Theoretical Pressure-Impulse Critical Curves for Buckling (normalized to P _o and I _o for 6061-T6 aluminum, L/D = 1)			99
5.3	Theoretical Pressure-Impulse Critical Curves for Buckling (same as in Fig. 5.2, but in actual pressure and impulse units)	•	•	101
5.4	Buckling of Shells with a/h = 187 from Quasi- Impulsive (HE sphere) Loads	,		103
5.5	Buckling of Shells with a/h = 187 from Quasi-Static (Shock tube) Loads	•	•	104
5.6	Buckling of Shells with a/h = 100 from Quasi- Impulsive (a-d), and Quasi-Static (e) Loads	•	•	105
5.7	Buckling of Shells with a/h = 61 from Quasi- Impulsive (a-d), and Quasi-Static (e, f) Loads	•		106
5.8	Increasing Damage to Shells with a/h = 53 from (a-c) Quasi-Impulsive, (d,e) Quasi-Static, and (f,d) Static Loads (Note similarity of failure mode from quasi-static loads (in d) and static loads (in f,g)	•	•	107
5.9	Buckling of Shells with a/h = 24 from Quasi- Impulsive (a-c), and Quasi-Static (d) Loads		•	108
5.10	Increasing Damage to Shells with a/h = 23 from Increasing Quasi-Static Loads	•	•	• :
5.11	Comparison of Buckling Modes of Shells with $a/h = 23$ under Quasi-Static (a), and Static (b) Loads	•	•	109
5.12	Shell Deformation Versus Peak Pressure from Spherical Charges			110
5.13	Experimental and Theoretical Pressure-Impulse Curves for Buckling 6(187)1-A6T6 Shells (group A12)	•	•	111
5.14	Experimental and Theoretical Pressure-Impulse Curves for Buckling 6(100)1-A6T6 Shells (group A13)		•	112

5.15	Experimental and Theoretical Pressure Impulse Curves for Buckling 6(61)1-A6T6 Shells (group A15)	113
5.16	Experimental and Theoretical Pressure-Impulse Curves for Buckling 6(24)1-A6T6 Shells (group A17)	114
5.17	Buckle Pattern in 6(120)1-A6T6 Shell Buckled from an Impulsive Load	118
5.18	Measured Buckling Patterns from Quasi-Impulsive Loads in Shells with Various a/h	:19
5.19	Shells of Various Length-to-Diameter Ratios Buckled from Quasi-Static Blast Loads	<u>:</u> 2. 0
5.20	Buckling of Cones with a/h = 187 and 94 from Quasi-Impulsive (a, b, d), and Quasi-Static (c, e, f) Loads	122
5.21	Buckling of Cones with a/h = 60 and 24 from Quasi- Impulsive (a, c), and Quasi-Static (b, d) Loads	123
5 22	Shearing and Tearing of 2024-T8 Shells with a/h = 24 from Increasing Quasi-Impulsive Loads	125
5,23	Shearing and Tearing of AZ31B Magnesium Shells with a/h = 61 from Quasi-Impulsive (a-c), and Quasi-Static (d) Loads	126
5.24	Buckling of Shells with a/h = 100 and 61 Under Axial Preloads and Subjected to Quasi-Static Loads	129
5.25	Static Buckling Interaction Curve for Lateral Pressure and Axial Stress	131
6.1	Circumferential Ridge Bulges in Metal Subshells from Quasi-Static (shock tube) Loads	134
6.2	Cracking of Micarta Shells from (a, b) Quasi-Impulsive Loads, (c, d, e) Quasi-Static Loads, and (f) Static Uniform Lateral Pressure	135
6.3	Sudden Plexiglas Shattering from Quasi-Impulsive Loads (in b, c, compared to a) and Sudden Disinte- gration from Quasi-Static Loads (in f, compared to d, e) (subshell a/h = 100)	136

6.4	Increasing Damage to Micarta-Covered Shells (subshell a/h = 100) from Increasing Quasi-Impulsive Loads
6.5	Typical Buckling of a Rubber-Covered Shell (sub- shell a/n = 100) from a Quasi-Static Load
6.6	Sudden Stripping off of Plexiglas Cover (subshell a/h = 61) from a Small Increase in Quasi-Static Load
6.7	Similarity of Longitudinal Plexiglas Cracks from a Quasi-Static Load and a Static Uniform Lateral Pressure (subshell a/h = 53)
6.8	Disintegration of a Micarta-Covered Shell (sub- shell a/h = 61) from a Quasi-Static Load (in c,d) Only 20 Percent Greater than a Threshold Cracking Load (in b)
6.9	Increasing Damag to Micarta-Covered Shells (subshell a/h = 53) from Increasing Quasi-Impulsive Loads (a, b, d) and Buckling and Cracking from Uniform Static Lateral Pressure (e)
6.10	Plexiglas Shattering from Quasi-Impulsive Loads and Comparison of Longitudinal Cracks from Quasi- Static and Static Loads (heavy subshell a/h = 23) 142
6.11	Increasing Damage to Micarta-Covered Shells from Increasing Quasi-Impulsive Loads (heavy subshell a/h = 23)
6.12	Heavy Damage to Micarta-Covered Shell (subshell a/h = 23) from a Quasi-Static Load (in a) and Cracking and Buckling from a Uniform Static Lateral Pressure (in b)
6.13	Magnesium (subshell a/h = 24) Shearing and Tearing in (c) Plexiglas and (3) Micarta-Covered Shells from Quasi-Static Loads
6.14	Cracking and Buckling of L/D = 2 Micarta-Covered Shells from Quasi-Static Loads, (subshell'h = 53 in a,b, and subshell a/h = 23 in c,d).

6. 15	Critical Pressure-Impulse Curves for 6(100)1-A6T6 Shells with Micarta and Plexiglas Covers		•	147
6.16	Critical Pressure-Impulse Curves for 6(61)1-A6T6 Shells with Micarta and Plexiglas Covers	•		148
6.17	Critical Pressure-Impulse Curves for 6(24)1-A6T6 Shells with Micarta and Plexiglas Covers			149
6. 18	Critical Pressure-Impulse Curves for 6(100)1-A6T6 Shells alone and with Micarta, Plexiglas, and Rubber Covers		•	151
6. 19	Critical Pressure-Impulse Curves for 6(61)1-A6T6 Shells alone and with Micarta, Plexiglas, and Rubber Covers	•	•	152
6.20	Critical Pressure-Impulse Curves for 6(24)1-A6T6 Shells alone and with Micarta, Plexiglas, and Rubber Covers		•	153
6.21	Crit_cal Pressure-Impulse Curves for Micarta-Covered Shells with 6061-T6 Aluminum Subshells of Various Thicknesses			154
6, 22	Delamination of Tape-Wound Refrasil Shells (subshell a/h = 100) from (a,b,c) Quasi-Impulsive Loads, and (d-h) Quasi-Static Loads	•	•	158
6.23	Delamination of Tape-Wound Carbon Phenolic Shells (subshell a/h = 100) from (a, b, c) Quasi-Impulsive Loads, and (d, e, f) Quasi-Static Loads	•	•	159
6.24	Moderately Severe Damage to a Tape-Wound NOMEX Shell (subshell a/h = 100) from a Quasi-Static Load .	•		160
6.25	Severe Damage to a Tape-Wound NOMEX Shell (sub-shell a/h = 100) from a Quasi-Static Load		•	161
6.26	Delamination of Tape-Wound Refrasil Shells (sub- shell a/h = 50) from (a,b,c) Quasi-Impulsive Loads, and (d,e,f) Quasi-Static Loads	•	•	162

6.27	Delamination of Tape-Wound Carbon Phenolic Shells (subshell a/h = 50) from (a, b, c) Quasi-Impulsive Loads, and (d-g) Quasi-Static Loads
6.28	Stress-Strain Curves for Plexiglas and Grade 79 Micarta
7.1	Uncovered Ribbed Shells, a/h = 100, 5 Ribs 169
7.2	Uncovered Ribbed Shells, a/h = 50, 2 Ribs 171
7.3	Plexiglas-Covered Ribbed Shells, a/h = 50, 2 Heavy Ribs
7.4	Micarta-Covered Ribbed Shells, a/h = 50, 2 Heavy Ribs
7.5	Foam-Filled Shells, a/h = 100, 8 lb/ft Foam 175
7.6	Foam-Filled Shells, $a/h = 100$, $12 lb/ft^3$ Foam 176
7.7	Foam-Filled Shells, $a/h = 100$, $18 lb/ft^3$ Foam 177
7.8	Foam-Finled Shells, $a/h = 61$, $8 lb/ft^3$ Foam 178
7.9	Foam-Filled Shells, $a/h = 61$, $12 lb/ft^3$ Foam 179
7. 10	Foam-Filled Shells, $a/h = 61$, $18 lb/ft^3$ Foam 180
7.11	Cross Section of Sandwich Shell 0: 049/0.030-inch Skins (Experiments C314-6, 7, 8, last experiment at P = 680 psi, I = 79,000 taps)
7. 12	Uncovered Sandwich Shells, 0.049/0.030-inch Skins, 1/4-inch Core
7.13	Uncovered Sandwich Shells, 0.030/0.030-inch Skins, 1/2-inch Core
7.14	Uncovered Sandwich Shells, 0.049/0.030-inch Skins, 1/2-inch Core
7. 15	Uncovered Sandwich Shells, 0.049/0.049-inch Skins, 1/2-inch Core

7.16	Cross Section of Micarta-Covered Sandwich Shell 0.030/0.030-inch Skins (Experiment C321-5, P = 1200 psi, I = 150,000 taps)
7. 17	Micarta-Covered Sandwich Shells, 0.030/0.030-inch Subshell Skins
7. 18	Micarta-Covered Sandwich Shells, 0.049/0.030-inch Subshell Skins
8.1	Pulse Shapes
8.2	Typical Critical Pressure-Impulse Curves for Buckling, Showing Load Regions
8.3	Buckling Patterns in Cylinders Subjected to Various Pulse Durations
8.4	Comparison of Buckling of Cylindrical Shells with Fixed Ends by an Impulsive Load of Cosine Distribution (left) and of Uniform Distribution (right). Cylinders are 3 inches in diameter made of 6061-T6 aluminum with L/D = 1, a/h = 24. Peak impulse = 104 taps for both cylinders (1 tap = 1 dyne-sec/cm ²) 199
8.5	Coordinates and Shell Nomenclature 200
8.6	Forces on Shell Element
8.7	Idealized Stress-Strain Relation 205
8.8	Time Variation of Hoop Membrane Force 213
8.9	Amplification Function
8.10	σ/E, Vs. ε for Materials in Experiments (Tensile Tests)
8.11	Amplification Vs. Impulse (Ideal impulses applied to 6061-T6 aluminum shell, D = 6 inch, a/h = 100, L/D = 1)
8.12	Comparison of Critical Pressure-Impulse Curves to Give Amplifications of 100, 1000, and 10,000 (Exponential pulse, same shell as in Fig. 8.11)

The second of th

48.79 (2005) 5340 (2005)

Comme

Tanada and a

i.i

11

8.13	Comparison of Critical Pressure-Impulse Curves for Constant Amplification (imperfection criterion) and for Plastic Bending Threshold (from deterministic forces) (Expendential pulse, 6061-T6 aluminum shells, D=6 inch, L/2/21)	223
8.14	Typical Theoretical Critical Pressure-Impulse Curve for Buckling (Exponential pulse, $\cos^2\theta$ distribution, same shell as in Fig. 8.11)	226
8. 15	Effect of Pulse Shape on Critical Curves for Buckling $(\cos^2\theta$ distribution, same shell as in Fig. 8.11)	227
8.16	Effect of a/h on Critical Curves for Buckling (Exponential pulse, $\cos^2\theta$ distribution; 6061-T6 aluminum, D = 6 inch, L/D = 1; curves normalized to P _o and I _o for each shell)	228
8. 17	Effect of a/h on Critical Curves for Buckling (Same as Fig. 8.16, but with no normalization)	229
8. 18	Effect of L/D on Critical Curves for Buckling (Exponential pulse, uniform load, 6061-T6 aluminum shells, D = 6 inch, a/h = 100)	230
8. 19	Effect of Material Properties on Critical Curves for Buckling—Shells of Equal Size (Exponential pulse, $\cos^2\theta$ distribution, D = 6 inch, a/h = 100, L/D=1)	231
8.20	Effect of Material Properties on Critical Curves for Buckling—Shells of Equal Weight (Same as Fig. 8.19, but a/h is adjusted to give shells of equal weight)	232
8.21	Idealized Stress-Strain Relation for Plastic Loading and Unloading	239
8.22	Notation—Laminated Shell	242
8.23	Theoretical Critical Pressure-Impulse Curves for Buck.ing—Comparison of Strain-Reversal Model with the Tangent-Modulus and Elastic Models (Triangular pulse, 606)-T6 aluminum shell,	

8.24	Effect of Magnitude of Imperfection on Critical Buckling Impulse, P = 400 psi, Critical Mode = 26 (same shell as in Fig. 8.23)	247
9.1	Shock Tube Arrangement for Observing Buckling in a Shell with a/h = 53	250
9.2	Framing Camera Photographs of Elastic Buckling of a Shell with a/h = 53. (6061-T6 aluminum, D = 3 inch, L/D = 1; time between frames 41.7 μ sec; estimated load P \approx 350 psi, I \approx 14,000 taps)	251
9.3	Framing Camera Photographs of Elastic-Plastic Buckling of a Shell with $a/h = 53$. (Same as in Fig. 9.2, except $P \approx 550$ psi, $I \approx 21,000$ taps)	253
9.4	Explosive Sphere Arrangement for Observing Buckling in a Shell with a/h = 250	256
9.5	Framing Camera Photographs of Elastic-Plastic Buckling of a Shell with a/h = 250. (6061-T6 aluminum, D = 3 inch, L/D = 1; time between frames 41.7 µsec; P = 25 psi, I = 500 taps)	257
9.6	Strain Records from Subcritical Response of a Shell with a/h = 61 (2024-T8 aluminum, D = 6 inch, L/D = 1; P = 245 psi, I = 32,000 taps; Sweep: 500 µsec/cm, Gain: 0.0009 in/in/cm, compression positive downward)	261
9.7	Strain Records from Buckling Response of a Shell with a/h = 61 (same shell as in Fig. 9.6, but P = 390 psi, I = 47,000 taps; Sweep: 1 msec/cm, Gain: 0.0033 in/in/cm)	262
9.8	Strain Record from Threshold Buckling Response of a Shell with a/h = 24 (2024-T8 aluminum, D = 6 inch, L/D = 1; P = 1310 psi, I = 161,000 taps; Sweep: 1 msec/cm, Gain: as shown on individual records, in/in/cm)	263
		-00

A. 1	Pressure-Instrumented Cylinder (6-inch diameter) 2	68
A.2	Kistler Model 601H Quartz Pressure Transducers 2	68
A.3	Gage Locations in 6-inch Pressure Cylinder 2	69
A.4	Pressure Records with and without Filtering 2	71
A.5	Filter Frequency Response in 29 kc Position	71
A.6	ARC Type LC-33 Blast Gage with Mounting Collar and Sleeve	72
A. 7	Pressure Calibration Arrangement	73
A.8	Pressure Calibration Records (2 runs on 2 gages, sweep 5 msec/cm)	74
A.9	Charge Sensitivity Vs. Pressure for Typical Kistler 601H Gage	75
B.l	Cylindrical Model Support Fixture (6-inch diameter) 2	78
B.2	Model Support Assembly (6-inch diameter) 2	79
B.3	Cone Support Assembly	81
B.4	Shock Tube Mounting Arrangements	83
B.5	Preload Fixture	84
B.6	Preload Fixture (assembly drawing, tension mode) 2	85
C. 1	Idealized Pressure Pulse on Cylindrical Model (θ = 0) 2	88
C.2	Average Specific Heats at Constant Volume Vs. Temperature	91
C.3	Ratio of Average Specific Heats Vs. Temperature 2	92
C. 4	Idealized Shock Tube	93
C.5	x-t Diagram	98
C. 6	x-t Diagram	00

ILLUSTRATIONS (Concluded)

C.7	Pressure Vs. Charge Ratio Curves	•	•		•	30
C.8	x-t Diagrams			•	•	304
C.9	Pressure Pulses on Cylindrical Models (6 = 0)					30

TABLES

3. 1	Measured Pressures on 7. 6-Inch-Diameter Cylinder at Various Distances from a 0.5-Pound Charge	•	•	30
3.2	Primacord Charges in 2-Foot Tube (6-foot charge length)		•	50
4.1	Data Summary		•	80
5.1	Effect of Length-to-Diameter Ratio on Buckling Pressures	•	•	121
5.2	Comparison of Buckling Pressures and Impulses for Cylinders and Cones		•	124
5.3	Pressures and Impulses for 10-Percent Deformation of Shells of Various Materials (6-inch Diameter)		•	127
5.4	Material Properties	•	•	128
5.5	Influence of Axial Preloads on Buckling Blast Pressures		•	130
6.1	Threshold and Catastrophic Quasi-Static Pressures for Covered Shells (Most experiments in 2-foot shock tube at 20 feet)	•	•	155
6.2	Comparison of Threshold Pressures for Various Shell Material and Wall Thickness Combinations (psi)	•	•	156
6.3	Summary of Quasi-Static Pressures from Shock Tubes Applied to Shells with Tape-Wound Covers			164
6.4	Summary of Quasi-Impulsive Loads from HE Spheres Applied to Shells with Tape-Wound Covers .	•	•	165
7.1	Quasi-Static Efficiencies of Various Uncovered Shell Designs (Pressures are for slight, moderate, and heavy damage, from Table 4.1)	•	•	191
7.2	Quasi-Static Efficiencies of Covered, Simple and Stiffened Shells			192

TABLES (Concluded)

8. 1	Material Properties (Tensile Test Data)	17
D. 1	Chronological Shot List—High Explosive Spheres 3	08
D. 2	Chronological Shot List—2-Foot-Diameter Shock Tube	12
D. 3	Chronological Shot List—4-Foot-Diameter Shock	10

1. INTRODUCTION

1.1 Background

のできないのできる ないかん かんしゅう かんしょう かんしょう しょうしょう しょうしょう

Cylindrical and conical shells are widely used as structural elements in aircraft, missile launch vehicles, satellites, and re-entry vehicles. For effective design it is necessary to know the critical loads at which this basic structural element fails. This report is concerned with the determination of the failure mechanisms and the corresponding critical loads for cylindrical and conical shells under transient surface loads--generated by nuclear weapon effects or other means--similar to those produced by blast waves. The range of shell thicknesses includes that of interest in re-entry vehicle design.

The dynamic response of a structure to a transient load depends on the relationships between the load duration and the characteristic times of the structure. For shell structures, transient surface loads are conveniently divided into four types, depending on load duration as follows:

- 1. Shock loads --duration comparable to or less than the shock transit time through the shell wall, possibly producing spalls or separation of the walls of a subshell/heat shield configuration
- 2. <u>Impulsive loads--duration</u> short compared to response of the structure as a shell
- 3. Quasi-impulsive loads--duration comparable to structural response times
- 4. Quasi-static loads--duration long compared to structural response times.

Previous investigations of the response of shell structures to transient surface loads were concerned mainly with shock loads and

^{*}This nomenclature was introduced in [1]. (Numbers in brackets designate references listed at the end of the report.)

impulsive loads applied to re-entry vehicles and satellites [2-5] and with quasi-impulsive and quasi-static blast loads applied to missile launch vehicles [6-8], simple shells typical of launch vehicles [9, 10], and airframe components. Launch vehicles and airframes are relatively thin-walled; re-entry vehicles, designed to withstand high re-entry loads, tend to be relatively thick-walled. Thus, current data on thick shells typical of re-entry vehicles are restricted to impulsive loads, and blast data are available mainly for shells much thinner than those of interest for re-entry vehicles. The present investigation fills some of the gaps between these previous studies by concentrating on the response of re-entry vehicle type shells to quasi-impulsive and quasi-static blast loads.

1.2 Basic Approach

There are about a half-dozen weapon effects of current interest thick result in surface loads ranging from shock loads to quasi-static loads. To determine structural response to each effect separately would be both expensive and time-consuming. If the problem is inverted, however, and structural response is first determined for a range of loads significant to the structure, it will then be relatively easy to determine structural response for a particular weapon effect. To fully exploit this approach it is essential that structural response be understood over the entire range of load durations from impulsive loads to quasi-static loads; only then can the influence of load characteristics on structural response be discussed in terms of the structure rather than in terms of a specific weapon effect.

A knowledge of the sensitivity of structural response to load characteristics is also useful for determining the accuracy to which the actual loads must be known and the accuracy to which they must be simulated in structural response studies. The need for such knowledge is painfully apparent, for example, in the shock-on-shock

^{*}A short description of these mechanisms, as they affect structural response, is given in [1].

problem associated with atmospheric encounters. In the present report the important load characteristics for shell-type structures are identified and critical loads for cylindrical shells, including those of re-entry vehicles, are given in terms of these load characteristics.

1.3 Characterization of Critical Loads

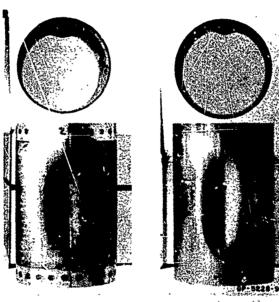
The overall problem of structural response to transient surface pressures is concerned with loads of differing shapes, distributions, and durations which are produced by various weapon effects. To generate a background of structural response information against which structural effects of these loads can be evaluated requires a basis for characterizing critical loads. In this section it is shown that the most important features of surface loads are peak pressure and impulse, and that critical loads are conveniently characterized in these terms.

Spatial distributions of loads from the weapon effects of interest here are smoothly varying, and experiments on structures indicate that for such loads the details of the distributions are not crucial to the maximum response. This is illustrated in Fig. 1.1 for impulsive loads



FIG. 1.1 COMPARISON OF BUCKLING OF CYLINDRICAL SHELLS WITH FIXED ENDS BY AN IMPULSIVE LOAD OF COSINE DISTRIBUTION (left) AND OF UNIFORM DISTRIBUTION (right). Cylinders are 3 inches in diameter made of 6061-T6 aluminum with L/D=1, a/n=24. Peak impulse = 10^4 taps for both cylinders (1 tap = 1 dyne-sec/cm²)

and in Fig. 1.2 for quasi-static loads. Figure 1.1 shows two identical cylindrical shells with rigid ends which exhibit the same peak deformation and local response mode under impulsive loads of the same peak impulse, although the cylinder on the left was loaded with a cosine distribution over one side and the cylinder on the right was loaded uniformly all around. Figure 1.2 shows two identical cylindrical shells subjected to loads of long duration which exhibit essentially the same peak deformation and response mode, although the one on the left was loaded on one side by a blast wave and the other was loaded by a uniform static pressure approximately equal to the peak blast pressure.



BLAST LOAD
PEAK PRESSURE 1400 psi
IMPULSE 1.7 x 105 taps

STATIC LOAD
PRESSURE 1500 psi

FIG. 1.2 COMPARISON OF BUCKLING FROM A QUASI-STATIC BLAST LOAD AND FROM A STATIC LOAD. Cylinders are as in Fig. 1.1

Further justification of this conclusion is given in Chapter 8.

Similar behavior is reported in subsequent chapters for more complex shells with plastic coverings and with internal stiffening. Hence, details of smoothly varying spatial distributions are not of great significance for such cylindrical shells for either short duration or long duration loads.

The pulse shape from most weapon effects of interest here is an almost instantaneous rise in pressure, followed by an exponential decay; however, special weapons are theoretically capable of producing a wide variety of pulse shapes. The variation in structural response with pulse shape is readily seen by examining simple theoretical models based on typical structural characteristics. * Consider first a linear elastic, single-degree-of-freedom system, such as a ring or long cylinder undergoing symmetric radial oscillations. We visualize that the cylinder is subjected to a pressure pulse, uniform all around the cylinder, with a given time variation. The response is computed over a range of peak pressures and the impulse at each pressure is adjusted so that the maximum deflection is the same for each combination of pressure and impulse. The resulting curve in the pressure-impulse plane is then an "iso-damage" curve and completely determines the loads of the given pulse shape which produce a specified maximum deflection.

These curves are drawn in Fig. 1.3 for exponential, triangular, and rectangular pulse shapes. In the region where the curves approach the vertical asymptote, pressure becomes unimportant and the response depends only on impulse (these are impulsive loads). In the region where the curves approach the horizontal asymptote, impulse becomes unimportant and the response depends only on pressure (these are quasi-static loads). In the intermediate region both pressure and impulse are significant (these are quasi-impulsive loads). The maximum spread between the curves occurs in the intermediate region. In this

More complex modes of failure exhibit the same general variation in peak response with pulse shape as these simple models (see Chapter 3).

region (along the line $P/P_o = I/I_o$) the pressure and impulse values for the rectangular and exponential loads differ by about 40 percent, and the values for the triangular and exponential loads differ by about 20 percent. For many applications, these differences are not significant.

Another model of practical interest is also concerned with the symmetric radial motion of a long cylindrical shell. In this model the material is taken to be rigid-plastic, i.e., assumed not to deform until the yield stress σ_y is reached, and then to deform with no increase in stress until the kinetic energy imparted by the pulse is dissipated and the stress falls below σ_y . Pressure-impulse curves for this model, found in the same way as for the elastic model, are shown in Fig. 1.4.

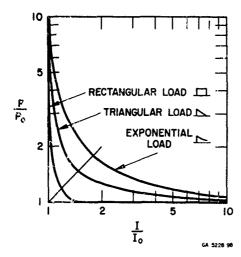


FIG. 1.3 COMPARISON OF LOADS REQUIRED TO PRODUCE THE SAME MAXIMUM DISPLACEMENT OF A LINEAR OSCILLATOR. Pois half the static load required to produce the given displacement and $I_{\rm o}$ is the ideal impulse to produce the given displacement.

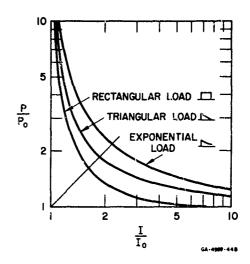


FIG. 1.4 COMPARISON OF LOADS REQUIRED TO PRODUCE THE SAME MAXIMUM DISPLACEMENT OF A ONE-DEGREE-OF-FREEDOM RIGID-PLASTIC MODEL. P_{o} is the static yield load and I_{o} is the ideal impulse required to produce the given displacement.

Again, for high pressures (intense, short loads) impulse is the important factor, and for large impulses (long loads) pressure is the important factor. The spread between the curves is similar to that in Fig. 1.3.

In summary, to an accuracy of about 40 percent, the response of these simple elastic and rigid-plastic structures to a wide range of pulse shapes depends only on peak pressure and impulse. In applications of present interest pulse shape is exponential or very nearly so and the examples above serve to demonstrate that even fairly large changes from an exponential shape produce small changes in critical curves characterized by peak pressure and impulse.

The experiments and theory presented in this report are all interpreted in terms of critical pressure-impulse curves. Theoretical estimates for these curves are made and are compared with experimental data over a wide range of pressures and impulses. In all cases the experimental data lie close enough to the theoretical curves that the general shape and asymptotes predicted by the theory are shown to be valid.

1.4 Scope of the Present Program

The program consists of three complementary efforts:

(1) generation of blast loads and measurement of the pressures resulting from diffraction around cylinders and cones; (2) experiments on a wide variety of shells to determine critical load curves; and

(3) development of theoretical models to explain observed response modes and give a means for predicting critical load curves.

Loads were produced by spherical charges of high explosives and by explosively driven shock tubes. Extensive data were recorded on pressure distributions produced around cylinders and cones using both techniques. Peak pressures ranged from 10 to 10,000 psi and durations ranged from about 0.05 to 5 milliseconds.

The shells tested were 3- and 6-inch-diameter cylinders and truncated cones which fall into the following broad categories:

- 1. Simple (unstiffened) metal shells
- 2. Simple covered shells
- 3. Stiffened metal shells
- 4. Stiffened covered shells.

The simple shells were of uniform wall thickness, with no stiffeners, and were clamped at the ends. To evaluate the influence of material properties such as elastic modulus and yield stress, shells of three widely used engineering metals were tested--6061-T6 aluminum, 2024-T8 aluminum, and AZ31B magnesium. Simple covered shells were inade of these same metals assembled into three nonmetallic covering materials. To bracket the critical load curves to be expected from a very broad range of heat shield properties, the covering materials used had properties ranging from brittle to fibrous to very flexible, and consisted primarily of Plexiglas, Micarta, and solid neoprene rubber, respectively. A few shells, supplied by LMSC, were made with tapewound refrasil, carbon phenolic, and NOMEX covers. The radius-tothickness ratios of both the covered and uncovered metal shells ranged mainly from 25 to 100, but a few tests were performed on uncovered shells with ratios as high as 250. The covers all had a radius-tothickness ratio of 12. The great majority of the shells were made with an unsupported length equal to the diameter, but for some, both uncovered and covered, the lengths ranged from two thirds to two diameters.

1...

lector's assessed

The stiffened metal shells were all made of 6061-T6 aluminum and, again, were clamped at the ends. Three types of stiffening were used: integral ring stiffeners, rigid-foam polyurethane (completely filling the shells), and sandwich shells with polyurethane as a filler between the walls. Equivalent radius-to-thickness ratios (based on a uniform aluminum wall of the same weight) ranged from 25 to 86. Stiffened covered shells were made using Plexiglas and Micarta.

Throughout the experiments both no-damage and severe-damage data were obtained. In the simple shell experiments (u. covered and covered) enough data were obtained to estimate the complete critical pressure-impulse curves. With the general shape of the critical curves thus established, sufficient experiments on stiffened shells were run to determine the critical load curves in the quasi-impulsive and quasi-static regions. About 650 experiments were run in all.

Experimental observations showed that over the entire range of pressure and impulse most of the uncovered shells and many of the covered shells failed by dynamic buckling. The theoretical investigation therefo .oncentrated on this type of failure. The investigation was aided by the results of a theory found to explain the buckling observed in re-entry vehicles and satellites subjected to impulsive loads [11-13], but previously observed buckling under quasi-impulsive and quasi-static loads [9, 10] had been summarized only with empirical formulas which were of little value here. In the present work, the concepts previously set forth to explain buckling from impulsive loads are extended to include quasi-impulsive and quasi-static loads. The problem is mere difficult because both pressure and impulse are important, and because the length of the shell becomes very important as the load duration becomes long. Nevertheless, a reasonably simple theory is established to explain the observed modes of failure and to calculate critical load curves over the entire pressure-impulse range.

1.5 Organization of the Report

The report is organized to give the reader three levels of detail. For the general reader, results and conclusions of the blast pressure measurements and the shell response experiments are given in Chapter 2, supplemented by a brief summary of the buckling theory, photographs of typical damaged shells, and the general levels of pressure and impulse at which failure occurs.

A more detailed discussion of the results is given in the main body of the report. Chapter 3 describes the experimental techniques and gives photographs of measured pressure pulses and extensive calibration curves for each technique. Chapter 4 describes all of the shells tested in the program and lists them in outline form, proceeding generally from simple to complex, to give the reader a better understanding of the scope of the structural experiments. The reader is also introduced to the shell and shot nomenclature to be used throughout the remainder of the report, and a tabulation is given of results

from all the shell experiments, following the outline form. Chapters 5, 6, and 7 give descriptions and photographs from the experiments on simple metal shells, simple covered shells and complex shells, respectively. Chapter 8 gives the derivation of the shell buckling theory and shows the effects on buckling thresholds of variations of load shape and distribution and of shell dimensions and materials. Chapter 9 gives the results of experiments in which the transient buckling of simple metal shells was observed with ultra-high speed motion pictures and with strain gages.

Finally, for the reader interested in the details of the experimental arrangements, Appendix A describes the pressure instrumentation and the heavy-walled pressure models, Appendix B describes the support arrangements for the structural models, and Appendix C describes the operation of the shock tubes and gives a theoretical interpretation of the measured pressures on the cylindrical models. A chronological list of all the experiments is given in Appendix D, but for most readers the listing in Chapter 4 will be more convenient.

2. SUMMARY

The results of the program are summarized in four parts:
(1) blast pressure measurements; (2) response of simple (unstiffened)
metal shells; (3) response of simple covered shells; and (4) response
of stiffened shells.

2.1 Blast Pressure Measurements

Quasi-impulsive loads were produced by 1/2- and 4-pound spherical high explosive (HE) charges, and quasi-static loads were produced by explosively driven shock tubes, one 20 feet long and 2 feet in diameter and another 30 feet long and 4 feet in diameter. To determine structural response in terms of the loads applied to the models, pressure distributions around rigid cylinders and cones were measured for each technique.

For both the HE spheres and the shock tubes the pressure distributions around the cylinders and the 9° cone were found to be given approximately by

$$p = (p_R - p_I)\cos^2\theta + p_I$$
, $-90^\circ < \theta < 90^\circ$

$$= p_I$$
 $90^\circ < \theta < 270^\circ$

where p_R is reflected pressure (from a rigid, flat wall), p_I is incident (free-field) pressure, and θ is angular position on the model with $\theta = 0$ facing the oncoming shock.

Over the front face (-90° < θ < 90°) the pressure rises suddenly upon arrival of the shock and subsequently decays to zero. For HE spheres the decay is exponential, and for the shock tubes the decay is nearly exponential, with an intermediate plateau of duration

corresponding to the length of the driver section. By contrast, over the back face the pressure builds up gradually to a maximum (in about 1 millisecond for the shock tubes) and then decays to zero.

For the high shock strengths required to damage shells of interest here, the reflected pressure is much greater than the incident pressure (i.e., $p_R >> p_I$). Furthermore, as shown throughout this report, structural response does not depend strongly on the details of the pressure distribution. Thus, for calculation of structural response it is adequate to describe the pressure on the shells and cones by the product of the pressure distribution of (2.1) and the time variation of the pressure at $\theta = 0$ (i.e., neglecting the change in shape of the small back face pressures).

Observed peak pressures and impulses at $\theta = 0$ on a 6-inch-diameter cylinder are given in Fig. 2.1. For the explosive spheres (the two curves on the left), distance from the charge varies along the curves, giving a pressure range of 10 to 10,000 psi and an impulse range of 500 to 20,000 taps. ** These impulses are about half those for reflection from a flat wall at the same distance.

The three curves on the right give peak pressures and impulses from the shock tubes operating at lengths of 10 and 20 feet for the 2-foot-diameter tube, and 30 feet for the 4-foot-diameter tube. Along these curves charge ratio tvaries giving peak pressures ranging from 20 to 3000 psi and impulses ranging from 5000 to 500,000 taps.

See Chapter 3 and Appendix C or a description of explosively driven shock tubes.

^{** 1} tap = 1 dyne-sec/cm² = 14.5×10^{-6} psi-sec.

TSee Chapter 3.

Charge ratio is the weight of the explosive charge in the tube normalized to the weight of the ambient air in the driver (explosive) end of the tube. A charge ratio of 1 corresponds to about 1.5 pounds of explosive in the 2-foot tube at 20 feet, and to 10 pounds in the 4-foot tube.

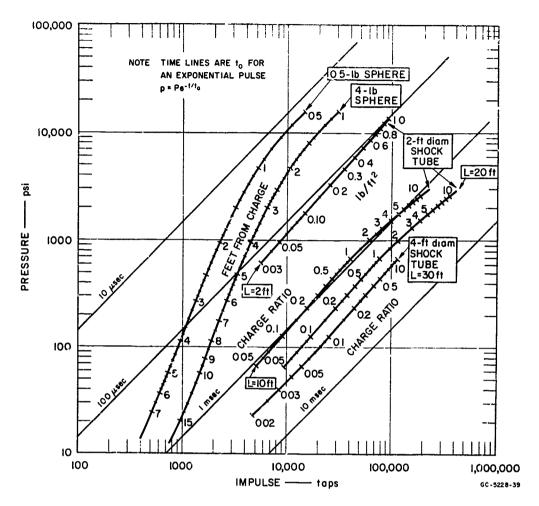


FIG. 2.1 PRESSURES AND IMPULSES FROM HIGH EXPLOSIVE SPHERES AND SHOCK TUBES (measured on a 6-inch-diameter cylinder at a gage facing a lateral blast)

The curve below that for 4-pound spheres gives pressures and impulses obtained with flat charges placed 2 feet from the mouth of the 2-foot tube, with charge weight in lb/ft^2 as a parameter.

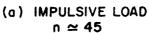
The range of pressures and impulses provided by these techniques was sufficient to cover the range from no-damage to severe damage for all the shells of interest. The pressures and impulses given are accurate to within approximately ± 15 percent.

STATE OF THE PROPERTY OF THE P

2.4 Response of Simple Metal Shells

The simple metal shells exhibited dynamic buckling as indicated in Fig. 2.2. Typically, the wavelength of the buckles was short for impulsive loads and increased monotonically with pulse duration until at long durations the wavelength of the buckles was comparable to that observed in static buckling.







(b) QUASI-IMPULSIVE LOAD n ≈ 13



(c) QUASI-STATIC LOAD n ≈ 7

FIG. 2.2 TYPICAL BUCKLING PATTERNS IN THIN CYLINDRICAL SHELLS SUBJECTED TO LATERAL BLAST LOADS OF VARIOUS DURATIONS

To predict buckling modes and critical loads, the dynamic buckling theory of Chapter 8 was developed. For impulsive loads the buckle wavelengths are much chorter than the shell length, and shell length can be neglected in the theory. Then the buckling threshold impulse is given by

$$I_o = a \left(\frac{95}{K}\right)^{1/4} \rho c \epsilon_y^{1/2} \left(\frac{a}{h}\right)^{-3/2}$$
 (2.2)

where a is radius, ρ is density, $c=\sqrt{E/\rho}$ is wave velocity, E is elastic modulus, ε_y is yield strain, and a/h is radius-to-thickness ratio. The constant K is a material parameter defined as the slope beyond yield of the curve of σ/E_t versus ε , where σ is compressive

stress, E_t is tangent modulus, and ε is compressive strain. This factor appears because, except for very thin shells (a/h > 500) which are not covered by (2.2), impulsive buckling takes place during circumferential plastic flow and resistance to flexure is governed by the post-yield tangent modulus. The shell model on which (2.2) is based is therefore called the "tangent-modulus" model.

For quasi-static loads buckling depends mainly on peak pressure, and it was found both experimentally and theoretically that the dynamic buckling pressure is very nearly the same as the uniform lateral static buckling pressure. For the shells tested in the current program this pressure is given by

$$P_o = 0.92 E \left(\frac{a}{L}\right) \left(\frac{a}{h}\right)^{-5/2}$$
 (2.3)

where L is shell length and other quantities are as defined previously.

For quasi-impulsive loads, pressure, impulse, and shell length must all be considered simultaneously. Shells of present interest buckle elastically in this range, so the static theory on which (2.3) is based was merely extended to include inertia forces. This is called the "elastic" model. To find the critical loads, the equations of motion of the flexural modes were integrated numerically.

The resulting critical curves for buckling over the entire range of loads are shown in Fig. 2.3 for 6-inch-diameter shells of 6061-T6 aluminum with L/D = 1 and various values of a/h. Each curve consists of two branches, one at high pressures from the tangent-modulus model and one at large impulses from the elastic model. Near the intersection of these branches the curves are dashed because the tangent-modulus model breaks down when buckling no longer takes place during the initial inward motion, and the elastic model breaks down when the membrane strain exceeds the yield strain. However, in Chapter 8 a more complex "strain-reversal" model shows that these effects do not significantly

change the critical curves. Also given in Chapter 8 are empirical formulas for generating critical curves for shells of other dimensions and materials.

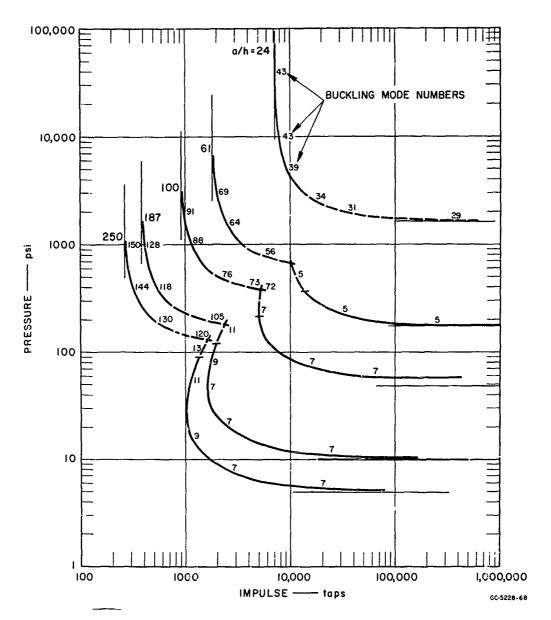


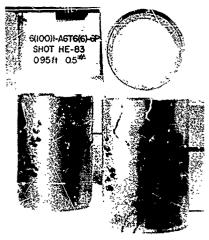
FIG. 2.3 CRITICAL CURVES FOR BUCKLING OF 6061-T6 ALUMINUM SHELLS D = 6 INCHES, L/D = 1, AND VARIOUS α/h

Experiments on shells with a/h = 24. 61, and 100 gave buckling loads within 50 percent of the critical curves from the theory over the entire range of pressure and impulse. The experiments also showed that, for quasi-impulsive loads, a load increment of about 50 percent was required to change the response from barely perceptible deformation to large buckling deformations, and in some cases to shearing and tearing of the shell. For quasi-static loads, a load increment of only a few percent was sufficient to change the response from minor damage to severe buckling, as in static buckling. A further increase in load of 20 to 50 percent, depending on the shell parameters, resulted in complete destruction.

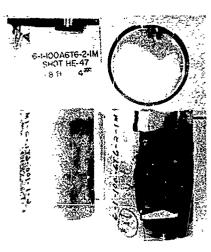
2.3 Response of Simple Covered Shells

As for the simple metal shells, sufficient experiments were performed with simple covered shells to determine critical pressure-impulse curves for buckling or cracking. The subshells were 6061-T6 aluminum of a/h = 24, 61, and 100 having covers of Plexiglas, Micarta, and neoprene rubber, with a/h = 12. With the shape of the curves thus established, less extensive experiments were run on shells with 2024-T8 aluminum and AZ31B magnesium subshells and with tape-wound covers.

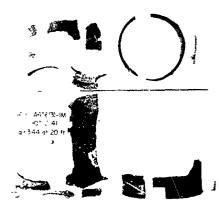
Typical damage from quasi-impulsive and quasi-static loads is shown in Fig. 2.4. Under quasi-impulsive loads the Plexiglas covers shatter (Fig. 2.4a) and the Micarta covers crack (Fig. 2.4b). Under quasi-static loads both the Plexiglas- and Micarta-covered shells disintegrated (Fig. 2.4c). Shells with tape-wound covers of either refrasil or carbon phenolic typically delaminated between the tape layers. Under quasi-impulsive loads, delaminations appeared over the entire surface facing the blast. Under quasi-static loads, delamination was invariably more extreme at one end, as shown in Fig. 2.4(d). The latter damage is associated with the direction of the oblique winding which results in higher between-tape stresses near one end. Shells with neoprene rubber covers buckled in the manner of the uncovered shells.



(a) PLEXIGLAS SHATTERING FROM A QUASI-IMPULSIVE LOAD



(b) MICARTA CRACKING FROM A QUASI-IMPULSIVE LOAD

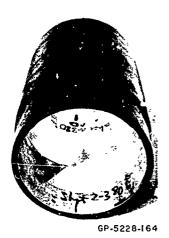


A616(3)-IM Y-IOT 2 41 a r 344 At 20 ft

(c) DISINTEGRATED SHELL FROM A QUASI-STATIC LOAD







Lİ

(d) DELAMINATION AND SHEARING OF A TAPE-WOUND SHELL FROM A QUASI-STATIC LOAD

FIG. 2.4 TYPICAL FAILURE OF COVERED SHELLS FROM BLAST LOADS

The loads which produced the damage in Fig. 2.4 were always within 50 percent of the loads that produced no damage. Under quasiimpulsive loads from HE spheres, threshold cracking and severe shattering of the Plexiglas shells occurred at virtually the same load: threshold and severe cracking of the Micarta shells were separated by a load increment of about 30 percent for subshells with a/h = 100and 61, and by about 50 percent for a/h = 24. Under quasi-static loads, threshold cracking and severe damage of both Plexiglas - and Micartacovered shells were separated by load increments smaller than the 10 to 20 percent increment between experiments. Load increments between threshold and severe damage for the tape-wound shells were generally larger, being about 50 percent for quasi-impulsive loads and about 30 percent for quasi-static loads. These load increments are higher than those for the Micarta-covered shells because of the higher resistance to longitudinal cracking, resulting in less tendency for the blast to crack and peel off the cover.

An example of the critical curves for various covered shells is given in Fig. 2.5 for a subshell of a/h = 61. The curves are typically hyperbolic in shape. The Micarta-covered shells are strongest, followed by the Plexiglas-covered shells, and the rubber-covered shells. Data from the Plexiglas- and Micarta-covered shells were found to be approximated within the ± 15 -percent accuracy of the data by the formula

$$(\frac{P}{P_0} - 1)(\frac{I}{I_0} - 1) = 1$$
 (2.4)

The pressure and impulse asymptotes for the Micarta-covered shells in Fig. 2.5 are $P_0 = 1300$ psi and $I_0 = 9000$ taps. This same curve can be used as an estimate for the critical curves for the shells with tape-wound covers of refrasil and carbon phenolic (see Chapter 6 for a more detailed comparison).

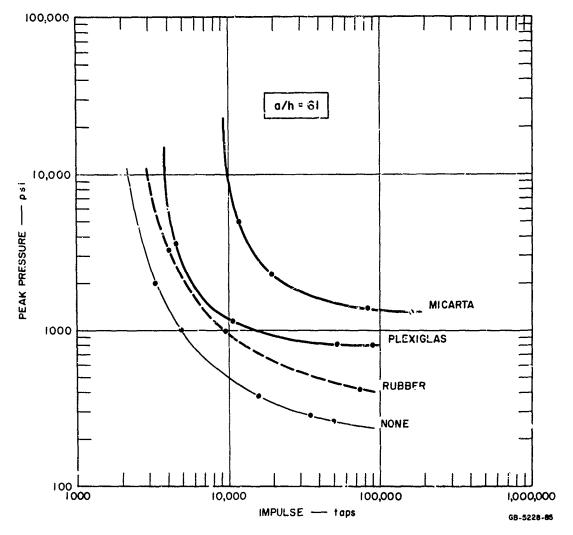


FIG. 2.5 CRITICAL FRESSURE-IMPULSE CURVES FOR BUCKLING OR CRACKING OF COVERED SHELLS (6061-76 aluminum subshells, L/D = 1, a/h = 61)

2.4 Response of Complex Shells

MEDICAL CONTRACTOR CON

Experiments on uncovered shells stiffened with circumferential ribs and having a/h = 100 and a/h = 50 showed that such stiffening can significantly increase the buckling pressure under quasi-static blast loads. For a/h = 100 the efficiency (based on the uniform lateral pressure required to produce hoop yield) increased from 17 percent with no ribs to 52 percent with ribs. For a/h = 50 the efficiency increased from 40 percent to 80 percent. The lower efficiency of the

ribbed shell with e/h = 100 was the result of shear buckling between the last rib and the support, caused by overall beam action shear stresses. Thus, in this shell, to utilize more fully the yield strength of the material, the thickness near the supports should be increased.

Uncovered shells were also found to be strengthened by stiffening with internal foam or by sandwich construction, but the efficiencies,
based on the yield pressure of a simple tube of equal weight, were
only about 40 percent compared to 80 percent for ribbed shells. The
low efficiency for the sandwich shells was unexpected and no satisfactory
explanation has been reached.

Covered shells stiffened by circumferential ribs or by sandwich construction were less efficient than covered shells with no stiffening. To the accuracy of the data, simple shells with a/h = 24, 61, and 100, covered with either Plexiglas or Micarta, all had efficiencies of about 65 percent. The efficiency of the ribbed shells was about 55 percent, and that of the sandwich shells was about 50 percent. However, in the Micarta-covered shells the ribs increased the pressure increment between threshold and severe damage from about 10 percent for the simple subshell to 50 percent for the ribbed subshell.

The decrease in efficiency with stiffening in the covered shells is attributed to the short, thick characteristics of the shells under investigation. In all these shells the overall length-to-diameter ratio was L/D = 1 and the covers had a/h = 12. The stiffening provided by such thick covers is already adequate to suppress buckling, and stiffening the substructure is not the most efficient way to increase the strength. Instead, it is likely that a local increase in thickness near the supports in a simple metal subshell would provide the strongest design.

The essential conclusion from all of the tests on covered shells is that the heat shield of a re-entry vehicle significantly increases the overall strength of the vehicle to resist surface loads. Thus, heat shield strength will significantly affect the design of a hardened vehicle.

2.5 Concluding Remarks

Peak pressure and impulse have been identified as the most significant load characteristics for structural response of shells subjected to transient surface loads. Critical curves in the pressureimpulse plane which separate regions of no damage from regions of severe damage are hyperbolic in shape. For buckling of simple metal shells these curves can be predicted by a reasonably simple theory. For both simple nietal shells and covered shells critical curves have been established experimentally over a wide range of parameters. In all cases, the gradient of damage across the curves was found to be very steep. Under impulsive and quasi-impulsive loads, doubling the load above the threshold of damage invariably results in complete destruction. Under quasi-static loads a 50-percent increase in load above that which produces threshold damage insures destruction, and for some structures under quasi-static loads, threshold damage and severe damage occu virtually the same load.

3. BLAST SIMULATION AND PRESSURE MEASUREMENTS

The blast pulses investigated in this program were obtained with spherical charges of high explosive, spherical charges of oxyacetylene gas, and explosively driven shock tubes. In this chapter the pressure pulses obtained from each technique are discussed and the general procedures for preparing and firing the shots are described.

For each technique, pressures on cylindrical models were measured as a function of angular position on the model. Measurements were made over a range of pressures, and curves were ultimately generated in the pressure-impulse plane for direct use in determining the sure-safe and sure-kill boundaries for the structural shells central to the theme of this investigation. Details of the pressure instrumentation system are given in Appendix A and some theoretical calculations on the pulses to be expected from the shock tube are given in Appendix C. Methods of supporting the instrumented and structural models are described in Appendix B.

3.1 General Remarks

The most significant parameters affecting blast loads obtainable with explosives are blast wave geometry (spherical, cylindrical, or plane), charge size, and charge-to-target distance. By varying these parameters it is possible to obtain loads covering the entire range of peak pressure and pulse duration necessary to determine critical load curves for shell structures of interest. For the shells in the current program this load range was obtained with charges not exceeding 10 pounds.

To the level of accuracy of present interest, blast waves from explosives are not affected significantly by the type of explosive used or by the density of the air used to transmit the blast wave. Differences in explosives are masked by the effects of the air between the charge and the target. The density of the air used to transmit the blast wave primarily affects the ratio of dynamic pressure to static pressure. The techniques described here are for air at sea level conditions, which result in a lower ratio of dynamic-to-static pressure and hence a lower ratio of front surface to back surface pressures than occurs in encounters above sea level. However, even at sea level conditions the ratio of front surface to back surface pressures on the model shells at failure is so high that for practical purposes the pressure distribution is the same as in a high altitude encounter. Also, as demonstrated in Chapter 8, for many situations, and in particular for the shells under investigation, spatial distribution is of secondary importance in determining critical load curves.

Spherical HE charge were used for moderately short pulse durations from 0.1 to 1.0 millisecond using mainly charge weights of 1/2 and 4 pounds. Spheres were used because they are relatively easy to make and because extensive data on incident and reflected pressures from spheres are available [14] so that measurements of diffracted pressures and structural testing could be run simultaneously.

Gas charges were investigated because preliminary calculations suggested they would provide somewhat longer duration pulses than the HE spheres. However, it was found by experiment that gas charges did not provide a range of pulses significantly different from those available from HE charges of comparable weight. Consequently, spherical gas charges were not used in the main structural response program.

Three types of pressures will be referred to throughout this report; incident, reflected, and diffracted. Incident pressure is the pressure behind a free-moving shock, as measured by a side-on pressure gage. Reflected pressure is the pressure experienced by an infinite rigid wall normal to the flow, as measured by a face-on gage. Diffracted pressure is the pressure experienced on a finite obstacle (such as a cylinder) over which the shock passes.

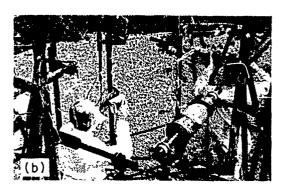
Shock tubes were used for pulses of durations from 0.5 to 5 milliseconds. As for the HE spheres, considerable data were available on explosively driven shock tubes [15] and the pressures and durations of interest were easily produced by charges of less than 10 pounds. Two tubes were used, one 4 feet in diameter and 30 feet long and the other 2 feet in diameter and 20 feet long. The smaller tube was used to give peak diffracted pressures above 500 psi because in the larger tube excessive charge weights would have been required to obtain these high pressures.

3.2 Spherical High Explosive Charges

The spherical HE charges were made of Composition C-2, which has a putty-like consistency at room temperature. Charges were formed in an aluminum mold which was later cooled to increase the rigidity of the explosive so that it would maintain its spherical shape upon removal for firing. An SRI PL2 detonator (made with a paper tube rather than metal, to eliminate fragments) was placed at the center of the charge by drilling into the sphere to a fixed distance with a coring tool. With the detonator in place, the explosive was packed around the leads and reshaped into the mold.

All shots were fired with the charge suspended 5 feet from ground level, as shown in Fig. 3.1. It was supported from the bottom by a styrofoam block held in place by thin wires on a telescoping pipe for height adjustment. Models were supported on pipe stands as shown. Vertical adjustment of the models was made by a carriage attached to the vertical uprights of each frame with U-bolts and fine horizontal adjustment was made by telescoping arms on the carriage. Model-to-charge distance was easily controlled to \pm 0.1 inch. The models were always set at the same height as the HE sphere so that any perturbations in spherical symmetry of the blast caused by the styrofoam HE support block would be the same for any model in the horizontal plane. However, no significant asymmetries were observed in either the pressure measurements or the model shots. Accurate





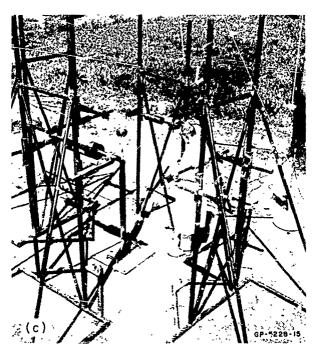


FIG. 3.1 GENERAL ARRANGEMENT OF SPHERICAL HE SHOTS

- (a) Locating cylindrical test models using a dummy sphere
- (b) Adjusting height and angular orientation of models
- (c) Charge in place with four models and stands

angular crientation of the models relative to the charge was maintained with a crescent-shaped pointer support aligned to a $\theta = 0$ line scribed on the model. The model was rotated until the pointer sighted at the center of a dummy hemisphere, as shown in Fig. 3.1(b).

An example of the diffracted pressure pulses measured on a 6-inch-diameter rigid cylinder is shown in Fig. 3.2. These are for

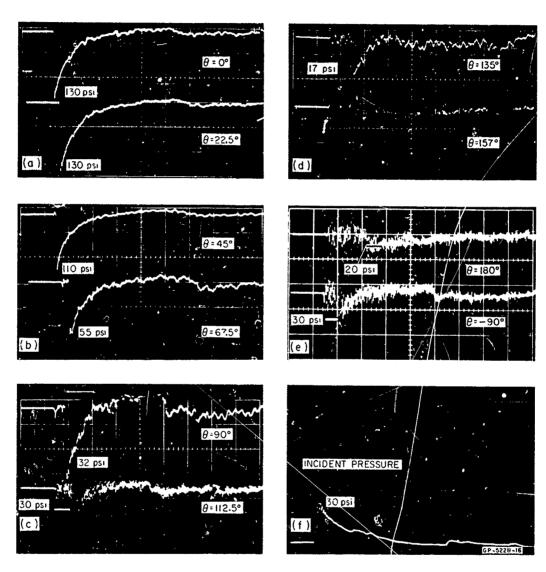


FIG. 3.2 PRESSURES ON A 6-INCH-DIAMETER CYLINDER 4 FEET FROM A 0.5-POUND C2 SPHERE (sweep rate 200 μ sec/cm, all traces; triggers staggered for ease in reading)

THE STATE OF STREET STATES AND THE STATES OF STATES OF STATES AND
a distance of 4 feet from the center of a 0.5-pound charge to the front surface of the cylinder. The angle θ is measured on the cylinder from the point facing the charge to the gage location, as shown in Fig. 3.3. Figure 3.2(f) gives the incident pressure at 4 feet, measured with an Atlantic Research LC-33 pencil blast gage. All of the cylinder pressures were measured with Kistler Model 601H quartz gages, with their signals filtered by a 96-kc low-pass filter to remove gage ringing oscillations. Further details of the pressure measurement techniques are given in Appendix A.

As will be seen later, the peak pressure at $\theta=0^\circ$ is the same as the peak reflected pressure from a flat wall. From Fig. 3.2 it is apparent that the peak pressure drops off with increasing angle θ until at $\theta=\pm90^\circ$ it has fallen to approximately the incident or side-on pressure measured by the blast gage. Over the back side of the cylinder the peak pressure appears to remain below the incident pressure, but at small distances from the charge it is difficult to read the back side pressures because they are so small relative to the gage oscillations caused by mechanical vibrations. In Fig. 3.2, the oscillations preceding the shock arrival at gages where $\theta \neq 0$ are caused by shocks transmitted through the model and subsequent vibrations of the model and gage. Examples of unfiltered traces are shown in Fig. 3.2(e).

Data from a series of records like those in Fig. 3.2 are summarized in Table 3.1 and plotted against distance from charge in Fig. 3.3. Scatter of the data is generally within about \pm 15 percent of the nominal pressure, but to get the best estimate of the variation in pressure with angle, the data were first smoothed by straight lines, as in Fig. 3.3. Using pressures from these straight lines, plots of pressure versus angle at various distances can be made as in Fig. 3.4. For comparison, Figs. 3.5 and 3.5 give peak incident and reflected (flat wall) pressures and impulses from [14]. Comparing these with Fig. 3.3 or Fig. 3.4 shows that, within experimental accuracy, the peak pressure at $\theta = 0^{\circ}$ is equal to the reflected pressure given in Fig. 3.6, and the peak pressure at $\theta = 90^{\circ}$ is close to the incident pressure in Fig. 3.5.

ここのないながれるで とのなる

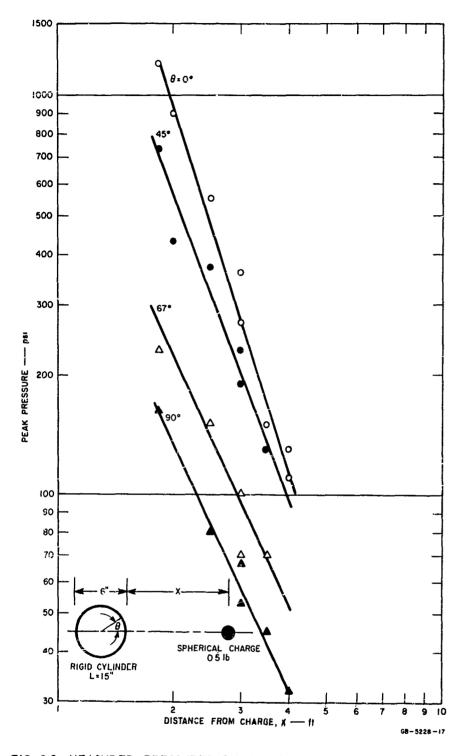


FIG. 3.3 MEASURED PRESSURES ON A 6-INCH-DIAMETER CYLINDER vs. DISTANCE FROM A 0.5-POUND SPHERE

Table 3.1

MEASURED PRESSURES ON A 6-INCH-DIAMETER CYLINDER AT VARIOUS DISTANCES FROM A 0.5-POUND CHARGE

Distance X (ft)	Shot No.	Angle θ Degrees							
		0	22.5	45	67.5	90	112.5	135	180
1.0	73	3700*		1400*	750*				
1.2	74	3200*	16u0 [*]	1100*	400*	300*	300*		
1.5	67	2300*		800	400	130*			
1.83	80	1200	1100	730	230	160	120		
2,0	61	900		430		120		ļ	50
2.5	62	550		370	150*	80*			
3.0	64	360		230	100	67		28	37
3.0	79	270	260	190	70	53	35*	22*	35*
3.5	65	150		130	70	45		22	25, 33
4.0	78	135	135	110	55	32	30	17	20

^{*}Gage oscillations resulted in poor accuracy.

A similar series of experiments was carried out with 4-pound charges with analogous results. An example of the pressures from this series is shown in Fig. 3.7 for a 6-inch-diameter model 6 feet from a 4-pound charge. Tests with both 0.5-pound and 4-pound charges were also run on 3.5-inch-diameter cylinders. Peak pressures were the same as for the 6-inch-diameter, and impulses at large distances were somewhat smaller.

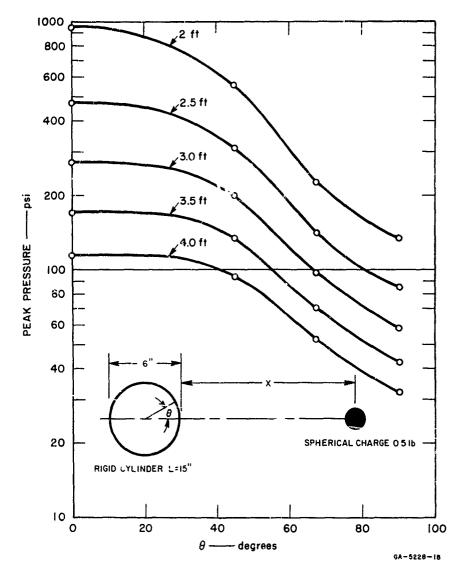


FIG. 3.4 PRESSURE DISTRIBUTION OVER FRONT FACE OF CYLINDER (smoothed data from 0.5-pound charge, Fig. 3.3)

The state of the s

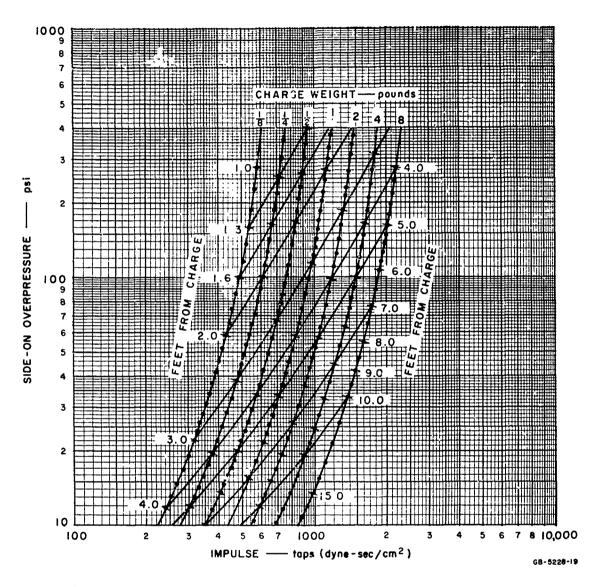


FIG. 3.5 INCIDENT (side-on) PRESSURE AND IMPULSE FROM PENTOLITE SPHERES (1 Tap = 14.5×10^{-6} psi-sec)

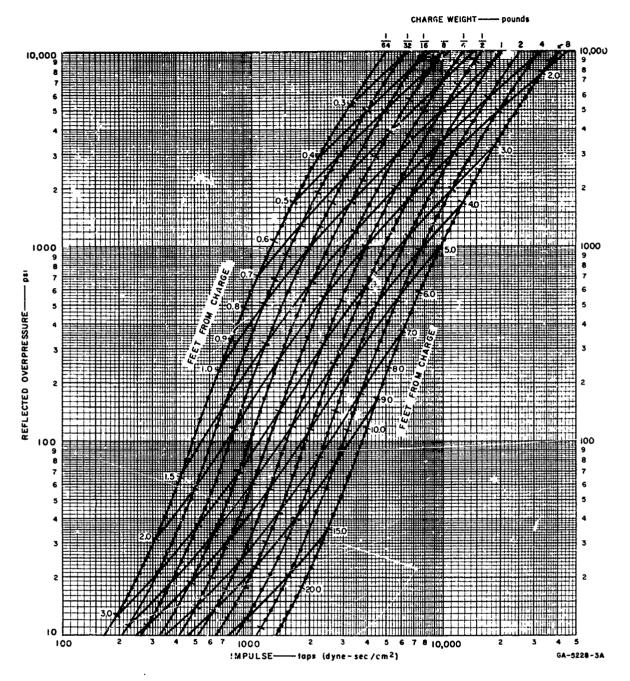


FIG. 3.6 REFLECTED (flat-wo!!) PRESSURE AND IMPULSE FROM PENTOLITE SPHERES

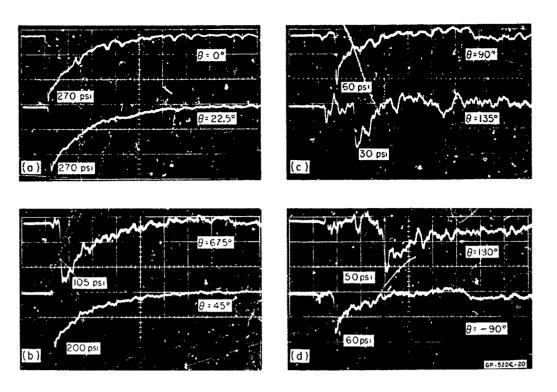


FIG. 3.7 PRESSURES ON A 6-INCH-DIAMETER CYLINDER 6 FEET FROM A 4-POUND C2 SPHERE (sweep rate 100 µsec cm, all traces, filtered at 96 kc)

These observations lead to a very simple empirical formula for peak blast pressures around a cylinder. Over the front surface, the curves in Fig. 3.4 are closely approximated by

$$p = (p_R - p_I) \cos^2 \theta + p_I$$
, $-90^\circ < \theta < 90^\circ$ (3.1a)

where p_J and p_R are the incident and reflected pressures at the given distance from the charge as plotted in Figs. 3.5 and 3.6. *Over the back surface, for use in a shell response problem it is sufficient to take

$$p = p_I$$
, $90^{\circ} < \theta < 270^{\circ}$ (3.1b)

The cos θ variation in pressure is consistent with Newton's highly simplified model of elastic rebound of the gas molecules.

The peak pressure occurs at slightly later times as θ increases toward $\theta = 180^{\circ}$ but, for $-90^{\circ} < \theta < 90^{\circ}$, this time delay is small compared to the total pulse duration. Since the response of the shell is governed almost entirely by the front surface pressure (see Chapter 8) it is reasonable for response problems to assume that

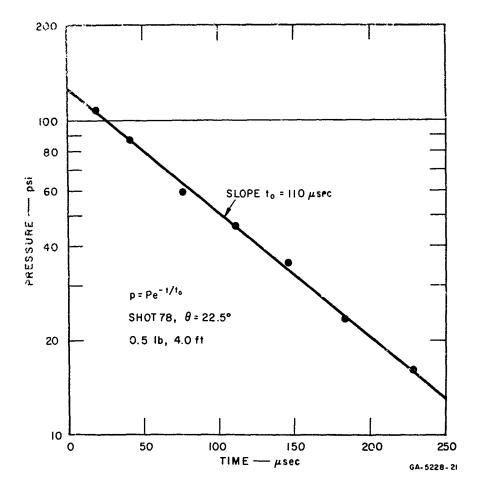
$$p(\theta, t) = \left[(1 - \frac{p_I}{p_R}) \cos^2 \theta + \frac{p_I}{p_R} \right] p_o(t) - 90^\circ < \theta < 90^\circ$$

$$= \frac{p_I}{p_R} p_o(t) \qquad 90^\circ < \theta < 270^\circ$$

where $p_{o}(t)$ is the measured variation of pressure with time at $\theta=0$ and, as already observed, $\rho_{o}(0)=p_{R}$. From Figs. 3.2 and 3.7, the time variation of pressure over the back surface differs somewhat from the front face pressure variation but again, the back side pressures have a negligibly small effect on the overall shell response and the time variation in Eq. (3.2) is taken to be uniform around the shell.

It remains to determine the time variation of pressure $p_o(t)$. In [14] it was reported that both the incident and reflected pressures decayed exponentially with time, so it is reasonable to expect that the diffracted pressures here also decay exponentially. To check this conjecture, data from oscilloscope traces as in Figs. 3.2 and 3.7 were replotted on semi-log paper as shown in Fig. 3.8. The data fall very close to a straight line, with the slight differences being attributed to errors in reading the scope traces.

Impulses at $\theta=0^{\circ}$ were determined from these semi-log plots by calculating time constants t_{\circ} in $p=Pe^{-t/t}$ o from the slopes and forming $I=Pt_{\circ}$. This was felt to be the most accurate procedure, first because it gave a rational basis for smoothing the sometimes oscillatory individual pressure traces, and second because it gave an accurate method of extrapolating to the actual peak pressure. The peak pressures measured directly from the traces were always low

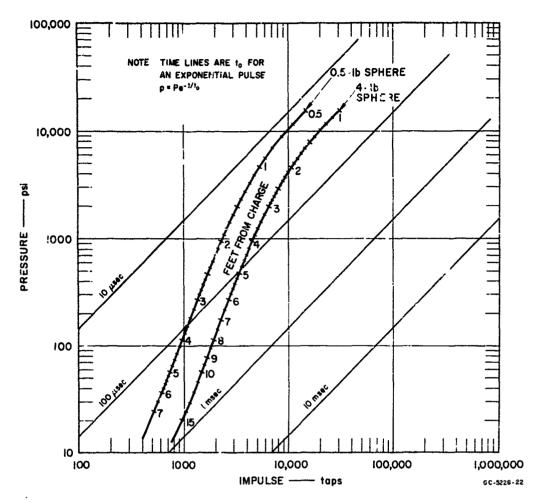


Seeking and a single of the seeking

FIG. 3.8 SEMI-LOG PLOT OF PRESSURE PULSE

because of the rise time of the gages and filter system, but the sudden jump of the traces was assumed to be an accurate measure of the true shock arrival time, so the semi-log plots could be extrapolated back to this time as a best estimate of the true peak pressure. Differences between the extrapolated pressure and the peak pressure directly from the traces ranged from 10 to 20 percent.

Figure 3.9 gives the pressures and impulses resulting from these calculations for both the 0.5-pound and 4-pound charges. Comparing these with the reflected pressures and impulses from a flat wall (Fig. 3.6) we see that the peak pressures are the same as the reflected pressures, but that the impulses are about 60 percent of the



THE REAL PROPERTY OF THE PROPE

FIG. 3.9 PRESSURE AND IMPULSE ON A 6-INCH-DIAMETER CYLINDER FROM HE SPHERES

reflected impulses. This is consistent with the expectation that the initial pressure should be the same at $\theta = 0^{\circ}$ on the curved cylindrical surface as on a flat wall, and that as the shock diffracts around the cylinder the pressure decays faster than if the flow were completely reversed as from a flat wall.

Pressures at distances less than about 1.5 feet for 0.5-pound spheres and about 3.0 feet for 4-pound spheres were very difficult to measure accurately because the small pulse durations were comparable to the periods of the gage oscillations and filter time constants. Pressures and impulses at smaller distances were therefore plotted in

Fig 3.9 using peak reflected pressures from Fig. 3.6 and impulses 60 percent of those in Fig. 3.6. The same procedure was used for distances greater than 8 feet because these low pressures were beyond the range of primary interest here and little data were obtained. Impulses in this range are probably somewhat overestimated because at greater distances one would expect the diffracted impulse to become a smaller fraction of the reflected impulse.

3.3 Spherical Gas Charges

In an attempt to produce blast pulses of longer duration with reasonably small charge weights, experiments were run on spherical charges of oxyacetylene gas which are quite large for a given weight limitation. The arrangement is shown in Fig. 3.10. Charges were

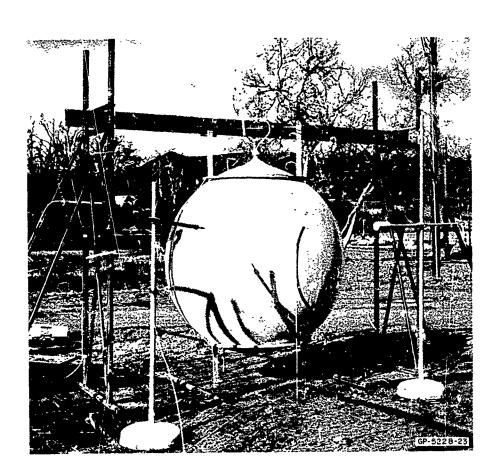
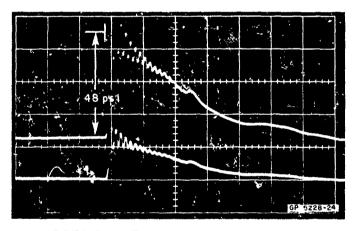


FIG. 3.10 GENERAL ARRANGEMENT FOR A 70-INCH-DIAMETER OXYACETYLENE GAS SPHERE

made using weather balloons inflated to 35 and 70 raches in diameter at pressures a few inches of water in excess of atmospheric pressure, and were centrally initiated with an electric spark. Both incident pressures and pressures on 6-inch-diameter models were measured, but little useful information was obtained from the cylinder pressure records because the gas charge pulse technique was discontinued before completion of the required electronic filtering system. Blast gage recordings of incident pressures, however, were quite satisfactory and provided useful data. Figure 3.11 shows a blast gage record of incident pressure 24 inches from the surface of a 35-inch-diameter sphere. Typically, these pressure traces tended to be more nearly triangular in shape rather than exponential as observed in pulses from HE spheres (compare with Fig. 3.2).

Incident pressure and impulse from a series of shots using 35-inch-diameter gas spheres are shown in Fig. 3.12. If these data are plotted in the incident pressure-impulse plane together with that for spherical HE charges (see Fig. 3.5), the resulting curve falls largely



UPPER TRACE = 2V/cm

LOWER TRACE = 5V/cm

BOTH TRACES = 100 μsec/cm

LC-33 GAGE SENSITIVITY 0.137 V/psi

FIG. 3.11 INCIDENT PRESSURE PULSE AT 24 INCHES FROM THE SURFACE OF A 35-INCH-DIAMETER OXYACETYLENE SPHERE

COLOR OF COLORS COLORS COLORS

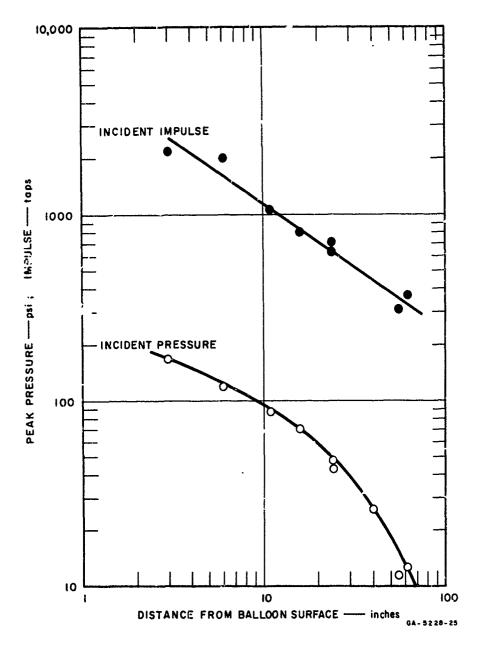


FIG. 3.12 INCIDENT PRESSURE AND IMPULSE FROM A 35-INCH-DIAMETER OXYACETYLENE SPHERE

in the area bounded by the curves labeled 4.0 feet and 5.0 feet and the 1/4-pound and 8-pound charge lines. Thus, the pressures are low compared to those available from HE spheres and the maximum impulse is comparable to that from an 8-pound HE sphere.

To estimate the diffracted pressure and impulse that would be produced on a cylinder, the reflected pressure-impulse curve corresponding to this incident pressure-impulse curve was first found. This was done by taking an equivalent HE charge weight and distance corresponding to each incident pressure-impulse point and looking up the corresponding reflected pressure-impulse point in Fig. 3.6. The reflected impulses were then reduced 40 percent (see discussion of Fig. 3.9) to obtain an estimate of the diffracted pressure-impulse around a 6-inch-diameter cylinder and the resulting curve was plotted in Fig. 3.13. The diffracted pressure-impulse curves for 0.5-pound

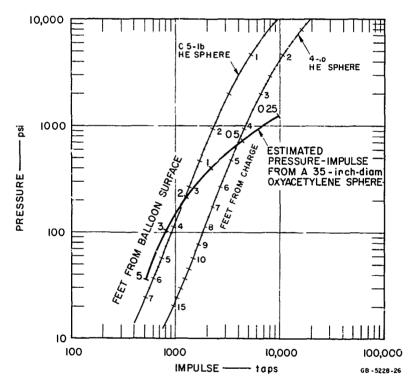


FIG. 3.13 COMPARISON OF DIFFRACTED PRESSURE-IMPULSE ON A 6-INCH-DIAMETER CYLINDER FROM GAS AND HIGH EXPLOSIVE SPHERES

こいととなるとはないからいないとうないのではないないとないないないない

and 4-pound HE spheres from Fig. 3.9 are also shown to give a graphical demonstration that any pulse produced by the gas sphere can also be produced at an appropriate distance from an HE sphere weighing no less than about 1/4 pound and no more than 8 pounds. Furthermore, the maximum pressure obtainable with an oxyacetylene sphere at one atmosphere is about 1000 psi. The only unique feature of the gas charge is that at small distances it produces a nearly triangular pulse shape. However, this was not felt to be a significant advantage in the present program and further work on gas charges was discontinued.

3.4 Explosively Driven Shock Tubes

A more direct method of obtaining pulses of duration longer than possible with spherical charges is to confine the flow from the explosive to one direction in order to eliminate loss associated with spherical expansion. For pulses of intermediate duration, this can be done with flat charges which generate a one-dimensional blast wave for distances small compared to the charge diameter [1,16]. These were not used for the present investigation because very little data were available on pulses from flat charges and the program could not wait for an extensive calibration. For longer durations, explosively driven shock tubes can be used. Several such tubes are in operation and data from the Air Force tube at the University of New Mexico [15] was used as a basis for the design of the SRI tubes.

Operation of these tubes is analogous to conventional shock tube operation in which gas in a high pressure <u>driver</u> section of the tube is suddenly released into a lower pressure <u>expansion</u> section of the tube, driving a shock wave in front of it [17]. In a conventional shock tube the driver pressure is built up slowly and then released by bursting a diaphragm. In the explosively driven tubes discussed here, the driver section is strung with lengths of primacord explosive and no membrane is used to separate the driver and expansion sections.

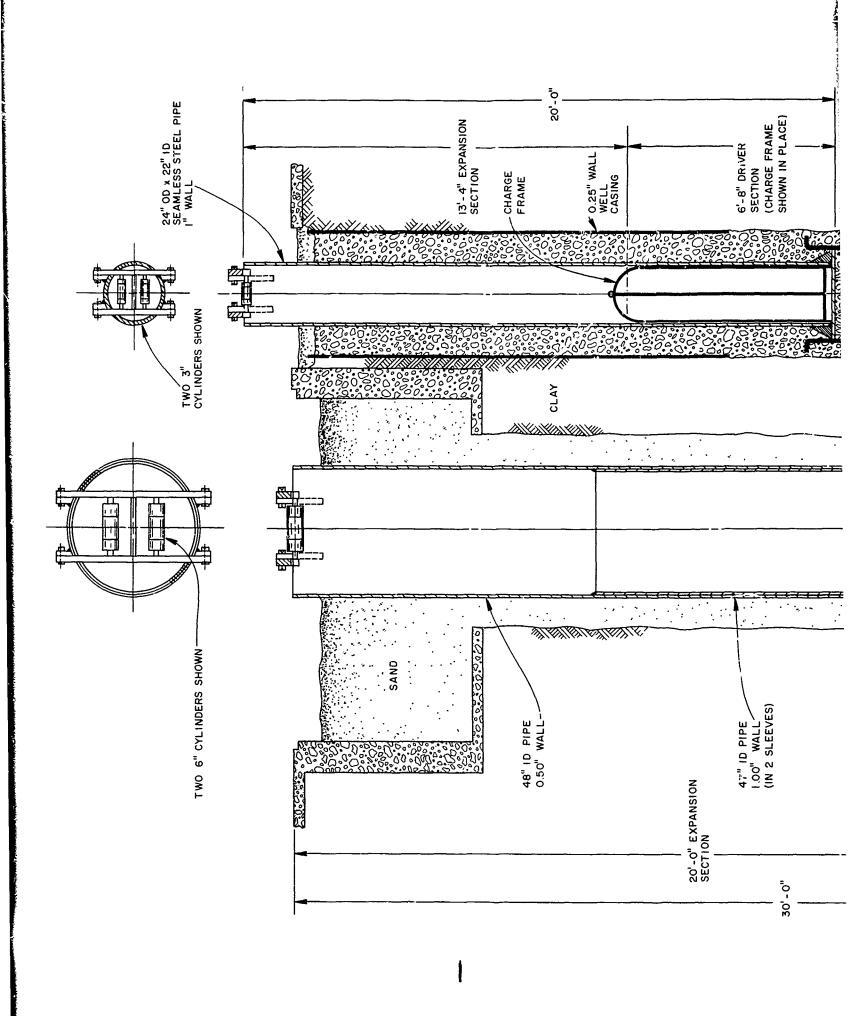
Detonation of the primacord produces a high pressure (and temperature) mixture of detonation products and air in a time short compared with the overall driver expansion time. Peak pressure, pulse shape, and pulse duration of the resulting shock wave can be varied by varying the amount of primacord, the length of the driver section, and the overall length of the shock tube.

... on a constitution of the constitution of t

3.4.1 Description of Shock Tubes and Firing Procedures

Two tubes were built in a vertical position adjacent to an existing electronic blockhouse. To minimize hazard from possible tube-wall failure, the tubes were placed in the ground with the open ends near ground level, as shown in Fig. 3.14. The "low pressure" tube is a steel pipe 4 feet in diameter and 30 feet long with a wall thickness varying from 1.25 inches in the lower 10 feet to 0.5 inch at the open end, as shown. The "high pressure" (2-foot) tube is a steel pipe 22 inches in inside diameter and 20 feet long, with a uniform 1-inch wall thickness. In both tubes, the primacord was suspended on steel charge frames as shown in Fig. 3.14 for the 2-foot tube. Models were supported at the open ends of the tubes either on the cross frames shown in Fig. 3.14 or, for 6-inch-diameter models in the 2-foot tube, in end cradles which bolted directly to the tube. An overall view of both tubes, showing also the cross frame swung out of the firing position on the 4-foot tube, is given in Fig. 3.15.

The sequence of loading the primacord and putting models in position is shown in Fig. 3.16 for the 2-foot shock tube. Six-foot lengths of primacord were taped to the charge frame (Fig. 3.16a) and then bundled together for detonation at the lower end (Fig. 3.16b). For large charges as shown, the bundles were made in four groups and these in turn were connected by smaller diameter primacord to a central initiation point. The completed charge is shown in Fig. 3.16c, and in Fig. 3.16d the charge is being lowered to the bottom of the tube. With the charge in place, test models were mounted at the top of the tube as shown in Fig. 3.16e or 3.16f. As discussed later, to obtain pulses of



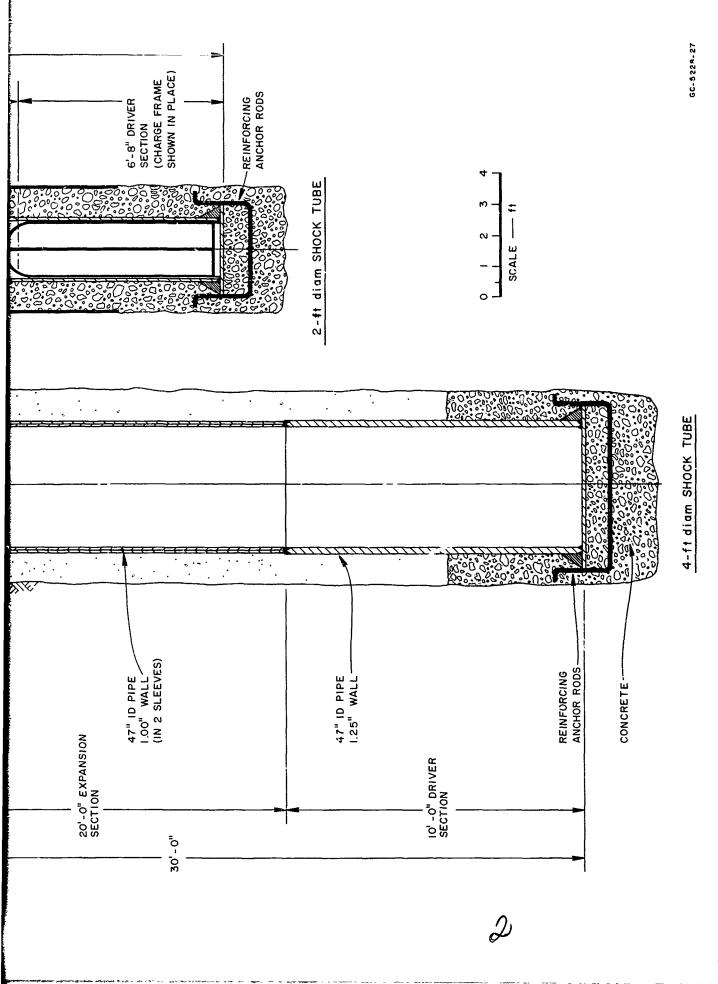


FIG. 3.14 LAYOUT OF SHOCK TUBES

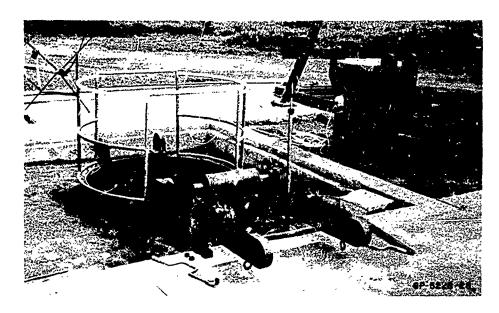


FIG. 3.15 OVERALL VIEW OF 4-FOOT AND 2-FOOT SHOCK TUBES

shorter duration, 3-foot lengths of Primacord were also used and placed with their lower ends 10 feet from the mouth of the tube rather than at the base of the tube. To obtain pulses of still shorter duration, flat charges were made in spirals as shown in Fig. 3.17 and placed two feet below the mouth of the tube (Fig. 3.17b).

Loading of the 4-foot tube was accomplished in much the same way, as portrayed in Fig. 3.18. Models and pressure gages were mounted on the cross frame (Fig. 3.18a), the Primacord was lowered into the tube (Fig. 3.18b), and then the cross frame was swung into place (Figs. 3.18c and 3.18d).

The model support fixtures were made so that either 6-inch- or 3-inch-diameter models could be tested in either tube. This was accomplished in the 4-foot tube by two cross frames, one which can accommodate 2 models of 6-inch diameter as in Fig. 3.18, and another which can accommodate 3 models of 3-inch diameter (not shown). In the 2-foot tube, either two models 3 inches in diameter or one model 6 inches in diameter can be tested, as shown in Fig. 3.16(e, f).

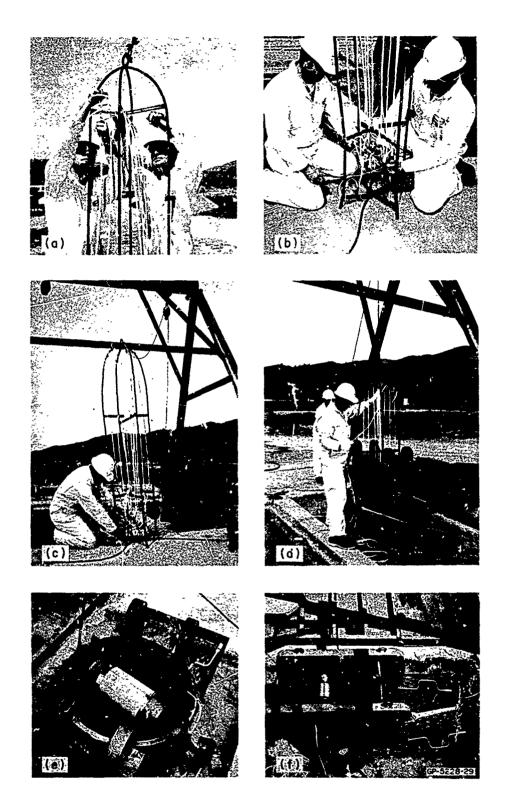
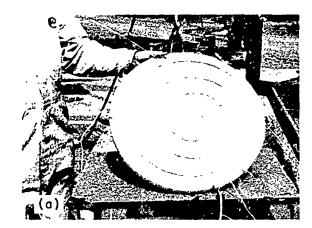


FIG. 3.16 LOADING SEQUENCE FOR THE 2-FOOT TUBE



T.

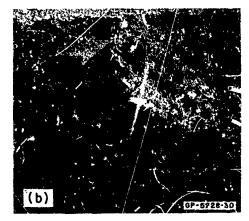


FIG. 3.17 FLAT CHARGES FOR SHORT PULSES

The capability of testing two cylinders simultaneously proved very useful, particularly in the early stages of the program in which both the shock tube pressure calibration and the critical model failure pressures were unknown. In these early experiments, one of the cylinder positions was filled by a rigid pressure-instrumented cylinder and the other with a structural shell model, allowing simultaneous determination of pressures and pulse shapes and the magnitudes required to damage models of interest. It was through this procedure that it was quickly determined that explosive charges in the 4-foot tube required to damage some of stronger shells would be of the order of 100 pounds, far too large for economic operation and producing a very high noise level.

3.3.2 Pressure Pulses from Shock Tubes

Using the pressure instrumentation described in Appendix A, diffracted pressure on 3.5-inch and 6-inch-diameter cylinders were measured in the shock tubes to obtain data similar to that found for high explosive spheres in Section 3.1. Shock tube pressures are given in considerably more detail than those for the HE spheres because the pulse shapes were more complex, and because published data for high pressure operation of shock tubes are very sparse. The 2-foot tube was used much more than the 4-foot tube

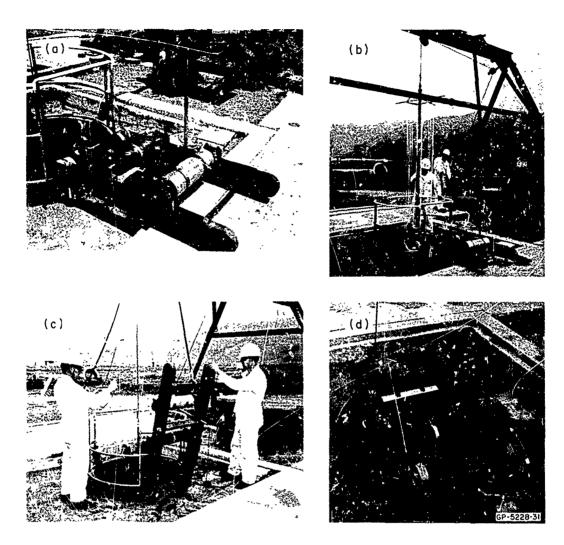


FIG. 3.18 LOADING SEQUENCE FOR THE 4-FOOT SHOCK TUBE

because of its higher pressure capability. It was also used at the three effective tube lengths described above, so the pressure data are much more comprehensive. In the following, the data for the 2-foot tube will be given first, proceeding from the full 20-foot length to 10 feet and to 2 feet. The 4-foot tube was calibrated and used only at its full length of 30 feet.

For given shock tube and driver section lengths, the pressure pulse can be varied by varying the amount of primacord in

the driver section. It is convenient to normalize the explosive weight in terms of the weight of air in the driver section. This ratio, between explosive and initial air weight per unit cross sectional area of the tube, is called charge ratio in [15] and is desonated by α . To a first approximation, scaled shock tubes give the same pressure for a given α , and a duration proportional to tube length. Pressure-impulse curves for the shock tubes are generated in the following with charge ratio α as a parameter in much the same way that curves were generated for spherical charges with distances from the charge as a parameter. Distance and charge weight are interchanged in the two applications because it is convenient to work with fixed spherical charge weights and fixed shock tube lengths.

Primacord configurations for the range of charge ratios used in a full-length calibration of the 2-foot tube are listed in Table 3.2. Four sizes of Primacord were used throughout the program: 40 grains/ft, 100 grains/ft (not used for Table 3.2), 200 grains/ft, and 400 grains/ft. The Primacord was spaced as evenly as possible over the tube cross section, using lighter weight Primacord for smaller charges so that, for most shots, a minimum of four strains was used. At very low charge ratios, the 4-foot tube was used so that several strands of the lightest weight Primacord could be used, rather than just a single strand as in Shot 2-253 (Table 3.2).

Pressure pulses at $\theta = 0^{\circ}$ (facing the shock) and at $\theta = 22.5^{\circ}$ on a 6-inch-diameter rigid cylindrical model are given in Fig. 3.19 for the full-length calibration series with charge ratios ranging from $\alpha = 0.025$ to $\alpha = 6.0$. For $\alpha > 1$ the pulse decays exponentially for about 1 millisecond, followed by a constant pressure plateau of from 1 to 2 milliseconds, and then a second but slower exponential decay to zero pressure. For $\alpha < 0.5$, the double jump in pressure seen in Fig. 3.19(a, b, c, d) was typical and has not yet been satisfactorily explained. However, the net impulse between the decay of the second pressure jump and the plateau pressure is very small

CONTRACTOR DESCRIPTION

Table 3.2

PRIMACORD CHARGES IN 2-FOOT TUBE (6-foot charge length)

Shot No.	Charge Ratio (α)	Total Primacord Weight (lbs)	Primacord Size (grains/ft)	Total Primacord Length (ft)	No. of Strands
253	0.025	0.034	40	6	1
252	0.050	0.068	40	12	2
96	0.125	0.172	40	30	5
91	0.50	0.68	200	24	4
92	1.00	1.37	400	24	4
93	2.00	2.74	400	48	8
94	4.00	5.49	400	96	16
95	6.00	8.21	400	144	24
	,	Į.	·		

compared to the overall impulse, and its influence on structural response is considered to be negligible.

Incident pressures were also measured and calculations show that, as in the spherical HE charges, the initial peak pressure is the reflected pressure of the incident shock. Calculations assuming steady flow with a particle velocity equal to the particle velocity behind the incident shock wave suggest that the pressure plateau recorded on the cylinder corresponds to the drag pressure as measured, for example, in [18]. Also, the time at which the second exponential decay begins agrees reasonably well with the calculated arrival time of the rarefaction wave from the bottom of the charge. (These calculations are given in Appendix C.) The rather strange double-pulse shape at $\alpha = 0.025$ is attributed to having only one strand of primacord (see Table 3.2) and demonstrates that the small diameter tube should not be used at such low pressures.

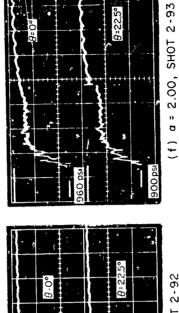
S Birthe ...

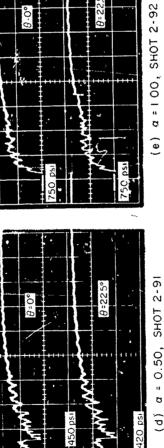
I

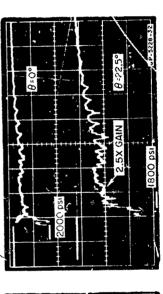
I

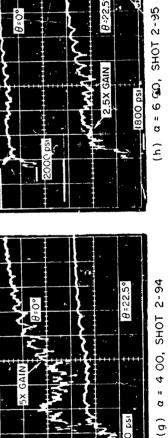
I

いっこうとうのはませんから、このからはなるないのでは、一般のないのでは、









a = 6 50, SHOT 2-35 (۲)

PRESSURE PULSES AT $\theta=0^\circ$ AND $\theta=22.5^\circ$ ON A CYLINDRICAL MODEL IN THE 2-FOOT SHOCK TIBE AT 20 FEET (sweep rate 1 msec/cm) FIG. 3.19

Pressures were also measured at several axial stations along the shell to observe possible variations in pressure with length. In both the rigid pressure models and the structural models, the overall length-to-diameter ratio was about three, but the unsupported length of the structural model itself had a length-to-diameter ratio of only one so that concern was mainly in pressures near the center section. Comparison of pressures measured along the central 9 inches of the 6-inch-diameter cylinder showed that there was no variation in pressure in this length in either the 2-foot or 4-foot shock tubes or in the spherical blasts.

Figure 3.20 gives pressure pulses at $\theta = 0^{\circ}$ on a 9° half-angle cone of mean diameter 6 inches and total length 15 inches. They are the same as the pressures in Fig. 3.19 from the cylindrical model, within the normal scatter of the data. Pressures were also measured toward the small and large diameter ends of the cone, and again, the pressures were the same as those at the center.

The distribution of pressure around a cylinder or come had essentially the same characteristics for all charge ratios so only one complete set of data is presented. This is given in Fig. 3.21 for $\alpha=2.0$. Typically, pressure decreased monotonically from $\theta=0^\circ$ to $\theta=180^\circ$. Figure 3.21e shows a slight pressure increase at 180° but this is an exception, attributed to the large percentage scatter in the data over the back surface. Over the side of the model facing the shock ($-90^\circ < \theta < 90^\circ$) the pressure rose suddenly upon arrival of the shock (Fig. 3.21a,b,c). The pressure recorded by gages on the back side of the model appeared to rise gradually to a peak about 1 millisecond after shock arrival. The exact shapes of the back side pulses are difficult to determine because the pressures are an order of magnitude lower than the front surface pressures, thus increasing the relative magnitude of gage ringing from model vibrations. The pressures recorded are a mean through the gage ringing oscillations.

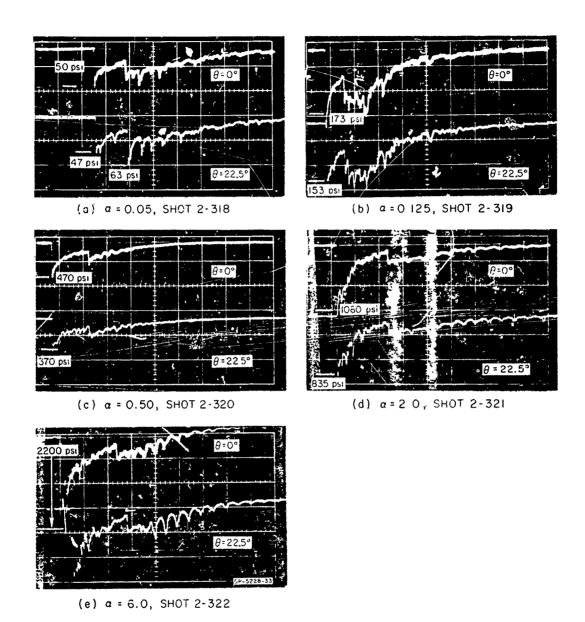
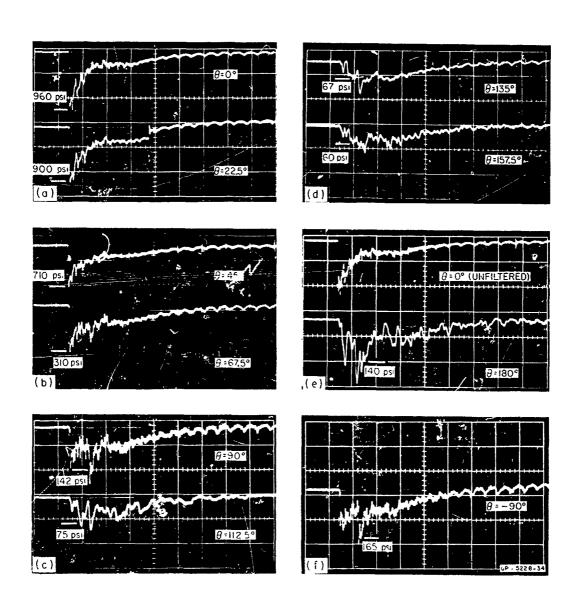
STATE OF THE PARTY


FIG. 3.20 PRESSURE PULSES AT θ - 0° AND θ = 22.5° ON A 9° CONICAL MODEL IN THE 2-FOOT SHOCK TUBE AT 20 FEET (sweep rate 1 msec/cm)



Tables and

FIG. 3.21 PRESSURE PULSES AT α = 2.0 AROUND A CYLINDRICAL MODEL IN THE 2-FOOT SHOCK TUBE AT 20 FEET (sweep rate 1 msec/cm)

Peak pressures from all the gages are plotted against charge ratio α in Fig. 3.22. The range of pressures at $\theta=0^{\circ}$ shows that the 2-foot tube can be used to produce pressures from 60 psi at $\alpha=0.05$ to 2000 psi at $\alpha=6$. Higher pressures can probably be achieved without damaging the tube wall but were not required for the models in the current program. Scatter of the data is within ± 10 percent except for $\theta>90^{\circ}$. A single dashed curve is given for $\theta=135$, 167, and 180° because the scatter is about $\pm 50^{\circ}$ and the data were thought reliable enough only to show the trend indicated. The significant observations for these back surface gages is that the pressures are low enough to be neglected compared to the front surface pressures.

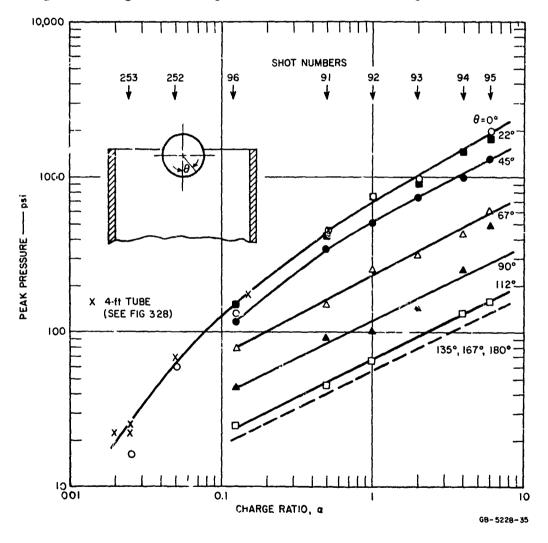


FIG. 3.22 PEAK PRESSURE vs. α FOR VARIOUS ANGLES ON A 6-INCH-DIAMETER CYLINDER IN THE 2-FOOT TUBE AT 20 FEET

A CONTRACTOR OF THE PERSON OF

Data from the smoothed curves in Fig. 3.22 are replotted against angle θ in Fig. 3.23. These curves show the monotonic decrease in pressure to $\theta\approx 140^{\circ}$. Within the accuracy of the data, the pressure is assumed constant for $140^{\circ}<\theta<180^{\circ}$. The data are plotted on semi-log paper to show that the functional variation with θ is about the same over the range of α given, except that the ratio of front surface to back surface pressure decreases slightly with α because of the decrease in $p_{\rm p}/p_{\rm T}$.

To evaluate the applicability of various simple analytic expressions for approximating the observed pressure distributions, the curve for $\alpha=2$ is replotted on linear paper in Fig. 3.24 along with $p(\theta)$ given by Eq. (3.1) and two other simple analytic expressions. These three approximation curves are given by

Curve (1)
$$p = (p_R - p_I)\cos^2\theta + p_I$$
 $-90^\circ < \theta < 90^\circ$ (3.1)
 $= p_I$ otherwise
Curve (2) $p = A\cos\theta + B$ all θ (3.3)
Curve (3) $p = C\cos\theta$ $-90^\circ < \theta < 90^\circ$ (3.4)
 $= 0$ otherwise

The simple $C\cos\theta$ over one side comes closest to the data over the front face except that it goes to zero with a finite slc at $\theta = 90^{\circ}$. This discontinuity in slope might be objectionable—some applications to structural response analysis. The $\cos^2\theta$ approximation in Eq. (3.1) overcomes this difficulty but gives a drop-off in pressure too fast near $\theta = 0^{\circ}$ and thus underestimates the pressure somewhat near $\theta = 30^{\circ}$. However, the maximum difference is about 15 percent, about the same as the experimental accuracy. The expression $A\cos\theta + B$ bears little relation to the measured pressure except near $\theta = 0^{\circ}$ and $\theta = 180^{\circ}$

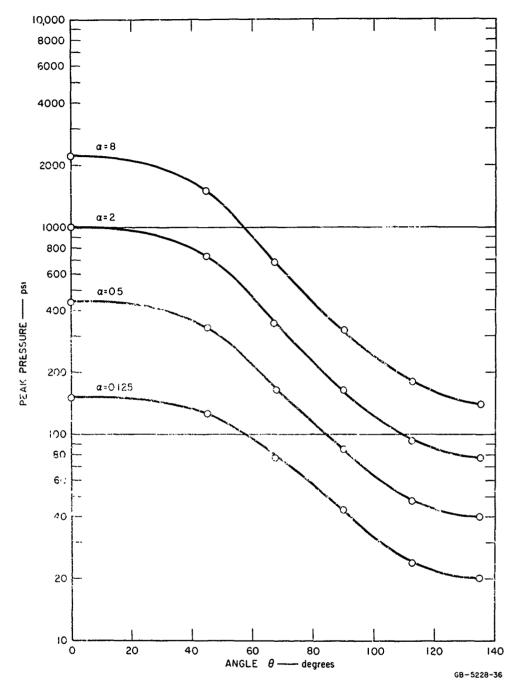


FIG. 3.23 PEAK PRESSURE vs. ANGLE FOR VARIOUS CHARGE RATIOS IN THE 2-FOOT TUBE AT 20 FEET (smoothed data from Fig. 3.22)

いこうこうない 一般のなってはないないのではないのであっている

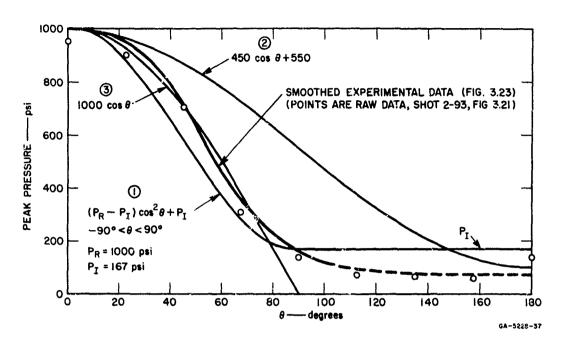
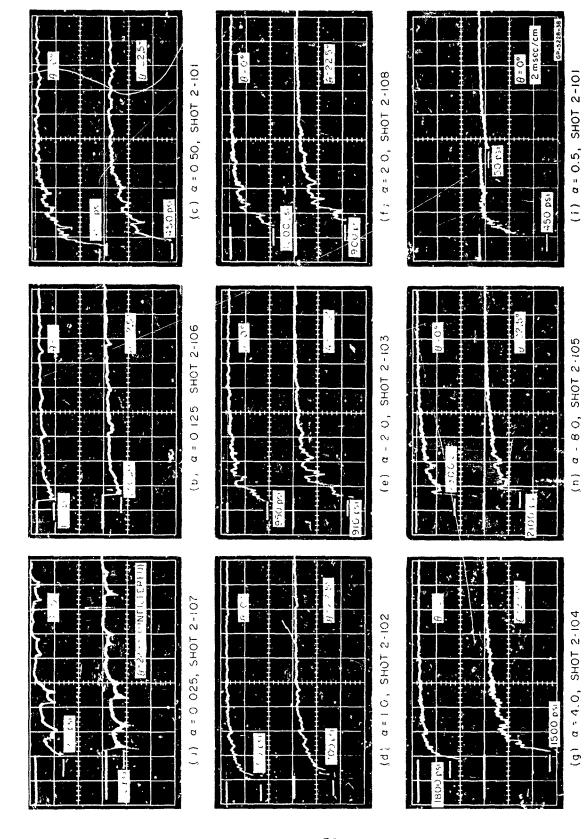


FIG. 3.24 COMPARISON OF OBSERVED PRESSURE DISTRIBUTION WITH SIMPLE ANALYTIC EXPRESSIONS

where it is adjusted to fit the data. As a simple approximate expression to be used for analysis. Curve (1) appears to match all the essential features of the distribution except the second derivative near $\theta = 0^{\circ}$. This pressure variation was used in the analysis in Chapter 8.

To obtain pulses of shorter duration, the 2-foot tube was also fixed with primacord charges arranged as for the shots in Table 3.2 but with a 3-foot length instead of 6 feet, and with the lower end of the charges placed 10 feet from the mouth of the tube. This allowed expansion in both directions from the charge; however, this resulted only in a reduction in the duration of the pressure plateau that was observed in shots at the full 20-foot length. This is seen by comparing Fig. 3.19 to Fig. 3.25, which gives pressure pulses from the 2-foot tube at 10 feet. A second effect of locating the charge halfway down the tube is a reflected shock from the bottom of the tube which travels back up the full length of the tube and applies a second shock



CHARGE RATIOS PRESSURE PULSES ON A 6-INCH-DIAMETER CYLINDER FOR VARIOUS IN THE 2-FOOT TUBE AT 10 FEET (sweep rate 500 $\mu \sec/cm$ except for i) FIG. 3.25

to the model. However, as shown in Fig. 3.25(i), the pressure and impulse of this second pulse are an order of magnitude smaller than in the main shock and it arrives about 7 milliseconds later. This time is long compared to the response time of the structural models so that the influence of the tiny second pulse can be neglected in structural testing.

The peak pressures in Fig. 3.25 fall, within experimental accuracy, on the curve given in Fig. 3.22 for the full-length tube, so the same pressure curves are used for both the full-length and half-length configurations. Pulse shapes are also very similar, and the impulses from the half-length configuration are only slightly less than half the full-length impulses. A plot of pressures and impulses for both are given in Fig. 3.26, together with additional data discussed below.

Still shorter pulses were produced in the 2-foot tube using flat spiral charges 2 feet from the models, as shown in Fig. 3.17. The resulting pulses at $\theta = 0^{\circ}$ and $\theta = 22.5^{\circ}$ are given in Fig. 3.27, and corresponding pressures and impulses are given in Fig. 3.26 by the curve labeled "2-foot tube, L=2 feet." Because the model was so close to the charge and the pulse duration was so short, reflections from the walls of the shock tube had a significant effect on pulse shape. At charges of 0.12 lb/ft² and less, wall reflections produced a double pulse effect (Fig. 3.27a, b). At larger charge ratios there was no distinct second shock, but the pulse shape was nearly rectangular rather than nearly exponential as were the shapes at longer tube lengths. Based on calculations given in Chapter 1, one would expect the rectangular shape to result in somewhat more severe structural damage at the same peak pressure and impulse. *

THE TRANSPORTER

To avoid wall reflections and obtain a more nearly exponential pulse of duration intermediate to those from a long shock tube and small HE spheres, large flat charges could be used on the ground with the model suspended above, but as mentioned earlier, this technique was not explored in the present program.

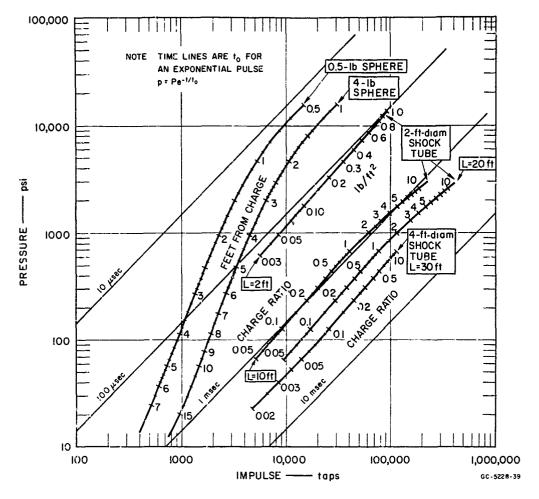
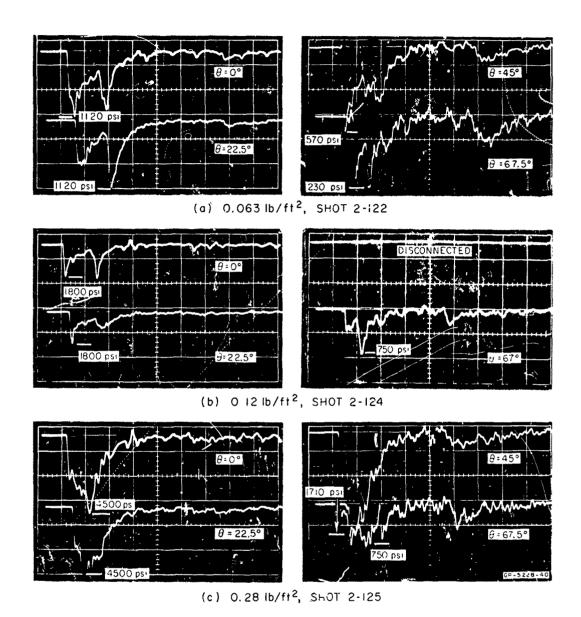


FIG. 3.26 PRESSURE-IMPULSE FROM SPHERICAL CHARGES AND SHOCK TUBES

Longer pulse durations and more satisfactory pulses at very low charge ratios were provided by the 4-foot tube at 30 feet. Pressure pulses for charge ratios from 0.020 to 0.50 are shown in Fig. 3.28. As in the 2-foot tube at low charge ratios, these pulses typically have a double jump character with the second jump occurring about 1.5 milliseconds after the initial shock. Peak pressures fall on the pressure versus charge ratio curves for the 2-foot tube, as shown by the crosses in Fig. 3.22. Again, peak pressures and impulses for these pulses are given in Fig. 3.26.

HORSELLE EN HOLDE


Transmitted of

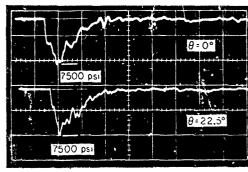
Sections And

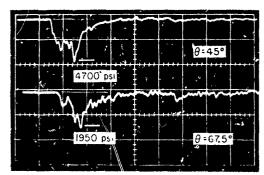
A PROPERTY.

は後

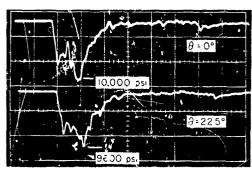
THE PROPERTY OF THE PARTY OF TH

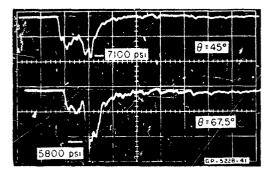
FIG. 3.27 PRESSURE PULSES ON A 6-INCH-DIAMETER CYLINDER IN THE 2-FOOT TUBE AT 2 FEET (sweep rate $100~\mu \rm sec/cm)$





(d) 0.55 b/ft^2 , SHOT 2-126





(e) 0.84 lb/ft^2 , SHOT 2-127

FIG. 3.27 (Concluded)

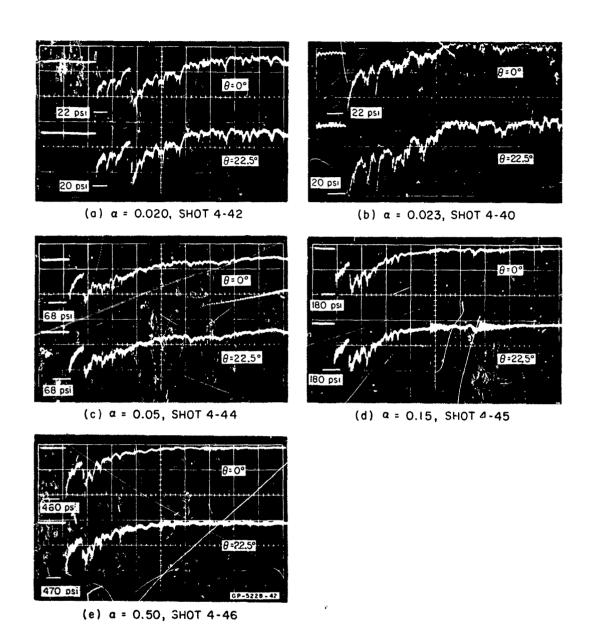


FIG. 3.28 PRESSUME PULSES ON A 6-INCH-DIAMETER CYLINDER IN THE 4-FOOT TUBE AT 30 FEET (sw-sp rate 2 msec/cm)

4. DETAILED DATA SUMMARY OF SHELL RESPONSE EXPERIMENTS

In this chapter, a detailed listing of pressures, impulses, model damage and other pertinent data is given for virtually all the shell response experiments. The three subsequent chapters constitute the main body of the report on shell response experiments, but this summary is given first so that the broad scope of the experiments will be well in mind when detailed results are discussed. Also, for the reader to be able to delve into the data for quantitative study, he must be familiar with the conventions adopted for shell model designations and shot numbers. A brief description is given here of all the models and their serial numbers. The shot number convention is described and then the grouping of the shell experiments according to program objectives is given, followed by the data.

4.1 Model Serial Numbers and Descriptions

As a means of identifying the models throughout the program and in the data summaries, each shell was given a serial number. These numbers also give a brief description of the dimensions, materials, and sometimes the configuration of the model. The simple cylindrical models are designated as in the example on the following page.

6 (61) 1 - A6T6(1) - 13M a b c d e f g

Number Position	Denotes	Examples
a	Cylinder diameter, inches	6 inches
b	Radius-to-thickness ratio	61
С	Length-to-diameter ratio	1
d	Subshell material	A6T6 = 6061-T6 aluminum A2T8 = 2024-T8 aluminum M31B = AZ31B magnesium
e	Tube stock number	1
f	Shell number in this series	13
g	Cover shell material	Blank = no cove: P = Plexiglas M = Grade 79 Micarta R = Neoprene rubber, 60 durometer RL = Refrasil CP = Carbon phenolic NX = Carbon phenolix (NOMEX)

All the metal subshells were 3 inches or 6 inches in diameter and were made from extruded tube or, in the very thin uncovered shells, rolled from sheet stock. Most of the extruded shells were tested with the as-received wall thicknesses; these were of diameter and radius-to-thickness ratios as follows: 3(53), 3(23), 6(61), and 6(24). The shells rolled from sheet stock and tack-welded with a lapped seam were: 3(250), 3(94), and 6(187). The 6(100) shells were machined from 6(61) extruded tube. The 2024-T8 shells were machined in the 2024-T0 condition and then heat-treated to the T8 condition.

The cover shells were 0.25-inch thick in the 6-inch-diameter models and 0.125-inch thick in the 3-inch-diameter models. The Plexiglas and Micarta were pressed on with no adhesive, and the solid neoprene rubber was bonded on with rubber cement. A few shells were

tested using tape-wound refrasil and carbon phenolic covers and were supplied by LMSC. These were bonded to the subshell with 0.030 inch of hard bond_r(B. F. Goodrich 5B).

In addition to the uncovered and covered simple cylinders, a series of uncovered cones was tested; these are designated by

$$C(60)9^{\circ}-A6T6-5$$

The nomenclature is the same as in the cylindrical shells except that the diameter position is replaced with C to denote cone, and the length-to-diameter ratio position is used to designate the 9-degree cone half-angle. The mean diameter of all the cones was 6 inches and the unsupported length-to-diameter ratio was unity, as in most of the cylindrical shells. All the cones were made by rolling sheet stock and welding a seam on the backside (away from the blast wave).

Ribbed shells are designated by

These were all machined from 6061-T6 aluminum tube having a 6-inch outside diameter and a 0.25-inch wall. The radius-to-thickness ratio (50 in the above example) refers to the thickness of the shell between ribs. The height of the ribs is the full 0.25 inch of the stock, minus the wall thickness. In the example above, "2 Rib" refers to two equally spaced ribs on the total 6-inch span (i.e., 2 inches from each rib to the nearest end support). The number (250) is the rib thickness, in mils. As in the simple shells, the P designates a Plexiglas cover.

Foam-filled shells are designated the same as simple shells with the addition of the foam density in pounds per cubic foot as follows:

The shells were made using polyurethane rigid foam, foamed in place

to completely fill the unsupported length e cept for a 2-inch-diameter hole to accept the model support rod.

Sandwich shells are designated by

6(49/30) - A6T6 - 3M

All were made with an inner skin of 6-inch-diameter extruded tube. The outer skin was generally made of 7-inch-diameter tubing, giving a skin spacing of slightly less than 0.5 inch. A few outer skins were made from 6.5-inch-diameter tubing, giving a skin spacing of about 0.2 inch (these are designated by "1/4"). The numbers in parentheses designate the skin thicknesses in mils, outer skin first, e.g., (49/30) has an outer skin 0.049-inch thick and an inner skin 0.030-inch thick. The unsupported length of all the sandwich shells is 6 inches, and the skins are spaced by solid aluminum rings for the 1.5-inch supported length at either end. The space between skins is filled with 24 lb/ft foamed-in-place rigid-foam polyurethane in all but one series, which is filled with 12 lb/ft foam (designated "12#F").

4.2 Shot Numbers

The shell response experiments were all run using blast waves from spherical H. charges, the 2-foot-diameter tube, or the 4-foot-diameter tube. Shot numbers using each technique are designated by HE-XXX, 2-XXX, and 4-XXX, respectively, and shots were numbered chronologically in each series. In each blast technique more than one model was often exposed in a single shot so the total number of shell experiments exceeds the total number of shots. A listing of all the shots in chronological order, giving the type of pressure instrumentation used, the shell serial numbers, and abbreviated shell damage comments, is given in Appendix D.

4.3 Shell Group Numbers

Data were originally gathered using shot numbers as the basic reference because this was a fixed sequence not subject to change.

For presentation of the results, however, it is necessary to regroup the data into a sequence relating to the program objectives, and hence to the shell models. In this grouping the shells naturally fall into an outline form, according to shell configurations and parameters under investigation. Each group of shells is assigned a three- or four-place alphanumeric label which relates to the position of the group in the outline. All of the shells in a group are of the same kind and hence there is a one-to-one correspondence between group number and model number. For example, group Al2 shells are all of model type 6(187)1-A6T6. However, the dash (serial) numbers are rearranged so that the shells in each group are listed in Table 4.1 in order of increasing blast pressures and impulses. Thus, the 18 shells in group Al2 are numbered in order from Al2-1 to Al2-18, while the model serial numbers (e.g., 6(187)1-A6T6(2)-3) relate to their manufacture and have no orderly progression in relation to the experiments. The group numbers have the further advantage over model numbers of being sequential in themselves so that when a group number is given in a table, graph, or photograph, the exact source of data is easily traced. This is done by means of an index, based on group numbers, given at the beginning of the shot data list.

A list of the shell groups is given twice, once in outline form and once as the index to the data list. The outline serves to acquaint the reader with the position of each series of experiments within the overall program. After becoming familiar with this organization, reference to a given group of shells is more conveniently made through the index. The shells are listed generally in order of increasing strength, starting with uncovered shells, going from thin to thick shells in each subheading, then on to covered shells, and finally to complex shells. Strain-gaged shells are listed separately because they fall outside the general terminal observation scheme of the main program. Another group of shells, photographed with a high-speed framing camera during blast response, are not listed here because the terminal observations are the same as similar shells already listed. The results of these experiments are discussed in Chapter 9.

TO THE REAL PROPERTY.

SHELL PARAMETERS

GROUP NUMBER

A. SIMPLE METAL SHELLS (Chapter 5)

l. Radius-to-Thickness Ratio

	sla	
1.1	$a/h = 250^*$	All
1.2	a/h = 187	A12
1.3	a/h = 100	A13
1.4	$a/h = 94^*$	A14
1.5	a/h = 61	A15
1.6	$a/h = 53^{*}$	A16
1.7	a/h = 24	A17
1.8	$a/h = 24_*$ $a/h = 23^*$	A18

2. Length-to-Diameter Ratio

$$2.1 a/h = 53*$$

2.1.1	L/D = 2.0	A211
2.1.2	L/D = 1.5	A212
2.1.3	L/D = 1.0	A213
2.1.4	L/D = 0.67	A214

$$2.2 a/h = 23$$

2.2.1	L/D = 2.0	A221
2.2.2	L/D = 1.5	A222
2.2.3	L/D = 1.0	A223

3. Cones

3.1	a/h = 187	A31
3.2	a/h = 94	A32
3.3	a/h = 60	A23
3.4	a/h = 24	A34

4 Materials

--- 6061-T6 aluminum (included under Al above)

4.1 2024-T8 aluminum

4, 1, 1	a/h = 100	A411
4, 1, 2	a/h = 61	A412
4.1.3	a/h = 24	A413
4, 1.4	a/h = 23	A414

^{*}Designates 3-inch diameter. All other models are 6-inch diameter.

4.2 AZ31B magnesium

4.2.1	a/h = 187	A421
4.2.2	a/h = 100	A422
4.2.3	$a/h = 61_{\psi}$	A423
4.2.4	$a/h = 50^{\circ}$	A424
4.2.5	a/h = 24	A425

5. Preloads

5.1 Uncovered

5.1.1	a/h = 100	A511
5.1,2	a/h = 61	A512

5.2 Micarta covered

5.2.1
$$a/h = 61$$
 A521

B. SIMPLE COVERED SHELLS (Chapter 6)

l. Micarta Only

1.1	a/h =	26.	Bll
1.2	a/h =	25 ~	B12

2. 6061-T6 Subshell

$$2.1 a/h = 100$$

2.1.1	Piexiglas	B211
2.1.2	Micarta	B212
2, 1, 3	Rubber	B213

2.2
$$a/h = 61, 53$$
*

2.2.1	Plexiglas, 61,	B221
2.2.2	Plexiglas, 53 [°]	B222
2.2.3	Micarta, 61	B223
2.2.4	Micarta, 53 [~]	B224
2.2.5	Rubber, 61,	B225
2.2.6	Rubber, 53°	B226

2.3 a/h = 24, 23*

2 2 1	701 1 1 04	2021
2.3.1	Plexiglas, 24,	B231
2.3.2	Plexiglas, 23 ^r	B232
2.3.3	Micarta, 24,	B233
2.3.4	Micarta, 23 ⁿ	B234
2 3 5	Pubber 23"	B235

3.	2024-7	re Alumii	num Subshell	
	3.1	a/h = 10	00	
		3.1.1	Rubber	B311
	3.2	a/h = 6	51	
		3.2.1 3.2.2	Plexiglas Micarta	B321 B322
		3.2.3	Rubber	B323
	3.3	a/h = 2		
		3.3.1 3.3.2 3.3.3 3.3.4	Plexiglas, 24* Plexiglas, 23* Micarta, 24* Micarta, 23* Rubber, 24	B331 B332 B333 B334
				B335
4.	AZ31B	Magnesi	um Subshell	
	4.1	a/h = 10	00	
		4.1.1	Rubber	B411
	4.2	a/h = 6		
		4.2.1	Plexiglas	B421
		4.2.3	Micarta Rubber	B422 B423
	4.3	a/h = 2	4	
		4.3.1	Plexiglas Micarta	B431
		4.3.3	Rubber	B432 B433
5.	Length	-to-Dian	neter Ratio	
	5.1 5.2		3, $L/D = 2$, Micarta 3, $L/D = 2$, Micarta	B51 B52
6.	Tape-	Wound Co	vers	
	6.1	a/h = 10	00	
		6.1.1 6.1.2	Refrasil Carbon phenolic I	B611 B612
		6. 1. 3		

Code Sales

ってころうかはしょうじょうないないのであるのできるというないできるというないできるというできるというできるというできるというできるというできるというできるというできるというできるというできるというできると

6.	2	a/h	=	61

6.2.1	Refrasil	B621
6.2.2	Carbon phenolic I	B622

C. COMPLEX SHELLS (Chapter 7)

1. Ribbed

1.1 Uncovered

1, 1, 1	h = 100	C111
1,1,2	a/h = 50	C112

1.2 Covered, a/h = 50

1,2,1	Plexiglas	C121
1,2,2	Micarta	C122

2. Foam-Filled

2.1 a/h = 100

	2	
2.1.1	Foam 8 lb/ft ³ 2	C211
2, 1, 2	Foam 12 $\frac{1}{2}$	C212
2.1.3	Foam 18 lb/ft ³	C213

2.2 a/h = 61

	2	
2.2.1	Foam 8 lb/ft ³ 2	C221
2.2.2	Foam 12 lb/ft $_{2}^{3}$	C222
2.2.3	Foam 18 lb/ft ³	C223

3. Sandwich

3.1 Uncovered

3.1.1	$h_0/h_i = 49/30,$	1/4" core [†]	C311
3.1.2	$h_0/h_1 = 30/30$		C312
3.1.3	$h_0/h_i = 49/30,$	12#/ft ³ core	C313
	$h_0/h_1 = 49/30$		C314
3.1.5	$h_0/h_i = 49/49$		C315

3,2 Covered

3.2.1
$$h_0/h_i = 30/30$$
, $1/2$ " core C321
3.2.2 $h_0/h_i = 49/30$, $1/2$ " core C322

Core thickness is 1/2 inch and density 24 lb/ft unless noted otherwise.

D. STRAIN-GAGED SHELLS (Chapter 9)

1. Uncovered

1.1	$a/h = 61_{\mu}$	D11
1.2	a/h = 53*	D12
1.3	a/h = 24	D13
1.4	a/h = 23*	D14

2. Covered

2.1
$$a/h = 23$$
, Micarta D21

4.4 Comments on the Data Summary List

The objective of each series of tests within a shell group was to determine the maximum blast loads that would produce no damage, and the minimum blast loads that would produce significant damage. For the uncovered shells, "significant" damage was arbitrarily selected to be a maximum permanent inward deflection equal to 10 percent of the shell radius. In the covered shells (except for rubber), first significant damage was taken to be cracking of the cover, which generally occurred at loads that produced permanent subshell deformations of a few percent. In some of the simple shell groups, sufficient data were obtained to plot permanent deformation versus blast load. In most of the shell groups the load level that produced severe damage, such as tearing of the metal or fragmenting of the cover, was also determined.

As discussed in the Introduction, loads that produced no damage and loads that produce damage can be separated in the pressure-impulse plane by critical curves for each shell. Thus, in a more general sense, the objectives consist of finding two curves in the pressure-impulse plane for each shell, one which is an upper bound on loads that produce no damage, and the other which gives loads that produce 16-percent deformation or cover cracking. These two curves are shown schematically in Fig. 4.1. To obtain points on these curves, a series of tests is run with a blast technique that gives a cross curve intersecting

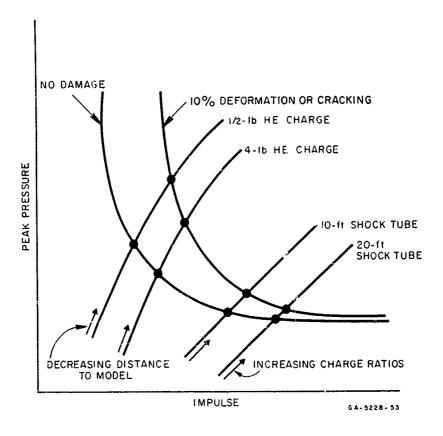


FIG. 4.1 SCHEMATIC OF SHELL CRITICAL CURVES AND BLAST TECHNIQUE CRUSS-CURVES

the damage curves as shown. In this program, cross curves were generated by running tests at various distances from fixed spherical charge weights, and at various charge ratios in shock tubes at fixed lengths. Determination of pressures and impulses along these cross curves is described in Chapter 3 and the curves are given in Fig. 3.26.

In the data summary, experiments in each shell group are listed in order of increasing pulse duration, i.e., proceeding generally from left to right in Fig. 4.1, starting first with 0.5-pound charges, then on to 4-pound charges and finally to the shock tubes. Along each of these cross curves, the experiments are listed in order of increasing pressure. For example, in Table 4.1 we see that group A12 consists of 18 experiments on shells of type 6(187)1-A6T6. The first 9 experiments used 0.5-pound HE spheres and the increase in damage with

A CONTRACTOR OF THE PROPERTY O

increasing pressure within these experiments is noted. The next 4 experiments, A12-10 through A12-13, are at a charge weight of 4 pounds, listed again in order of increasing pressure. Still longer durations (and higher impulses) were obtained in experiments A12-14 and A12-15 using the 2-foot tube at 10 feet, and finally, the longest pulses in this series are listed as A12-16 through A12-18 and were performed in the 4-foot tube at 30 feet.

To make Table 4. l as concise as possible, several abbreviated comments and conventions were adopted. The column headed "charge weight (lbs) or ratio a" gives either the weight of the explosive charge in a spherical blast experiment or the charge ratio in a shock tube experiment. The next column gives either distance from the spherical charge or the effective length of the shock tube as described in Chapter 3. In the 2-foot tube, the length of the primacord charge and the effective rube length are in the ratio 6:20 unless otherwise noted. In the 4-foot tube they are in the ratio 1:3. A few shots were run at other charge configurations to investigate their effect on pulse shape, but were not described in Chapter 3 in the interest of brevity. Flat charges (such as the spirals described in Chapter 3) are denoted by F and the distance given is from the charge to the top of the shock tube. The peak pressures and impulses given are at shot zero on the model and are taken from the calibration curves in Fig. 3.26 for each technique, or directly from scope records from unique shots.

Damage to the models is given by a qualitative description plus the maximum radial deformation of the metal shell (or subshell) in percent of radius. The meanings of the abbreviated descriptions will become clear during discussions in the following chapters, in which many photographs of damaged models are given. Briefly, the terms occurring most frequently have meanings as follows:

Simple Metal Shells

These fail almost exclusively by buckling, preceded in thicker shells at lower loads by some permanent deformation without observable

buckling (see Figs. 5.4 through 5.11). If no permanent deformation at all is observed, the comment "no damage" is given to emphasize that no brittle fracture has occurred. Shells with permanent deformation but without buckling carry the comment "no buckling." Buckled shells are denoted by "buckled" or, if the wavelength of the buckling is appreciably shorter than in the static pattern, by "wrinkling." The number of lobes in the buckled front surface is often given. The mode number associated with these lobes, of course, is usually several times the number of lobes. In the thinner shells under high loads, the shell sometimes dishes in after the buckling occurs and these are so noted. Under extreme loads, the entire shell sheared and blew off the holding fixture.

Simple Covered Shells

In these shells, the damage description usually refers to the cover since it fails first, by cracking (see Figs. 6.4 through 6.12). Cracks running circumferentially (usually along the supporting end plugs) are called "C-cracks." Cracks running axially (usually near shot zero, extending inward from C-cracks at an end plug) are called "L-cracks."

The Plexiglas-covered shells often shattered and, in the shock tube experiments, the crack pattern sometimes appeared in the shape of an hourglass when viewed from the load of side. The rubber-covered shells generally buckled as in the uncovered shells. Tape-wound covers always failed first by circumferential cracks ("delaminations") between tape layers (see Fig. 6.25). The tape-wound carbon phenolic covers seldom cracked longitudinally. In all of the hard covered shells, the subshell often deformed very locally near one or both end plugs, forming a "circumferential ridge bulge" (see Fig. 6.1).

Complex Shells

These failed in the same modes observed in the simple shells. In the sandwich shells, deformation of both the outer and inner skirs is sometimes given, outer skin first.

It is recommended that the reader only browse through the data summary table, and then proceed directly to Chapters 5, 6, and 7. The table is intended to be used in detail only by those who need information not given elsewhere (not all of the data from the nearly 700 experiments are plotted or tabulated), or who want to obtain data on a specific type of shell without searching for it in the text.

GROUP NUMBER INDEX TO DATA SUMMARY

territoria e en estadore e e en estadore estado en en estadores.

∢	SIMPLE UNCOVERED	RED SHEL	ST	ĕ	SIMPLE COVERE	COVERED SYELLS			C. COMPLEX SHELLS	ราว		á	STRAIN-CAGED SHELLS	SHELLS	
Group No.	Cylinder Type	No. of Tests	Page	Group No.	Cylinder Type	No. of Tests	Page	Group No.	Cylinder Type	No. of Tests	Page	Group No.	Cylinder Type	No. of Tests	Page
۸۱.	Radius-to-Thickness Rat	kness Rati	21	В1.	Micarta Only				Cl. Ribbed						
A 12	3(250)1-A6T6 6(187)1-	ဖွဲ့ဆိုင္		B12	6.5(26)1-Micarta 3(25)1-"	9 7	99	C113	6(100)1-5Rib(030) 6(50)1-2Rib(250)	-:-	27 27	D12	6(61)1-A2T8 3(53)1-A6T6 6(24)1-A2T8	ξi 4 ι	51 51
A14	3(94)!- "	7 51 5		B2.	Aluminum 6061-T6 Subshell	6 Subshell			6(50)1-2Rib(250)-M	- =	22		3/23/1-A6T6	4.0	55 55
A 16	3(53)1	34.5	2	B211 B212	6(100)1-A6T6-P		9 2		Cc. Foam-Filled						
8. V		27	n m	B213	" -R" " 'B'		~ ~		6(100)1-A6T6-8#F	10	13				
A2.	Length-to-Diameter	seter Ratio	٥.	B222 B223	3(53)1- "-P	13 /		C2213	18年2月 11 -18年5		122				
A211	3(53)2-A6T6	m r	m r	B224	3(53)1- "-M		. 00 oc		124年	7	1111				
A213	3(53)1- "	* 27	n en e	B226	3(53)1- "-R	4.4	000		400000000000000000000000000000000000000	Į.	:				
A221	3(23)2- "	4 W	.) 4ª	B232	3(23)1P		8,9		TO THE PARTY OF TH						
A222	3(23)1.5- "	m*	**	B233	6(24)1- " -M		66	C3112	6(49/30)-A6T6-1/4 6(30/30)-A6T6	၁ ဖ	<u> </u>				
-		•	r	B235	3(23)1- " -R		6		6(49/30)-A6T6-12#F	~	7				
A3.				B3.	Aluminum	2024-T8 Subshell			6(49/30)-A6T6 6(49/49)-A6T6	6-9	<u> </u>				
A31	C(187)90-A6T6		4						6(30/30)-A6T6-M	S	4				
A32	C(94)90- "	. 0 w	* *	B311	6(100)1-A2T8-R		60		6(49/30)-A6T6-M	∞	*				
¥3	C(24)90- "		* 4	B322	M- " -1(19)9		0.								
A4.	Materials			B323 B331	6(51)1- " -R 6(24)1- " -P	. 0 m	22								
				B332	3(23)1- " -P		01								
A411	6(190)1-A2T8	ر س	੍.	B333	6(24)1- " -M		22								
V413	6(24)1-	2 7	* 4	B335	6(24)1- "-R	• ~	22								
A414	3(23)1- " 6(187)1-M31B	∞ 4	Ś	34.	Magnesium M31B	Subshell									
A422	6(100)1- "	6	'n	B411	6(100)1-M31B-R		01								
A424	6(61)1- "	9	ı,	B421	6(61)1- "-P		22								
A425	6(24)1- "	. 2	'n	B423	6(61)1- "-R		=:								
A5.	Pre1-ade			B431	6(24)1- "-PM	~ r~ r	==:								
A511	6(100)1-A6T6	15(34)	9	D#33	1 angth -to-Diameter	i i	:								
A512 A521	6(61)1- " 6(61)1-A6T6-M	7(2*) 2(1*)	99	•	3(53)2-A6T6-M		=								
			•	B52	3(23)2M	m	=								
				В6.	Tape-Wound Covers	밁									
				B611	6(100)1-A6T6-RL		==								
				B613	XN- :		=								
				B621 B622	6(50)1-A6T6 -RL 6(50)1-A6T6 -CP	ر. در	11								
						•									

Selected shots repeated for comparison.

THE CONTRACT OF THE PROPERTY O

do in the test of a state of the the date.

Table 4.1
DATA SUMMARY (Sages 1 and 2)

Figure No.		5. 4(a) 5. 4(b)	5.4(c) 5.4(d) 5.4(e)	5.5(a) 5.5(a) 5.5(b)	5.6(a) 5.6(b)	5.6(c) 5.6(d) 5.6(e)		
Damage	Inciplent wrinkling. Well developed short wrinkles; no dishing in. Short wavelength wrinkling; no dishing. Short wavelength wrinkling, no dishing. Bury short wavelength wrinkling; dishing. Buckling creases, 4 lobes.	No damage. Short wavelength wrinkling; no dishing. Short wavelength wrinkling. Wrinkling. Moderskely short wavelength wrinkling. Moderskely short wavelength wrinkling.	Wrinkling, slight dishing, shear wrinkle one end. Wrinkling, influenced by shear. (7075T6 by m.stake) Wrinkling and dishing-in. No dumage. Wrinkling object we willing; dishing.	Wrinkling; no dishing. No damage. Buckled, 4 iobes. Buckled, 3 lobes. Buckled, 4 lobes.	Buckling. Buckling. Wrinkling, shear wrinkles at one end. Buckling.	Short wavelength wrinkling. Buckled, 1 lobe. No damage. No damage. No damage. Buckled, 3 lobes. Buckled, 2 lobes.	No damage. No buckling. Pushed in; shear wrinkles each end. Pushed in; single shear buckles one side. Dished in; single shear buckles one side. Uniform deformation over length; no apparent wrinkles. No apparent buckling. No damage. No damage. No damage.	No Duckled, 3 lobes. Sheared ends, 3-lobe buckle to mandrel, Buckled to mandrel, Buckled to mandrel.
Metal (% w/a)	1. 3 10. 8. 16. 30. 6.	6. 15 1. 74 1. 74 6. 7	19.5 5.7 27. 0.0 0.3 21.8	12. 0 0. 0 9. 0 22. 22.	8 4 4 0 0 5	4.11. 9.0.0.0.0.0.0.0.0.0.0.0.0.0.0.0.0.0.0.	11.58 11.58 11.58 11.58	0.0
Cylinder No.	3(250) 4.A6T6 [4]-2 (1)-12 (1)-13 (1)-10 (1)-10 (1)-10 (1)-1	6(187)1-A6T6(2)-3 (2)-2 (2)-6 (2)-6 (2)-4 (1)-6 (1)-10	6(187)1-A7T6(1)-2 6(187)1-A6T6(2)-5 (11)1-1 (1)-1 (1)-2	(1) (2) (3) (4) (4) (4) (4) (4) (4) (4) (4) (4) (4	6(100)1-A6T6(7)-3 (7)-3 (7)-1 (7)-1 (7)-1 (7)-1	5 (C)	3 (94)]-A6T6 (1)-30 (1)-12 (1)-13 (1	
I (taps) × 10 ⁴	0.052 0.073 0.169 0.142 0.21	0.079 0.095 0.102 0.108 0.108	0.115 0.125 0.125 0.142 0.162 0.162	0. 190 0. 40 0. 52 0. 58 0. 82 1. 07	0.143 0.165 0.205 0.23	0.34 0.92 0.96 0.82 1.60 1.75	0. 113 0. 135 0. 157 0. 157 0. 188 0. 275 0. 315 0. 92	1.00
P (ted)	24 27 27 27 140 170	65 106 130 147 153	170 220 220 52 52 72 102	107 50 28 88 50 50 50	300 420 700 175 270	460 126 66 38 75 82 82	182 260 370 470 570 570 270 325 380 126	155
Distance (ft) or Tube (ft)	7. 00 5.20 13.50 10.50 7.50	4.4.E.E.E.E.	3.50 3.20 10.50 9.30 8.30	8.20 10. 30. 30.	2.20 2.20 3.20 6.30 6.30	5. 10 20. 20. 30. 30.	3.40 2.25 2.25 2.35 5.00 5.00 10.00	, , , , , , , , , , , , , , , , , , ,
Charge Wt. (lbs) or Ratio a	0.54 44 44 0.017			0.038 0.053 0.023 0.029	000 000 44 44	0, 100 0, 050 0, 050 0, 057 0, 063 0, 114		0.062 0.125 0.057 0.280F
Shot No.	HE-81 HE-80 HE-51 HE-50 HE-49	HE-72 HE-71 HE-75 HE-91 HE-81	HE-89 HE-76 HE-77 HE-51 HE-53	HE-54 2-132 2-131 4-19 4-20	HE-62 HE-61 HE-60 HE-39	HE-37 2-141 2-28 4-16 4-29 4-15	HE-65 HE-66 HE-66 HE-64 HE-64 HE-42 HE-41 2-24 2-25	2-15 2-16 4-29 2-53
Group No.	A11-1	A12-1	-10 -10 -11	111111111111111111111111111111111111111	A13-1 -2 -3 -5 -6	110	A14-1 -2-1 -3-1 -5-1 -6-1 -10-1 -10-1	11.11.11

5.7(a)	5.7(b) 5.7(c) 5.7(d)	5.7(e) 5.7(f)		5.3(0)	5.8(c)	5. 8(d) 5. 8(e)	5.8(£)
No buckling. Uniorm displacement full length; perhaps threshold. One-pronounced lobe; perhaps wrinkling. Buckled. Winkled.	Dished in, but outward hump from short wavelength activity. Two closely-spaced inward lobes. Short wavelength wrinkling and dishing-in. Short wavelength wrinkling and dishing-in. Buckled, I lobe.	No damage. No bucking. Buckled, I lobe tending toward diamond. Buckled, I lobe. Buckled to mandrel, 2 lobes.	Weak shell? (Compare with HE-69) No damage. No bucking. Uniform daplacement full length; no bucking. Wribhing. 1 lobe. Wribhing and caving-in; (weak shell? compare with HE-74).	One lobe, with evidence of wrinkling. No buckling. Slight buckling one end, Dished-in; some wrinkling. Buckled, 1 lobe. Buckled, 1 lobe.	Sheared one end, metal wrapped around mand el. No damage. Buckling dimple near one end. No buckling. Buckled, 1 lobe. Slight buckling.	No damage. No buckling. Ends sheared. Buckled to mandrel. No damage. No damage. Buckled, 1 lobe. Blew off. No damage. No damage. No damage. No damage. Suckled, 1 lobe.	Very slight marks at end pluge. One end sheared to mandrel. Single lobe about 10%. Single lobes about 30%.
3.52	26. 17. 39. 21.	0.0 0.5 27. 22.	5.2 0.0 1.6 10.4 40.	18. 0.75 3.5 37.4 12.5 15.6	> 30. 0.0 6. 1. 25.	29.000 29.000 29.0000 29.00000	0.0
6 (61)1-A6T6 (4)-12 (4)-12 (1)-11 (1)-4 (1)-4	2 (1) (1) (2) (3) (4) (4) (4) (4) (4) (4) (4) (4) (4) (4	9-6-6-6-6-6-6-6-6-6-6-6-6-6-6-6-6-6-6-6	3 (53) 1-A6T6 (1)-23 (1)-24 (1)-27 (1)-22 (1)-23 (1)-23 (1)-25	(1) -2 + (1)		(1) -12 (1) -12 (1) -12 (2) -12 (3) -13 (4) -13 (5) -13 (6) -13 (7) -14 (7) -15 (7) -1	3 (53)1-A6T6 (1)-14
0.26 0.285 0.335 0.40	0.48 0.55 0.76 0.84 2.60	2.5 4.1.4 7.6 7.6	0.235 0.235 0.285 0.335 0.35	0.36 0.35 0.50 0.50	0.75 0.56 0.80 1.40	7744446 574474 5887446 5500000	
1150 1420 2000 670 810	1350 2500 2950 400	260 44.0 44.0	950 950 1420 2000 2150 2300	2300 750 1225 1690 1080 1430	2400 590 870 440	4 4 5 5 5 5 5 5 5 5 5 5 5 5 5 5 5 5 5 5	175 250
1.85 1.70 1.50 4.50	3.90 3.50 2.70 2.50	15. 20. 30.	2.00 2.00 1.70 1.50 1.45	3.55 3.55 3.85 3.40	2, 12, 75 2, 1		20.
000	****	0.0000 33.53 46.33	000000 000000	0.00044	0. 023F 0. 030F 0. 030F 0. 047F	0.000 0.000	0.28F 0.50F static
HE-65 HE-64 HE-63 HE-28	HE-27 HE-26 HE-25 HE-24 2-129	2-30 2-30 2-109 4-13 4-12	HE-73 HE-69 HE-82 HE-82	HE-74 HE-13 HE-14 HE-95	HE-25 2-75 2-76 2-166 2-165 2-64	2-67 2-26 2-52 2-162 2-162 2-3 4-9 4-9 4-31	2-51 2-54
A15-1	45.00	11.	A16-1 -2 -3 -4 -5		113 114 115 116 118	144144 4444444444444444444444444444444	-31 -32 -33 -34

A CONTRACT OF THE PROPERTY OF

FALL STATES OF THE STATES OF T

Table 4, 1 (Continued, Pages 3 and 4)

Figure No.	5. 9(a) 5. 9(b) 5. 9(c)	5. 9(d)			· · · · · · · · · · · · · · · · · · ·	5.11(a)	5.10(c) 5.10(c) 5.11(b)	5. 19(a)	5.19(b)	5. 19(c)	5. 19(4)
Damage	One lobe off-center (out of line with 66 and 70). No buckling. Gently bowed-in. Dimpled. Don lobe off-center. No buckling.	No buckling. Dished-un, more one side. Ends sheared, 1-lobe deflection to mandrel. No buckling. No dished, 1 lobe. No dished.	No buckling. No buckling. One lobe, mostly at one end., One lobe, deflection at one end. One lobe, off-center.	No damage. Metal pushed in around mandrel, Pushed in, more one end. Localized at one end. Metal pushed in around mandrel,	No buckling. Sheared one end, single lobe to mandrel. No buckling. No buckled, I lobe. No buckling.	Single lobe, skewed across zero line. Single lobe, max. at two-thirds span. Buckled, I lobe. Buckled, I lobe. No drnage,	No buckling. Buckled to mandrel, 1 lobe. Buckled to mandrel. No damage. Single lobe about 10%.	No buckling. No buckling. Buckled to mandrel.	No damage. Slight markings by enc pluge. Buckled I lobe, tendency to diamond.	No damage. Buckled, 1 lobe.	No damage. No damage. Sught markings by end pluge. Buckled, 1 lobe.
Metal (% w/a)	10.8 4.0 8.2 13.6	3.5 0.0 16.7 2. 22.	0.3 0.9 14. 19.	> 30. > 30. > 5.6 > 30.	<0.5 <1.0 35.	42. 13. 25. 25. 0.0	2.0	<1.0 <1.0	0.0 4.3	29.	0.00 0.00 0.00 0.00
Cylinder No.	6 (24)1-Acr6 (3)-3 (3)-6 (3)-3 (3)-2 (3)-6 (3)-6	(3)-1 (3)-1 (3)-1 (3)-1 (3)-1	3 (23)1-A6T6 (1)-12 " (1)-12 " (2)-20 " (1)-13 " (1)-13	99 4 7	(1)-19 (1)-2 (2)-23 (2)-24 (1)-15	(1) -13	(1) -1	3 (53)2-A6T6 (2)-1 " (2)-2 " (2)-1	3(53)1.5-4 6T6(2)-2 (2)-2 (2)-2	3 (53)1-A6T6 (1)-28 " (1)-10	3(53)2/3-A6T6(1)-1 (1)-1 " (1)-1 " (1)-1 " (1)-2
I (tape) x 10 ⁴	0.59 0.59 0.69 0.81 0.91	0.98 0.98 3.25 16.2 18.0	0.40 0.49 0.52 0.60	0.50 2.30 0.97 1.12 1.50	1.65 1.85 5.0	0.0.0.5. 0.0.0.0.0.0.0.0.0.0.0.0.0.0.0.0	16.2 18.0 19.5	2.05	3.05	4.6	5.7 6.7 7.9
P (psi)	5100 5100 6200 7800 9000	3800 3800 4600 4000 1280 3400 800	2750 3900 4300 5200 9000	1775 16000 3800 4600 7000	1800 2200 1500	1100 1530 1290 1400 1530 1000	1280 1400 1530 640 1500 1500	155 180 220	200 240 260	350	410 480 560 680
Distance (ft) or Tube (ft)	0.95 0.95 0.75 2.40	2.20 2.20 2.20 2.20 3.00 3.00	1.30 1.10 1.95 0.70	2.50 1.00 2.20 2.00 1.60	i i i i i i	20.00.00 20.00.00	20. 20. 30.	20. 20. 20.	20. 20. 20.	20.	20°. 20°. 20°.
Charge Wt. (lbs) or Ratio a	0,0,0,0,0 \$2,0,0,0,0,0,0,0,0,0,0,0,0,0,0,0,0,0,0,0	0.267F 3.50	00000 00000	9944 9944	0, 14F 0, 17F 0, 11F 0, 133F 0, 52F	0.65F 3.50 2.50 2.00 2.00	3.50 3.50 4.00 0.91	0. 125 0. 150 0. 187	0. 17 0. 21 0. 25	0.37	0.46 0.57 0.75 1.00
Shot No.		HE-32 HE-30 HE-29 2-167 2-29 2-40 4-18		HE-19 HE-22 HE-33 HE-24 HE-23		2-60 2-61 2-61 2-59 2-27		2-217 2-219 2-218	2-201	2-163	2-20 4 2-205 2-206 2-207
Group No.	A17-1 1-2-1 1-4-4-4-4-4-4-4-4-4-4-4-4-4-4-4-4-4-4		A18-1	97-860	12114	-16 -19 -19 -20 -21	75777	A211-1	A212-1 -2 -3	A213-1	A214-1 -2 -3 -4

Action Control of

	5. 19(e)	5. 19(f)	5.20(a) 5.20(b) 5.20(c)	5.20(d) 5.20(e) 5.20(f)	5.21(a) 5.21(b)	5.21(c) 5.21(d)	· · · · · · · · · · · · · · · · · · ·			
No buckling. No buckling. Diamond shape incipient.	No buckling. (Shot 2-211 repeat identical.) Buckled, I lobe. Buckled to mandrel.	No buckling. Buckled to mandrel.	No bucking. Wrinkling: no dishing-in. Wrinkling, no dishing in. Incipient buckling, 3 lobes. Buckled, 3 lobes.	No buckling. Wrinkling, sonie disbing-in. Wo buckling. No buckling. Buckled. 3 lobes. Buckled. 3 lobes.	No buckling. No buckling. No buckling. Buckling. Buckled. 1 lobe. Buckled, 2 lobes.	No buckling. Dimple off-center at large end. No buckling. Buckled, I lobe.	No damage. No damage. Buckied, 2 lobes, crack on crease.	No bucking. No bucking. No bucking. Localised at one end. No bucking. Skew 3-lobe bucking.	No damage (S.G. 4th shot this site). Incipient buckling, very localized in θ. Buckled, 1 love. (S.G. 5th shot this side.) Buckled, 1 lobe. Buckled, 1 lobe towards dishoon side. Buckled; 1 lobe towards dishond, crack.	No buckling. Buckled, 1 lobe.
, s, s,	2. 50.	2, 29.	6.8 8.1.	0.45 10.4 0.0 0.0 10.	0.75 8.4 <0.5 12. 29.	0.4 13.9 2.	0.0	0.67 3.8 10.8 41.	9.0 9.	< 0.5 11.
3 (23)2-A6T6 (2)-3 (2)-1 (2)-2	3(25)1,5-A6T6(2)-3 " (2)-2 " (2)-1	3 (23) 1-A6T6 (1)-7 " (1)-16	0, 123 C(187)9° AGT(1)-4 0, 163 (1)-1 0, 171 (1)-5 0, 24 (1)-2 0, 74 (1)-3	C(94)9°-A6T6(1)-4 (1)-7 (1)-1 (1)-8 (1)-9 (1)-9 (1)-9	C(60)9°-A6T6(1)-1 (1)-6 " (1)-5 " (1)-7 " (1)-7	G(24)9°-A6T6(1)-1 " (1)-1 " (1)-2 " (1)-3	6(100)1-A2T8(1)-4 " (1)-4 " (1)-4	6 (61) 1-A2T8(1)-4 (1)-4 (1)-9 (1)-7 (1)-7 (1)-7	35.55.55.55.55.55.55.55.55.55.55.55.55.5	6 (24) 1-A2T8(1) .9
6.8 7.9 8.5	10.0 12.0 14.5	16.1	0.123 0.163 0.171 0.44	0.27 0.34 0.56 1.16 1.35 2.10	0.36 0.48 3.20 3.45	0.87 1.07 12.0 16.2	1. 16	0.50 0.75 0.75 0.60 0.69		16, 2 17. 0
590 680 730	840 1000 1190	1310	37 72 82 31 50	260 450 66 80 95 160	550 1000 220 250 250 275	3200 4400 1000 1280	80 95 126	1080 1430 2450 670 730 910	300 330 330 340	1280 1360
20°. 20°.	20. 20.	20.	12.00 9.30 8.90 20.	6.15 20. 20. 20. 20.	20. 20. 20. 20.	2.40 2.05 20.	20. 20. 20.	3.80 2.70 2.70 2.70	300.00 300.00 300.00	20.
0.80 1.00 1.12	1.50 2.00 2.50	3.00	66	4# 0.050 0.052 0.075 0.125	44 0.187 0.22 0.25	2.00 3.00	0.062 0.075 0.100	666	0.28 0.33 0.33 0.33	3.25
2-231 2-227 2-228	2-210 2-209 2-298	2-23	HE-141 HE-140 2-307 2-308	HE-137 HE-138 2-309 2-304 2-304 2-303	HE-135 HE-136 2-301 2-310 2-300	HE-133 HE-134 2-306 2-305	2-144 2-145 2-146	HE-102 HE-103 HE-104 2-196 2-197 2-198	2:215 2-98 2-216 2-99 2-271	2-279
A221-1 -2 -3	A222-1	A223-1	A31-1 -2 -3 -4	A32.1.2.2.4.4.4.5.5.6.6.6.6.0.0.0.0.0.0.0.0.0.0.0.0.0.0	A33-1 2 -3 -4 -5	A34-1 -2 -3 -4	A411-1	A412-1 -22-1 -4455-6		A413-1

The stands of the second secon

Table 4.1 (Continued, Pages 5 and 6)

Figure No.	5.22(c) 5.22(d)		5.23(a) 5.23(b) 5.23(c) 5.23(d)		
Damage	No damage. No bucking. Bucking at one end. Torn at one end plug. Sheared at one end plug. Cylinder forn apart on loaded side. No bucking.	Buckled, 4 lobe. No damage. Wrinkling. Wrinkling. Wrinkling. Wo damage. Buckled 1 lobe, tending towards diamond No damage. No damage. Buckled 1 lobe. Buckled 1 lobe.	No buckling. No buckling. No buckling. No buckling. Ends sheared, driven to mandrel. Wrinkling and dishing. Buckled, sevoral lobes, plus dishing-in. No damage. Buckled I lobe, in diamond shape. No damage. Sheared and torn off.	No damage Buckled, 3 lobes. No damage. No damage - (reverse side)	No buckling. No pronounced buckling. Buckled, 1 lobe. Buckled, 1 lobe fairly flat. Buckled, and sheared at both ends. One lobe diamond deformation, quite flat over length No buckling. Buckled, 1 lobe. Buckled, 1 lobe. Buckled, 1 lobe. Buckled, 1 lobe. Sheared both ends to mandrel. Buckled, sheared 2" along each end.
Metal (% w/a)	2.5 15. 47. 47. 30. 77. > 30. > 30.	1404 3440 1004 0	2.8 3.3 7.7 7.30. 20. 18. 0.0	25. 0.0 0.0 0.0	3.00 1.00 1.00 1.00 1.00 1.00 1.00 1.00
Cylinder No.	3(23)1-A?T8(1)-2 (1)-2 (1)-4 (1)-4 (1)-4 (1)-5 (1)-3 (1)-10 (1)-10 (1)-10		6(61) 1-M31B (1)-2 (1)-3 (1)-3 (1)-3 (1)-3 (1)-4 (1)-6	3(50)1-M31B (-)-9 (-)-9 (-)-10 (-)-10 (-)- (-)-	6(24) 1-M31B(1)-7 (1)-8 (1)-10
1 (taps) x 10 ⁴	0.97 1.28 1.33 1.35 1.45 1.60 17 0	0.35 0.235 0.235 0.235 0.235 0.358 0.36	0.27 0.33 0.33 0.33 0.35 0.93 1.26 1.35	0.30 0.56 1.16 1.64 1.80 2.05	0.50 0.67 0.683 0.78 1.022 1.25 1.25 6.7 6.7
P (pst)	3800 5700 5700 5900 6700 7500 1360	66 17 102 142 190 66 66 95 17 17 28 285	260 340 430 530 126 126 126	300 595 80 120 135	1080 2000 2950 2950 11170 1470 680 680 680
Distance (ft) or Tube (ft)	2. 20 1. 80 1. 79 1. 76 1. 65 20. 55	10: 10: 10: 10: 10: 10: 10: 10: 10: 10:	80000000000000000000000000000000000000	2 5 5 5 5 5 5 5 5 5 5 5 5 5 5 5 5 5 5 5	2000 2000 2000 2000 2000 2000 2000 200
Charge Wt. (lbs) or Ratio a	3.25	0.000 0.017 0.017 0.017 0.017 0.017 0.017 0.017 0.017	44 44 44 44 44 0.100 0.150 0.150 0.075	0 014F 0.030F 0.062 0.094 0.108	4444 0.00065 0.00000 0.0000 0.0000 0.0000 0.0000 0.0000 0.00000 0.00000 0.00000 0.00000 0.00000 0.00000 0.00000 0.00000 0.000000
Shot No.	HE-102 HE-103 HE-109 HE-107 HE-106 HE-104 2-100	2-119 4-28 4-24 HE-56 HE-55 HE-58 2-117 2-118 4-22 4-23	HE-55 HE-54 HE-59 HE-57 HE-57 2-195 2-110 2-79 2-79	2-174 2-175 2-15 2-20 2-21 2-16	HE-53 HE-57 HE-57 2-179 2-178 2-178 2-280 2-280 2-245 2-245 2-390 2-377 4-39
Group No	A414-1 -2 -3 -4 -4 -5 -6 -6 -8	A 22 22 22 24 25 43 64 64 64 64 64 64 64 64 64 64 64 64 64	A423.1 2.2 2.4 3.1 6.1 6.1 1.0 1.0	A424-1	A425 -1 -2 -2 -2 -4 -4 -4 -4 -4 -4 -4 -4 -4 -4 -4 -4 -4

		5.24(a) 5.24(b)	5.24(c)	5.24(d)		6.2(b) 6.2(d)	6.2(f)	6.3(b) 6.3(c)	6. 3(e) 6. 3(f)
(1bs)	00	3800T 4000F 3160T 3500T 3400T	4000C 3800C 3610C	0 0 0 3300T 3000T 3200T	3000£				ar each end
	00	4900T 5000T 4850T 4850T 3800T	2500C 3850C 3750C 3770C	0 0 0 0 5 100T 5000T	C 5500T	<u>.</u>	pan center.	t one end. both ends	e in Al. ne
Convertional fixture. No damage. Conventional fixture. No damage. Conventional fixture. Buckled 3 lobes. Preload fixture. No damage.		No damage. No damage. Buckled, 3 lobes. Buckled, 3-lobe symmetrical. Buckled, 3-lobe symmetrical.	No damage. No damage. No damage. Buckled,3 lobes.	Conventional fixture. No buckling. Conventional fixture. Single lobe. Preload fixture. No damage. Preload fixture. No damage. No damage. Buckled single lobe. Buckled single lobe.	C-cracks both ends. (Conv. fixture) C-crack one end 1 1/2" long.	No damage. No damage. No damage. No damage. C-cracks at both end plugs. Disintegrated and blew off.	C-cracks at end plugs. X-cracks at span center. C-cracks at end plugs.	No cracks. L-cracks. Plastic shattered off loaded side. Cracked full length. Hourglass cracks both ends.	No cracks. No cracks. No cracks. circumferential-ridge bulge in Al. near each end Blew off.
0.000	12.	0.0 0.0 17. 23. 21.	0.0 0.0 0.0 24.	27. 27. 0.0 0.0 20. 21.	5.2	0.17 > 30. 0.07 1.		2.6	3.00
6(100)1-A6T6 (7)-10 (7)-10 (7)-10 (5)-16	(5)-16	(5)-14 (5)-15 (5)-17 (6)-17 (5)-14	(9)-18 (9)-18 (9)-18 (9)-18	6 (61) 1-A6T6 (1)-10 (1)-2 (1)-17 (1)-17 (1)-17 (1)-17 (1)-19 (1)-18	6 (61) 1-A6T6 (3)-7M " (3)-8M	6 5(26)1-Micarta-5	3(25)1-Micarta	-A6T6	(7)-15F (7)-15P (6)-7P (7)-15P
0.96 1.60 1.75 0.96	1.16	0.96 1.35 1.52 1.52 1.52	0.45 0.45 0.96 1.35	3.45 2.9 3.45 3.45 4.0	14 0	0.84 0.92 1.04 7.9 10 0		0.49 0.54 0.56 0.58	6.4 7.9 7.9
99	95	66 95 110 126 110	31 31 95 95	275 330 225 225 275 225 275 320	1150	2900 3450 4200 680 840 1000	450	4400 4400 4700 5100	540 680 760
20. 30. 20.	20.	20.000 20.000	20. 20. 20.	00.00.00 00.00.00 00.00.00	20.	2.50 2.30 2.10 20.10 20.20		1. 10 1. 05 1. 0 0. 95	20. 20. 20.
0.050	0.062	0.050 0.075 0.087 0.100 0.087	0, 025 0, 025 0 050 0, 075	0.25 0.33 0.19 0.25 0.25 0.31	2.50	44 44 1.00 1.50 2.00	static	\$\$\\\\\\\\\\\\\\\\\\\\\\\\\\\\\\\\\\\\	0.50 0.69 1.25
2-28 4-29 4-15 2-254	2-251	2-246 2-248 2-256 2-247 2-249	2-257 2-265 2-266 2-267	2-30 2-109 2-295 2-296 2-294 2-293	2-42	HE-173 HE-174 HE-175 2-88 2-89 2-87		HE-84 HE-85 HE-83	2-135 2-136 2-137 2-138
A511-1 -2 -3	2,4		13 - 13 - 15 - 15 - 15 - 15 - 15 - 15 -	A512-1 -2 -3 -4 -5 -6	A521-1	B11-1	B12-1	B211-1 -2 -3 -4	v. 54. 8

^aUncovered shell, originally with rubber.

A STATE OF THE STA

ble 4. l (Confinued, Pages 7 and 8)

	Figure	6.4(6)	6.4(c) 6.4(d)	6.5(b,c)		6.6(b)	6. 7(a)	6.7(6)		6.8(b) 6.8(c, d)
	Damage	No cracks. No cracks. Hailine C-crack one end. Hailine C-rack one end. Na buckling. No cracks. Hairine cracks at end plugs.	C- and L-cracks at end plugs. One lobe, C-cracks both ends, L-crack nearly full length. Sheared to mandrel one end, severe Micarta cracking, No cracks, Micarta deformation 1%, C-ridge one end 3.5% Light C-cracks both end plugs, subshell ridge near one end.	No buckling. Wrinking at one end. No damage No damage. Buckled, 2 lobes.	No damage. No cracks. No cracko. Platic se battered, hourglass pattern. No damage.	Plexiglas cracked off one side. L-cracks extending to center if from one end. No Plexiglas damage. Plexiglas deformation <0.5%. Plexiglas stripped off one side. Shell buckled.	No cracks. Plastic shattered over front face. Plastic shattered off one side. Plastic stripped off. Plastiglas cracked at one end. L-crack full length at shot zero. Hourglass at ends. No cracks.	L-crack full length at shot zero. L-crack full length. L-shaped crack extending from one end. Flattened to mandrel. Plexaglas stripped. Disintegrated. Wrong cylinder. No Plexaglas cracks. Single lobe about 15%.	Hairline C-cracks both ends, dimple in subshell center. No cracks. L-cracks extending several inches in from each end. No cracks. Hairline C-crack one end; L-crack full length. L-crack full length; C-cracks both ends. No Micarta damage. Micrack full dended side.	
ages can	Metal (% w/a)		6.7 16. >30. 3.47	0.67 0.0 0.0 40.	0.0	8 1.68 1.48 27.	0.24.8.4.6.2	તું હું હું	5.7 1.0 5.2 0.0 2.17 4.5	4.85 2.12 5.05
Table 4. I (Continued, Fages (and o)	Cylinder No.	6(100)1-A6T6(2)-9M (2)-9M (2)-13M (2)-4M (2)-9M (1) (2)-1M (2)-1M (2)-2M	(2)-3M (3)-16M (3)-16M (1)-11M (1)-15M (2)-8M	6(100)1-A6T6(8)-7R (8)-13R (8)-2R (8)-2R (8)-2R	6 (61) 1-A6T6(5)-9P (5)-9P (5)-6P (5)-7P (5)-7P (5)-4P	(5)-4P (5)-5P (5)-10P (5)-8P	3 (53) 1-A6T6(1)-10P (1)-10P (1)-12P (1)-12P (1)-13P (1)-13P (1)-13P (1)-13P	(1)-11p (1)-2p (1)-3p (1)-3p (1)-7p (1)-4p	6 (61) 1-A6T6(9)-12M (9)-12M (9)-13M (1)-5M (1)-5M (1)-5M (1)-5M (1)-5M (1)-5M (1)-5M	(3)-3M (3)-6M (3)-7M (3)-1M
	1 (taps) x 10 ⁴	0.44 0.55 0.55 0.69 0.92 1.10	1 19 1.28 1.28 10.0 12.0	0.23 0.34 1.60 2.3 2.9	0.34 0.36 0.49 0.88	1. 15 5. 8 8. 40 10. 0	0.0.0.0.0.0.0.0.0.0.0.0.0.0.0.0.0.0.0.	7.9 10.0 10.0 12.0	0.68 0.75 0.82 1.10 1.50 1.70	8.8 12.0 14.4 18.0
	d (18d)	3300 4400 4700 5600 6400 3400	5100 5650 5650 840 1000	950 2000 75 110 140	1670 2000 2300 4000 970	1290 925 725 840	1700 5700 2900 3800 1150 1000	680 840 840 1000 1770 900	6400 7000 8000 4650 7000 8200 1800	1350 1000 1150 1400
	Distance (ft) or Tube (ft)	1.2 1.05 1.05 0.90 0.85 30 2.00	1.90 1.80 1.80 20.	2, 00 1 50 30, 30,	1. 60 1. 50 1. 40 2.	20. 20.	2, 55 1, 50 2, 50 2, 20 10, 5	200. 200. 200. 200.	0.85 0.75 0.75 1.60 1.49	20. 20. 20.
	Charge Wt. (lbs) or Ratio a	00000 (000000 (0000000 (0000000 (000000 (00000 (0000)	1.5 4.4.4. 0.00 4.4.4.4.	0.5# 0.5# 0.057 0.086 0.114	0.5*	0.074F 1.75 2.15 1.50	12.5 2.50 1.00 1.00	1,00 1,50 1,50 2,00 5,00	######################################	3.25
	Shot No.	HE-79 HE-80 HE-74 HE-78 HE-81 HE-46	HE-48 HE-95 HE-47 2-278 2-44	HE-101 HE-108 4-25 4-26 4-27	HE-92 HE-93 HE-94 HE-96 2-180	2-181 2-134 2-133 2-133	HE-15 HE-17 HE-35 HE-34 2-65 2-55	2-4 2-49 2-14 2-1	HE-90 HE-91 HE-92 HE-42 HE-43 HE-44 2-169	2-130 2-276 2-42 2-41
	Group No.	8212-1 -2 -3 -4 -4 -6	110	8213-1 -2 -3 -4 -5	B221-1 -2 -3 -4 -4	97.86	B222-1 -2 -3 -4 -6 -6	869777	B223-1 -2 -3 -4 -5 -6	9 7 7 7

51 E1 · 以下分析: 在

丁二世教之歌 ちゃっちゃっ

CALL CONTRACTOR CONTRA

3-foot charge length

10(0)

and the second of the second o

Table 4, 1 (Continued, Pages 9 and 10

Figure No.	6. 10(c)	6. 10(d)	····	6. 11(a) 6. 11(b) 6. 11(c) 6. 11(d)		6. 12(a) 6. 12(b)				
Damage	Plastic shattered off loaded side. Plastic shattered off loaded side. Plastic shattered completely off. Howeglas cracking at both end plugs. L-crack at shot zero, hourglass cracks. No cracks.	No Plexiglas cracks. L-crack full length at shot zero. L-track full length at shot zero. L-track removed, at shot zero. L-haped cracks and L-crack. Aluminum sheared long C-crack one end, L-crack 2/3 span centrally.	No cracks Complete longitudinal crack. C-cracks both ends. Hit by rack, no valid % deformation	Haurine C-cracks both ends C-cracks both ends, L-crack at center, I lobe bucking No cracks. Haurine C-cracks both ends, long, thru-crack 1/2 length. Hairine C-cracks both ends, long, thru-crack full length Sheared one end to mandrel, Micarta off loaded side.	C-cracks at both end plugs. No Micarta cracks C-cracks both ends, L-crack half length C-cracks at both end plugs. C-cracks both end plugs. No cracks both ends. L-crack half length. No cracks. (S.c.)	No cracks. No cracks. Micarta deflection 4%. (S.G., aircady had one shot 2-16Q.) C-crack one end very light. Micarta removed; front sheared, back buckled in. Short L-crack at midspan, over 20% subshell lobe. No micarta dange.	Micarta removed, front sheared to mandre!. Misarta removed, front sheared, back buckled in. No cracks. No cracks.	No buckling. No buckling. No buckling. No buckling. Buckled, I lobe at one end. No pronou.ced buckling. Buckled, 2 lobes. No buckling. Buckled to mandrel.	Incipient buckle to outside on shot zero Rubber blew off, shell ruptured on blast side.	No cracks. L-crack full length at shot zero. C-ridge one end 2.0%
Meta! (% w/n)	29 39 54. 4. 5.	25. 10. 10.	9.0	4.7 15.6 1 8.4 10.	4.4.4.6.0 0.0	સ્ જ્યું તુ	3.	₩¢÷; ₹¢; ₹; ₹¢; ₹; ₹¢; ₹; ₹¢; ₹; ₹¢; ₹; ₹¢; ₹; ₹¢; ₹; ₹¢; ₹; ₹¢; ₹¢	i	0.37
Cylinder No.	3(23)1-A6T6(1)- 3P (1)- 5P (1)- 6P (1)- 6P (1)- 2P (1)- 9P (1)- 1P	(1)-10P (1)-1P (1)-12P (1)-12P (1)-4P	6(24)1-A6T6(1)-2M (1)-2M (1)-5M	3(23) 1-A6T6(1)-12M (2)-17M (1)-6M (1)-1M (1)-1M (1)-2M (1)-3M	(1)-13M (2)-19M (2)-19M (1)-18M (1)-14M (1)-14M	(1)-10M (1)-16M (1)-16M (1)-18M (1)-18M (1)-18M	(1)-4M (1)-5M (1)-10M (1)-10M	3(23)1-A6T6(1)-2.R (1)-5.R (1)-6.R (1)-7.R (1)-4.R (1)-1.R (1)-9.R (1)-9.R	6(100)1-A2T8(1)-1R	6(61)1-A2T8(1)-4P
1 (taps) × 10 ⁴	1.45 1.50 1.62 8.2 15.0	19 5 22.7 25 5	1.88 2.10 25.5	0. 90 1. 05 1. 10 1. 28 1. 40 1. 40	2. 9 2. 15 2. 7 9. 0 15. 0	19.5 22.7 25.5 31.5	22.0 31.5 19.5 30.0	0.55 0.63 0.97 0.97 1.28 18.0	5.3	10.0
P (psi)	5700 7000 7700 2300 1500	1530 1770 1950 1650 1900	9100 10300 1950	9000 10500 4650 5650 6290 9000	6200 2600 3300 2450 2130 1000	1530 1770 1950 2300 2375 1500	1600 2300 1530 1530	2500 3800 3800 1280 1400	140	1,000
Distance (ft) or Tube (ft)	1. 65 1. 60 1. 52 20. 20.	20.	1.40 1.30 20.	0.70 0.65 2.00 1.80 1.70 1.70	20.05.20.20.20.20.20.20.20.20.20.20.20.20.20.	.0.0.0 20.00 20.00 20.00	20. 20. 20.	7.00 6.90 0.80 0.80 2.20 2.20 2.00 2.00 2.00 2.0	30.	20.
Charge Wt. (lbs) or Ratio G	8 8 9 4 4 4 4 4 4 4 4 4 4 4 4 4 4 4 4 4	4.00 5.00 6.00 static	***00	0.0 N N 4 4 4 4	0.290F 0.160F 0.210F 9.00 7.00	4.00 6.00 8.00 8.00 8.00 8.00	8.8.4.4 000.00 000.00 000.00	0000	0.114	1.50
Shot No.	HE-41 HE-43 HE-40 2-66 2-18 2-13	2-48 2-70 2-45	HE-49 HE-50 2-43	H7-83 HE-90 HE-38 HE-37 HE-35	2-73 2-171 2-170 2-72 2-74 2-160	2-9 2-161 2-19 2-10 2-10	2-12 2-10 2-9 2-17	HE-84 HE-85 HE-87 HE-59 HE-56 2-46 2-50	4-38 2-258	2-272
Group No.	B232-7 -8 -9 -10 -11	113	B233-1	B234-1 -22 -4-1-3	- 19 - 19 - 12 - 12	11.	-19	B235-1 -3 -3 -4 -6 -6 -7	B311-1	B321-1

Land to the state of the state

Securior S

Privaters of

Established I

distance of the same

Total And

Service Services

No cracks. G-cracks at end plugs. C-cracks at end plugs. C-cracks at end plugs, peeling at $\frac{4}{2}$ 45 .	No buckling. No buckling. Very short wavelength wrinkles near shot zero. No buckling. Buckled, I lobe. Sheared to mandrel; rubber OK.	No cracks. L-c s at shot zero, from one end. Cylinder and mount fixture blew out of tube. Bolts sheared.	Cylinder completely blown off fixture.	No cracks - Micarta 1%. No cracks . Light C-crack at one plug Micarta 1.5%	No cracks.	No buckling. Vo buckling.	No buckling. Buckled, 2 lobes.	No cracks. No cracks. L-crack full length, hourglass cracks one end. No cracks. L-crack full length; 1 ourglass cracks one end. No cracks. L-crack half length; hourglass crack one end. No cracks. Disintegrated. C-cracks at one end plug. C-cracks at both end plugs. No cracks. No cracks. No cracks. No cracks. No cracks. C-cracks. No cracks. C-cracks.
0.23 0.83	6.13 2.5 0.0 16.	0.95		2.28	<2.	0.5	23.	2000 2000 2000 2000 2000 2000 2000 200
6(61)1-A2T8(1)-3M " (1)-1M " (1)-2M	6(61)1-A2T8(1)-5R (1)-2R (1)-4R (1)-4R (1)-3R (1)-3R	6(24)1-A2T8(1)-1P " (1)-2P " (1)-3P	3(23)1-A2T8(1)-4P	6(24)1-A2T8(1)-4M " (1)-2M " (1)-5M	3(23)1-A2T8(1)-2M	6(24)1-A2T8(1,.2R	6(100)1-M31B(1)-2R	6(61)1-M31B(1)-4P (1)-4P (1)-3P (1)-3P (1)-2P (1)-1P (1)-1P (1)-1P (1)-5P (1)-5P (1)-5M (1)-3
14.0	0.36 1.28 7.4 8.5 8.5 8.5	22.7 27.0 31.5	31.5	22.0 25.5 25.5	31.5	16.2	1.22	0.000 444.000 444.000 444.000 6.000
1500	2300 1100 1450 350 420 480	1770 2050 2300	2300	2900 1950 1950	2300	1280 1400	57	200 850 850 850 850 850 850 840 840 840 840 840 840 840 840 840
20. 20. 20.	2. 2. 2. 30. 30.	20. 20. 20.	30.	10. 20. 20.	20.	20.	30. 30.	4 4 4 4 4 4 4 4 4 4 4 4 4 4 4 4 4 4 4
3.50	0.54 0.064F 0.37 0.46 0.57	5.00 6.50 8.00	9.00	12. 53 6. 00 6. 00	8.00	3.50	0.043	444 444 0.030F 0.046F 1.00 0.057 0.075F 0.095F 1.50 0.87 1.50 0.87
2-275 2-154 2-374	HE-98 3-199 2-200 2-283 4-37	2-285 2-311 2-289	2-290	2-366 2-284 2-365	2-290	2 .286 2-287	4-34	HE-106 HE-107 2-167 2-153 2-153 2-153 2-140 2-185 2-18
B322-1	B323.1 -2 -3 -4 -5 -6	B331-1 -2 -3	B332-1	B333-1	B331-1	B335-,,	B411-1	8 22 22 24 25 25 25 25 25 26 26 26 26 26 26 27 26 26 26 27 26 26 26 26 27 26 26 26 26 26 26 26 26 26 26 26 26 26

I

1

The property of the property o

N. Carlot

CALLERY SHOW THE PARTY

*3-foot charge length.
b4.5-foot charge length.
c6-foot charge length.
dy-foot charge length.

Table 4, 1 (Continued, Pages 11 and 12)

THE REPORT OF THE PARTY OF THE

Figure No.		(32)	6. 13(e)		6. 14(b)	6.14(d)	6.22(b)	6.22(g,h)	6.23(b) 6.23(c) 6.23(e) 6.23(f)	6.24	6.26(b) 6.26(c) 6.26(e,f)
Daage	Incipient buckling. No buckling. Rubber blown off; subshell sheared, torn to mandrel.	Two L-cracks full length, hourglass one end. Plexiglas largely cracked off No cracks. S-shaped crack full length, hourglass one end. No cracks. L- and C-cracks over half length Plexiglas shown off subshall shaped and cora	No cracks. C cracks at end plugs. C cracks at end plugs. Mical end file. No -racks. No -racks at both end plugs. C-cracks at both end plugs. C-cracks at both end plugs.	No buckling. No buckling.	G-crack at one end. Buckled to mandrel front and back.	No Micarta damage. No Micarta damage. ("everse of 2-232) Buckled to mandrel, Micarta peeled off.	No damage. Slight delamnation, greatest at ends. Delaminations 2 1/2" long at end plugs. Cover breaking up.	No damage Light delaminations at end plugs. Light delaminations at plugs, delaminations at midspan Full C-delamination one end, subshell sheared to manazel.	Incipuent tape dela mination at end plugs. Tape delamination over whole area. Tape delamination at plugs and several axial stations No cracking evident. Delamination 6" long near one end. Delamination full circumf, near one end, with C-ridge under	No damage. Delaminations at both ends. D'lamination one end, extending through to plug, C-ridge. Severe delamination both ends, subshell C-ridge.	Incipient tape delamination as end plugs. Tape delamination at several axial stations. Incipient tape delamination at end plugs. Gridge at one end; severe delam. 90% circumf, and Lecracks at end.
Metal (% w/a)	2. < 1.	3.50 10. 1.56 2.80 1.63	0.88 1.45 4.05 1.53 2.52 4.02	1. 5.	.;	4.5	0.0 0.48 0.3	0.0 0.28 0.39	0.73 2.6 3.0 2.0 20.0	0.3 2.0 8.0	1.6 2.4 1.07 0.5
Cylinder No.	6(61)1-M31B(1)-2R (1)-3R (1)-1R	6(24)1-M31B(1)-5P (1)-2P (1)-5P (1)-5P (1)-3P (1)-3P	6(24)1-M31E(1)-2M (1)-2M (1)-4M (1)-4M (1)-3M (1)-5M (1)-5M (1)-5M	6(24)1-M31B(1)-3R (1)-1R	3(53;2-A6T6(2)-3M (2)-1M	3(23)2-A(.T6(2)-1M " (2)-1M " (2)-3M	6(100)1-A6T6*RL5 "-RL5 "-RL1	" -RL3 " -RL3 " -RL3	6(100)] - A6T6-CP5 CP5 CP4 CP4 CP2	6(100)1-A6T6-NX2 -NX3 -NX4 -NX4	6(50)1-A6T6-RL5 -RL3 -RL1 -RL1 -RL1 -RL1
1 (tape) x 10 ⁴	0.51 1.72 2.4	1.34 5.3 6.4 9.3	1.30 1.67 1.2 2 11.0 14.0	7.7	7.9 8.8	10.0 12.0 16.2	0.76 0.87 1.11	7.9 12.0 14.0 19.5	0.98 1.11 1.38 10.0 12.0 16.1	7.9 12.0 13.5 16.1	1.11 1.25 1.60 16.1 22.7
d (bed)	530 126 180	1560 1900 1000 800 800 925	1473 1950 1400 1770 925 1150	420	089	840 1000 1280	2500 3200 4600 7000	680 1000 1150 1530	3800 4600 6300 840 1000 1310	680 1000 1120 1310	4600 5400 7500 1310 1770
Distance (ft) or Tube (ft)	2. 20. 20.	2 2 2 1 1 0 . 2 . 2 . 2 . 2 . 2 . 2 . 2 . 2 . 2 .	2 5 5 5 5 5 5 5 5 5 5 5 5 5 5 5 5 5 5 5	30.	20.	20. 20. 20.	2.70 2.40 2.00 1.60	20. 20. 20.	2.20 2.00 1.70 20.20	20. 20. 20.	2.00 1.84 1.55 20.
Charge Wt. (lbs) or Ratio a	0. 327F 0. 30 0. 15	0.092F 0.114F 1.50 2.00 1.37 1.75	0.085F 0.1175 3.50 5.00 1.75 2.50	0.46	1.00	3.00	4444	2.90 4.00	4444 2.00 3.00 3.00	2.00 2.34 3.00	%4440.00
Shot No.	2-194 2-156 2-155	2-188 2-151 2-151 2-149 2-281 2-148	2-191 2-190 2-114 2-113 2-282 2-86 2-85	4-35 4-36	2-229	2-232 2-233 2-234	HE-176 HE-175 HE-177 HE-177	2-235 2-236 2-237 2-238	HE-127 HE-128 HE-131 2-241 2-240 2-239	2-380 2-381 2-383 2-382	HE-130 HE-129 HE-132 2-269 2-268
Group No.	B423-1 -2 -3	B431-1 -22 -33 -5-	B432-1 -2 -3 -4 -6	B433-1	B51-1	B52-1 -2 -3	B611-1	297.8	B612-1 -2 -3 -4 -5	B613-1	B621-1

A PROPERTY OF

The state of the

Print, -

Partin Chall

Contracted Co.

The straight

Editoria e

Separation of

A Constanting

STATE OF STREET

6 27(b) 6.27(c) 6.27(e) 6.27(e)	7. 1(c) 7. 1(c) 7. 1(f) 7. 1(g)	7.2(b) 7.2(c) 7.2(e) 7.2(e)	7. 3(c) 7. 3(d) 7. 3(f)	7.4(c) 7.4(d) 7.4(d)
No damage. Gircum, tage delam, over entire loaded side. Gircum tage delam, over entire loaded side. Severe delaminations over entire loaded side. Incipient delam, at plugs; light delum, at half span + 90° Subshell C-ridge 5. 5% one end. Delams 1/2 circum.	No buckling. Uniform deformation full length. Pushed in more one end, and between ribs. Deformation at end plugs just visible. No buckling, beding between plug and last rib. Shear buckling between end and tast rib. Cylinder blew off in pieces.	No buckling. No buckling. Dishock in between ribs. Dishock in between ribs. Nearly uniform deformation along length. Nearly uniform deformation along length Thin well; poor machining, wrinkling between ribs. More deflection at one end. Flat across span, no buckling. No buckling. No buckling. Buckling. Buckling.	No cracks. No cracks. Plexiglas shattored on loaded side. Plexiglas abattored completely off, test one ond. No cracks; Plexiglas deformation < 1%. No cracks; Plexiglas deformation 1%. Plexiglas stripped off.	Hairline G-crack at one end. Hairline G-cracks both ends. L-crack half length one end. Hairline G-cracks are end plug. Hairline G-cracks are for blug. Hairline G-cracks are end plugs. No cracks. Micarta 0.5%. No cracks. Micarta 1%. G-crack one end Micarta 1.5% G-cracks both ends. G-cracks both ends 11/2" each side zero. G-cracks both ends 11/2" each side zero. G-cracks both ends 11/2" each side zero. G-cracks both ends 1.2" each side zero.
0.0 0.37 10.4 0.43 2.35	0.43 8.22 6.53 6.65	25. 1. 2. 2. 2. 3. 3. 3. 3. 3. 3. 3. 3. 3. 3. 3. 3. 3.	0.5 3.5 2.2. 7.	2 2 2 2 2 2 2 2 2 2 2 2 2 2 2 2 2 2 2
6(50)1-A616-GP1 - GP1 - GP2 CP2 CP4 CP4	6(100)1-5Rib(030)-(4)-12 -(4)-12 -(4)-12 -(5)-12 -(5)-8 -(5)-8 -(4)-8 -(4)-8	6(50)1-2Rib(060)-(1)-7 -(1)-7 -(3)-15 -(3)-15 -(3)-15 -(1)-3 -(1)-3 -(1)-14 -(1)-17 -(1)-17 -(1)-18 -(1)-18 -(1)-18 -(1)-18 -(1)-18 -(1)-18 -(1)-18		6(50)1-2Rab(250)-5M
0.98 1.20 1.50 1.85 19.5 24 0	0,275 0,365 0,42 2,4 3,2 4,0 5,3	0.000000000000000000000000000000000000	0.67 0.83 0.97 1.67 10.0	0. 97 1. 12 1. 45 1. 60 1. 60
3800 5100 7000 9000 1150 1870	270 550 760 180 250 320 440	670 1560 1780 1920 2000 2500 2500 600 600 600 600	2000 2900 3800 130 130 1000	3800 4700 5700 6700 7500 840 1180 1180 1160 11650
2.20 1.90 1.60 20.20 20.20	6.00 4.80 20.20. 20.	20.00 20.00	3.00 2.50 2.20 20.50 20.	2. 20 2. 20 1. 1. 65 2. 0. 20 2. 0. 20 2. 0. 20 2. 0. 20
4444000 *****000	44 44 0.15 0.22 0.33	444444 45500%	11.2 00.2 00.2 00.2 00.2 00.2 00.2 00.2	- 96,44,4
HE-173 HE-174 HE-179 2-244 2-243 2-243	HE-110 HE-111 HE-113 2-221 2-242 2-222 2-220	HE-109 HE-116 HE-116 HE-116 HE-117 2-225 2-224 2-223	HE-119 HE-120 HE-121 HE-118 2-344 2-262 2-263	HE-126 HE-125 HE-123 HE-123 E-260 2-260 2-261 2-264 2-264 2-298
5,2-1 2,4-1 3,4-1-5	C111-1-1-1-1-1-1-1-1-1-1-1-1-1-1-1-1-1-	C112-1	C121-1 -2 -3 -4 -6	C1222-1 -3 -3 -4 -6 -6 -6 -7 -7 -10 -10

Table f. 1 (Continued, Pages 13 and 14)

Figure No.	7.5(b)	7.5(c) 7.5(e) 7.5(f)	7.6(b) 7.6(d) 7.6(e)	7.7(c) 7.7(e) 7.7(g) 7.7(g)	7.8(b) 7.8(c) 7.8(f) 7.8(g)	7.9(c) 7.9(d) 7.9(g)	7. 10(b)	7. 10(e)
Damage	No damage. Wrinkling over most-deformed half-length. Wrinkling. Slight wrinkling near most deformed end.	Uniform deflection over length. No bucking Some wrinking near most deformed end. No damage. After wrinkles near one end. Wrinkled over loaded axic.	No buckling. Very short wavelength wrinkling. No buckling. No buckling. Where and 1%. Pushed in one end. Wrinkled and pushed in flat on loaded side.	No damage. No buckling. Uniform deflection over length, wrinkling. No buckling. A few wrinklea. Wrinkled at one end. Sheared, and wrinkled at one end.	No buckling. Uniform deflection over length; some wrinkling. Dished in. No demage. No buckling. Buckled, 3 lobes. Buckled and caved in.	No buckling, Uniform deflection over length. Slight centing. Uniform deflection over length, plus some wrunkling. Uniform deflection over length, plus some wrunkling. Verbucking, Deflection same across span. Sheared one end, wrinkled.	No damage. No bucking. Pushed in more near one end. Some wrinkling near damaged end. O. re wrinkling near damaged end. Pushed in at areas of low fown strength.	No damage. No damage No buckling. No buckling. Sheared at low density end, 6% at other end.
Metal (% w/a)	0.0 5.3 7.7	1.2 9.0 0.0	1.0 12.5 1. 3.	0.0 0.84 1.2. 4 4.5 30.	20. 5 20. 5 3. 0	2. 4. 8. 4. 9. 1. 5. 5. 4. 9. 5. 5. 4. 9. 5. 5. 9. 9. 5. 9.	0.0 0.63 5.15 7.0 9.2	0.0 0.0 0.0 4.1.5 33.4.1.3
Cylinder No.	6(100)1-A6T6(7)8#F-4 (4)8#F-3 (4)8#F-3 (4)9#F-1 (7)8#F-4	(7)8億万-4 (9)9年5-1 (4)8億万-1 (4)8億万-1 (4)8億万-1 (10)8億万-2	6(100)1-A6T6(4)124F-4 (4)124F-1 (4)124F-1 (4)124F-1 (4)124F-1	6(100)1-A6T6(5)184F-2 (4)204F-4 (5)184F-2 (5)184F-2 (4)204F-2 (4)204F-1 (4)204F-1	6 (61) 1-A6T6(10)8#F-2 (10)8#F-2 (10)8#F-3 (10)8#F-3 (10)8#F-4 (10)8#F-4 (9)8#F-4	6(61) 1-A6T6(10)10#F-4 (11)11#F-4 (10)11#F-4 (10)12#F-2 (10)12#F-3 (10)12#F-3 (10)12#F-3 (10)12#F-2	6 (61) 1-A6T6(10)18#%-5 (10)18#F-5 (10)20#F-1 (10)20#F-1 (10)20#F-1 (10)17#F-3	(10)745-1 (10)1745-1 (10)1745-4 (10)1745-4 (10)1745-1
I (taps) x 10 ⁴	0.32 0.37 0.44 0.45	0.00.48 9.4.4 9.45	0.47 0.67 5.6 6.7	7.44 0.80 1.25 8.9 11.0 14.3	0.00 4.00 7.4.00 7.4.00 7.4.00 7.4.00 7.4.00 7.4.00 7.4.00 7.4.00	0,60 0.83 0.90 1.00 6.9	0.48 0.67 0.98 1.11 1.25 1.50	5.3 7.9 11.0 12.0
P (pei)	380 550 810 880 1000	1000 1700 180 275 400	950 2000 470 560 840	810 2700 5400 760 925 1173	1000 2500 3200 350 440 590	1550 2900 3300 4000 590 680	1000 2000 3800 4600 7000	440 680 840 925 1000 1530
Distance (ft) or Tube (ft)	5.40 4.80 4.20 7.10	3.90 3.20 20. 20.	3.00 20. 20. 20.	4, 20 2, 60 20, 1, 84 20, 20, 20, 20, 20, 20, 20, 20, 20, 20,	3, 90 2, 70 20, 40 20, 20, 20, 20, 20, 20, 20, 20, 20, 20,	3, 33 2, 50 2, 35 2, 15 20, 20, 20, 20, 20, 20, 20, 20, 20, 20,	3.90 3.00 2.20 2.00 1.84	20. 20. 20. 20. 20.
Charge Wt. (lbs) or Ratio o	33333	0.00 4.44 4.45 6.00 1.55 4.30 4.30 4.30 4.30 4.30 4.30 4.30 4.30	0.54 0.75 1.50	1.25 2.75 3.50 3.00	0.37 0.37 0.80 1.25	0.1.5 0.4.4.4.8 0.00 0.00	333333	0.50 1.00 2.1.75 6.00 4.00
Shot No.	HE-152 HE-151 HE-150 HE-155 HE-153	HE-154 HE-156 2-342 2-329 2-326	HE-152 HE-153 2-341 2-325 2-326	HE-147 HE-148 HE-149 2 310 2-317 2-315 2-333	HE-148 HE-150 HE-149 2-338 2-330 2-332	HE-151 HE-158 HE-159 HE-154 2-327 2-324 2-323	HE-142 HE-144 HE-144 HE-145 HE-146	2-312 2-313 2-343 2-339 2-314 2-315
Group %o.	C211-1	94.86.1	C212-1 -2 -3 -4	C213-1 -2 -3 -4 -6 -6	C221-1 -2 -3 -4 -6 -6	C222-1 -2 -3 -4 -6 -6	(222-11-22-1	-10 -10 -11

電影

The same

7. 12(c) 7. 12(e) 7. 12(f)	7.13(b)	7 13(d) 7.13(e)		7. 14(c) 7. 14(d)	7. 14(g, h)	7. 15(b) 7. 15(c) 7. 15(c) 7. 15(d)	7. 17(c) 7. 17(d) 7. 17(e, f)	7. 18(b) 7. 18(c)	7.19(a,b)	7. 10(c. d)	7. 19(e)
Constant deflection over span. No buckling. Inside wall sees—d at one end plug. Internal defle 4% one end at shear ridge. Shear ior d over ± 600.	No buckling. Fushed in and wrinkled at one end. No buckling.	Writkling of outer skin. No buckling. (reverse side shot) Buckled, I sharp lobe.	Buckled, 1 lobe. Fuam compressed 50%. Blew off.	No damage. No damage. No buckling. Wribkling outer skin, deep narrow lobe both skins. Sligh wrinkling outer skin.	No damage. Do buckling. (shot same side as 2-257) Buckled, I lobe. (reverse side of 2-358)	No buckling. Uniform deformation over length. Uniform deformation over length. Inching outer skin. No buckling. (reverse side of 2-360) Buckled of lobe, both akins together. Ladded side sheared to mandrel both ends.	No cracks. C-cracks at end plugs. C-cracks at end plugs. C-cracks at end plugs. Buckling of inner skn at one end, Micarta 2%, C-cracks.	No cracks. Cocracks at end plugs. Cocracks at end plugs. Micarak ragmanted on load side. Subshell sheared	Localized deformation of subshell at one end. Micarta 0.5%, no cracks.	Bending, shear buckle inside one end. Micarta 1%, C-cracks both ends. As above, shear buckles name both ends. Micaria 2%.	C-cracks both ends. Cylinder blew off, shearing at end pluge.
1,37 / 0,12 8,70 / 2,8 19,3 / 15,5 0,5 1,5	1.3 / 0.0 11.5 / 0.97 0.5	3. 1. 6. / 5.5	17. / 10.	0.0 0.0 0.33 / 0.0 13.4 / 8.4 6.7 / 2.9	0.0 1. 13. / 16.	0.8 / 0.1 3.6 / 0.2 8.7 / 2.14 <0.5	0.3 / 0.0 0.3 / 3.0 0.93 / 4.8 4.5 / 10.5 8.	0.3 / 3.8 0.87 / 1.98 0.77 / 0.85 30. />30.		11.	-
6(49/30)16T6-25#F-1 25#F-1 25#F-2 25#F-3 25#F-3	6(30/30)1-A6T6-23#F-2 -23#F-2 -25#F-1		-12#F-2 " -12#F-1	-2345-2 -2345-2 -2345-2 -2455-4 -2345-3		6(49/49)1-A6T6-26#F-4 -24#F-1 -24#F-1 -24#F-1 -24#F-1 -34#F-1	6(30/30)1-A6T0-24F-3M -25F-2M -25F-3M -24F-3M -24F-3M	6(49/30)1-A4T6-25#F-3M -25#F-3M -24#F-2M -24#F-6M	-23#F-1M	24F-1M	" -26#F-5M
0.65 0.87 0.95 6.2 7.9 8.5	3.45 3.45	1.4.9	5.3 16.2	0.48 0.60 0.70 0.91	1.26.	0.67 0.90 1.05 5.2 7.9 15.0	0.91 1.12 1.67 1.80 15.0	1.40 2.00 2.30	12.0	16. 1	24.0
1850 3200 3600 530 680 730	950 950 275	330 390 530	440 1280	1000 1550 1850 2150 2900 3450	530 533 580	2000 3300 4100 530 680 1200	3450 4600 8000 6760	6300 8700 9600 11500	7000	1530	1800
3.10 2.40 2.25 2.00 2.00	29. 4. 00 29. 00	20. 20.	20. 20.		20.	3.00 2.35 2.10 20.20.	2.30 2.00 1.50 20.44	1, 43 1, 43 1, 35 1, 23	20.	20.	20.
0.1.1 44420 1000	44 44 0.25	0.33 0.41 0.67	3.00	*****	0.67	0.67 2.00 2.70	2. 2.444. 7.000.	***	2.00	8 %	5.30
HE-171 HE-172 2-367 2-370 2-370	HE-160 HE-157 2-353	2-354 2-355 2-356	2-335	HE-155 HE-156 HE-167 HE-161 HE-163	2-358	HE-164 HE-165 HE-166 2-361 2-360 2-345	HE-171 HE-172 HE-177 2-364	HE-167 HE-168 HE-169 ITE-179	2-362	2-378	2-379
03 11-1 12-1-1-1-1-1-1-1-1-1-1-1-1-1-1-1-1	C312-1 -2 -4	297	C313-1	0314-1 	2 7 8	C315-1 -2 -3 -4 -5	C321-1	C322-1	r,	۲ ۹	89

*1/4" foarn wall.

Table 4 j (Continued, Page 15)

でいる 本のできる 一般を変えている。

Figure No.				
Damage	No buckling. No buckling. Sheared, tore and blew off	No buckling. Single lobe in diamond shape. Nice records of flip-through. Singl's lobe.	No buckling. No buckling. Sherred, tore and blew off.	No buckling. No buckling. No buckling. Same side. Buckled to mandrel. No damage.
Metal (% w/a)	000000000000000000000000000000000000000	0.0 11. 19.0 19.0 19.0	0.00 0.00 2.50 5.05	%
Cylinder No.	6(61)1-A2T8(1)-5	3(53)1-A6T6(1)-28	6(24)1-A2T8(1)-2	3(23)1-A6'f6(2)-21 " " 3(23)1-A6'f6(1)-16M
1 (taps) × 10 ⁴	4.3.3.3.4 4.3.3.15 7.4.4.3.15 1.5.15 1.5.15	2.8.4.4. 8.4.1.1. 2.4.4.0. 4.4.0.0	6.2 6.2 8.5 12.0 13.5 19.5	16.1 12.0 7.9 17.5 12.0 22.7
P (psi)	180 245 300 300 330 245 245 245	225 225 225 320 330 350 420	530 530 730 1000 1120 1310 1530	1310 1000 680 1400 1770
Distance (ft) or Tube (ft)	000000000000000000000000000000000000000	3 3 6 6 6 6 6 6 6 6 6 6 6 6 6 6 6 6 6 6	000000000000000000000000000000000000000	20. 20. 20. 20. 20.
Charge Wt. (lbs) or Ratio a	0.22 0.33 0.28 0.28 0.28 0.28	0.19 0.22 0.31 0.41 0.25 0.37 0.40	0.67 1.17 2.00 4.3.00 4.00	3.00 2.00 1.00 3.30 5.00
Shot No.	2-212 2-214 2-214 2-215 2-216 2-25 2-270 2-370 2-337	2-346 2-348 2-348 2-349 2-350 2-162 4-31	2-362 2-369 2-371 2-372 2-374 2-374	2-128 2-157 2-158 2-159 2-160 2-161
Group No.	D11-1 -3 -3 -4 -5 -6 -7 -9	-11 -12 -13 -15 -15 -15 -15 -15 -15	D13-1 -2-2-3-4-5-4-5-5-5-5-5-5-5-5-5-5-5-5-5-5-5-5	D14-1

T

Carried A

Procuserad

5. RESPONSE OF SIMPLE METAL SHELLS

In this chapter, results from the dynamic buckling theory in Chapter 8 are summarized and compared with extensive experiments on simple metal shells. The theory is summarized in Section 5.1. In Section 5.2 sufficient data are presented for shells with L/D = 1 and a/h = 187, 100, 61, and 24 to allow comparison with theory over the complete critical pressure-impulse range. In Section 5.3 experiments on buckling are presented and compared with theory for variations in L/D, geometry (cones compared with cylinders), shell materials, and axial preloads. Throughout the chapter, the data are given in the same order as listed in the general Data Summary in Table 4.1, and photographs are presented to show modes of damage and the sensitivity of damage to increases in load.

5.1 General Remarks on Dynamic Buckling Theories for Simple Shells

Simple metal shells subjected to external surface pressures of any duration fail primarily by dynamic buckling. For thin shells (radius-to-thickness ratios larger than 30), failure is dominated by buckling. Relatively thick-walled shells (radius-to-thickness ratios less than 30) yield to an extent that might be called failure before buckling takes place, but ultimately, at sufficiently large loads, even these shells fail by buckling. Adequate theories are available for predicting failure by yielding [19], but relatively little information is available on buckling. Here we concentrate on buckling

Fuckling loads for cylindrical shells subjected to very short or very long loads are readily determined. If the duration of the pulse is sufficiently short, buckling depends only on impulse, and the impulse required to cause buckling car be predicted by one of several simple theoretical models, depending on the radius-to-thickness ratio and material properties [11, 12, 20]. If the duration of the pressure is

sufficiently long, buckling can be predicted with static theory [21] even though blast pressures rise almost instantaneously to their peak pressure. The dynamic overshoot caused by the sudden rise occurs mainly in the membrane response of the shell and in cylindrical shells generally has little influence on the buckling. Thus, as load duration increases, the blast buckling pressure asymptotically approaches the static buckling pressure.

At intermediate durations (quasi-impulsive loads) calculations are somewhat more difficult, but are still manageable. These calculations are given in Chapter 8; the simple formulas for impulsive and static buckling are given here so that the general effects of parameter variations on experimental results can be understood.

Static buckling of a cylindrical shell under uniform lateral pressure occurs at †

$$P_o = 0.92E \left(\frac{a}{L}\right) \left(\frac{h}{a}\right)^{5/2}$$
 (5.1)

where P_0 is pressure, E is Young's modulus, <u>a</u> is cylinder radius, L is cylinder length, and h is wall thickness. Formula (5.1) is taken from [21] and is the asymptotic form for large $Z = \sqrt{1-\nu^2} L^2/ah$ of a solution which can be found using Donnell's equations assuming simply supported ends. The formula is valid for Z > 100 (lower limit of Z), and for modes with four or more waves around the circumference (corresponding to the upper limit of Z). All of the shells in the present investigation fall within this range.

^{*}For spherical caps or arches, which fail by "snap-through" buckling, the mode which generates the membrane thrust is also the buckling mode. For these structures the dynamic overshoot results in quasistatic buckling pressures lower than the static buckling pressures [22, 23].

[†]The coefficient 0.92 was calculated using Poisson's ratio $\nu = 0.3$.

Impulsive buckling of very thin cylindrical shells occurs at impulses given by

$$I_o = 2\rho ca \left(\frac{h}{a}\right)^2$$
, $\frac{a}{h} \approx \frac{2}{\epsilon_v}$ (5.2)

where I_0 is impulse at the threshold of buckling, ρ is material density, $c = \sqrt{E/\rho}$ is wave velocity, ϵ_y is yield strain, and other quantities are as given earlier. Formula (5.2) is based on elastic buckling [12], which imposes the restriction given on a/h in terms of the yield strain.

Thicker shells buckle while membrane plastic flow is taking place and the flexure, and hence buckling, is determined by the tangent modulus \mathbf{E}_t . For many metals, $1/\mathbf{E}_t$ increases approximately linearly with strain beyond yield (data for a few alloys of aluminum, magnesium, and titanium are given in [13] and [20]). With this simplified material behavior, buckling of relatively thick shells occurs at impulses given by

$$I_o = 1.3 \left(\frac{33}{K}\right)^{1/4} a(\rho \sigma_y)^{1/2} \left(\frac{h}{a}\right)^{3/2} , \frac{a}{h} \approx \frac{1}{\epsilon_y}$$
 (5.3)

where K is the average slope beyond yield of the curve of σ/E_t versus compressive strain ε . For the materials referred to above, K is close to 30. Formula (5.3) is Eq. (6.29) from [20] with the multiplier 1.0 replaced by 1.3.

A graph of P_O and I_O versus a/h from these formulas is given in Fig. 5.1 for shells made of 6061-T6 aluminum, taking $E = 10 \times 10^6$ psi, $\sigma_y = 42,000$ psi, and K = 33. As mentioned, these values of P_O and I_O are for shells loaded uniformly all around. In Chapter 8 it is shown that these values are also valid for smoothly varying pressure distributions over one side of a cylinder. It is also

The increased multiplier is used here to fit un heavy in Chapter 8, in which more extensive numerical calculations were performed and which uses a somewhat larger amplification of imperfections in the buckling criterion.

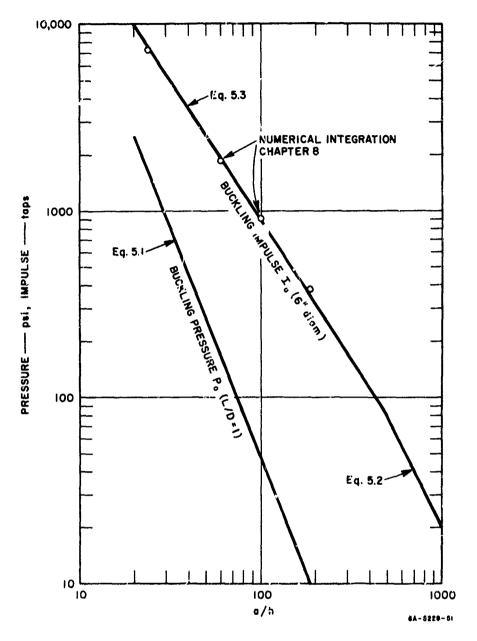


FIG. 5.1 IDEAL IMPULSE I AND STATIC PRESSURE P TO PRODUCE BUCKLING IN 6061-T6 ALUMINUM SHELLS

shown in Chapter 8 that the critical pressure-impulse curves for buckling under a uniform pressure all around and a pressure varying as $\cos^2\theta$ over one side differ only slightly from each other. The maximum difference, about 30 percent, occurs for intermediate pressures and impulses (quasi-impulsive loads).

For comparison with the experiments given in this chapter, buckling threshold curves were calculated (Chapter 8) using an exponential pulse shape and pressure distributions given by Eq. (3.1) (essentially a $\cos^2\theta$ variation over one side) which approximates the observed blast pressures described in Chapter 3. The resulting curves for 24 < a/h < 250 and L/D = 1 are given in Fig. 5.2. These are all normalized to P_0 and I_0 (which can be found from Fig. 5.1) so that the shapes of the curves for various a/h can be easily compared.

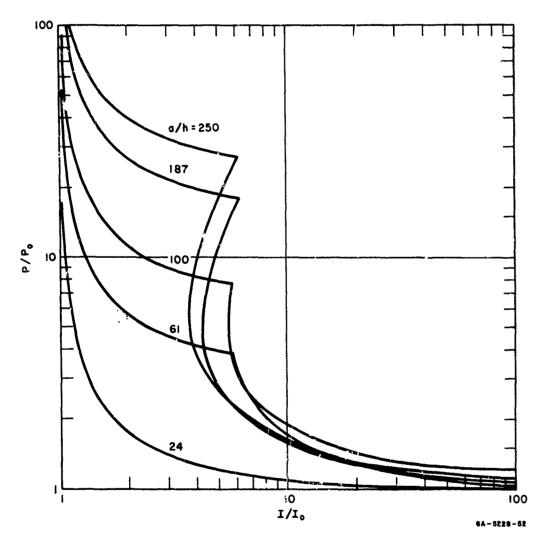


FIG. 5.2 THEORETICAL PRESSURE-IMPULSE CRITICAL CURVES FOR BUCKLING (normalized to P $_{\rm o}$ and I $_{\rm o}$ for 6061–T6 aluminum, L/D = 1)

The object of the state of the

The general trend is for the curves to move upward in the quasiimpulsive region as a/h increases. The curve for a/h = 24 is closely approximated by the hyperbola given by

$$(\frac{P}{P_{o}} - 1) (\frac{I}{I_{o}} - 1) = 1$$
 (5.4)

The curves for larger a/h consist of two branches, one for loads that tend to be impulsive (producing buckling in very high order modes) and another for loads that tend to be static (buckling in lower order modes). Two branches appear in the pressure-impulse curves for the thinner shells because buckling from impulsive loads is dominated by the strain-hardening or "tangent" modulus, while buckling from quasi-static loads is dominated by the elastic modulus. Because of this, the two branches have been called the "tangent-modulus" and "elastic" branches. The shape of each branch is approximately hyperbolic, as in Eq. (5.4). For the tangent modulus branch $I_{\rm O}$ is given by Eq. (5.3) and the asymptotic pressure $P_{\rm T}$ is approximately 0.75% h/a. For the elastic branch $I_{\rm E}$ is approximately 5 pca (h/a) and $P_{\rm O}$ is given by Eq. (5.1).

The cross-over between these branches in Fig. 5.? moves to higher P/P as a/h increases. Thus, for thin shells the pressure must be very high compared to P in order to produce very high order buckling. However, in absolute magnitude, impulsive pressures for thin shells are lower because P itself decreases faster than the shift in the normalized curves. This is shown in Fig. 5.3, in which the curves of Fig. 5.2 are repeated in actual pressure and impulse units. In the area of the cross-over, a more complicated "strain-reversal" theory must be used, but it is shown in Section 8.8 that the more complex theory does not change the basic character of the curves. Also shown are examples of typical calculated buckling mode numbers at various pressure-impulse combinations on each curve. The calculated mode numbers on the impulsive branches tend to be higher than those observed. This is attributed to the use of material properties from tension rather than compression tests and to neglecting strain-reversal in the calculations (the strain-reversal model gives mode numbers of about half of those given). These points are discussed more fully in Chapter 8.

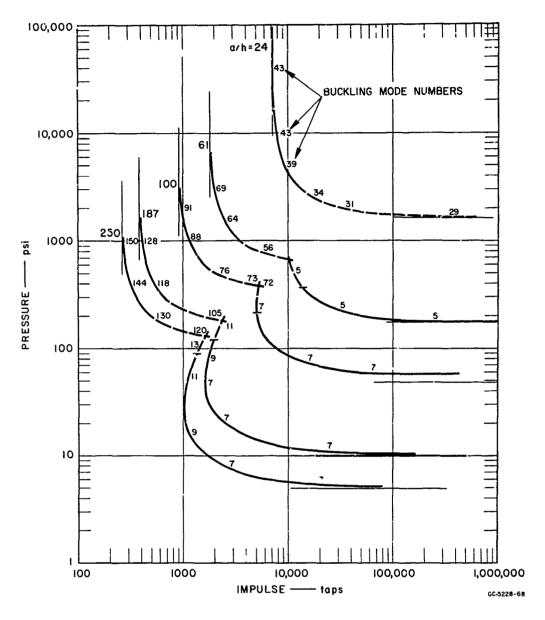


FIG. 5.3 THEORETICAL PRESSURE-IMPULSE CRITICAL CURVES FOR BUCKLING (same as in Fig. 5.2, but in actual pressure and impulse units)

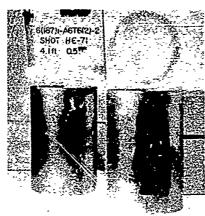
5.2 Experiments to Determine Critical Pressure-Impulse Curves for Buckling

動物を total でんく

Photographs of shells of various a/h buckled from blast low is are shown in Figs. 5 4 through 5.11. Most of the shells are 6 inches in diameter (groups A12, A13, A15, and A17) but a few 3-inch-diameter shells (taken from groups A16 and A18) are also shown where comparable data were not available from the 6-inch experiments. Each photograph shows three views of a model—a front view looking directly at the loaded area, a side view, and a top view. The side and top views are seen through mirrors so the images are somewhat smaller and the view orientation is reversed from the normal 3-view engineering drawing convention. Thus, in the top view the damaged side of the shell is at the top of the circle rather than at the bottom as it would appear in a drawing. This should be kept in mind, particularly for shells that have been loaded on both sides in two separate experiments.

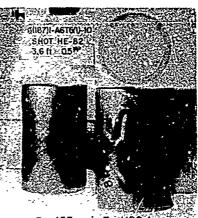
5.2.1 Comparison of Theoretical and Experimental Buckling Loads

The most apparent observation from the photographs is that all of the shells have buckled into one form or another. Before going more into detail concerning the modes of buckling, the loads required to produce buckling are compared with the loads predicted in Fig. 5.3. To do this, two critical pressure-impulse curves are extracted from the experimental data on each shell group. The first is a curve that gives the upper bound on loads that produce no permanent deformation, and the second is a curve that gives pressure-impulse combinations required to produce 10-percent deformation. Figure 5.12 gives maximum radial deformation (in percent of shell radius) versus pressure from 1/2-pound and 4-pound HE spheres. The data fall on reasonably smooth curves, so the pressures that produce 0-percent and 10-percent deformation can be estimated. Figures 5.13 through 5. 16 give some of these same data plotted on a pressure-impulse diagram for each radius-to-thickness ratio (a/h = 187, 100, 61, and 24). Also included are data from the shock tube experiments, which are the higher numbered experiments toward the right in the plots. Only the data from Table 4.1 that gave deformations closest to 0-percent,

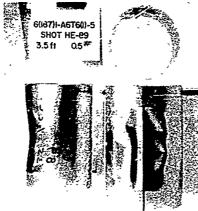


Altophical and the desired the section

P=106 psi, I=950 taps (a) A12-2



P = 153 psi, I = 1100 tape (b) A12-6



P = 170 psi , I = 1150 taps (c) A12-7



P = 220 psi, I = 1250 taps (d) A12-9



P= 102 psi, I =1850 taps (e) A12-12

FIG. 5.4 BUCKLING OF SHELLS WITH a/h = 187 FROM QUASI-IMPULSIVE (HE Sphere) LOADS

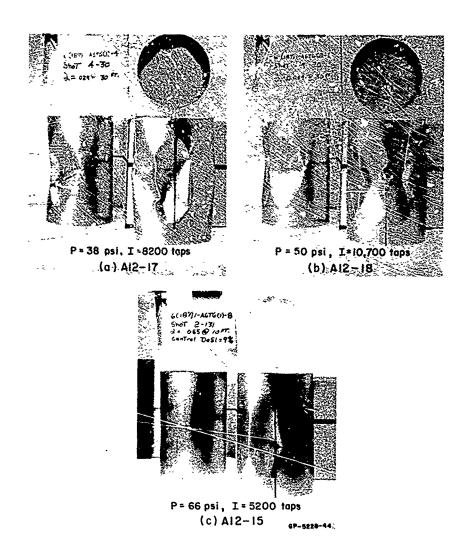
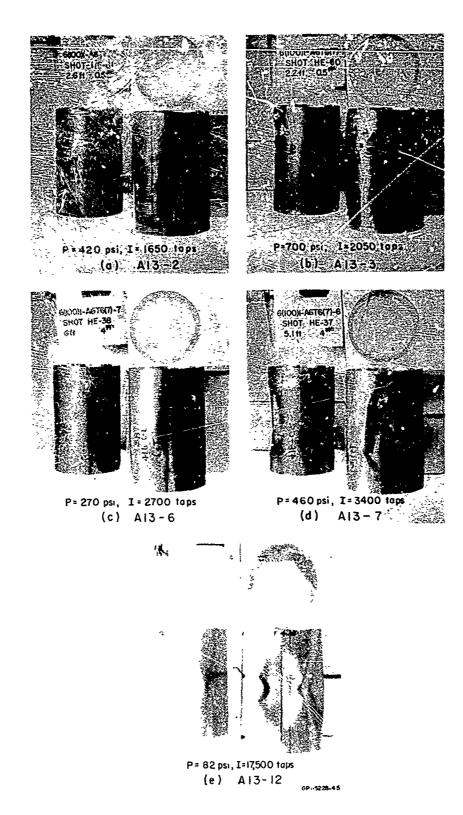


FIG. 5.5 BUCKLING OF SHELLS WITH $\alpha/h = 187$ FROM QUASI-STATIC (Shock Tube) LOADS

5-percent, and 10-percent deformation are plotted, in order to reduce the clutter. In all the shock tube experiments there was either no damage or buckling with deformations of about 30 percent, so only the highest unbuckled and lowest buckled points are given.



BANGARAMATARES ESTABARA LIGAR CAREACTER ANTA

The second secon

£ .

FIG. 5.6 BUCKLING OF SHELLS WITH $\alpha/\hbar=100$ FROM QUASI-IMPULSIVE (a-d), AND QUASI-STATIC (e) LOADS

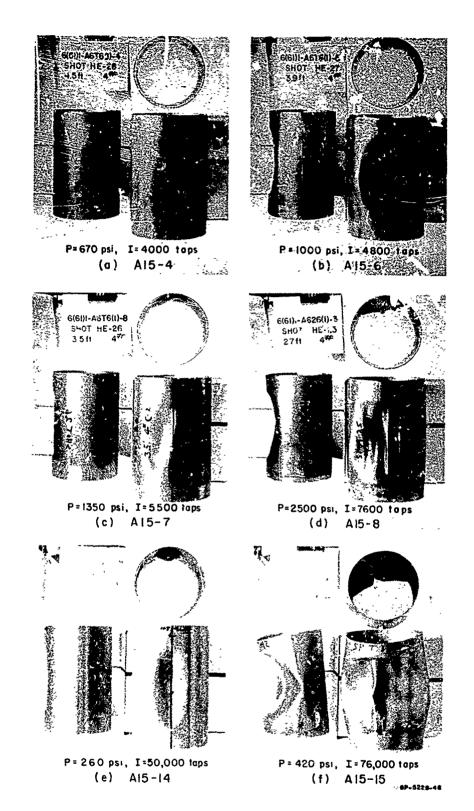


FIG. 5.7 BUCKLING OF SHELLS WITH $\alpha/h = 61$ FROM QUASI-IMPULSIVE $(\alpha-d)$, AND QUASI-STATIC (e,f) LOADS

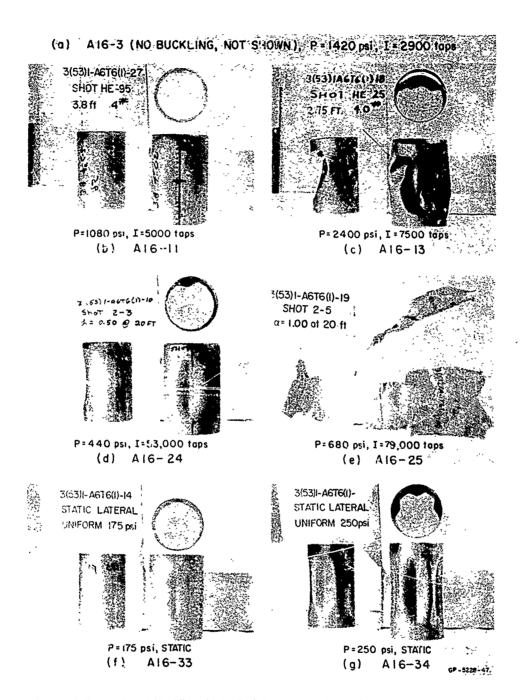


FIG. 5.8 INCREASING DAMAGE TO SHELLS WITH a/h = 53 FROM (a-c) QUASI-IMPULSIVE. (d,e) QUASI-STATIC, AND (f,g) STATIC LOADS [Note similarity of failure mode from quasi-static loads (in d) and static loads (in f,g)]

\$ OVER LINES ON THE

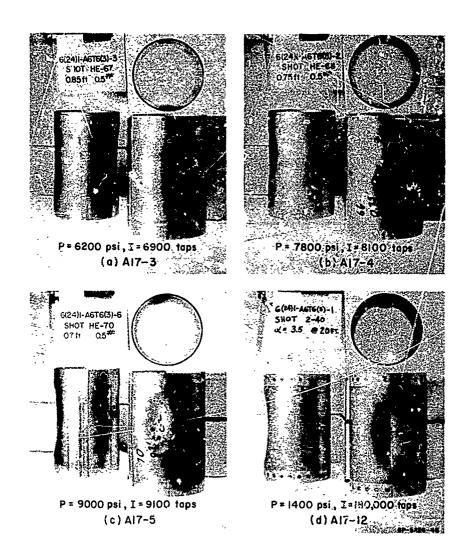


FIG. 5.9 BUCKLING OF SHELLS WITH α/h . 24 FROM QUASI-IMPULSIVE (a-c), AND QUASI-STATIC (d) LOADS

The curves labeled "10 percent buckling deformation" were drawn through the points in Fig. 5.12 which give 10-percent deformation from the HE charges, and between the no damage and buckled points from the shock tube data. Since no data were obtained for impulsive loads, * the curves were extended at higher pressures

^{*}This was beyond the scope of the present program.

(a) A18-22 (UNDAMAGED, NOT SHOWN) a= 3.00 AT 20 ft, P=1280 psi, I=162,000 taps

I

こうに、アントゥングンでは、「そうできる」のできるから、おからないないできるからなっている。「おからないないないないないないないないないないない。

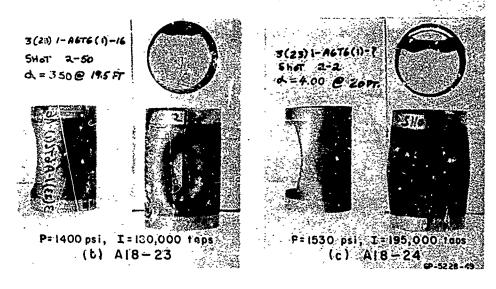


FIG. 5.10 INCREASING DAMAGE TO SHELLS WITH $\alpha/h=23$ FROM INCREASING QUASI-STATIC LOADS

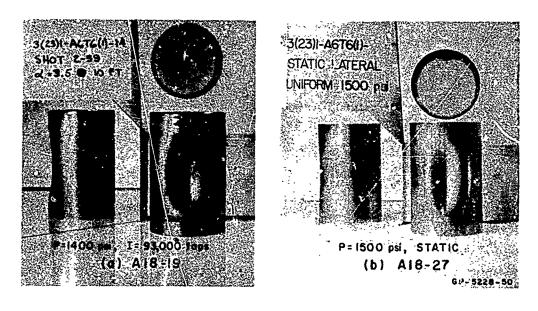


FIG. 5.11 COMPARISON OF BUCKLING MODES OF SHELLS WITH $\alpha/h=23$ UNDER QUASI-STATIC (a), AND STATIC (b) LOADS

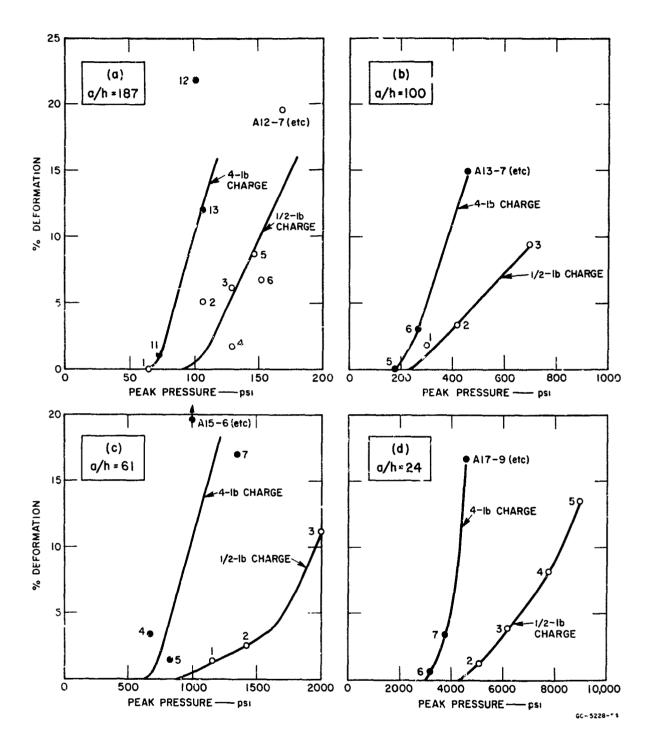


FIG. 5.12 SHELL DEFORMATION VERSUS PEAK PRESSURE FROM SPHERICAL CHARGES

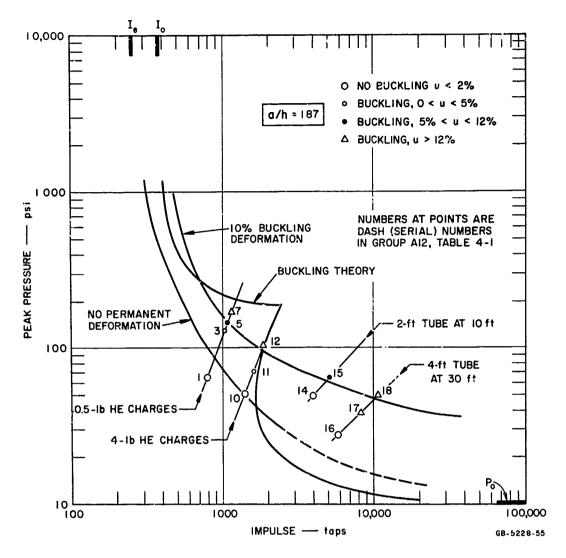


FIG. 5.13 EXPERIMENTAL AND THEORETICAL PRESSURE-IMPULSE CURVES FOR BUCKLING 6(187)1-A6T6 SHELLS (group A12)

toward the impulse threshold for buckling as given by Eq. (5.3). Experimental verification of the theory in this impulse range is given in [20]. The curves labeled "n permanent deformation" were obtained in a similar manner and at very high pressures are drawn asymptotic to the ideal impulse that just brings the shell material to the yield strain (assuming a uniform pressure all around which, from [24], is a good

^{*}The yield strain for 6061-T6 aluminum is 0.004.

approximation). This impulse is given by

$$I_e = \rho ch \epsilon_y$$
 (5.5)

where ε_y is yield strain.

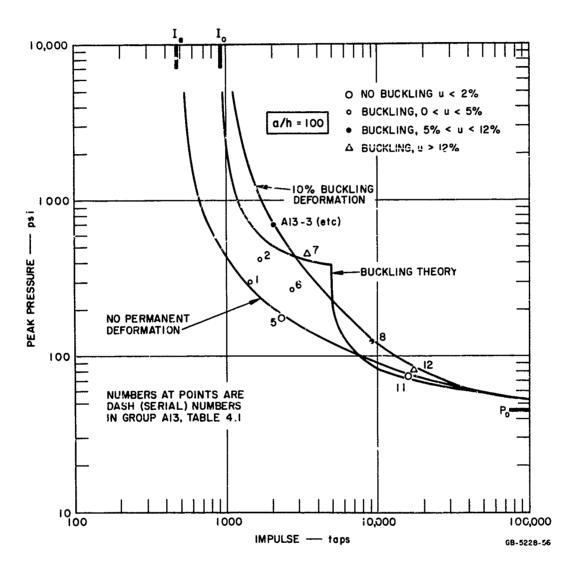


FIG. 5.14 EXPERIMENTAL AND THEORETICAL PRESSURE-!MPULSE CURVES FOR BUCKLING 6(100)1-A6T6 SHELLS (group A13)

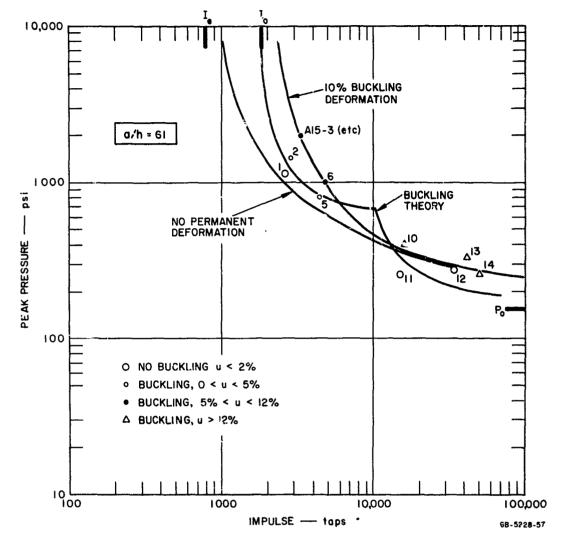


FIG. 5.15 EXPERIMENTAL AND THEORETICAL PRESSURE IMPULSE CURVES FOR BUCKLING 6(61)1-A6T6 SHELLS (group A15)

For the thicker shells, the no-damage and 10-percent deformation curves tend to separate toward impulse loads and come very close together for quasi-static loads. The behavior at long loads is in agreement with the observation in static buckling that the shell suddenly collapses at a well-defined pressure. The separation between the no-damage and 10-percent deformation curves for impulsive loads is a consequence of the shells being relatively thick, the separation becoming wider as a/h decreases. This may be seen by forming the

Open Service Annual Control of the C

ratio of the impulse for buckling to the impulse given by Eq. (5.5) to give purely elastic response. For shells with a/h \approx 1/ ϵ_y , we use the buckling impulse given by Eq. (5.3) and the ratio becomes

$$\frac{I_o}{I_e} = 1.3 \left(\frac{1}{\epsilon_y} \frac{h}{a}\right)^{1/2}, \qquad \frac{a}{h} \approx \frac{1}{\epsilon_y} \qquad (5.6)$$

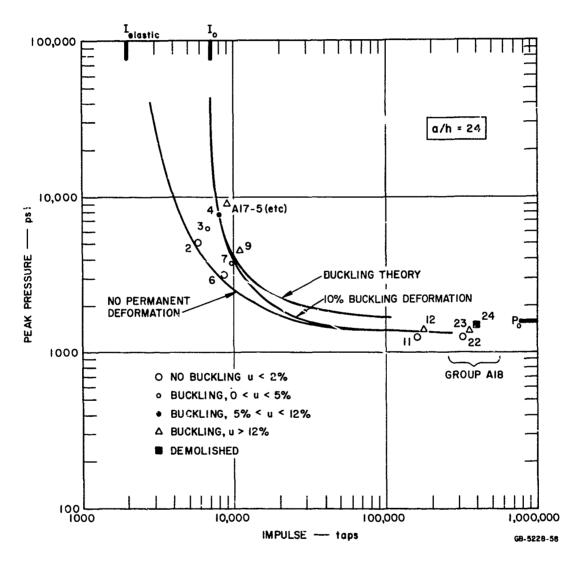


FIG. 5.16 EXPERIMENTAL AND THEORETICAL PRESSURE-IMPULSE CURVES FOR BUCKLING 6(24)1-A6T6 SHELLS (group A17)

For very thin shells, the buckling impulse from Eq. (5.2) is used, giving

できる。 からなる では からないない いっぱん かっか いもいかい

$$\frac{I_o}{I_e} = \frac{2}{\varepsilon_y} \frac{h}{a}$$
, $\frac{a}{h} > \frac{2}{\varepsilon_y}$ (5.7)

The two expressions do not give the same ratio at $a/h = 2/\varepsilon_y$ because the approximations made in deriving Eq. (5.6) become more serious near $a/h = 1/\varepsilon_y$. Nevertheless, at $a/h = 2/\varepsilon_y$ the expressions differ by only 10 percent so that for practical purposes either formula shows that the buckling threshold and elastic limit in uniform radial vibrations essentially coincide (i.e., $I_0 = I_e$) at

$$a/h = 2/\epsilon_{y} \tag{5.8}$$

For thicker shells, the shell yields in membrane motion before it buckles. Thinner shells buckle before the elastic limit is reached. This crossing of I_e from the left to the right of I_o in the pressure-impulse plane suggests that for very thin shells the no damage and buckling curves will come close together at both the impulsive and static asymptotes and differ most widely for quasi-impulsive loads. A hint of this type of behavior is seen in Fig. 5.13 for a/h = 187.

Deformation much in excess of 10 percent occurs for loads only slightly above those that produce 10-percent deformation. This is shown in Figs. 5.8 and 5.10. Figure 5.8(a-c) gives a sequence of three shells subjected to quasi-impulsive loads of increasing magnitude. The shells are from group A16, 3 inches in diameter, with a/h = 53. At P = 1420 psi and I = 2900 taps, no buckling occurs (photo not shown). At P = 1080 psi and I = 5000 taps, the deformation was 12 percent and at P = 2400 psi and I = 7500 taps the shell was severely buckled and sheared off at one end. Thus, in doubling pressure and impulse the response goes from no significant damage to severe buckling and shearing. Figure 5.8(d,e) shows two similar shells subjected to quasi-static loads of increasing magnitude. At 380 psi and 44,000 taps the shell was undamaged (photo not shown), at 440 psi

and 53,000 taps the shell was buckled to 29 percent, and at 680 psi and 79,000 taps the shell was sheared off both ends and blown into the sky. These impulses are so large that only pressure is significant (see Fig. 5.15). Thus, an increase in load by a factor of 680/380 = 1.8 changes the response from no damage to complete destruction.

Progressive damage of shells with a/h = 23 is shown in Fig. 5.10 (a, b, c) for quasi-static loads. At pressures ranging from 1280 psi to 1400 psi to 1530 psi the response ranged from no damage to severe buckling to shearing at both ends. Thus for these shells the load ratio from no damage to destruction is only 1.2.

To compare theory with experiment in Figs. 5.13 through 5.16, the theoretical buckling curves from Fig. 5.3 have been drawn. In general, the agreement between the theoretical curves and the 10-percent buckling deformation curves is remarkably good. For all but a/h = 24, the experimental curves lie upward and to the right of the theoretical curves, away from the regions of the theoretical cusp. Tone would expect the load that produces 10-percent buckling to exceed the theory because the theory is concerned with a buckling threshold. However, the theoretical buckling loads are somewhat larger than the observed thresholds in the HE sphere experiments. In any case, the theory predicts buckling loads to closer than 50 percent over the entire range of pressure and impulse. A larger difference appears in the elastic branch for the thin shell (a/h = 187, Fig. 513) but this is most likely due to the method of deciding whether buckling has occurred. Thin shells must have very large buckling deformations before easily observed permanent deformation occur. It is very likely that large elastic buckling deformations occurred for pulses below the

As mentioned, the theory is known to be invalid in this region.

However, in Chapter 8 curves calculated in this cusp region using the "strain-reversal" model do not differ appreciably from the curves shown from the simpler models.

curve labeled "no permanent deformation," but the shell returned to its original shape and the response was tabulated as "no buckling." This type of elastic buckling was actually observed with a high-speed camera; it is described in Chapter 9. For thicker shells, the threshold of buckling is followed very closely by easily observed plastic deformations, which is the only observed quantity here.

5.2.2 Modes of Deformation

電影工程 できたとうこと

The modes of buckling for quasi-static loads agree very well with the theory and with modes from static experiments. Two examples showing that there is no difference between the quasi-static and static modes of buckling are shown in Figs. 5.8 and 5.11. Figure 5.8(d) shows an a/h = 53 shell buckled from a shock tube blast load. The mode of buckling is identical to that shown in Fig. 5.8(f), which is a similar shell buckled with a static lateral pressure uniform all around the circumference. Figure 5.8(g) presents another static experiment showing more fully developed buckling. Figure 5.11 gives a similar comparison for a/h = 23.

In order to produce the very high order wave numbers associated with the tangent-modulus theory, the pressure must be large compared to the pressure required to yield the shell. An example of such buckling is shown in Fig. 5.17 for a 6-inch-diameter aluminum shell with a/h = 120. This shell was subjected to an impulsive load with a peak pressure of about 2000 psi by a uniform 1.5-inch layer of oxyacetylene gas over a 0.5-inch layer of flexible foam neoprene. The number of waves around the circumference is n = 45, which is the order of magnitude predicted by the tangent-modulus theory.

For quasi-impulsive loads, Figs. 5.4 through 5.11 show clearly that the mode number of buckling increases with pressure as predicted by the theory. For a quantitative comparison, shells buckled from the quasi-impulsive loads provided by spherical HE charges were carefully measured with a device which continuously records radial

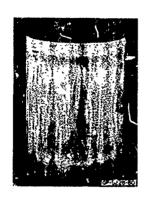


FIG. 5.17 BUCKLÉ PATTERN IN 6(120)1-A6T6 SHELL BUCKLED FROM AN IMPULSIVE LOAD

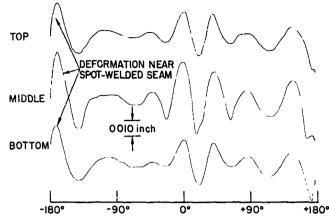
deflection as a function of angle. Plots of $w(\theta)$ for shells of a/h = 187. 100, and 61 are shown in Fig. 5.18. In each case, a distinct regular pattern of buckling appears on the loaded side of the shell. Taking the wavelength between crests of the three waves near $\theta = 0^{\circ}$ for the shell with a/h = 187 gives a wave number of n = 13 (i.e., 13 waves around the circumference). Similarly, for a/h = 100 we obtain n = 7 and for a/h = 61 we obtain n = 5. Comparing these to the theoretical curves in Fig. 5.3 we see that these are the wave numbers associated with the

upper pressure limit of the elastic buckling branch. From Table 4.1 and Figs. 5.13, 5.14, and 5.15, the loads in these experiments are all near or slightly to the left of the cusp region of the theory. Thus it appears that in this region elastic behavior dominates the precipitation of buckling, but plastic hinge formation, not easily amenable to analysis, shifts the experimetal buckling threshold to the left, giving a smooth transition to the plastic theory branch.

5.3 Effects of Parameter Changes on Blast Buckling

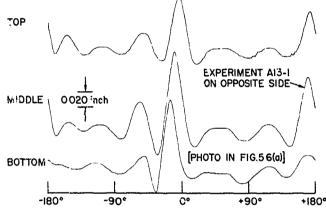
5.3.1 Length-to-Diameter Ratio

in experiment groups A211 through A223, 3-inch-diameter shells with a/h = 53 and a/h = 23 and various length-to-diameter ratios were subjected to quasi-static loads in the 2-foot shock tube at 20 feet. Figure 5.19 shows the buckled shells from these experiments. In all cases the mode of buckling is a single inward lobe at shot zero at a wavelength corresponding to that observed in static buckling. The strange shape of the shell in Fig. 5.19(a) was caused by the shell wrapping around the 1.5-inch-diameter central rod in the test fixture.

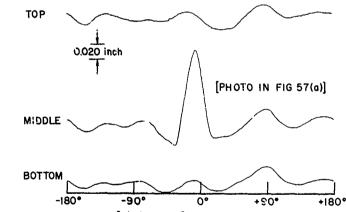


PRINCE OF THE PROPERTY OF THE

(a) EXPERIMENT AI2-II [6(187)I-A6T6], P=72 psi. I=1620 taps (9.3 ft FROM 4-Ib HE)



(b) EXPERIMENT Al3-2 [6(100)1-A6Te], P=420 psi, I=1650 taps (2.6 FROM 1/2-1b HE)



(c) EXPERIMENT AI5-4 [6(61)1-A6T6], P = 670 psi, I = 4000 taps (4.5 ft FROM 4-1b HE)

FIG. 5.18 MEASURED BUCKLING PATTERNS FROM QUASI-IMPULSIVE LOADS IN SHELLS WITH VARIOUS a/h

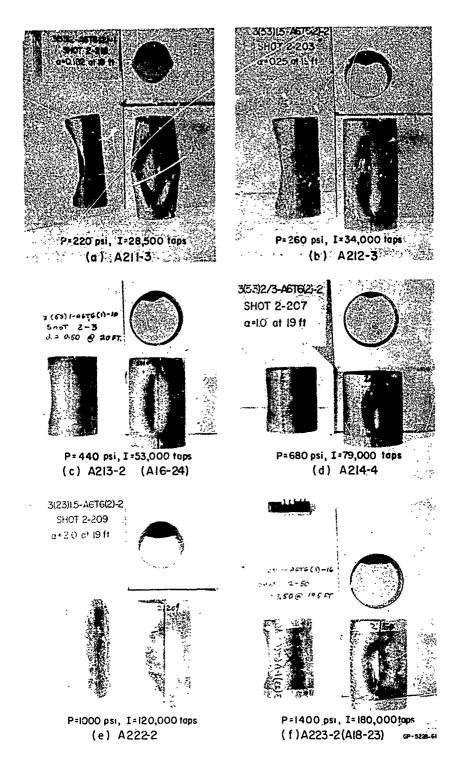


FIG. 5.19 SHELLS OF VARIOUS LENGTH-TO-DIAMETER RATIOS BUCKLED FROM QUASI-STATIC BLAST LOADS

Table 5.1 gives the observed blast pressures, taken from Table 4.1, for buckling and no buckling of each 'ype of shell.

Table 5.1

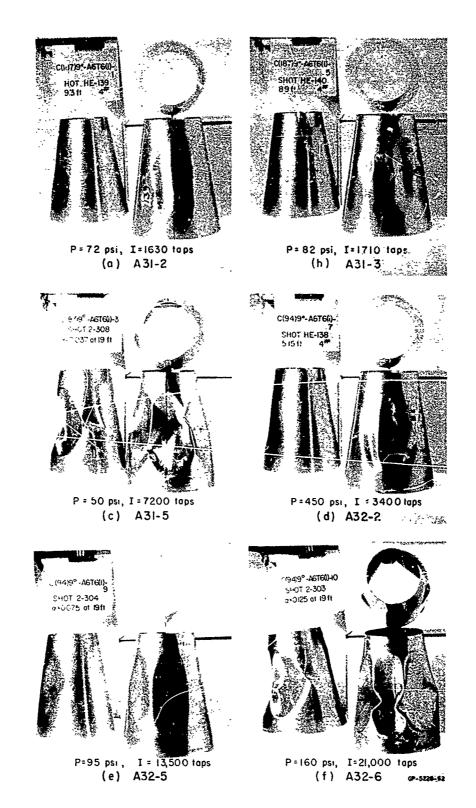
EFFECT OF LENGTH-TO-DIAMETER RATIO ON BUCKLING PRESSURES

	a/h = 53				a/h = 23				
	Pressure (psi)				Pressure (psi)				
L/D	P, Shock Tube		P _o	Pave/Po	P, Shock Tube		Po	Pave/Po	
	Unbuckled	Buckled	Calculated		Unbuckled	Buckled	Calculated		
2,0	180	220	113	1,77	680	730	900	0.78	
1.5	240	260	150	1.67	840	1000	1200	0.77	
1.0	350	440	226	1,75	1310	1400	1800	0.75	
0.67	560	680	340	1.87				*	

Also listed are the calculated static buckling pressures \mathbb{F}_0 from Eq. (5.1) and the ratios of the observed blast buckling pressures to the calculated P_0 (using the average between the buckled and unbuckled pressures). For a/h = 53 these ratios range from 1.67 to 1.87, which can be considered a constant ratio within the accuracy to which the threshold can be estimated. Similarly, for a/h = 23 th. ratios range from 0.75 to 0.78, which can also be considered constant. These observations demonstrate that the linear variation of peak pressure with length-to-diameter ratio, predicted by the blast buckling theory [Eq. (5.1)] is correct. The ratio is greater than unity for a/h = 53 because for these relatively thin shells the duration of the pulse is not sufficiently long to appear as a static load. The ratio is less than unity for a/h = 23, probably because some yielding takes place. The important observation here is that the observed failure pressures are proportional to shell length.

5.3.2 Comparison of Cones to Cylinders

Figures 5.20 and 5.21 show truncated cones with a 9° half-angle, buckled from blast loads. The shells are groups A31



The state of the s

FIG. 5.20 BUCKLING OF CONES WITH $\alpha/h=187$ AND 94 FROM QUASI-IMPULSIVE (a,b,d), AND QUASI-STATIC (c,e,f) LOADS

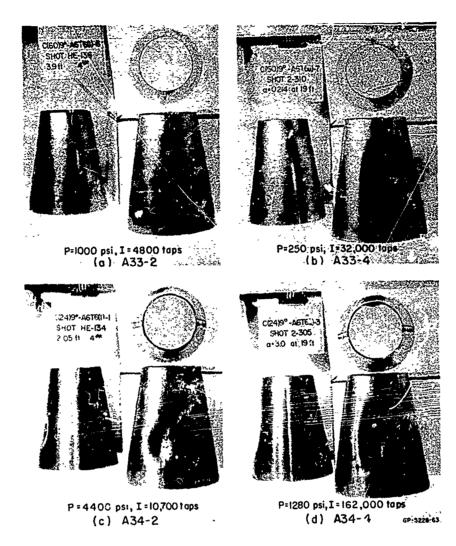


FIG. 5.21 BUCKLING OF CONES WITH a/h=60 AND 24 FROM QUASI-. IMPULSIVE (a,c), AND QUASI-STATIC (b,d) LOADS

to A34 in Table 4.1; each shell has a mean diameter of 6 inches and an unsupported length of 6 inches. The modes of buckling are essentially the same as those observed in corresponding cylinders in Figs. 5.4 through 5.9. A comparison of the buckling loads for the cones and cylinders is given in Table 5.2, using values from Table 4.1. In all cases the cone and cylinder buckling loads are essentially the same and it is concluded that, for this small cone angle, cylinders and cones behave identically under blast loads.

THE STREET STREET

Table 5.2

COMPARISON OF BUCKLING PRESSURES AND IMPULSES
FOR CYLINDERS AND CONES

	6" D	iameter C	Cylinder	6'' Diameter Cone			
a/h	4# HE		Tube at 20 Ft.	4# HE		Tube at 20 Ft.	
	P (psi)	I (taps)	P (psi)	P (psi)	I (taps)	P (psi)	
187	90	1,700	34	82	1, 650	35	
100 *	460	3,200	79	450	3,200	87	
61	920	4,600	290	1080	5,000	235	
24	4000	10,000	1330	4000	10,000	1140	

^{*}a/h = 94 for cones.

5.3.3 Blast Buckling of Shells of Various Materials

In addition to the 6061-T6 aluminum shells discussed above, tests were run on shells made from 2024-T8 aluminum and from AZ31B magnesium. The most apparent difference in response of these materials is that both the 2024-T8 aluminum and the AZ31B magnesium shells tended to shear and tear more easily than the 6061-T6 aluminum; hence the spread is smaller between threshold loads and loads that demolish the shells. This is illustrated in Fig. 5.22 for 2024-T8 aluminum shells with a/h = 23. In Fig. 5.22(a, b) (photos not shown) the shell was undamaged at a load of 3800 psi and 9700 taps, and was deformed 2.5 percent with no buckling at a load of 5700 psi and 12,800 taps. In Fig. 5.22(c) a load of 6700 psi and 14,500 taps sheared one end, and in Fig. 5.22(d) an increase in load to only 7500 psi and 16,000 taps completely tore up the loaded side of the shell. Thus an increase in pressure and impulse of only 30 percent over that which produced only threshold damage resulted in complete destruction.

- (a) A 414-1 (UNDAMAGED, NOT SHOWN) P=3800 psi, I=9700 taps
- (b) A414-2 (2.5% DEFORMATION, NOT SHOWN) P=5700psi, I=12.800 taps

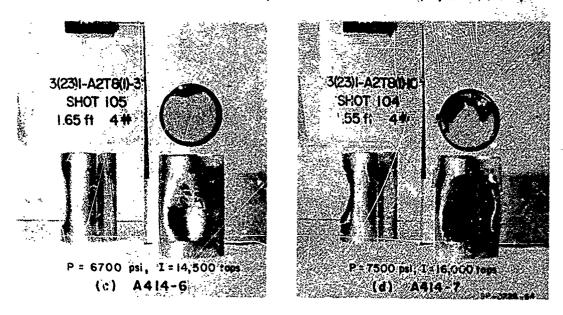
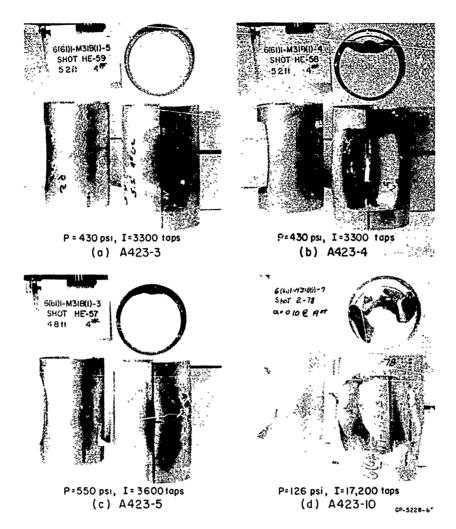


FIG. 5.22 SHEARING AND TEARING OF 2024-T8 SHELLS WITH $\alpha/h=24$ FROM INCREASING QUASI-IMPULSIVE LOADS

Similar behavior of AZ31B magnesium is shown in Fig. 5.23 for shells with a/h = 61. In Fig. 5.23(a), a pressure and impulse of 430 psi and 3300 taps produced 7-percent deformation with no buckling, while in Fig. 5.23(b) the same pressure and impulse applied to a similar shell sheared off both ends on the loaded side. However, in Fig. 5.23(c) the shell sustained a load of 550 psi and 3600 taps with a 20-percent deformation but did not shear. Magnesium showed a tendency to shear and tear at long loads also, as shown by Fig. 5.23(d). Here a pressure of 126 psi completely sheared and tore the loaded side, while at 95 psi a similar shell was undamaged.

A comparison of loads required to give 10-percent deformation in shells made of the three materials is given in Table 5.3 for a/h = 100, 61, and 24. The failure pressure and impulse combinations (from a 4-pound spherical charge) decrease in going from 2024-T8 to 6061-T6 to AZ31B, as one would expect, since both Young's



一般のできながらなっていない はんま しょうきゅうこう

THE PERSON NAMED IN COLUMN

(e) A 423-9 (UNDAMAGED, NOT SHOWN) P=95 psi, I=13,500 taps

FIG. 5.23 SHEARING AND TEARING OF AZ31B MAGNESIUM SHELLS WITH α/h = 61 FROM QUASI-IMPULSIVE (α -c), AND QUASI-STATIC (d) LOADS

modulus and yield stress decrease (see Table 5.4). For he long pulses (for example, from the 20-foot shock tube), he ever, the theory predicts that the buckling pressures should depend only on Young's modulus. To check this prediction, the static collapse pressures given by Eq. (5.1) are also tabulated, along with the ratio between the observed failure pressures and the limiting theoretical pressure. For the two aluminum alloys, this ratio is the same for the a/h = 61 and a/h = 24 shells (equal to about 1.9 and 0.8, respectively) but differs

Table 5.3

PRESSURES AND IMPULSES FOR 10-PERCENT DEFORMATION OF SHELLS OF VARIOUS MATERIALS (6-INCH DIAMETER)

Con	Test Configuration		HE	2-Foo, Tube at 20 Feet			
a/h	Material	P (psi)	I (taps)	P No Damage (psi)	P Buckled (psi)	Pott	Pave/Po
100	2024-T8 6061-T6 AZ31B	 460 165	3,200 2,200	95 75 28	126 82 50	45 45 27	2.40 1.75 1.45
61	2024 T8 6061-T6 AZ31B	2000 920 430	6, 500 4, 600 3, 400	300 275 95	300 300 126*	155 155 93	1.86 1.93 1.18
24	2024-T8 6061-T6 AZ31B	 4000 2300	 10,000 7,200	1280 1260 350	1360 1400 560 [†]	1600 1600 960	0.82 0.83 0.47

Shearing rather than buckling.

Control Court Colors desirable Sections of relative to the Colors of the

from the a/h = 100 shells (2.40 for 2024-T8 compared to 1.75 for 6061-T6). This difference was surprising and at present is unexplained. At a/h = 100 for AZ31B magnesium the ratio is 1.45; this is somewhat low, but is probably the result of not determining the experimental buckling pressure to great accuracy (for this particular shell, from Table 5.3, the buckling pressure is known only to be between 28 and 50 psi). The ratios are also quite low for the magnesium shells of a/h = 61 and 24, but these low ratios are definitely attributable to the low magnesium strength. The a/h = 61 shell failed at 126 psi by shearing before its full resistance to buckling could develop (see Fig. 5.23d). The a/h = 24 shell yielded rather than buckling elastically because the elastic buckling stress exceeds the yield stress. This is confirmed in Table 4.1 which shows the gradual increase in deformation with pressure in experiments A425-8, 9, 10.

Yielding rather than buckling.

^{††}From Eq. (5.1)

Table 5.4

MATERIAL PROPERTIES

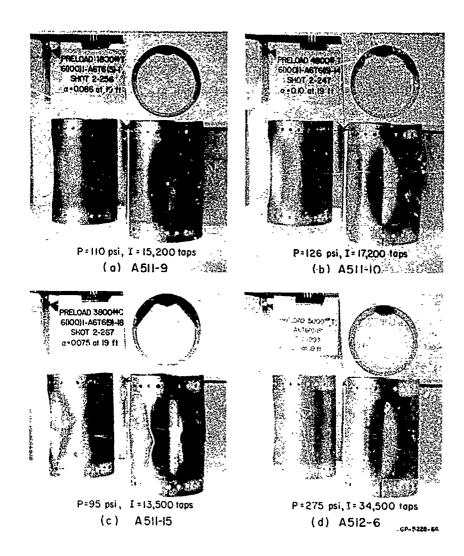
	Young's Modulus	Yield Stress		
Material	E (psi x 10 ⁶)	σy (psi x 10 ³)		
2024-T8	11.0	66		
6061-T6	10.0	42		
AZ31B	6.0	24		

These data tend to support the basic variations in buckling pressures and impulses with material constants as predicted by the theory, but definitely point out that failures by other mechanisms, such as end shearing, must also be examined when material strength is limited. The gradient of damage with applied load is steeper for less ductile materials, as one would expect.

5.3.4 Effects of Axial Preloads

To determine the increase or decrease (if any) in quasi-static biast buckling pressures when a shell is put under tensile or compressive axial preload, three series of experiments were performed in the 2-foot shock tube (shell groups A511, A512 and A521 in Table 4.1). The axial preloads were applied by a fixture described in Appendix B. The initial tension was transmitted to the shell by means of a row of screws through the holes seen in the buckled shells in Fig. 5.24, and was measured by strain gages mounted on an end yoke which was calibrated in a standard testing machine.

Tests were run on 6(100)1-A6T6 shells under both 5000 pounds initial tension and 3800 pounds initial compression, and on 6(61)1-A6T6 shells under 5000 pounds tension. The buckling



AND THE PERSON NAMED OF TH

FIG. 5.24 BUCKLING OF SHELLS WITH $\alpha/h=100$ AND 61 UNDER AXIAL PRELOADS AND SUBJECTED TO QUASI-STATIC LOADS

pressures are summarized in Table 5.5 along with pressures for shells with no preload. In the shells with a/h = 100 the estimated threshold buckling pressure increased from 78 psi with no preload to 102 psi under 5000 pounds tension. This increase is about twice that which would be predicted by a static buckling interaction curve.

Table 5.5

INFLUENCE OF AXIAL PRELOADS ON BUCKLING BLAST PRESSURES

a/h	100 61					
Preload (lbs)	No Damage	Buckled	Threshold*	No Damage	Buckled	Threshold*
0	75	80	78	275	330	300
5000T	95	110	102	225	275	260
3800C [†]	66	95	73			

^{*}Estimated (usually averaged) from no-damage and buckled pressures.

The measured static interaction curve, taken from [25], is shown in Fig. 5.25. To use this curve, we calculate the classical axial buckling stress from $\sigma_{c\ell} = 0.6$ Eh/a = 60,000 psi, and the static lateral buckling pressure from Eq. (5.1), which gives $P_o = 45$ psi. Also, the axial stress from 5000 pounds preload is $\sigma_{x} = 8900$ psi. Taking the interaction curve to be linear in the region near $\sigma_{x} = J$, as in Fig. 5.25, this preload should increase the buckling pressure by

$$\frac{\Delta P}{P_o} = \frac{\Delta \sigma_x}{\sigma_{c\ell}} = \frac{8900}{60,000} = 0.148$$
 (5.9)

Assuming this ratio would be the same under a blast load, the increment in blast pressure would be

$$\Delta P = 0.148P$$
 = (0.148)(78) = 11.6 psi

This is about half the pressure increment of 24 psi in Table 5.5.

Under 3800 pounds compression, Table 5.5 shows a decrease in buckling pressure from 78 psi to 73 psi, an increment of 5 psi. The increment from Eq. (5.9) using 3800 pounds compression is 8.8 psi. The agreement between experiment and theory in this example is better than the accuracy of the measured pressures.

T = tension; C = compression.

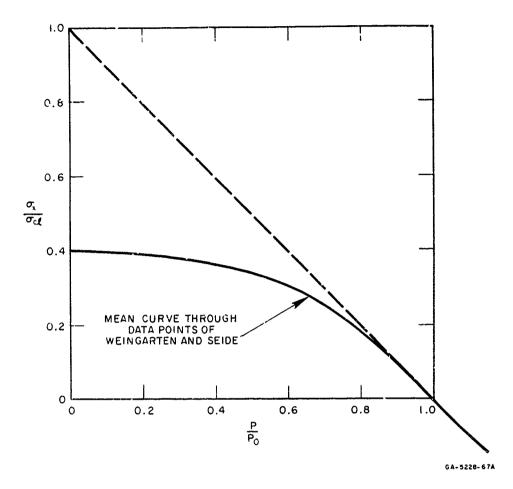


FIG. 5.25 STATIC BUCKLING INTERACTION CURVE FOR LATERAL PRESSURE AND AXIAL STRESS

The a/h = 61 shells in Table 5.5 show a 13-percent decrease in buckling pressures with 5000 pounds tension preload, which reflects only that the thresholds were not determined to this accuracy. Equation (5.9) would predict an increase in buckling pressure of 9 percent, too small to be observed without an exorbitant amount of testing.

Finally, a test was run on a 6(61)1-A6T6-M shell (as above, but with a Micarta cover) under 5500 pounds tensile preload, and it failed at the same load as a similar shell with no preload.

(These are experiments A521-1 and -2 in Table 4.1.)

In conclusion, it appears that moderately small axial pre-stresses (small compared to the classical static buckling stress) produce only small changes in the blast failure pressures. To the accuracy of the present tests, the percentage increase in pressure can be predicted by the static interaction curve.

6. RESPONSE OF SIMPLE COVERED SHELLS

This chapter gives the experimental results from tests on simple covered shells. The covered shells consist of metal subshells (6061-T6 aluminum, 2024-T8 aluminum, AZ31B magnesium) of various radius-to-thickness ratios, and cover shells with properties ranging from brittle (Plexiglas) to fibrous (grade 79 Micarta) to flexible (50 durometer neoprene rubber) and tape-wound cover shells of refrasil and carbon phenolic. A qualitative description of the modes of failure is presented first; next the pressure-impulse failure boundaries are given, and the strengths of shells of various materials are compared; finally, the results from the experiments on tape-wound shells are presented.

6.1 Failure Modes and Load-Damage Sensitivity

Failure modes do not vary significantly with subshell material or radius-to-thickness ratio; most of the examples of failure modes given here are for 6061-T6 aluminum subshells. The photographs in Figs. 6.1 through 6.14 illustrate typical damaged shells. The shells appear in the same sequence as in Table 4.1. This table should be consulted for further details and for similar experiments for which no photographs are given. The figures are intended to be self-explanatory; therefore only a few summarizing remarks are given here.

The first evidence of damage was permanent deformation of the metal subshell. As a rule, the permanent deformation was uniform along the length of the subshell under the peak load. Occasionally, however, a circumferential ridge bulge developed in the subshell near one end, as shown in Fig. 6.1 (for shells covered with Plexiglas and tape-wound carbon phenolic). The ridges tended to be more pronounced for the tape-wound covers because of localized failure between the tape layers. This is discussed in more detail in Section 6.4.

The second of th



(a) B211-7, PLEXIGLAS COVER P=680 psi, I=79,000 taps

開発が発出者で会会 年にはまめった。ラニュをよう

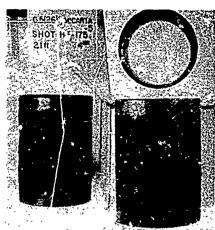
(b) B622-6, CARBON PHENOLIC COVER P=1530 psi, I=195,000 taps

FIG. 6.1 CIRCUMFERENTIAL RIDGE BULGES IN METAL SUBSHELLS FROM QUASI-STATIC (shock tube) LOADS

For the rubber-covered shells, the next failure mode was buckling (like that discussed in Chapter 5 for uncovered shells) as shown in Fig. 6.5.

For the Plexiglas - and Micarta-covered shells, the next failure mode was cracking or shattering of the covers. This is shown in Fig. 6.2 for Micarta shells with no subshell. Generally, the first cracks to appear in the Micarta shells were circumferential cracks near the end plugs (Fig. 6.2d.) At higher loads the cracks spread over the entire loaded area, as shown in Figs. 6.2(b) and 6.4(d). The shell in Fig. 6.2(f) was subjected to a static lateral pressure and the crack pattern appears to have followed a buckle lobe such as was observed in the metal shells shown in Chapter 5. Plexiglas tends to shatter more easily than Micarta (see Fig. 6.3b and c). For the quasi-static loads produced by the shock tubes, both the Micarta and Plexiglas shells completely disintegrate when the cracking spreads. Figures 6.3(f) and 6.8(d) show the remnants from two such experiments.

(a) BII-2 (UNDAMAGED, NOT SHOWN)
P=3000 psi, I = 9200 taps



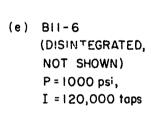
P=4200 pai, 1=10,400 tops (b) BII=3

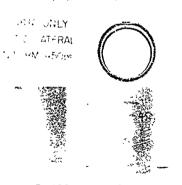
65(24)1-Munife-3 Short 2-89 d.+1.50@ 20 ft.

(c) BII-4 (UNDAMAGED, NOT SHOWN) P = 680 psi, I = 79,000 taps



P=840 psi, I=100,000 taps (d) BII-5





P=450 psi, STATIC .

(f) BI2-1 GP-1228-69

FIG. 6.2 CRACKING OF MICARTA SHELLS FROM (a, b) QUASI-IMPULSIVE LOADS, (c, d, e) QUASI-STATIC LOADS, AND (f) STATIC LINIFORM LATERAL PRESSURE

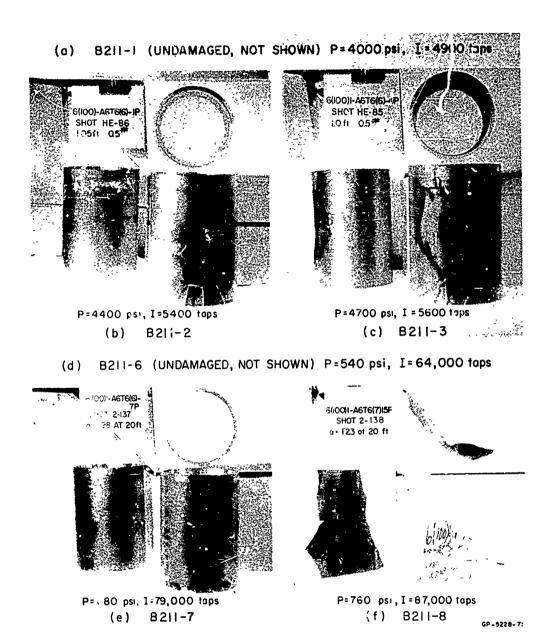
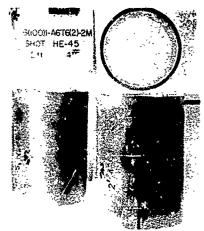


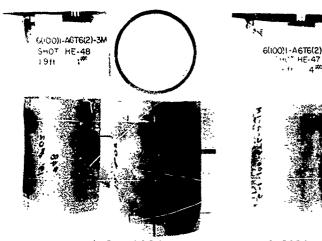
FIG. 6.3 SUDDEN PLEXIGLAS SHATTERING FROM QUASI-IMPULSIVE LOADS (in b, c compared to a) AND SUDDEN DISINTEGRATION FROM QUASI-STATIC LOADS (in f, compared to d, e) (subshell a/h = 100)

The state of the s

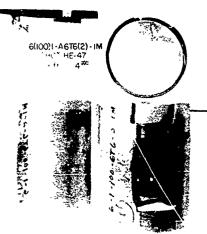
(a) B212-5 (UNDAMAGED, NOT SHOWN) P=3400 psi, I=9200 taps



P=4650 psi, I=11,000 taps (b) B212-6



P=5100 psi, I=11,900 taps (c) B212-7



P=5650 psi, I=12,800 tops (d) B212-9 GP-5228-7

FIG. 6.4 INCREASING DAMAGE TO MICARTA-COVERED SHELLS (subshell a/h = 100) FROM INCREASING QUASI-IMPULSIVE LOADS

(a) B213-4 (UNDAMAGED, NOT SHOWN) P=110 psi, I=23,000 taps

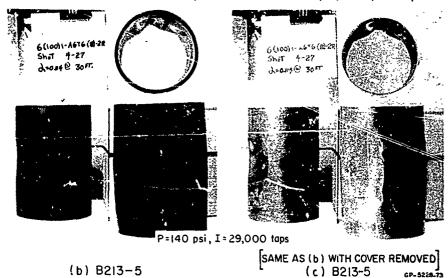
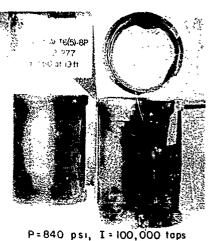


FIG. 6.5 TYPICAL BUCKLING OF A RUBBER-COVERED SHELL (subshell a/h = 100) FROM A QUASI-STATIC LOAD

(a) B221-8 (SUBSHELL 1.7%, NO PLEXIGLAS CRACKS, NOT SHOWN)
P=725 psi, I=84,000 taps



P=840 psi, I=100,000 tops (b) B221-9 GP-5228-74

FIG. 6.6 SUDDEN STRIPPING OFF OF PLEXIGLAS COVER (subshell $\alpha/h = 61$) FROM A SMALL INCREASE IN QUASI-STATIC LOAD

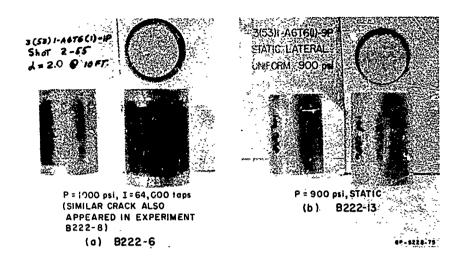


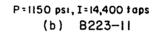
FIG. 6.7 SIMILARITY OF LONGITUDINAL PLEXIGLAS CRACKS FROM A QUASI-STATIC LOAD AND A STATIC UNIFORM LATERAL PRESSURE (subshell a/h = 53)

Short of disintegrating, under quasi-static loads a longitudinal crack extending the full length appears in the Plexiglas shells (Fig. 6.7a). This damage is probably associated with subshell buckling, as can be seen by comparing Fig. 6.7(a) with Fig. 6.7(b), which shows a longitudinal crack and subshell buckling in a statically tested shell. In the shock tube tests, the longitudinal crack usually extended from several cracks at each end, giving the "hourglass" pattern evident in Fig. 6.7(a). Similar examples for subshells with a/h = 23 are shown in Fig. 6.10(c, d).

For Plexiglas-covered shells subjected to either long or short loads, the transition from small permanent subshell deformation to complete shattering was very abrupt. This is demonstrated in Fig. 6.3(a,b) for quasi-impulsive loads and in Fig. 6.3(e,f) for quasi-static loads on 5(100)1-A6T6-P shells, which show that increases of a few percent in load above the threshold resulted in shattering (quasi-impulsive loads) or disintegration (quasi-static loads). Figure 6.6 shows the same effect for quasi-static loads applied to 6(61)1-A6T6-P shells. Other examples are listed in Table 4.1.

6(6))-ASTUB-7R SNOT 2-42 A= 2.50@ 20 %

(a) B223-10 (SUBSHELL 2.1%, NO MICARTA DAMAGE, NOT SHOWN) P=1000 psi, I=120,000 taps



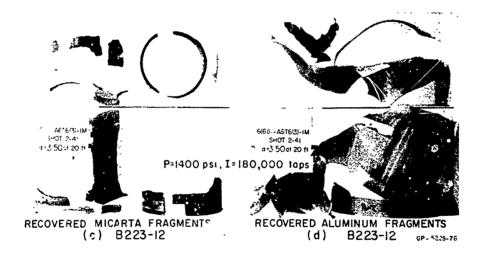


FIG. 6.8 DISINTEGRATION OF A MICARTA-COVERED SHELL (subshell $a/h=\mathfrak{d}1$) FROM A QUASI-STATIC LOAD (in c, d) ONLY 20 PERCENT GREATER THAN A THRESHOLD CRACKING LOAD (in b)

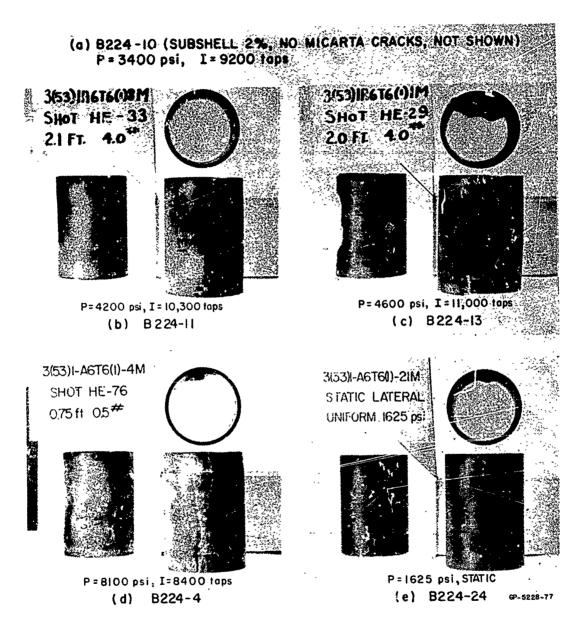


FIG. 6.9 INCREASING DAMAGE TO MICARTA-COVERED SHELLS (subshell a/h = 53) FROM INCREASING QUASI-IMPULSIVE LOADS (a, b, c) AND BUCKLING AND CRACKING FROM UNIFORM STATIC LATERAL PRESSURE (e)

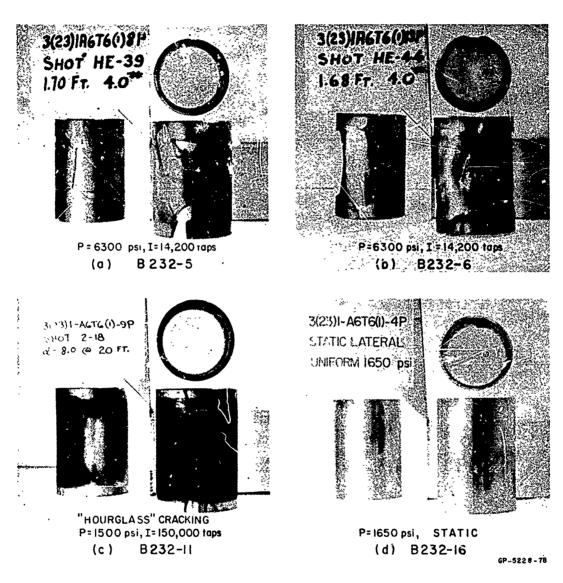


FIG. 6.10 PLEXIGLAS SHATTERING FROM QUASI-IMPULSIVE LOADS AND COMPARISON OF LONGITUDINAL CRACKS FROM QUASI-STATIC AND STATIC LOADS (heavy subshell a/h = 23)

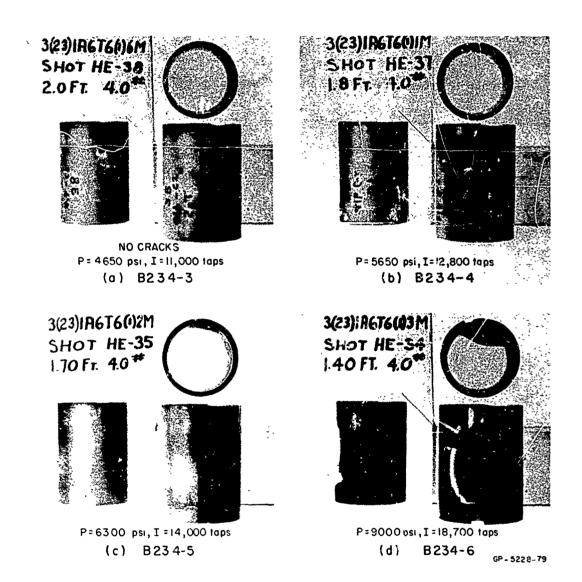
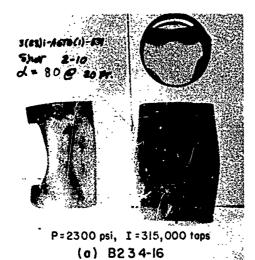


FIG. 6.11 INCREASING DAMAGE TO MICARTA-COVERED SHELLS FROM INCREASING QUASI-IMPULSIVE LOADS (heavy subshell a/h = 23)



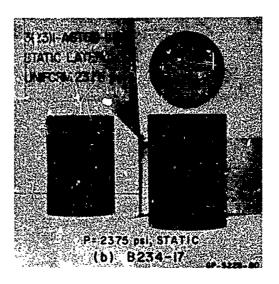


FIG. 6.12 HEAV! DAMAGE TO MICARTA-COVERED SHELL (subshell a/h = 23)
FROM A QUASI-STATIC LOAD (in a) AND CRACKING AND BUCKLING
FROM A UNIFORM STATIC LATERAL PRESSURE (in b)

For Micarta-covered shells under quasi-static loads the transition from small deformations to disintegration was just as abrupt as for the Plexiglas shells. This is illustrated in Fig. 6.8 for 6(61)1-A6T6-M shells. Here a pressure of 1000 psi produced 2-percent subshell deformation but no cracking; at 1150 psi circumferential cracks appeared, and at 1400 psi the shell was completely destroyed. Thus, the transition from hairline cracks to complete destruction occurs over a pressure increment smaller than the 10- to 20-percent increment between experiments. Similar behavior was observed with 3(23)-A6T6-M shells (see Fig. 6. 12 and experiments B234-13 to 16, Table 4. 1).

For Micarta-covered shells under quasi-impulsive loads the transition was not as abrupt but still occurred over a relatively small load increment. This is illustrated in Fig. 6.4 for 6(100)1-A6T6-M shells. A load of 3400 psi and 9200 taps produced no damage at all; a load of 4650 psi and 11,000 taps produced circumferential cracks; a load of 5100 psi and 11,900 taps produced both longitudinal and circumferential cracks; and finally, a load of 5650 psi and 12,800 taps fragmented the Micarta over the loaded area and sheared and tore the subshell. Thus an increase in pressure and impulse of about 50 percent

above the no-damage level resulted in complete destruction. Similar examples are shown in Fig. 6.9 for 3(53)1-A6T6-M shells and in Fig. 6.11 for 3(23)1-A6T6-M shells.

In all these examples, the subshell material was 6061-T6 aluminum. Similar behavior was observed with 2024-T8 aluminum and AZ31B magnesium. The only unique damage observed was caused by the tendency of magnesium to shear, resulting in the fracture pattern shown in Fig. 6.13 for 6(24)1-M31B-P and 6(24)1-M31B-M shells. With these shells, the individual Plexiglas and Micarta fragments sheared through the front face of the subshell like cookie cutters through dough.

- (a) B431-5 (NO CRACKS, NOT SHOWN) P=800 psi, I=93,000 taps
- (b) B431-6 (C- AND 1_-CRACKS, NOT SHOWN) P=925 psi, I=110,000 taps
- (d) B432-3 (C-CRACKS A: PLUGS, NOT SHOWN) P=1400 psi, I = 93,000 taps



B431-7

(c)

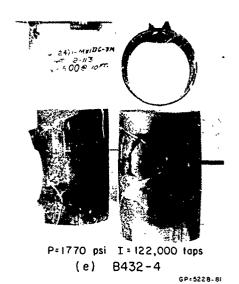


FIG. 6.13 MAGNESIUM (subshell $\alpha/h = 24$) SHEARING AND TEARING IN (c) PLEXIGLAS AND (e) MICARTA-COVERED SHELLS FROM QUASI-STATIC LOADS

Longer shells (L/D = 2) failed in much the same manner but buckling was more apparent. Micarta-covered shells 3(53)2-A6T6-M and 3(23)2-A6T6-M tested with quasi-static loads are shown in Fig. 6.14. The failure pressures are approximately half those of corresponding shells with L/D = 1 (see Figs. 6.8c and 6.12a).

(a) B51-1 (C-CRACK AT ONE END, NOT SHOWN) B52-2 (NO CRACKS, NOT (c) SHOWN) P=1000 psi, P = 680 psi, I = 79,000 taps I = 120,000 taps 3(23)2-A6T6(2)-3M SHOT 2-234 3(53)2-A6T6(2)-IM a=300 at 19 ft SHOT 2-230 a=125at 19 ft P = 760 psi, I = 88,000 taps P = 1280 psi, I = 162,000 taps (b) B.51-2 (d) B52-3 GP - 5 228 - 62

FIG. 6.14 CRACKING AND BUCKLING OF L/D=2 MICARTA-COVERED SHELLS FROM QUASI-STATIC LOADS, (subshell a/h=53 in a, b, and subshell a/h=23 in c, d)

6.2 Critical Pressure-Impulse Curves

The results of the tests illustrated in the preceding figures are conveniently summarized in the pressure-impulse plane, as were the simple metal shell data. Figures 6.15 through 6.17 give critical curves for 6061-T6 aluminum shells with Plexiglas and Micarta covers for subshell radius-to-thickness ratios of a/h = 100, 61, and 24. The data points shown are from Table 4.1 and include those for the experiments discussed above. The number attached to each point is the dash

number of the experiment in each shell group as listed in Table 4.1. An abbreviated version of the damage listed in Table 4.1 is repeated in the figures, giving the percent subshell deformation and a description of the cover damage. The narrow load increments between no damage and severe damage are now more apparent. In the cases for which only two experiments were performed on a given cross-curve, a wide spread in 'load level was chosen to insure that the no-damage and severe-damage levels would be bracketed.

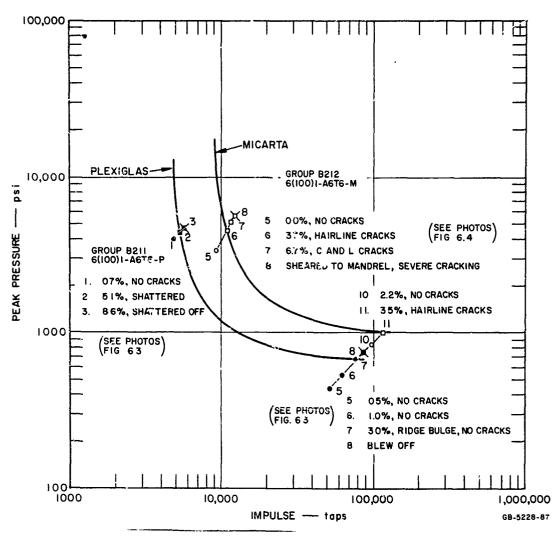


FIG. 6.15 CRITICAL PRESSURE-IMPULSE CUI VES FOR 6(100)1-A6T6 SHELLS WITH MICARTA AND PLEXIGLAS COVERS

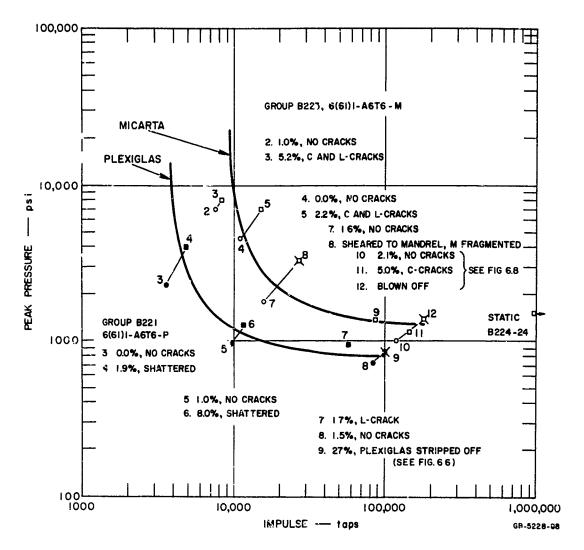


FIG. 6.16 CRITICAL PRESSURE-IMPULSE CURVES FOR 6(61)1-A6T6 SHELLS WITH MICARTA AND PLEXIGLAS COVERS

Within the experimental accuracy of ± 15 percent, the data are fix by nyperbolas of the form

$$(\frac{P}{P_0} - 1) (\frac{I}{I_0} - 1) = 1$$
 (6.1)

where P_o and I_o are quasi-static and impulsive asymptotes. This form was suggested by the theoretical results for buckling of thick-walled metal shells, discussed in Chapters 5 and 8, and by the

equivalent one-dimensional model discussed in Chapter 1. The data from the shock tube experiments fall well out along the quasi-static asymptotes, so that P_o is well established. Data from the spherical HE charges, however, are not at pressures sufficiently high to firmly establish the impulsive asymptotes. *

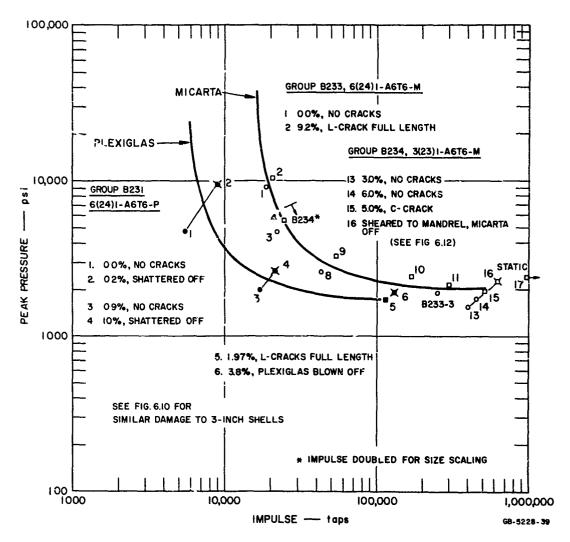


FIG. 6.17 CRITICAL PRESSURE-IMPULSE CURVES FOR 6(24)1-A6T6 SHELLS WITH MICARTA AND PLEXIGLAS COVERS

Experiments with impulsive loads of very short duration were beyond the scope of this program.

The reasonableness of the impulsive asymptotes indicated in Figs. 6. 15 through 6.17 can be tested by comparing them with the asymptotes for long shells with impulses applied uniformly around the circumference. The subshell is taken to be rigid-plastic and the cover to be elastic so that, to produce a maximum hoop strain ε , the impulse is given by

$$I_o^2 = (\rho_m h_m + \rho_c h_c) (2\sigma_y h_m \epsilon + h_c E_c \epsilon^2)$$
 (6.2)

where

 ρ_{m} , ρ_{c} = density of metal and cover materials

 h_{m} , h_{c} = wall thicknesses of metal and cover shells

 σ_{y} = yield stress of metal

E = Young's modulus of cover material*

Using (6.2), the impulse asymptotes shown for the Plexiglas covers gives a hoop strain of 1.5 percent, and the Micarta shells give 4 percent. Both are reasonable and one would expect the brittle Plexiglas to fail at a smaller strain.

Using the same model, a simple formula for P_0 can be obtained to serve as a basis of comparison for various shell designs. This is the pressure required to bring the shell to a specified strain in symmetric radial deformation, neglecting the ends, and is given by

$$P_{o} = \frac{1}{a} (\sigma_{v} h_{m} + h_{c} E_{c} \varepsilon)$$
 (6.3)

Here it is assumed that the critical strain is at least equal to the yield strain of the subshell. For a given allowable ε , arguments given in [26] show that this P_0 is an upper bound on the pressure required to cause failure. If failure occurs at pressures significantly below P_0 , internal stiffening to prevent buckling, or local increases in subshell

^{*}Stress-strain curves for Micarta and Plexiglas are given in Fig. 6.28.

thickness to prevent shearing at the supports, might improve the design. This is discussed further in Chapter 7.

H

Figures 6. 18 through 6. 20 give the critical curves from Figs. 6. 15 through 6. 17, with the clutter of data points removed and

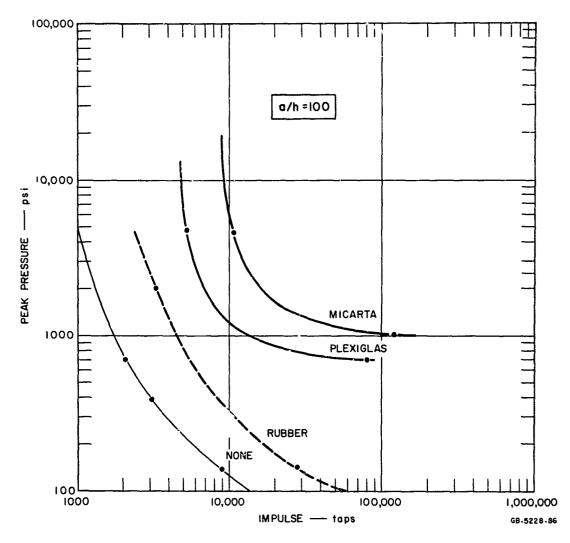


FIG. 6.18 CRITICAL PRESSURE-IMPULSE CURVES FOR 6(100)1-A6T6 SHELLS ALONE AND WITH MICARTA, PLEXIGLAS, AND RUBBER COVERS

the curves for rubber-covered shells and bare shells added. The curves show that the Micarta-covered shells are strongest, followed by Plexiglas (except for a/h = 24), then rubber, and finally by the bare shell.

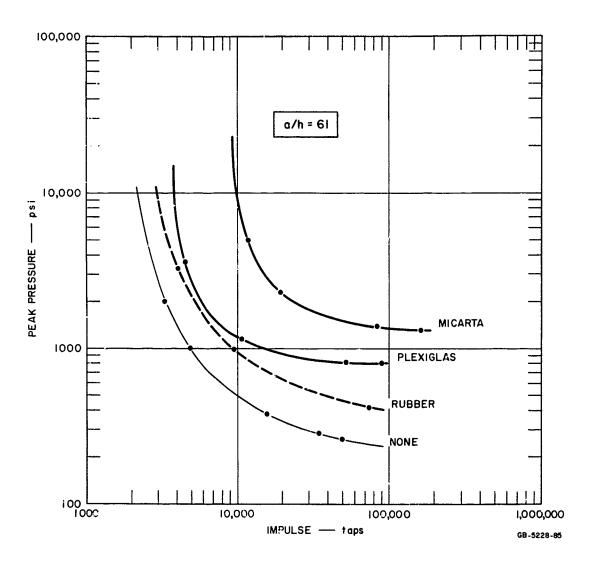


FIG. 6.19 CRITICAL PRESSURE-IMPULSE CURVES FOR 6(61)1-A6T6 SHELLS ALONE AND WITH MICARTA, PLEXIGLAS, AND RUBBER COVERS

The points on these curves do not represent actual data points, but merely indicate that a sequence of experiments were run on the corresponding blast techniques cross-curve as shown in rigs. 6.15 through 6.17.

For a/h = 24, the subshell is so thick that it can support the flexible rubber at large loads with only a few percent deformation; Plexiglas shatters at a lower impulse because of the small allowable strain. Quasi-static failure pressures for the Plexiglas - and Micarta-covered shells range from 700 psi for 6(100)1-A6T6-P to 2000 psi for 6(24)1-A6T6-M. The impulsive asymptotes range from 4000 taps to 16,000 taps for the same shells. Rubber-covered shells are relatively weak, of course, except for a/h = 24, where the subshell is thick enough to dominate the overall strength.

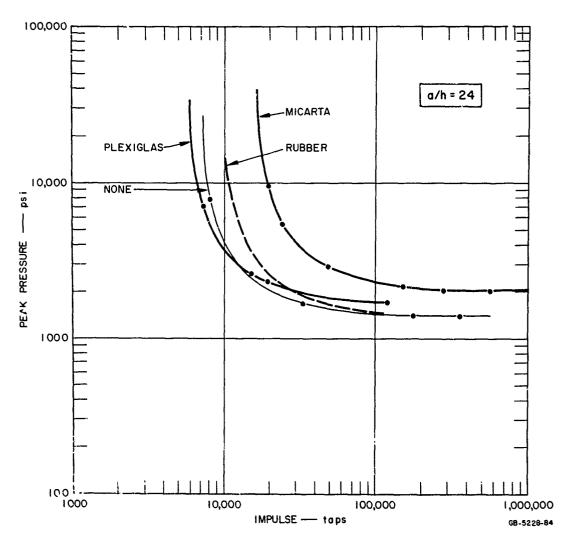


FIG. 6.20 CRITICAL PRESSURE-IMPULSE CURVES FOR 6(24)1-A6T6 SHELLS ALONE AND WITH MICARTA, PLEXIGLAS, AND RUBBER COVERS

In Fig. 6.21 curves are drawn for subshells of various a/h, all covered with Micarta with a/h = 12. A curve is also drawn for a Micarta shell with no subshell, which shows the Micarta shell is quite strong by itself. Thus, to give a significant percentage increase in strength the subshell must be quite thick. For example, a subshell with a/h = 61 gives only a 50-percent increase in strength over the unsupported Micarta shell.

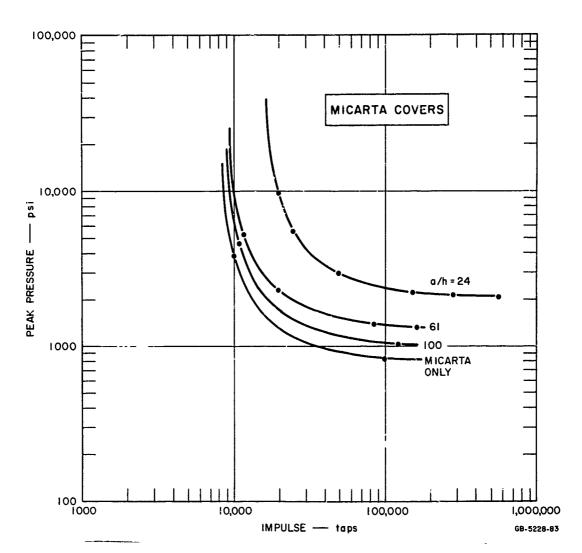


FIG. 6.21 CRITICAL PRESSURE-IMPULSE CURVES FOR MICARTA-COVERED SHELLS WITH 6061-T6 ALUMINUM SUBSHELLS OF VARIOUS THICKNESSES

6.3 Comparison of Critical Loads for Various Subshell Materials

Critical leads for covered shells with subshells of various materials were compared mainly for quasi-static loads produced in the 2-foot shock tube at 20 feet. The results are summarized in Table 6.1. Critical quasi-impulsive loads, for subshell metals other than 6061-T6, were compared using data obtained with 4-pound HE spheres. The results of both types of tests are given in groups B311 through B433 in Table 4.1.

Table 6.1

THRESHOLD AND CATASTROPHIC QUASI-STATIC PRESSURES
FOR COVERED SHELLS
(Most Experiments in 2-Foot Shock Tube at 26 Feet)

				Quasi-Static Pressure (psi)				
Subshell Material	a/h	Cover	Group No.	No Buckling or Cracking	Buckling or Cracking	Destroyed*		
2024-T8	24 24 24 24	Mirarta Plexiglas Rubber None	B333 B331 B335 A431	1950 1770 1400 1280	1950 2050 1360	2300 [†]		
	61 61 53 61	Micarta Plexiglas Rubber None	B322 B321 B323 A412	1000 840 350 300	1150 1000 420 330	 		
6061~T6	24 24 24 24	Micarta Plexiglas Rubber None	B233 B231 B235 A17	1770 1330 1280 1280	1950 1770 1400 1400	2300 1950 1530		
	61 61 61	Micarta Plexiglas Rubber None	B223 B221 B225 A15	1000 725 440 275	1150 680 330	1400 [†] 840 		
AZ31B	24 24 24 24	Micarta Plexiglas Rubber None	B432 B431 B433 A425	925 800 480 350	1150 925 470	1150 [†] 680		
	61 61 61 61	Micarta Plexiglas Rubber None	B422 B421 B423 A423	620 540 126 95	840 	1080 [†] 680 [†] 180 126		

^{*}In all cases, the Micarta or Plexiglas was removed by the blast. $\dagger_{\mathrm{Disintegrated}}$.

or and a second residence of the second

For each combination of subshell material, wall thickness, and cover material, Table 6.1 gives (1) the maximum pressure for which no buckling or no cover cracking was observed, (2) the pressure at which buckling or cracks appeared, and (3) for most shell combinations, the pressure which caused complete destruction. This table demonstrates that, over the entire range of the shells tested, the critical load curves for threshold buckling or cracking and for complete destruction differ by 10 to 20 percent, or less, since the load increment between tests was also 10 to 20 percent.

To permit the various shell materials to be compared more readily, Table 6.2 gives threshold pressures extracted from Table 6.1.

Table 6.2

COMPARISON OF THRESHOLD PRESSURES FOR VARIOUS SHELL MATERIAL AND WALL THICKNESS COMBINATIONS (psi)

Cover	Subshell a/h	Subshell Material					
Material		2024-T8	6061-T6	AZ31B	None		
Micarta	24 61 100	1950 1150 	1950 1150 1000	1150 840	840 840 840		
Plexiglas	24 61 100	2050 1000 	1770 780 700	925 600 			

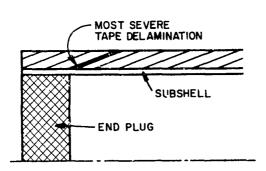
The increase in strength in going from 6061-T6 to 2024-T8 aluminum subshells is generally smaller than the pressure increments between tests. The AZ31B magnesium shells, however, are significantly weaker than aluminum shells of either type. The critical pressures of the AZ31B shells are about 50 percent of those for the 6061-T6 shells for a/h = 24, and are about 70 percent for a/h = 61. The magnesium shells also tend to shear more easily, as shown in Fig. 6.13.

6.4 Shells with Tape-Wound Covers

Data from all the experiments on shells with tape-wound covers of refrasil, carbon phenolic, and NOMEX are given in groups B611 through B622 in Table 4.1. Photographs of the damaged shells from these experiments are presented in Figs. 6.22 through 6.27 in the same order as in Table 4.1.

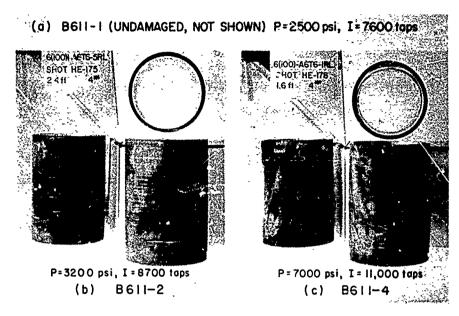
The dominant mode of failure for all these shells is delamination between the tapes. Because only a limited number of experiments was performed, it is difficult to estimate the amount of permanent subshell deformation that occurs before delaminations appear, but in experiments B612-4 and B621-4 approximately 0.5-percent deformation was observed with no delaminations. In the other experiments permanent deformation was always accompanied by delamination.

In quasi-impulsive experiments using 4-pound HE spheres, delaminations typically appeared over the entire load area. These are most easily seen in Figs. 6.22(b, c), 6.23(b), and 6.27(c). In the quasi-static experiments using the 2-foot shock tube at 20 feet, incipient delaminations invariably first appeared under the peak load near the end plugs because the rigid constraint produced high local stresses in the cover. Also, at higher loads, the most severe damage always occurred at the end of the shell favoring the direction of the tape laminations, as shown in the sketch. The tapes which terminate



near the inner side of the end plug tend to separate because of the highly localized bending and shear forces in this area. At the opposite end the tape orientation is such that the tapes that terminate near the inner side of the end plug are supported by the plug and damage is not nearly as severe. This occurred

in all the shells, as can be seen in Figs. 6.22(g), 6.23(f), 6.24, 6.25, 6.26(e), and 6.27(f). Because of this cover failure, large local deformations also appeared in the subshell at the same end. Figure 6.24(e)



- (d) B611-5 (UNDAMAGED, NOT SHOWN) P=680 psi, I=79,000 taps
- (e) B611-6 (LIGHT DELAMINATIONS, NOT SHOWN)
 P=1000 psi, I=120,000 taps
- (f) B611-7 (LIGHT DELAMINATIONS, NOT SHOWN)
 P=1150 psi, I=140,000 taps

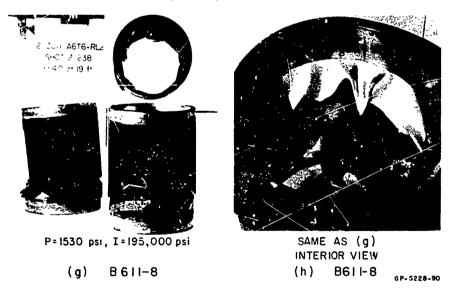
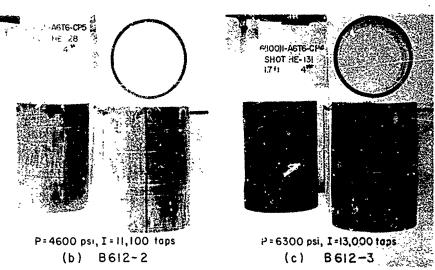


FIG. 6.22 DELAMINATION OF TAPE-WOUND REFRASIL SHELLS (subshell a/h = 100) FROM (a, b, c) QUASI-IMPULSIVE LOADS, AND (d-h) QUASI-STATIC LOADS

(1) B612-1 (ONE LIGHT DELAMINATION, NOT SHOWN) - 1



(d) B612-4 (UNDAMAGED, NOT SHOWN) P=840 psi, I=100,000 taps

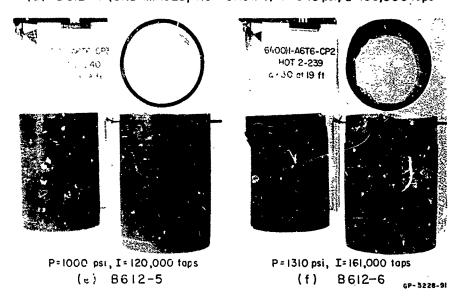


FIG. 6.23 DELAMINATION OF TAPE-WOUND CARBON PHENCLIC SHELLS (subshell $a/h \approx 100$) FROM (a, b. c) QUASI-IMPULSIVE LOADS, AND (d, e, f) QUASI-STATIC LOADS

shows a typical sharp circumferential ridge in the subshell, and Fig. 6.25(e) shows the local buckling which occurs due to high shear stresses (to carry the overall side load) on either side of the peak blast load.

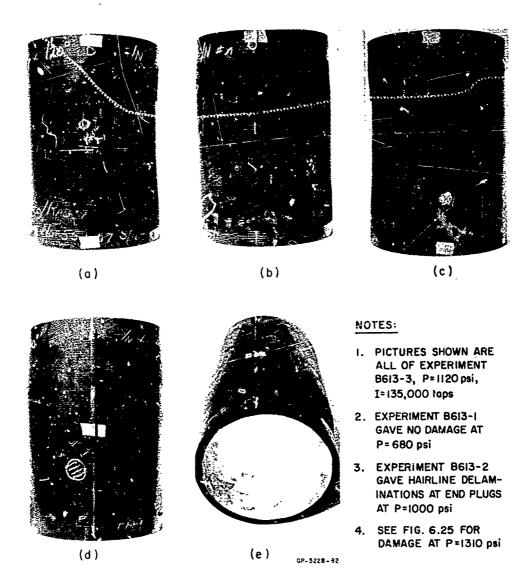


FIG. 6.24 MODERATELY SEVERE DAMAGE TO A TAPE-WOUND NOMEX SHELL (subshell $\alpha/h=100$) FROM A QUASI-STATIC LOAD

the section of the se

(Esc. Division of the control

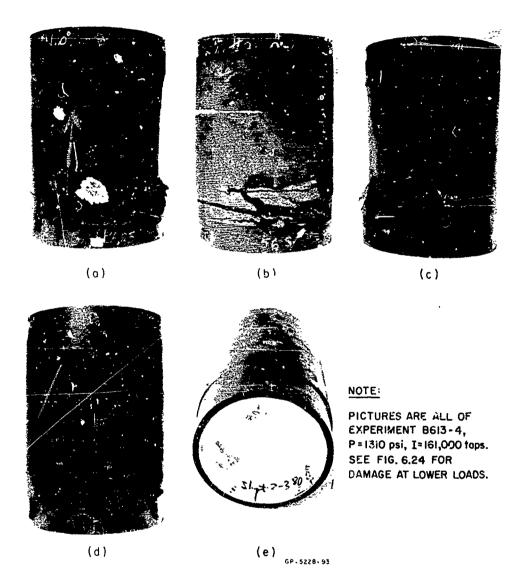
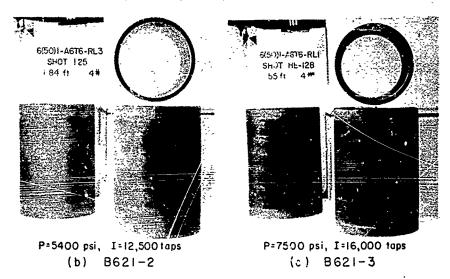


FIG. 6.25 SEVERE DAMAGE TO A TAPE-WOUND NOMEX SHELL (subshell $\alpha/h=100)$ FROM A QUASI-STATIC LCAD

(a) B621-1 (LIGHT DELAMINATIONS AT ENDS, NOT SHOWN) P=4600 psi, I=11,100 taps



(d) B621-4 (UNDAMAGED, NOT SHOWN) P=1310 psi, I=161,000 tops

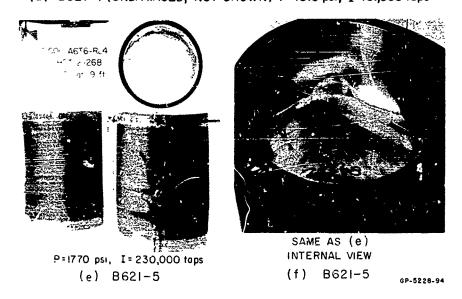


FIG. 6.26 DELAMINATION OF TAPE-WOUND REFRASIL SHELLS (subshell a/r=50) FROM (a,b,c) QUASI-IMPULSIVE LOADS, AND (d,e,f) QUASI-STATIC LOADS

P=5100 psi, I=12,000 taps
(b) 8622-2

(c) 8622-4

(d) 8622-1 (UNDAMAGED, NOT SHOWN) P=3800 psi, I=9800 taps

(e) 8500-A6T6-CPS

SHOT-HE-173

(a) 8500-A6T6-CPS

SHOT-HE-173

(b) 8622-2

(c) 8622-4

(d) B622-5 (LIGHT DELAMINATIONS, NOT SHOWN)
P=1150 psi, I=140,000 taps

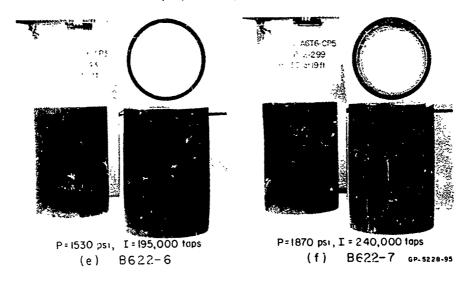


FIG. 6.27 DELAMINATION OF TAPE-WOUND CARBON PHENOLIC SHELLS (subshell $\alpha/h=50$) FROM (a, b, c) QUASI-IMPULSIVE LOADS, AND (d-g) QUASI-STATIC LOADS



P=1870 psi, I=240,000 taps SAME AS (f), INTERIOR VIEW (g) B622-7

FIG. 6.27 (Concluded)

Quasi-static pressures at which no damage, incipient delamination, and severe damage was observed in shells with tape-wound covers are listed in Table 6.3. For all three of the tape-wound cover materials the pressures are about the same and are in the same range as those for the Micarta-covered shells (see Table 6.1). With a subshell of a/h = 100, incipient delamination occurs between 800 and 1000 psi and severe damage occurs between 1000 and 1300 psi.

Thus the load increment between threshold damage and severe damage appears to be about 30 percent, in contrast to a very small load increment for the Micarta shells. This difference is attributed to the high resistance of the tape-wound shells to longitudinal cracking, which keeps the cover from being peeled off by the blast.

Table 6.3

SUMMARY OF QUASI-STATIC PRESSURES FROM SHOCK
TUBES APPLIED TO SHELLS WITH TAPE-WOUND COVERS

Subshell	Cover	Quasi-Static Pressure (psi)				
(6061-T6) a/h	Material	No Damage	Incipient Delamination	Severe Damage		
100	Refrasil	680	1000	1530		
100	Carbon phenolic	840	1000	1310		
100	NOMEX	680	1000	1310		
50	Refrasil	1310		1770		
50	Carbon phenolic	~ -	1150	1870*		

^{*}Damage not as severe as in other shells.

The response of tape-wound shells to quasi-impulsive loads is summarized in Table 6.4. As for quasi-static loads, the increments in load from no damage to severe damage are larger than for the Micarta-covered shells (compare Table 6.4 to Micarta shells, Table 4.1).

Table 6.4

SUMMARY OF QUASI-IMPULSIVE LOADS FROM HE SPHERES APPLIFD TO SHELLS WITH TAPE-WOUND COVERS

	Cover Material	Quasi-Impulsive Loads (4-pound HE spheres)						
Subshell (6061-T6) a/h		o Damage		Incipient Delamination		Severe Damage		
		P (osi)	[(taps)	P (psi)	I (taps)	P (psi)	I (taps)	
100	Refrasil	2500	7600	3200	8,700	7000	15, 000	
100	Carbon phenclic			3800	9,800	6300	13,800	
50	Refrasil			4600	11, 100			
50	Carbon phenolic	3800	9800	5100	12,000	9000	18, 500	

These tests on tape-wound shells were insufficient to establish critical pressure-impulse curves; however, the data fall close enough to the Micarta curves to suggest that the Micarta curves could be used as a first estimate for the tape-wound shells.

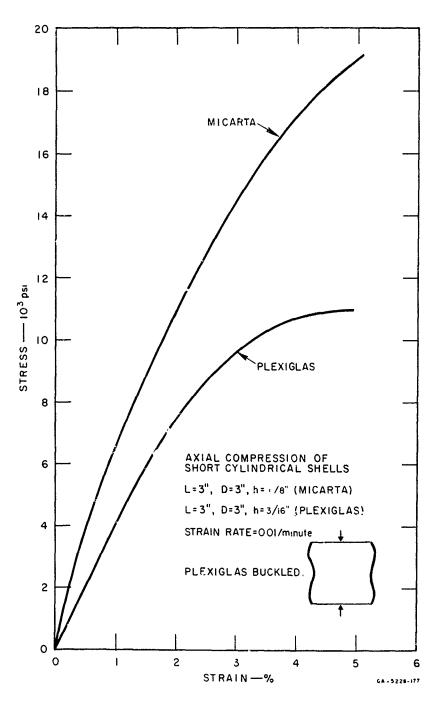


FIG. 6.28 STRESS-STRAIN CURVES FOR PLEXIGLAS AND GRADE 79 M!CARTA

7. RESPONSE OF COMPLEX SHELLS

It was observed in Chapter 5 that all of the uncovered shells failed by buckling and in Chapter 6 that buckling also influenced the response of covered shells. This suggests that these shells can be strengthened by stiffening. In this chapter experiments are reported on uncovered and covered shells stiffened with internal circumferential ribs, rigid-foam polyurethane, and sandwich construction. All of the shells were 6061-T6 aluminum and were nominally 6 inches in diameter. Each type of shell was tested using quasi-impulsive loads from 4-pound HE spheres and quasi-static loads from the 2-foot shock tube at a 20-foot length. The data are listed in the C groups of Table 4.1. In the following discussion, photographs of the damaged shells are presented and comments are made on the effectiveness of each stiffening design. At the end of the chapter, pressures and impulses from the most pertinent experiments are summarized in tabular form for comparison of the complex designs with each other and with the simple shells discussed in Chapters 5 and 6. No critical pressure-impulse curves for failure are presented, since only two points were determined for each shell; however, a reasonable estimate of the critical curves can be made using these points and the hyperbolic shape given in Fig. 6.21 (Eq. 6.1).

7.1 Ribbed Shells

7.1.1 Uncovered Shells with Circumferential Ribs

Two types of shells were used in this series of experiments, one set with a between-rib radius-to-thickness ratio of a/h = 100 and the other with a/h = 50. In both types the number and size of the ribs were designed so that the buckling stress in both general and local (between-rib) instability under uniform lateral pressure was approximately equal to the yield stress (43,000 psi). The shells were all made from 6-inch outside diameter extruded tubing with a 0.25-inch wall,

giving a rib height of 0.25 inch minus the wall thickness between ribs. As with the simple shells, the total unsupported length was 6 inches. These design constraints resulted in the following dimensions for the two designs:

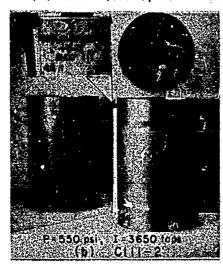
<u>a/h</u>	Wall Thickness (inch)	Number of Ribs	Rib Width (inch)	Rib Height (inch)	Rib Spacing (inches)
100	0.030	5	0.030	0.220	1
50	0.060	2	0.060	0.190	2

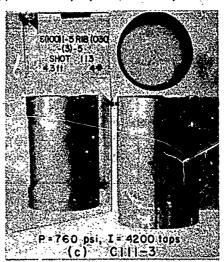
In both designs the ratio of rib height to rib width is smaller than in a minimum weight design (i.e., the circumferential stiffness is correct, but the ribs are heavier than necessary), but this does not affect the shell buckling characteristics. Furthermore, these ribs are so light that they are probably not very different from those in practical design.

The experimental results for the stiffened shells with a/h = 100 are given in Fig. 7.1. The shells shown in Fig. 7.1(a-c) were tested with 4-pound HE spheres and those in Fig. 7.1(d-g) were tested with the 2-foot shock tube. * In both the quasi-impulsive (HE spheres) and quasi-static (shock tube) experiments, no buckling either between ribs or by general instability occurred, demonstrating that the rib design was satisfactory. However, as shown in Fig. 7.1(f), under the quasi-static pressure of 320 psi shear buckling occurred between the end plug and the last rib due to the high shear stresses from overall beam-bending action. Large deformations from local bending and buckling near the ends are also evident in the quasi-impulsive experiment shown in Fig. 7.1(b). These observations suggest that a better design would result if the shell thickness were increased near the ends.

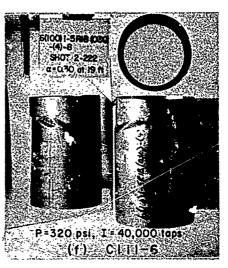
This scheme of presentation will be used throughout this chapter; first the quasi-impulsive experiments will be given and then the quasi-static experiments, each in order of increasing load. The type of experiment is shown on the lettered cards in the photographs, but the two types can also be distinguished because the quasi-static impulses are much larger and the pressures are lower.

(a) CIII-I (0.5 %, NOT SHOWN) P=270 psi, I=2750 taps





- (d) CIII-4 (UNDAMAGED, NOT SHOWN) P=180 psi, I=24,000 taps
- (e) CIII-5 (1% DEFORMATION, NOT SHOWN) P=250 psi, I=32,000 taps



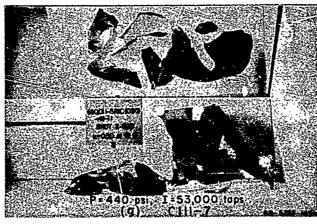


FIG. 7.1 UNCOVERED RIBBED SHELLS, a/h = 100, 5 RIBS

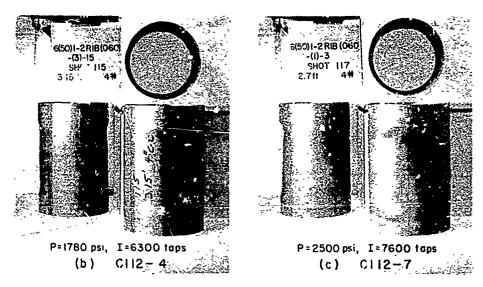
From Fig. 7. 1(e, f), it is apparent that the critical pressure under lateral blast is between 250 and 320 psi. Comparing this with the symmetric yield pressure of $\sigma_{\rm h}/a = 430$ psi, it is apparent that shear buckling significantly reduced the critical pressure below the yield pressure. At 440 psi the shell was torn to pieces, as shown in Fig. 7. 1(g).

Experimental results for the stiffened shells with a/h = 50 are given in Fig. 7.2. As shown in Fig. 7.2(b), under quasi-impulsive loads the ribs prevented buckling. Instead, the shells exhibit a plastic deformation uniform along the length. The ribs also prevented elastic buckling under quasi-static loads; however, plastic buckling occurred as shown in Fig. 7.2(e,f). This occurred at a pressure between 680 and 780 psi, which is close to the nominal yield pressure of 860 psi. Because of the thicker walls, shear buckling at the ends did not occur as for the shells with a/h = 100, and the design objective of buckling near the yield limit was achieved.

7.1.2 Covered Shells with Circumferential Ribs

Design of the ribs for the covered shells was not based on a rational buckling criterion as for the uncovered shells because it was not possible to specify the boundary conditions between the cover and subshell, and because the subshell buckles plastically. Instead, the circumferential ribs in these shells were merely made large enough to assess whether ribs would significantly enhance structural strength. The ribbed subshells were machined from 0.25-inch wall, 6-inch outside diameter, 6061-T6 aluminum tubing. Two ribs were machined in the shell, with 2 inches between ribs and 2 inches between each rib and the nearest end support. The between-rib wall thickness was 0.060 (a/h = 50) and the ribs were 0.25 inch wide and 0.19 inch high.

(a) C112-2 (1% DEFORMATION, NOT SHOWN) P=1080 psi, I=5000 taps



(d) C112-8 (VERY SLIGHT DEFORMATION, NOT SHOWN) P=500psi, I=60,000 taps

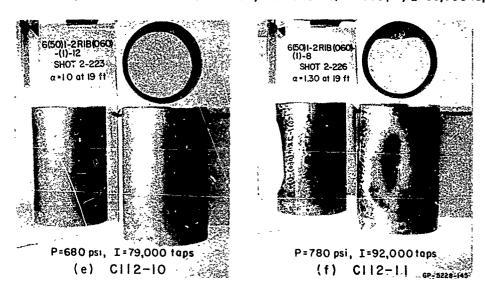
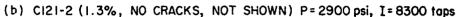


FIG. 7.2 UNCOVERED RIBBED SHELLS, a/h = 50, 2 RIBS

The results of the tests on Plexiglas-covered shells are shown in Fig. 7.3. The modes of failure are similar to those in the simple covered shells (see Figs. 6.3 and 6.6) but the loads are somewhat higher, with values about 20 percent higher than the critical pressure-impulse curve for an a/h = 61 monoccque subshell in Fig. 6.19.

(a) C!21-1 (0.5%, NO CRACKS, NOT SHOWN) $P=2000\,\mathrm{psi}$, $I=6700\,\mathrm{taps}$



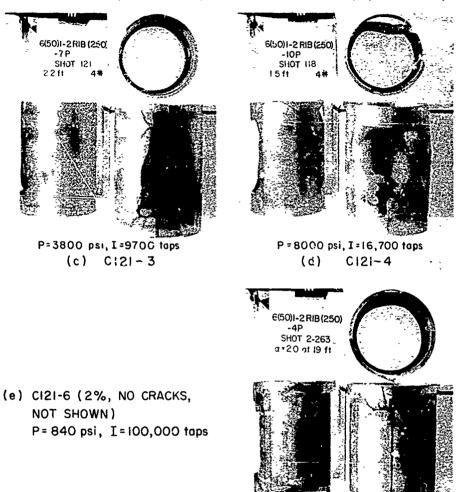


FIG. 7.3 PLEXIGLAS-COVERED RIBBED SHELLS, $\alpha/h = 50$, 2 HEAVY RIBS

P=1000 psi_ I=120,000 taps

C:21-7

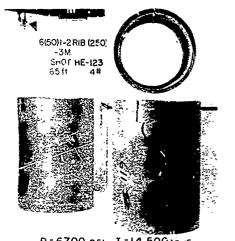
CF - 5228-146

(f)

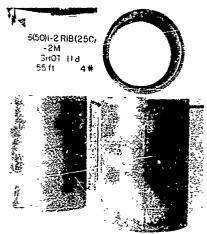
The results of the tests on Micarta-covered shells are shown in Fig. 7.4. Again the response modes are similar to those of the unstiffened shells and the threshold loads are essentially the same. However, the ribs significantly increased the severe-damage loads. A quasi-static pressure of 1400 psi destroyed the unstiffened shell (shell B223-12), but produced only 5-percent subshell deformation

and minor circumferential cracks at the ends of the stiffened shell (Fig. 7.4g). At 1950 psi the stiffened shell in Fig. 7.4(i) seems to be on the verge of disintegration. Thus the ribs have increased the severe-damage load by almost 50 percent.

- (a) C122-1 (2.5%, HAIRLINE C-CRACK, NOT SHOWN)
 P=3600 psi, I=9700 taps
- (b) C122-3 (2.2%, C-CRACKS, NOT SHOWN) P=5700 psi, I=13,000 taps



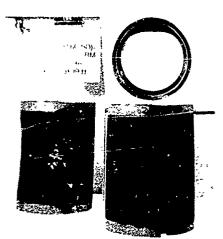
P=6700 psi, I=14,500 icus (c) C122-4



P=7500 psi, I=16,000 taps (d) C122-5

NOT SHOWN

- (e) B122-7 (2%, NO CRACKS), P=1000 psi, I=120,000 taps
- (f) B122-8 (2.5%, C-CRACK), P=1180 psi, I=140,000 taps
- (g) B122-9 (5%, CRACKS AS IN (d) ABOVE),
 P=1400 psi, I=180,000 taps
- (h) B122-IO (7%, CRACKS AS IN (d) ABOVE), P=1650 psi, I=210,000 taps



P=1950 psi, I =255,000 taps (i) C|22-11 GP-5228-147

FIG. 7.4 MICARTA-COVERED RIBBED SHELLS, a/h = 50, 2 HEAVY RIBS

7.2 Foam-Filled Shells

The shells in these experiments were made by completely filling (except for the 2-inch diameter steel support rod) uncovered shells with rigid polyurethane from. The shells were 6061-T6 aluminum with a/h = 61 and 100 and the polyurethane was foamed in place at densities of 8, 12, and 18 lb/ft³. The crushing (yield) stresses of the foam at these densities were found to be 200, 500, and 1000 psi, based on indentation tests with a 0.25-inch diameter ball indented to 0.100 inch (see [27] for a description of this procedure). Indentation tests were made at several axial and circumferential stations and the crushing stress near the bottom end of the pour was found to be as high as twice the values given above. However, the shell deformation data given here are the maximum that occurred in the shell and are to be associated with the crushing stresses given above.

Results from the entire series of experiments are given in Figs. 7.5 through 7.10. The foam significantly increased the buckling loads and wave numbers compared to those for the unfilled shells.

7.3 Sandwich Shells

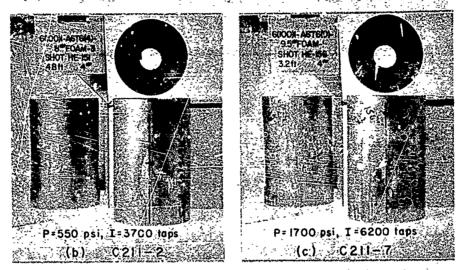
7.3.1 Uncovered Sandwich Shells

Most of the sandwich shells were made of concentrically placed shells 6 inches and 7 inches in diameter, spaced apart by 1.5-inch long end rings as shown in the sectioned cylinder in Fig. 7.11. The unsupported length between rings was 6 inches and the shells were supported in the standard fixtures described in Appendix B. The annular volume between the aluminum shells was filled with rigid polyarethane (24 lb/ft³) foamed and bended in place, giving a core thickness of 0.47 inch. Indentation tests showed that the crushing stress of the foam ranged from 1200 to 2500 psi, either value being larger than required to prevent core failure. * Combinations of outer and inner skin

With a foam density of 12 lb/ft³ (shell group C313), the foam crushed before the inner skin deformed, demonstrating the need for a higher strength core.

thicknesses of 0.049 and 0.030 inch were used, as shown in groups C311 and C315 in Table 4.1. In addition to the shells with 0.47-inch core thickness described above, one group (C311) had a wall spacing of 0.21 inch.

(a) C211-1 (UNDAMAGED, NOT SHOWN) P=380 psi, 1=3200 taps



(d) C211-8 (UNDAMAGED, NOT SHOWN) P=180 psi, I=24,000 taps

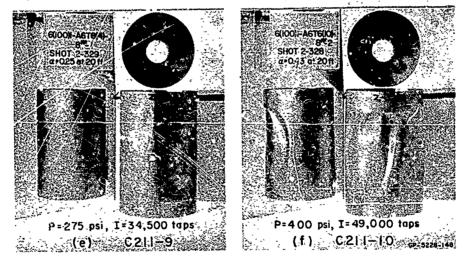
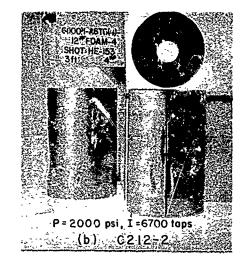
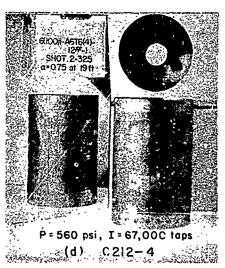


FIG. 7.5 FOAM-FILLED SHELLS, a/h = 100, 8 lb/ft3 FOAM

(a) C212-1 (1%, NOT SHOWN). P=950 psi, I=4700 taps



(c) C212-3 (1%, NO BUCKLING, NOT SHOWN) P=470 psi, I=56,000 taps



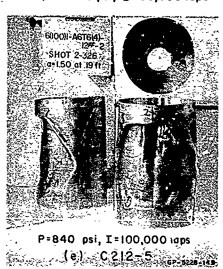


FIG. 7.6 FOAM-FILLED SHELLS, a/h = 100, $12 lb/ft^3$ FOAM

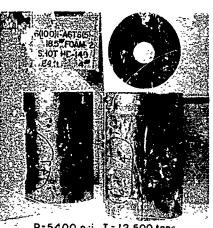
(a) C213-1 (UNDAMAGED, NOT SHOWN) P=810 psi, I=4400 tops

THE PROPERTY OF THE PROPERTY O

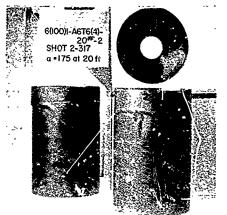
(5) C2:3-2 (0.8%, NOT SHOWN), P=2700 psi, I=8000 taps

(d) C2:3-4 (SLIGHT DEFORMA-TICN, NOT SHOWN)

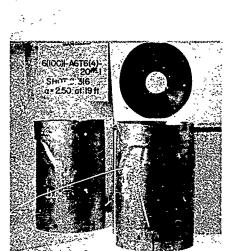
P = 760 psi, I = 89,000 taps



P=5400 psi, I = 12,500 tops (c) C213=3



P=925 psi, I=110,000 taps (e) C213-5



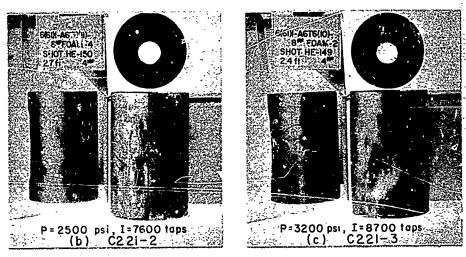
P=1170 psi, I=143,000 taps (f) C213=6



P=1310 psi, I=161,000 taps (g) C213-7 _{GP-5228-150}

FIG. 7.7 FOAM-FILLED SHELLS, a/h = 100, 18 lb/ft3 FOAM

(a) C221-1 (1%, NO BUCKLING, NOT SHOWN) P=1000 psi, I=4800 taps



- (d) C221-4 (UNDAMAGED, NOT SHOWN) P=350 psi, I=44,000 tops
- (e) C221-5 (3%, NO BUCKLING, NOT SHOWN) $P = 440 \, \text{psi}$, $I = 53,000 \, \text{taps}$

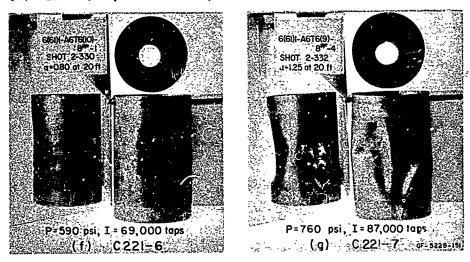
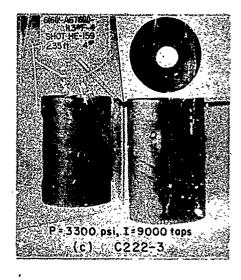
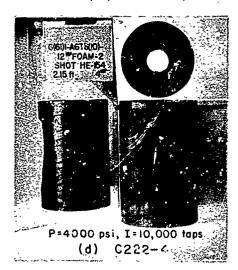


FIG. 7.8 FOAM-FILLED SHELLS, a/h = 61, 8 lb/ft^3 FOAM

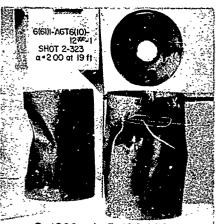
- (a) C222-1 (2%, NO BUCKLING, NOT SHOWN) P=1550 psi, I=6000 taps.
- (b) C222-2 (4.9% DENT, NOT SHOWN) P=2900 psi, I=8300 taps



| 100mm | 100mm | 100mm | 100mm | 100mm | 100mm | 100mm | 100mm | 100mm | 100mm | 100mm | 100mm | 100mm | 100mm | 100mm | 100mm | 100mm | 100mm | 100mm | 100mm | 100mm | 100mm | 100mm | 100mm | 100mm | 100mm | 100mm | 100mm | 100mm | 100mm | 100mm | 100mm | 100mm | 100mm | 100mm | 100mm | 100mm | 100mm | 100mm | 100mm | 100mm | 100mm | 100mm | 100mm | 100mm | 100mm | 100mm | 100mm | 100mm | 100mm | 100mm | 100mm | 100mm | 100mm | 100mm | 100mm | 100mm | 100mm | 100mm | 100mm | 100mm | 100mm | 100mm | 100mm | 100mm | 100mm | 100mm | 100mm | 100mm | 100mm | 100mm | 100mm | 100mm | 100mm | 100mm | 100mm | 100mm | 100mm | 100mm | 100mm | 100mm | 100mm | 100mm | 100mm | 100mm | 100mm | 100mm | 100mm | 100mm | 100mm | 100mm | 100mm | 100mm | 100mm | 100mm | 100mm | 100mm | 100mm | 100mm | 100mm | 100mm | 100mm | 100mm | 100mm | 100mm | 100mm | 100mm | 100mm | 100mm | 100mm | 100mm | 100mm | 100mm | 100mm | 100mm | 100mm | 100mm | 100mm | 100mm | 100mm | 100mm | 100mm | 100mm | 100mm | 100mm | 100mm | 100mm | 100mm | 100mm | 100mm | 100mm | 100mm | 100mm | 100mm | 100mm | 100mm | 100mm | 100mm | 100mm | 100mm | 100mm | 100mm | 100mm | 100mm | 100mm | 100mm | 100mm | 100mm | 100mm | 100mm | 100mm | 100mm | 100mm | 100mm | 100mm | 100mm | 100mm | 100mm | 100mm | 100mm | 100mm | 100mm | 100mm | 100mm | 100mm | 100mm | 100mm | 100mm | 100mm | 100mm | 100mm | 100mm | 100mm | 100mm | 100mm | 100mm | 100mm | 100mm | 100mm | 100mm | 100mm | 100mm | 100mm | 100mm | 100mm | 100mm | 100mm | 100mm | 100mm | 100mm | 100mm | 100mm | 100mm | 100mm | 100mm | 100mm | 100mm | 100mm | 100mm | 100mm | 100mm | 100mm | 100mm | 100mm | 100mm | 100mm | 100mm | 100mm | 100mm | 100mm | 100mm | 100mm | 100mm | 100mm | 100mm | 100mm | 100mm | 100mm | 100mm | 100mm | 100mm | 100mm | 100mm | 100mm | 100mm | 100mm | 100mm | 100mm | 100mm | 100mm | 100mm | 100mm | 100mm | 100mm | 100mm | 100mm | 100mm | 100mm | 100mm | 100mm | 100mm | 100mm | 100mm | 100mm | 100mm | 100mm | 100mm | 100mm | 100mm | 100mm | 100mm | 100mm | 100mm | 100mm | 100mm | 1



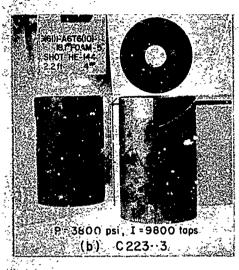
- (e) C222-5 (0.5%, PIO BUCKLING, NOT SHOWN)
 P=590 psi, X=69,000 taps
- (f) C222-6 (1.5%, NO BUCKLING, NOT SHOWN)
 P=680-psi, I=79,000 taps



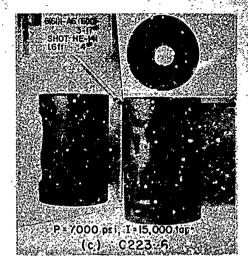
P=1000 psi, I=120,000 taps (g) C222-7 GP-5228-152

FIG. 7.9 FOAM-FILLED SHELLS, a/h = 61, 12 lb/ft^3 FOAM

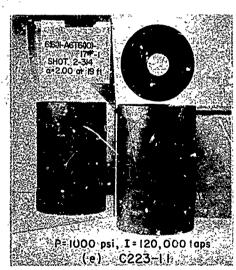
(a) C223-2 (0.6%, NO BUCKLING, NOT SHOWN) P=2000 psi, 1=6700 tops



THE REPORT OF THE PROPERTY OF



(d) C223-8 (UNDAMAGED, NOT SHOWN) P=680 psi, I=79,000 taps



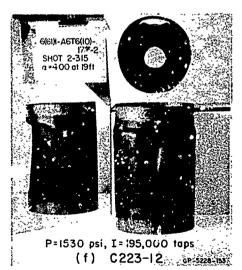


FIG. 7.10 FCAM-FILLED SHELLS, a/h = 61, 18 lb/ft^3 FOAM

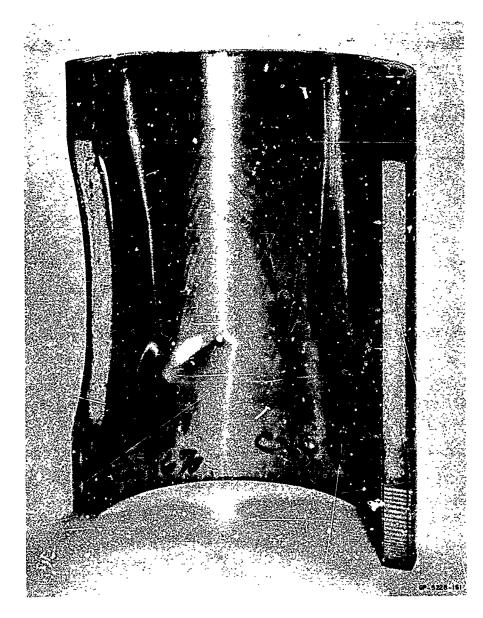


FIG. 7.11 CROSS SECTION OF SANDWICH SHELL 0.049/0.030-inch SKINS (Experiments C314-6, 7, 8, last Experiment at P = 680 ps i, $I = 79,000 \; taps$)

The results of the experiments with 24 lb/ft³ cores are given in Figs. 7.11 through 7.15. Under quasi-impulsive loads, permanent deformation consisted of short wavelength wrinkling of the outer skin (Figs. 7.13b and 7.15c) and sometimes of the outer and inner skins (Fig. 7.14d). Under quasi-static loads the dominant mode of deformation was general instability, as indicated in Figs. 7.14(g) and 7.15(e). However, there was also a tendency for the outer skin to wrinkle (Fig. 7.13e), and for the shells to shear at the ends (Figs. 7.12f and 7.15f).

7.3.2 Covered Sandwich Shells

The subshells for these tests were the same as for the uncovered shells described immediately above. Micarta sleeves were pressed over the outer skin, giving the final configuration shown in Fig. 7.16. Two sets of covered shells were made and tested, one with outer and inner wall thickness of 0.030/0.030 inch and the other with thicknesses of 0.049/0.030 inch. Test results are given in Figs. 7.16 through 7.18. Surprisingly, as shown in these figures, severe deformation of the subshell occurred with only minor circumferential cracks in the Micarta at the end plugs. The cross-section in Fig. 7.16 shows that cracking of the Micarta was confined to the outer fibers in the area of the peak load. At sufficiently high loads, severe cracking of the Micarta and shearing of the aluminum occurred. This is shown in Fig. 7.18(c) for a quasi-impulsive load and in Fig. 7.18(h) for a quasi-static load.

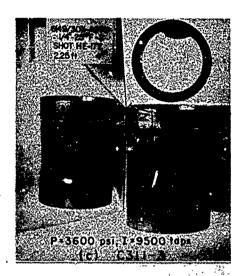
7.4 Comparison of Critical Quasi-Static Pressures for Stiffened and Unstiffened Shells

It is convenient to compare the strength of the various shell designs on the basis of an efficiency defined by the ratio of the critical quasi-static blast pressure to the uniform lateral pressure required to bring the shell to yield in hoop compression. For the complex shells, this yield pressure is calculated by lumping all of the substructure weight into a tube of uniform thickness. For the foam-filled shells,

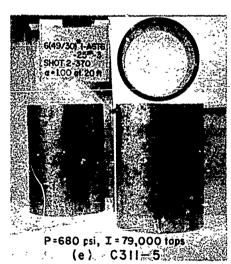
(a) C311-1 (1.4/0.1%, NOT SHOWN) P=1850 psi, I=6500 taps

THE RESERVE OF THE PARTY OF THE

(b) C3II-2 (8.7/2.8%, NOT SHOWN) P=3200 psi, I=8700 taps



(d) C311-4 (0.5/9.5%, NOT SHOWN) P=530 psi, I=62,000 taps



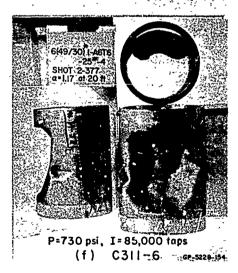
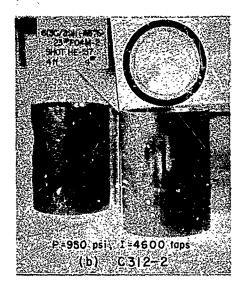
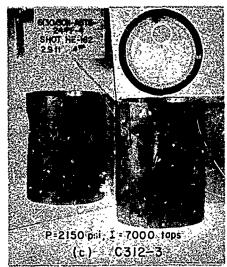


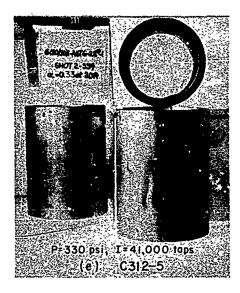
FIG. 7.12 UNCOVERED SANDWICH SHELLS, 0.049/0.030-inch SKINS, 1/4-inch CORE

(a) C312-1 (1.3/0.0%, NOT SHOWN) P=950 psi, I=4600 taps





(d) C312-4 (0.5%, NOT SHOWN) $P=275 \, \text{psi}$, $I=34,800 \, \text{taps}$



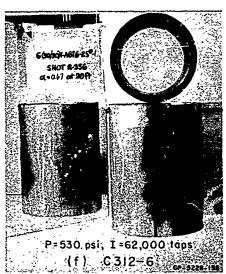
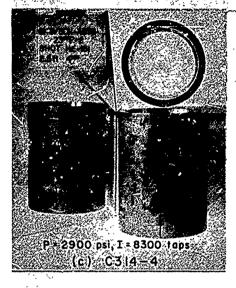
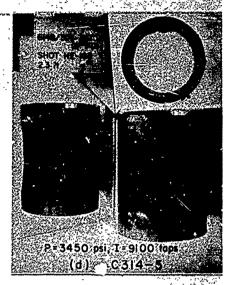


FIG. 7.13 UNCOVERED SANDWICH SHELLS, 0.030/0.030-inch SKINS, 1/2-inch CORE

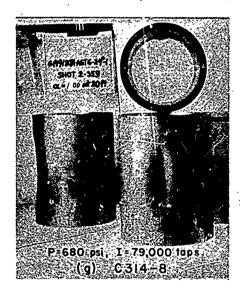
(a) C314-2 (UNDAMAGED, NOT SHOWN) P=1550 psi, I=6000 taps

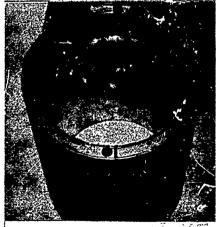
(b) C314-3 (0.3/0.0%, NOT SHOWN) P=1850 psi, I=6500 taps





- (e) C314-6 (UNDAMAGED, NOT SHOWN) P=330 psi, I=41,000 tops
- (f) C314-7 (1%, NOT SHOWN) P=530 psi, I=62,000 taps 🗸 🤏 🚉

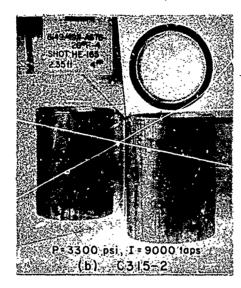




SAME AS (g), INTERIOR VIEW
(h) C314-8 GP-5228-156

FIG. 7.14 UNCOVERED SANDWICH SHELLS, 0.049/0.030-inch SKINS, 1/2-inch CORE

(a) C315-1 (0.8/0.1%, NOT SHOWN) P=2000 psi, I = 6700 taps





(d) C3!5-4 (SLIGHT DEFORMATION, NOT SHOWN) P=530psi, I=62,000 taps

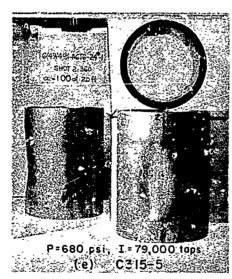




FIG. 7.15 UNCOVERED SANDWICH SHELLS, 0.049/0.049-inch SKINS, 1/2-inch CORE

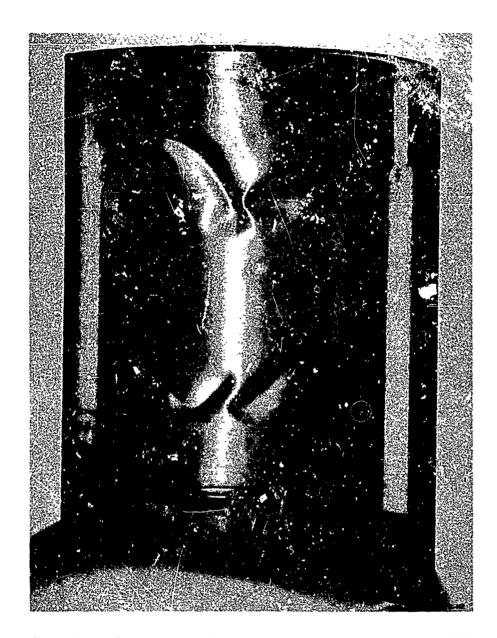


FIG. 7.16 CROSS SECTION OF MICARTA-COVERED SANDWICH SHELL 0.030/0.030-inch SKINS (Experiment C321- , P = 1200 psi, I = 150,000 taps)

- (a) C321-1 (UNDAMAGED, NOT SHOWN) P=3450 psi, I=9100 taps
- (b) C321-2 (3%, C-CRACKS, NOT SHOWN) P=4600 psi, I=11,200 taps

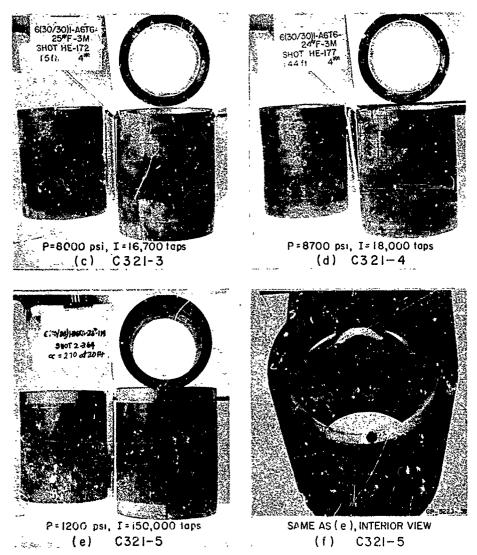


FIG. 7.17 MICARTA-COVERED SANDWICH SHELLS, 0.030/0.030-inch SUBSHELL SKINS

the weight of foam assigned to the structure is that of a 1-inch annulus, with any further interior foam weight being assigned to payload. For the sandwich shells the core density is taken as 10 lb/ft rather than the 24 lb/ft used in the experiments because an optimum design would probably use aluminum honeycomb of approximately this density.

The efficiency is

$$\eta = \frac{P}{P_y}$$
, $P_y = \sigma_y \frac{\bar{h}}{a}$ (7.1)

where

P = quasi-static failure pressure

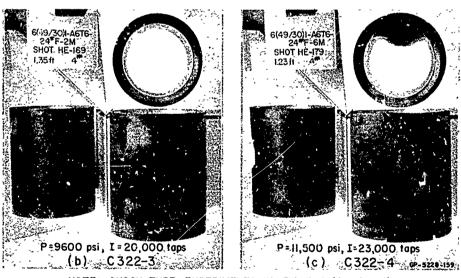
P_v = yield pressure of equivalent weight tube

 σ_{\perp} = yield stress = 43,000 psi

h = thickness of equivalent weight aluminum wall

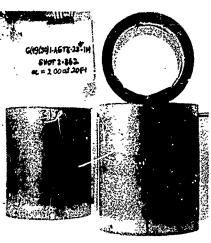
a = radius

(a) C322-1 (0.3/3.8%, NO CRACKS, NOT SHOWN) P=6300 psi, 1=14,000 taps



NOTE: SHOCK TUBE EXPERIMENTS IN FIG. 7.18 (Concluded)

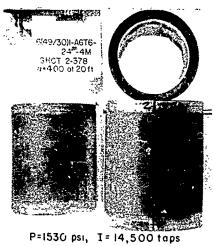
FIG. 7.18 MICARTA-COVERED SANDWICH SHELLS, 0.049/0.030-inch SUBSHELL SKINS



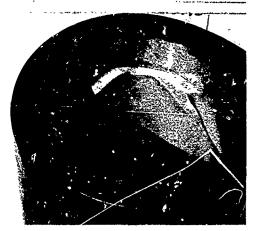
P=1000 psi, I=120,000 taps (d) C322-5



SAME AS (d), INTERIOR VIEW (e) C322-5



P=1530 psi, T=14,500 tap (f) C322-7



SAME AS (f), INTERIOR VIEW
(g) 322-7



P=1800 psi, I=240,000 tups (h) C322-8

FIG. 7.18 (Concluded)

The efficiencies of the various uncovered shells are given in Table 7.1. The thin unstiffened shells are relatively inefficient, as one would expect, with $\eta = 17$ percent for a/h = 100 and $\eta = 40$ percent for a/h = 61. However, $\eta = 72$ percent for a/h = 24, because at L/D = 1 the buckling and yield stresses are very close for this shell thickness.

Table 7.1

QUASI-STATIC EFFICIENCIES AVARIOUS UNCOVERED SHELL DESIGNS (Pressures are for slight, 1...derate, and heavy damage, from Table 4.1)

Simple			Ribbed				Foam-Filled				Sandwich			
a/h	p (ps1)	η	Config- uration	a/h	p (psi)	٠,	Config- uration	a/h	p (psi)	η	Config- uration	a/h	p (psi)	η
100	75 80	17%	(100)/5R1b	86	250 320	52%	(100) 8#	34	180 275 400	21%	(49/30)1/4	35	530 680 730	49%
61	270 320	40%	(50)/2R1b	47	680 780	80%	(100)12#	30	470 560 840	37%	(30/30)1/2	37	390 530	38%
24	1270 1400	72%					(100)18#	22	760 925 1280	45%	(49/30)1/2	30	530 680	40%
							(61) 8#	28	350 440 760	27%	(49/49)1/2	26	530 680	35%
							(61)12#	25	590 680 1000	38%				
							(61)18#	20	840 1000 1530	45%				

The rib-stiffened shells are relatively efficient, with $\eta=52$ percent for a/h=100 and $\eta=80$ percent for a/h=61. As mentioned earlier, the efficiency for a/h=100 could be increased by increasing the wall thickness near the end supports to carry the shear load. However, at truly impulsive loads it is possible that the rib separation is too large to prevent short wavelength wrinkling between the ribs [13].

The foam-filled shells give efficiencies ranging from 21 percent to 45 percent. The sandwich shells performed surprisingly poorly, with efficiencies near 40 percent for all four designs.

For the covered shells, efficiencies were calculated using reference pressures given by

$$P_{y} = \frac{1}{a} (\sigma_{y} \bar{h} + E_{c} \varepsilon_{c} h_{c}) \qquad (7.2)$$

where

E = Young's modulus of cover material

ec = failure strain of cover material, taken as 0.015 for both Micarta and Plexiglas

h = cover thickness

and other quantities are as previously defined. Results for covered shells with simple, ribbed, and sandwich subshells are given in Table 7.2.

Table 7.2

QUASI-STATIC EFFICIENCIES OF COVERED, SIMPLE AND STIFFENED SHELLS

SIMPLE				RIBBED						SANDWICH				
Subshell Micarta		Lucite		Subshell		Micarta		Lucite		Subshell		Mica	rta	
a/h	p (psi)	Ľ	p (psi)	η	Config- uration	a/h	p (psi)	η	p (psi)	η	Config- uration	a/h	p (ps1)	η
100	840 1000	71%	520 750	66%							(30/30)1/2	37	1200	52%
61	1000 1150	66%	725 840	63%	(50)/2Rib	40	1000 1130	53%	840 1000	57%	(49/30)1/2	30	1000 1280	48%
24	1770 1950	67%	1500 1750	63%				•						

All of the simple shells have efficiencies near 65 percent. The ribbed shells have efficiencies near 55 percent, which is somewhat less than in the simple shells because the threshold of damage changes very little with the addition of ribs. The efficiencies of the sandwich shells are approximately 50 percent.

These results suggest that the shells here are so short (L/D = 1) and the combined subshell-cover wall thickness so large that buckling is not the dominant mode of failure and stiffening decreases rather than increases the efficiency. It would be better to increase the wall thickness of the simple shells near the end supports, to carry the shear better and hence avoid cracking of the cover and shearing of the subshell at the ends. For longer or thinner shells, stiffening increases efficiency, as demonstrated by data listed in Table 7.1 for uncovered shells.

こう 一のことのというないないないないないないないないないできることできることできることがあるというできることがあるというできることがあるというできることがあるというできることがあるというできることが

8. THEORY—DYNAMIC BUCKLING OF CYLINDRICAL SHELLS

8.1 Introduction

In this chapter an analysis is given for the buckling of cylindrical shells subjected to transient surface pressures ranging in duration from an ideal impulse to durations so long that the buckling is essentially static. At each extreme the analysis becomes relative simple; theories for these have already been reported in the literature.

For very short durations the load is characterized entirely by the impulse. Also, for such loads the wavelength of the buckling is so short that the length of the shell is unimportant. Thus two parameters, load duration and shell length, are eliminated from the problem and the solutions become particularly simple. These are given in [11] for relatively thick shells and in [12] for very thin shells. Simple buckling threshold formulas for both cases are given in [20].

For very long durations the load is characterized entirely by peak pressure and, although the length of the shell must be considered, it is shown here that inertia forces can be neglected and the solution is again relatively simple. This is a classical static buckling problem and is given in several standard texts, for example [28]. Between these extremes, pressure, duration, shell length, and inertia forces must all be considered. No previous investigations of this problem are known to the authors. The present analysis treats this problem and contains the simple theories as special cases.

The problem taken is that of a simply supported cylindrical shell subjected to external surface pressures. Two distributions of lateral pressure are considered; a uniform pressure all around, and a pressure varying as $\cos^2\theta$ over one side, typical of an intense lateral blast load. The time variations of pressure considered are triangular and exponential in shape, as shown in Fig. 8.1, and are

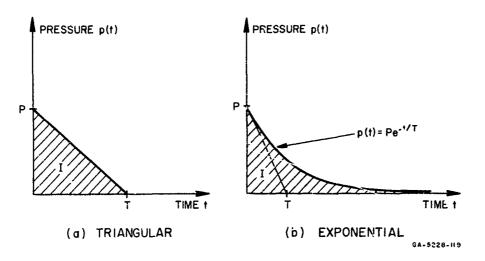


FIG. 8.1 PULSE SHAPES

assumed to be the same all around the shell--that is, the pressure is simply the product of a single time variation and a spatial variation. Pertinent shell parameters considered are radius-to-thickness ratio a/h, length-to-diameter ratio L/D, and shell material.

Although variations in pressure distribution and pulse shape are investigated, it has been postulated (see Chapter 1) that the most significant load characteristics are peak pressure and impulse. Therefore, in the theory to follow, loads that cause buckling are characterized by these quantities, and for each type of shell a "critical curve" for buckling is generated, as shown in Fig. 8.2. Critical curves are generated for uniform and $\cos^2\theta$ load distributions and for triangular and exponential shapes, in order to assess the influence of these parameters. In all cases, the peak pressure and impulse in the curves are for the location on the shell of the maximum pressure, with the impulse (per unit surface area) being the area under the pressure-time curve. For the triangular pulse the impulse is I = PT/2, where T is pulse duration, and for the exponential pulse the impulse is I = PT, where T is the pulse time constant as shown in Fig. 8.1.

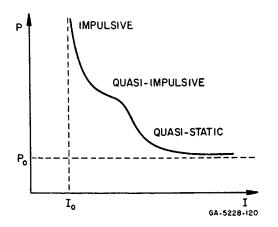
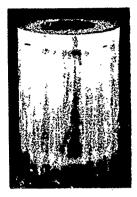


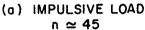
FIG. 8.2 TYPICAL CRITICAL PRESSURE-IMPULSE CURVES FOR BUCKLING, SHOWING LOAD REGIONS

Since the analysis is rather lengthy, the reader may want to complete Section 8.2 on theoretical models and then skip to Section 8.6 for the results. Sections 8.3, 8.4, and 8.5 give the equations of motion, the character of the solutions, and a discussion of the criteria used for buckling. Section 8.7 gives a derivation of an approximate expression for the impulsive buckling threshold and Section 8.8 gives an analysis based on a more complex shell model.

8.2 Idealized Models

Figure 8.3 shows three shells subjected to loads in each of the load regions indicated indicated in Fig. 8.2. The shell on the left was subjected to an impulsive load and has buckled into a very high order pattern with n = 45 waves around the circumference. The shell in the center was subjected to a quasi-impulsive load and has buckled into a pattern corresponding to n = 13. The shell on the right was subjected to a quasi-static load and has buckled into n = 7, very close to the static pattern for this shell. Thus, depending on the location of the load point in the pressure-impulse diagram, the mode of response of the shell varies widely, the buckle wavelength increasing monotonically from a very short wavelength pattern for impulsive loads to an essentially static buckling pattern for very long loads. For impulsive loads impulse is the dominant factor, for quasi-impulsi loads both pressure and impulse are important, and for quasi-static rads pressure is the dominant factor. In the analysis three corresponding models are used-a "tangent-modulus" model for impulsive loads, an "elastic" model for quasi-static loads, and a "strain-reversal" model for a narrow range of quasi-impulsive loads for which neither of the other models is applicable. The range of applicabinty of each model depends mainly on a/h and the yield strain of the shell material.







(b) QUASI-IMPULSIVE LOAD $n \simeq 13$



(c) QUASI-STATIC LOAD n = 7

<u>;</u> :

Ĺ

FIG. 8.3 BUCKLING PATTERNS IN CYLINDERS SUBJECTED TO VARIOUS PULSE DURATIONS

For impulsive loads it has been found that for all but very thin shells buckling takes place during plastic flow [11, 12]. Thus, in this region the theory must allow for plastic response. Since the buckling takes place during membrane plastic flow, without strain reversal, the buckling motion is governed by the tangent modulus, and hence the name for this model. Fortunately, as shown in Fig. 8.3, the response to impulsive loads is in relatively high order modes; thus the effects of the ends are unimportant beyond a few wavelengths from the ends. In the tangent-modulus model, the shell will be treated as infinitely long and the analysis will follow that given in [13], except that finite pulse durations will be considered.

The elastic model is so called because for long loads most metal shells of present interest buckle at pressures sufficiently small that during buckling the response is elastic. From Fig. 8.3(c) it is evident that the boundary conditions at the ends must be satisfied as in static buckling because the wavelength of the buckling depends on this constraint. Since the buckling behavior is elastic, a reasonably simple extension of static theory is made by including inertia terms. Also, as in static buckling the membrane forces are found by neglecting end effects, but it is required that the flexural modes satisfy the end conditions.

The strain-reversal model is postulated for a range of quasiimpulsive loads for which the mode number is sufficiently high to
neglect end effects, but for which significant buckling deformations
take place only after the shell has deformed plastically due to uniform
radial motion, unloaded elastically during buckling, and then deformed
again plastically. This type of behavior is beyond the scope of the
tangent-modulus model. Because it is relatively complex and serves
mainly to support the general character of the critical curves from
the simpler models, analysis of the strain-reversal model is deferred
to Section 8.8.

For asymmetric loads in all three models, the circumferential membrane stress is found from the motion of the hoop (n = 0) mode, with the shell taken to be under an "equivalent" uniform pressure. For the tangent-modulus and the strain-reversal models, the equivalent pressure is taken as the peak pressure of the actual load since the buckle wavelength is short compared to the circumference. Payton [24] demonstrated that this gives a reasonable approximation for impulsive elastic response, and experiments show that it is also reasonable for impulsive plastic response. This is demonstrated in Fig. 8.4, which shows that shells buckled plastically from a uniform

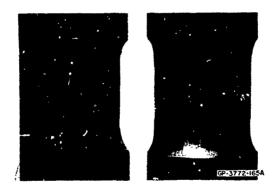


FIG. 8.4 COMPARISON OF BUCKLING OF CYLINDRICAL SHELLS WITH FIXED ENDS BY AN IMPULSIVE LOAD OF COSINE DISTRIBUTION (left) AND OF UNIFORM DISTRIBUTION (right). Cylinders are 3 inches in diameter made of 6061-T6 aluminum with L/D=1, a/h=24. Peak impulse = 10^4 taps for both cylinders (1 tap = 1 dyne-sec/cm²)

impulse and from an asymmetric impulse of the same peak value exhibit the same buckling in the area of the peak load. For the elastic model, the equivalent pressure is taken as an average pressure over a buckle half-wavelength in the area of the peak load. This pressure is only slightly less than the peak pressure and, in the static case, Almroth's results [29] show that this procedure gives a reasonable estimate of the buckling pressure.

8.3 Equations of Motion

8.3.1 Tangent-Modulus Model

The notation adopted is indicated in Fig. 8.5. Displacements are assumed to consist of a uniform radial displacement plus inextensional flexural deformations consisting of oath radial and tangential displacements. The assumption of inextensional flexural deformations is valid if the wavelengths of the flexural modes are large in comparison with the shell thickness [30].

As indicated in Figs. 8.5 and 8.6, $w^*(\theta,t)$ represents the inward radial displacement from a perfectly circular form. It is convenient to express this as the sum of two displacements, the initial

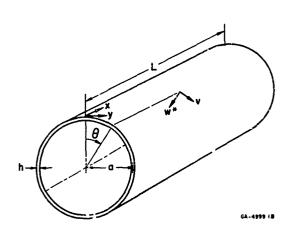


FIG. 8.5 COORDINATES AND SHELL NOMENCLATURE

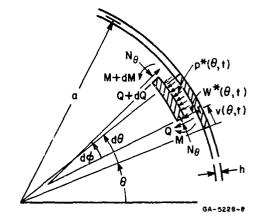


FIG. 9.6 FORCES ON SHELL ELEMENT

unstressed deformation of the shell $w_i(\theta)$, and the additional displacement during the shell motion $w(\theta, t)$ so that

$$w^*(\theta, t) = w_i(\theta) + w(\theta, t)$$
 (8.1)

The curvature change of the shell from the initial unstressed position is denoted by $\kappa(\theta,t)$ and is given to terms of first order by

$$\kappa(\theta, t) = \frac{1}{a^2} \left(\frac{\partial^2 w}{\partial \theta^2} + w \right)$$
 (8.2)

where a is the radius of the shell. Similarly, $\chi^*(\theta,t)$ is taken as the curvature change from a perfectly circular shape,

$$\kappa^*(\theta, t) = \frac{1}{a^2} \left(\frac{\partial^2 w^*}{\partial \theta^2} + w^* \right)$$
(8.3)

From the definition of curvature as rotation per unit arc length, the angle $d\Phi$ in Fig. 8.6 is given by

$$d\Phi = d\theta + n * ad\theta$$

or

$$\frac{1}{a} \frac{\partial \Phi}{\partial \theta} = \frac{1}{a} + \kappa^* \tag{8.4}$$

Dynamic equilibrium in the radial direction requires that, for a unit axial length of the shell,

$$-\frac{1}{a}\frac{\partial Q}{\partial \theta} - \frac{N_{\theta}}{a}\frac{\partial \Phi}{\partial \theta} + p^* - \rho h \frac{\partial^2 w}{\partial t^2} = 0$$
 (8.5)

where $N_{\theta}(\theta,t)$ is the membrane force, $Q(\theta,t)$ is the shear force per unit length, and $p^*(\theta,t)$ is the external pressure, positive as shown

in Fig. 8.6. Also, p is the shell density, h the shell thickness, and t the time. Neglecting rotary inertia, moment equilibrium of the shell element gives

$$Q - \frac{1}{a} \frac{\partial M}{\partial \theta} = 0 ag{8.6}$$

where $M = M(\theta, t)$ is the moment per unit axial length of the shell.

Eliminating Φ and Q in (8.5) yields the governing equation of motion in terms of the forces in the shell

$$\frac{1}{a^2} \frac{\partial^2 M}{\partial \theta^2} + \frac{N_{\theta}}{a^2} \left[a + \left(\frac{\partial^2}{\partial \theta^2} + 1 \right) \left(w + w_i \right) \right] - p^* + \rho h \frac{\partial^2 w}{\partial t^2} = 0 \quad (8.7)$$

For the tangent-modulus model, the stress differential across a section is governed by the tangent modulus E_t at the average circumferential hoop strain e_c . The moment-curvature relation is then

$$M(\theta, t) = \frac{E_t}{1 - v^2} \chi I$$
, $I = \frac{h^3}{12}$ (8.8)

For strains above the elastic limit of the material, the value of Poisson's ratio ν is not precisely known. However, the effect of ν is known to be small and the properties of the materials are not known to an accuracy that would make further investigation of its effect of any real value. Hence, it will be retained as shown so that (8.8) is consistent in the elastic range.

Substituting (8.8) into (8.7) and using (8.2) gives

$$\frac{E_t^I}{a^4(1-v)}\left(\frac{\partial^2 w}{\partial \theta^4} + \frac{\partial^2 w}{\partial \theta^2}\right) + \frac{N_\theta}{a^2}\left[a + \left(\frac{\partial^2}{\partial \theta^2} + 1\right)(w + w_i)\right] - p^* + \rho h \frac{\partial^2 w}{\partial t^2} = 0 \quad (8.9)$$

TO TO LEER LOOK TO THE WORK THE WAR THE WAR TO SEE THE WORK THE WO

It is convenient to introduce the constants

$$\alpha^2 = \frac{h^2}{12a^2}$$
 , $c^2 = \frac{E}{\rho(1-v^2)}$ (8.10)

and dimensionless forms of the displacement and time variables

$$u = \frac{w}{a}$$
, $u_i = \frac{w_i}{a}$, $\tau = \frac{ct}{a}$ (8.11)

Also, we define

$$\sigma_{\theta} = \frac{N_{\theta}}{h}$$
, $p(\theta, \tau) = p^*(\theta, \tau) \frac{a(1-\sqrt{2})}{hE}$ (8.12)

where σ_{θ} is the average circumferential stress and $p(\theta, \tau)$ a dimensionless pressure function. Inserting these last three equations into (8.9) yields

$$\frac{\partial^{2} \mathbf{u}}{\partial \tau^{2}} + \frac{\alpha^{2} \mathbf{E}_{t}}{\mathbf{E}} \frac{\partial^{4} \mathbf{u}}{\partial \theta^{4}} + \left(\frac{\alpha^{2} \mathbf{E}_{t}}{\mathbf{E}} + \frac{\sigma_{3}(1 - v^{2})}{\mathbf{E}}\right) \frac{\partial^{2} \mathbf{u}}{\partial \theta^{2}}$$

$$+ \frac{\sigma_{\theta}(1 - v^{2})}{\mathbf{E}} (1 + \mathbf{u}) = \mathbf{p} - \frac{\sigma_{\theta}(1 - v^{2})}{\mathbf{E}} (\mathbf{u}_{i} + \frac{\partial^{2} \mathbf{u}_{i}}{\partial \theta^{2}})$$

$$(8.13)$$

It remains to obtain a relation between $\,\sigma_{\theta}^{}\,$ and $\,u\,$ so as to eliminate $\,\sigma_{\theta}^{}\,$ from (8.13).

Because of the original assumption of inextensional flexural deformations, the effect of flexural modes on the average circumferential strain is restricted to second order terms [30]. Therefore if the radial deformation $u(\theta, \tau)$ is expressed in the series form

$$u(\theta, \tau) = u_0(\tau) + \sum_{n=1}^{\infty} u_n(\tau) \cos n\theta$$
 (8.14)

to first order accuracy the hoop membrane strain will be a function

of u only and is given by

$$\epsilon_{O}(\tau) = u_{O}(\tau)$$
 (8.15)

The series (8.14) contains only cosine terms since it will be assumed for simplicity that the initial imperfection and the pressure are symmetrical about $\theta = 0$. Thus writing these in a similar form, they are represented by

$$u_{i}(\theta) = \sum_{n=1}^{\infty} \delta_{n} \cos n\theta ,$$

$$p(\theta, \tau) = p_{o}(\tau) + \sum_{n=1}^{\infty} p_{n}(\tau) \cos n\theta$$
(8.16)

Substituting these three series into (8.13) yields

$$\begin{bmatrix} \ddot{u}_{o} + \frac{\sigma_{\theta}(1-v^{2})}{E} & (1+u_{o}) - p_{o} \end{bmatrix}$$

$$+ \sum_{n=1}^{\infty} \begin{bmatrix} \ddot{u}_{n} + (n^{2}-1) \left(n^{2}\alpha^{2} \frac{E_{t}}{E} - \frac{\sigma_{\theta}(1-v^{2})}{E}\right) u_{n} - p_{n} - \frac{\sigma_{\theta}(1-v^{2})}{E} (n^{2}-1)\delta_{n} \end{bmatrix} \cos n\theta = 0$$
(8.17)

where

$$(,) = \frac{91}{9} ()$$

Since ϵ_0 , and thus σ_θ , is assumed to be independent of θ , each expression in square brackets must vanish because of the orthogonality of the cosine functions; therefore

$$\ddot{u}_{o} + \frac{\sigma_{\theta}(1 - v^{2})}{E} (1 + u_{o}) = p_{o}$$
 (8.18)

and

$$\ddot{u}_{n} + (n^{2}-1) \left(n^{2} \frac{\alpha^{2} E_{t}}{E} - \frac{\sigma_{\theta}(1-v^{2})}{E}\right) u_{n} = p_{n} + (n^{2}-1) \frac{\sigma_{\theta}(1-v^{2})}{E} \delta_{n}$$
(8.19)

Since u_o is the average circumferential hoop strain, it is negligible compared to unity and (8.18) reduces to the linear equation

$$\ddot{u}_{o} + \frac{\sigma_{\theta} (1 - v^{2})}{E} = p_{o}$$
 (8.20)

For a shell initially at rest in an unstressed position, the initial conditions are

$$u_n(0) = \dot{u}_n(0) = 0$$
, $n = 0, 1, 2, ...$ (8.21)

For impulsive loads the pressure terms on the right-hand side of (8.19) and (8.20) vanish, but the initial conditions become

$$u_n(0) = 0$$
 $\dot{u}_n(0) = \frac{I_n}{\rho hc}$, $n = 0, 1, 2, ...$ (8.22)

where

$$I(\theta) = I_0 + \sum_{n=1}^{\infty} I_n \cos n\theta$$
 (8.23)

is the impulse applied to the shell.

To determine the motion in the radial mode, the stressstrain curve will be approximated by two straight lines as shown by the dashed lines in Fig. 8.7. This is a reasonable simplification since the

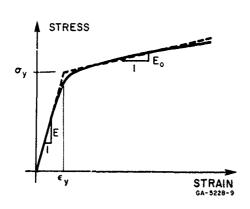


FIG. 8.7 IDEALIZED STRESS-STRAIN RELATION

radial motion is a function of the hoop stress, and this is not significantly different for the actual and approximate curves.

The motion of the flexural modes, however, is strongly dependent upon the slope of the stress-strain curve and is not represented to the same accuracy by the straight lines; thus in (8.19) a continuously changing tangent modulus will be used.

As shown in Fig. 8.7, we take σ_y and ε_y as the yield stress and yield strain in a uniaxial stress field, and Ξ_0 as the stress-strain modulus beyond the yield point. Then the stress σ_{θ} is given by

$$\sigma_{\theta} = \frac{E}{1 - v^{2}} u_{o} , \qquad 0 \le u_{o} \le (1 - v^{2}) \varepsilon_{y}$$

$$\sigma_{\theta} = \sigma_{y} + \frac{E_{o}}{1 - v^{2}} [u_{o} - (1 - v^{2}) \varepsilon_{y}] , \qquad (1 - v^{2}) \varepsilon_{y} \le u_{o}$$

$$(8.24)$$

where it is assumed that the membrane deformation occurs in plane strain.

Substituting (8.24) into (8.20) yields the following equation for $\,\mathbf{u}_{_{\mathrm{O}}}$

$$\ddot{u}_{o} + u_{o} = p_{o} , \qquad 0 \le u_{o} \le (1 - v^{2}) \varepsilon_{y}$$

$$\ddot{u}_{o} + \frac{E_{o}}{E} u_{o} = -\left[1 - \frac{E_{o}}{E} (1 - v^{2})\right] \varepsilon_{y} + p_{o} , u_{o} > (1 - v^{2}) \varepsilon_{y}$$
(8.25)

For triangular or exponential pressure pulses of interest, (8.25) is easily solved. Then with u_0 known, σ_θ and E_t can be evaluated as functions of time and inserted into (8.19) to determine the motion of the flexural modes. Unfortunately, the coefficients in (8.19) are then time dependent and there is no clear analytical solution. Thus, the equations for the flexural modes will be integrated numerically. However, to determine the character of the flexural motion, σ_θ and E_t can be assumed constant, which allows an analytical solution to be found. This is done in Section 8.4.

Aller Carried Park

8.3.2 Elastic Model

The governing equations of motion for the elastic model will use the well known Donnell equations [31] with the addition of inertia terms. As is done in the static buckling analysis of cylindrical shells, which agrees well with experiments, the uniform radial deformation is assumed independent of the length and end conditions, but it is required that the superimposed flexural deformations satisfy the end constraints. This assumption allows the equation of motion to be separated into individual uncoupled equations for each mode.

The equation of equilibrium in the radial direction

is

$$D\nabla^{4}w + N_{x} \frac{\partial^{2}}{\partial x^{2}} (w + wi) + \frac{2N_{x\theta}}{a} \frac{\partial^{2}}{\partial x \partial \theta} (w + wi) + \frac{N_{\theta}}{a^{2}} \frac{\partial^{2}}{\partial \theta^{2}} (w + wi)$$

$$(8.26)$$

where N_x , $N_{x\theta}$, N_{θ} are the membrane forces with the sign convention chosen so that compression is considered positive, D is the flexural rigidity of the shell wall, and ∇^2 the Laplacian operator:

$$D = \frac{Eh^3}{12(1-v^2)}$$
, $\nabla^2 = \frac{\partial^2}{\partial x^2} + \frac{\partial^2}{a^2\partial\theta^2}$.

The force $\,N_{\,\theta}\,$ is taken as the sum of two parts, one caused by the uniform radial deformation and the other caused by flexural deformations; thus

$$N_{\theta} = \frac{Eh}{1-v^2} \frac{w_0}{a} + \frac{\partial^2 F}{\partial x^2}$$
 (8.27)

where F is a stress function for the membrane forces produced by flexural deformations, and $w_{_{\rm O}}$ represents the uniform radial deformation. The membrane forces $N_{_{\rm X}}$ and $N_{_{{\rm X}}\theta}$ are assumed to be

independent of any uniform radial motion, and for the flexural motion are given in the usual manner in terms of F,

The compatibility condition between the midsurface strains then requires that

$$\nabla^4 \mathbf{F} = \frac{\mathbf{Eh}}{\mathbf{a}} \frac{\partial^2 \mathbf{w}}{\partial \mathbf{x}^2} \tag{8.29}$$

The use of a stress function in the manner shown satisfies static equilibrium in the x and y directions (Fig. 8.5), but neglects the small in-plane inertia forces.

It is convenient to introduce the nondimensional variables

$$\xi = \frac{x}{a}$$
, $u = \frac{w}{a}$, $u_i = \frac{w_i}{a}$, $\ell = \frac{L}{a}$, $\tau = \frac{ct}{a}$ (8.30)

and express u, u_i , and p in the series forms

$$u(\xi, \theta, \tau) = u_0(\tau) + \sum_{n=1}^{\infty} u_n(\tau) \cos n\theta \sin \frac{\pi\xi}{\ell}$$
 (8.31)

$$\mathbf{u_i}(\xi, \theta) = \sum_{n=1}^{\infty} \delta_n \cos n\theta \sin \frac{\pi \xi}{\ell}$$
 (8.32)

$$p^{*}(\xi, \theta, \tau) = \frac{Eh}{a(1-v^{2})} \left[p_{O}(\tau) + \sum p_{n}(\tau) \cos n\theta \sin \frac{\pi\xi}{\ell} \right]$$
 (8.33)

Representing the radial deformation by (8.31) assumes simple support conditions for the flexural motion, as well as restricting the deformation to a half-wave in the axial direction. This later assumption is made on the basis of experience with static buckling and experimental results of dynamic buckling. Although the assumption of simple supports is not representative of the actual test conditions

in the present program, experiments show that the buckling load is not very dependent on the type of support. Since simple supports are the easiest to handle analytically, they are used here exclusively. To comply with the assumed form of the displacement, the initial imperfections and the nonuniform portion of the pressure are also taken to vary sinusoidally in the axial direction.

Using (8.30) and (8.31) in (3.29) yields

$$\frac{1}{a^4} \left(\frac{\partial^2}{\partial \xi^2} + \frac{\partial^2}{\partial \theta^2} \right)^2 F = -\frac{Eh}{a^2} \sum_{n=1}^{\infty} \frac{\tau^2}{\ell^2} u_n \cos n\theta \sin \frac{\pi \xi}{\ell}$$

from which it can be concluded that, for simple supports, F is of the form

$$F = \sum_{n=1}^{\infty} \alpha_n u_n \cos n\theta \sin \frac{\pi \xi}{\ell}$$
 (8.34)

where α_n are constants.

Using (8.27, 28, 30, 31, 32, and 33), taking F in the form of (8.34), and dropping all second order terms in u_n , the equilibrium equation (8.26) can be separated to give

$$\ddot{u}_{0} + u_{0} = p_{0}$$
 (8.35)

and

$$\ddot{\mathbf{u}}_{\mathbf{n}} + \left[\alpha^{2} (\mathbf{n}^{2} + \frac{\pi^{2}}{\ell^{2}})^{2} + \frac{(1 - \nu^{2})(\frac{\pi}{\ell})^{4}}{(\mathbf{n}^{2} + \frac{\pi^{2}}{\ell^{2}})^{2}} - \mathbf{n}^{2} \mathbf{u}_{0} \right] \mathbf{u}_{\mathbf{n}} = \mathbf{p}_{\mathbf{n}} + \mathbf{n}^{2} \mathbf{u}_{0} \delta_{\mathbf{n}}$$
(8.36)

n = 1, 2, 3...

The initial conditions are taken as

$$u_n(0) = \dot{u}_{0}(0) = 0$$
, $n = 0, 1, 2, ...$

Equation (8.35) can usually be solved analytically and the resulting expression for u_o substituted into (8.36), but as was the case for the tangent-modulus model, the resulting equations for the flexural modes must be integrated numerically since no analytical solution is apparent.

For the static case, in which all derivatives with respect to time vanish, (8.35) gives

$$u_o = p_o$$

Substituting this into (8.36) we have

$$u_{n} = \frac{p_{n} + n^{2}u_{o}\delta_{n}}{\alpha^{2}(n^{2} + \frac{\pi^{2}}{\ell^{2}})^{2} + \frac{(1 - v^{2})(\frac{\pi}{\ell})^{4}}{(n^{2} + \frac{\pi^{2}}{\ell^{2}})^{2}} - n^{2}p_{o}}$$

The buckling pressure is reached when the denominator vanishes and $u_n \to \infty$. This condition gives

$$(p_o)_{cr} = \frac{1}{n^2} \left[\alpha^2 (n^2 + \frac{\pi^2}{\ell^2})^2 + \frac{(1 - \nu^2)(\frac{\pi}{\ell})^4}{(n^2 + \frac{\pi^2}{\ell^2})^2} \right]$$

which defines a critical pressure for each mode number. This agrees with the result presented in [31] for laterally loaded, simply supported shells.

8.3.3 Generalized Forces from an Asymmetric Load

In Chapter 3 it was shown that the pressure from a lateral blast load can be approximated by

$$p(\theta, t) = (p_r - p_i) \cos^2 \theta + p_i$$
 $-\pi/2 \le \theta \le \pi/2$ (8.37)
= p_i $\pi/2 \le \theta \le 3\pi/2$

where p_r and p_i are reflected and incident pressures, both assumed to have the same functional dependence on time. Expanding (8.37) into the Fourier series

$$p(\theta, t) = p_0 + \sum_{n=1}^{\infty} p_n \cos n\theta$$

yields for the flexural modes

$$p_2 = \frac{1}{4} (p_r - p_i)$$
, $p_n = 0$ $n = 4, 6, 8...$

$$p_n = \frac{4}{\pi} (p_r - p_i) \frac{\frac{n+1}{2}}{n(n^2 - 4)}$$
 $n = 1, 3, 5...$
(8.38)

For simplicity in this chapter we take p_i = 0 , since in all the experiments p_i << p_r .

For an asymmetric load the membrane stress varies around the shell, but to find the buckling motion for a spatially varying membrane stress would be very cumbersome. Instead, we will use the equations already derived under the assumption of a uniform pressure, using an average pressure over a buckle half-wavelength in the area of the peak load where the buckling occurs. This pressure is

$$p = \frac{1}{2} (p_r + p_i) + \frac{1}{2} (p_r - p_i) \frac{\sin \pi/n}{\pi/n}$$
 (8.39)

where n is the critical flexural mode (found by iteration). Since only the u_0 membrane mode is used, the time variation of stress is also not exact, but the experiments in Chapter 9 show that the membrane oscillations are near the hoop mode frequency. Again, to reduce the number of parameters, we take $p_i = 0$.

8.4 Character of the Solutions

The governing equations of motion for the tangent-modulus and elastic models exhibit the same general features--that is, a single equation to determine the motion of the uniform hoop mode, and then for each flexural mode an equation that contains the hoop membrane force as a coefficient. The equations can be put in the form

$$\ddot{u}_{o} + \frac{N_{\theta}}{Eh} (1 - v^{2}) = p_{o}$$
 (8.40)

and

$$u_n^2 + (w_n^2 - \beta_n N_\theta) u_n = p_n + \beta_n N_\theta \delta_n$$
, (8.41)

where w_n are the (no-load) bending frequencies and β_n are constants.

The major feature of the solutions is that for a sufficiently large value of N_{θ} the coefficient of u_n in (8.41) becomes negative, and the solution becomes hyperbolic in character rather than oscillatory. Thus, for some modes the flexural deformations can grow to appreciable values. The general problem is to determine the pressure-impulse levels that cause a particular flexural mode or group of flexural modes to grow to a significant magnitude, as well as to determine the region of the pressure-impulse plane in which each of the idealized models is applicable.

8.4.1 Tangent-Modulus Model

The tangent-modulus model is applicable for impulsive loads, which in the limit are equivalent to an initial velocity. If the initial velocity is sufficiently high, the hoop stress developed in uniform radial motion will exceed the elastic limit and plastic flow will occur. During the inward motion the hoop force N_{θ} initially increases with deflection as indicated in Fig. 8.8, and is proportional to the elastic modulus. When the membrane strain reaches the yield strain,

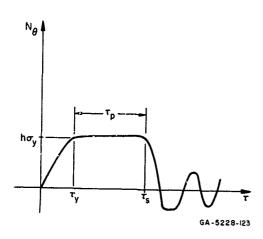


FIG. 8.8 TIME VARIATION OF HOOP MEMBRANE FORCE

 N_{θ} becomes nearly constant. When the inward motion ceases, the shell rebounds and N_{θ} decreases rapidly, being governed again by the elastic modulus. The subsequent radial motion, except for the first rebound, is elastic and sinusoidal as indicated in Fig. 8.8.

In Fig. 8.8, τ_y indicates the time of first yielding and τ_s the time at which the inward motion stops.

Between τ_y and τ_s the hoop strain is in the plastic range and resistance to bending is governed by the tangent

modulus. Since the tangent modulus is relatively low and the hoop force is a maximum, the major part of the flexural growth occurs during this period.

An approximate solution which indicates the controlling parameters and the character of the major part of the flexural motion is readily obtained for constant N_{θ} and E_{t} . Assuming that $\delta_{n}=0$, and that at $\tau=\tau_{y}$ flexural displacements are zero but flexural velocities are not, the solution of (8.19) yields

$$u_n(\tau) = \dot{u}_n(\tau_y) \frac{\sinh q_n(\tau - \tau_y)}{q_n}$$
 (8.42)

where

新の本語を言いている。 こう

$$q_n^2 = (n^2 - 1) \left(\frac{\sigma_\theta (1 - v^2)}{E_t} - n^2 \alpha^2 \right) \frac{E_t}{E}$$
 (8.43)

Figure 8.9 is a graph of the "amplification function,"

given by

$$\frac{\sinh q_n (\tau - \tau_y)}{q_n}$$

and shows that a band of flexural modes is highly amplified. The most amplified mode, at the peak of this curve, occurs at the maximum value of $\,\mathbf{q}_n$, which gives $\,n$ as the integer nearest to

$$n = \left(\frac{1}{2} \frac{\sigma_{\theta}(1-v^2)}{\alpha^2 E_t}\right)^{1/2} = \frac{a}{h} \left(\frac{6\sigma_{\theta}(1-v^2)}{E_t}\right)^{1/2}$$
 (8.44)

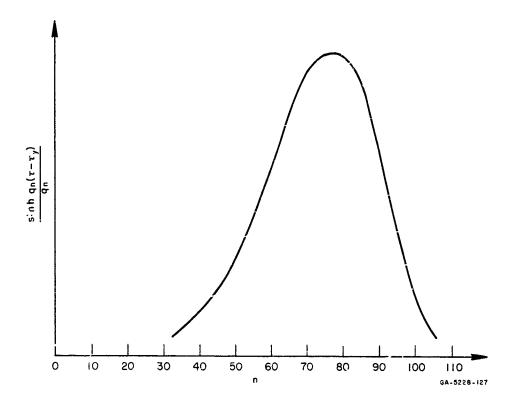


FIG. 8.9 AMPLIFICATION FUNCTION

Thus, the most amplified mode is directly proportional to a/h and to $\sqrt{\sigma_{\theta}/E_{t}}$. If σ_{θ}/E_{t} is known at $\tau = \tau_{s}$ then (c. 44) should give an upper bound on the most amplified mode. This appearance of a band of amplified modes is typical of buckling under both impulsive and quasi-impulsive loads and forms the basis of the buckling criteria discussed in the next section.

The magnitude and velocity of the flexural motion can be seen from (8.42) to be highly dependent upon the character of q_n . From (8.43) it is seen that the ratio σ_θ/E_t determines the sign of q_n^2 and hence determines whether the motion is hyperbolic or oscillatory in nature. Thus σ/E_t is the material property that determines the type of motion. A plot of σ/E_t is given in Fig. 8.10 for the materials of interest in this report. To determine E_t , σ_θ is found from Fig. 8.7 for each value of ε , and E_t is then determined from Fig. 8.10.

From Fig. 8.10 it is apparent that, at least in the first part of the plastic range, the σ/E_t curves can be approximated by an empirical relation ** of the form

$$\frac{\sigma}{E_t} = K(\varepsilon - \varepsilon_y)$$
 , $\varepsilon \ge \varepsilon_y$ (8.45)

Values of the material constant K in this formula and other material properties used throughout this chapter are given in Table 8.1.

^{*}Since E_t actually decreases during the inward motion, low order modes are the most highly amplified initially, but as the hoop strain increases higher order modes become dominant.

^{**} The accuracy of the stress-strain data does not warrant further refinement of this empirical expression.

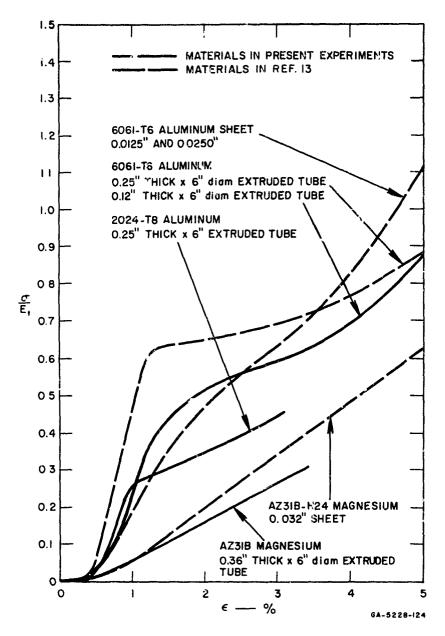


FIG. 8.10 $\sigma/\rm E_{t}$ vs. ϵ FOR MATERIALS IN EXPERIMENTS (Tensile Tests)

Table 8.1

MATERIAL PROPERTIES
(Tensile Test Data)

Material	E (psi)	σy (psi)	E _o /E	ν	к	ρ (lb/in ³)	
6061-T6 Al.* 2024-T8 Al. AZ31B Mag.	10×10^{6} 11×10^{6} 6×10^{6}		0.006 0.033 0.05	0.3 0.3 0.3	30 35 10	0.098 0.100 0.064	

E - modulus of elasticity

v - Poisson's ratio

K - constant associated with tanger t modulus [Eq. (8.45)]

o - density

8.4.2 Elastic Model

For the elastic model, $N_{\theta}(1-v^2)/Eh=u_{o}$ and the governing equations are

$$\ddot{u}_{o} + u_{o} = p_{o}$$
 (8.40)

$$\ddot{u}_n + n^2(\omega_n^2 - u_0)u_n = p_n + n^2u_0\delta_n$$
 (8.47)

where, from (8.36)

$$n^{2}\omega_{n}^{2} = \alpha^{2}(n^{2} + \frac{\pi^{2}}{\ell^{2}})^{2} + \frac{(1 - \nu^{2})(\frac{\pi}{\ell})^{4}}{(n^{2} + \frac{\pi^{2}}{\ell^{2}})^{2}}$$
(8.48)

^{*}Data received late in the program showed $\sigma_{\rm y} = 42,000$ and $E_{\rm O}/E = 0.033$ to give a better fit to the stress-strain curve. Using these values $I_{\rm O}$ was found to be lowered by approximately 5 percent.

When p is constant, the solution for u has the particularly simple form $u_0 = p_0 + A \cos \tau + B \sin \tau$, where A and B depend on the magnitude of p and the initial conditions existing at the time of application of the pressure. Substitution of this solution into (8.47) results in a Mathieu type of equation for u_n [30], and if taken at face value would predict instabilities at very low values of A and B. However, instabilities of this type require a continuous input of energy, and in this case the energy must come from the kinetic and strain energy of the uniform hoop mode. This type of instability is a resonance condition between a particular flexural mode or small group of flexural modes and the hoop mode; numerical integration in [30] of equations similar to (8.47) shows that it takes a large number of oscillations of the hoop mode before the flexural amplitudes build up so that there is an appreciable energy transfer from the hoop mode to the flexural mode. It is difficult to imagine how appreciable permanent plastic buckling deformations (the type of postbuckling response of interest here) can be produced by gradually increasing oscillations, since the available energy is small and would be extracted by small plastic deformations during each oscillation so that large deformations would never result. Experiments (see Chapter 9) show that buckling takes place with little or no oscillations and is essentially a single growth to large deformations. In the following analysis, only flexural modes with hyperbolic growth will be considered as significant for buckling.

A rough upper bound on the critical mode number for a given pressure can be calculated by taking the value of u_0 to be used in (8.47) to be the steady-state response to a step pressure pulse. Then $v_0 = p_0$, and the solution of (8.47) becomes

$$u_n = \frac{\dot{u}_n(0)}{n(p_0 - w_n^2)^{1/2}} \sinh[n(p_0 - w_n^2)^{1/2}], \text{ for } p_0 > w_n^2$$

The most amplified mode then corresponds to the value of n that makes $n^2(p_0-\omega_n^2)$ a maximum. This is given by the value of n that satisfies

$$2\alpha^{2} \left(n^{2} + \frac{\pi^{2}}{\ell^{2}}\right) - \frac{2(1 - v^{2})\left(\frac{\pi}{\ell}\right)^{4}}{\left(n^{2} + \frac{\pi^{2}}{\ell^{2}}\right)^{2}} = p_{o}$$

For most shells the second term may be neglected compared to the first. Then for $n>>\pi/\ell$, we obtain the approximate formula

$$n = \left(\frac{p_0}{2a^2}\right)^{1/2} = \left(6p^* \frac{1-v^2}{E}\right)^{1/2} \left(\frac{a}{h}\right)^{3/2}$$
 (8.49)

Results of numerical calculations given in Section 8.6 show that for peak pressures up to twice the static buckling pressure this formula is fairly accurate, but for higher pressures the critical modes from (8.49) are higher than those found from numerical integer ion.

8.4.3 Buckling Growth

These examples show that, for both the tangent-modulus and elastic models, at sufficiently high loads the flexural modes grow hyperbolically. At high pressures many modes grow, giving a band of amplified modes as demonstrated for the tangent-modulus model in Fig. 8.9. At pressures not far above the static buckling pressure, only a few modes grow hyperbolically. In either case, the mode or modes into which the shell buckles are those which exhibit the largest growth. In the following section we discuss the means by which this growth is initiated and the criteria to be used in estimating loads that produce growth large enough to give threshold permanent deformation.

8.5 Buckling Criteria

8.5.1 General Remarks

In the present problem buckling criteria are based on a growth in magnitude of the critical modes. This is in contrast to static buckling in which a sudden decrease in load-carrying capacity

or a large increase in deformation occurs at a critical load (eigenvalue), or to dynamic buckling of a spherical cap or arch in which snap-through occurs at a fairly well defined load.

As shown in the preceding section, if flexural motion is initiated a group of critical modes can quickly grow to large amplitudes. Flexural motion can be initiated by deterministic generalized forces resulting from an asymmetric load distribution (e.g., a cos eload over one side) or by random nonuniformities. The deterministic forces are found from a Fourier expansion of the given pressure distribution and, for the distributions of interest here, the amplitudes decrease with the cube of the wavenumber. Under quasi-static loads, the deterministic forces can be significant, since the wavenumbers of the critical modes are small. Hence in the elastic model, both deterministic forces and imperfections must be considered. If the wavenumbers of the critical modes are sufficiently high, the deterministic forces become so small than random imperfections dominate. This is the case for impulsive loads; hence only random imperfections are used in the tangent-modulus model.

8.5.2 Tangent-Modulus Model

For this model we assume that small-amplitude imperfections of all wavelengths are present and that the dominant modes will be selected by the amplification function [33]. It can be shown that effects of imperfections in shell shape are likely to dominate effects of imperfections in pressure distribution, so only amplification of imperfections in shell shape need be considered. Figure 8. Il shows the amplification of the most amplified mode as a function of ideal impulse for an aluminum cylinder (6061-T6) with a/h = 100. The amplification varies from 1000 to 10,000 for an impulse increase of only 12 percent. For a/h = 24 this same amplification variation occurs with a 15-percent increase in impulse, and for a/h = 250 with a 10-percent increase. For a maximum flexural displacement of 1 percent of the radius, which is easily observed, the corresponding amplitude of the nonuniformities for an

amplification of 1000 is 10⁻⁵ times the radius. For a cylinder with a/h = 100 this corresponds to 1/1000 of the wall thickness. In static buckling, assumed imperfections of 1/100 of the wall thickness give good agreement with experiments [28, p. 197]. The short-wavelength imperfections for dynamic buckling would be expected to be somewhat less; hence imperfections of 1/1000 in wall thickness are not unreasonable. On the basis of these results, for the tangent-modulus model the threshold impulse for buckling is taken as that which corresponds to an amplification of 1000.

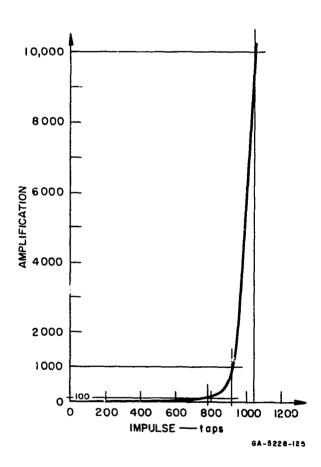


FIG. 8.11 AMPLIFICATION vs. IMPULSE (Ideal impulses applied to 6061-T6 aluminum shell, D = 6 inch, a/h = 100, L/D = 1)

8.5.3 Elastic Model

For this model the problems of a uniform pressure and an asymmetric pressure must be treated separately because the corresponding deterministic forces differ significantly. For a uniform pressure there are no deterministic forces for the flexural modes and the criterion stated for the tangent-modulus model is used. At essentially static loads a change in amplification from 1000 to 10,000 occurs for an arbitrarily small increase in pressure above the static buckling load. For finite pulse durations the change in amplification from 1000 to 10,000 corresponds to a small change in load as for the tangent-modulus model. This is indicated in Fig. 8.12 which shows that curves of constant amplification of 100, 1000, and 10,000 are reasonably close together over the entire load range for both the elastic model and the tangent-modulus model.

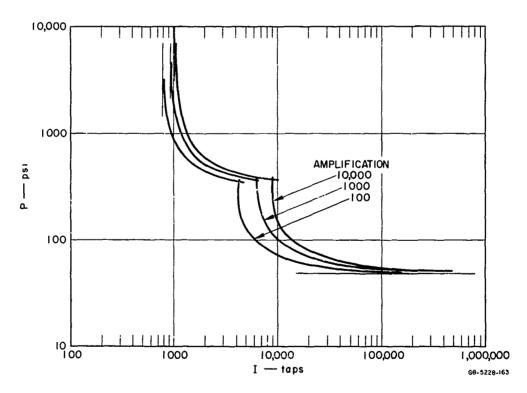


FIG. 8.12 COMPARISON OF CRITICAL PRESSURE-IMPULSE CURVES TO GIVE AMPLIFICATIONS OF 100, 1000, AND 10,000 (Exponential pulse, same shell as in Fig. 8.11)

For an asymmetric pressure generalized forces from the load must be considered in addition to random imperfections. Since the generalized forces are deterministic, the buckling criterion for this effect is based on flexural amplitudes that give a plastic bending strain. To compare this criterion with a constant amplification criterion, critical curves were calculated for amplifications of 100 and 1000 and plotted together with a critical curve based on plastic bending strains initiated by deterministic forces. These are given in Fig. 8.13 for L/D = 1 shells with a/h = 61 and a/h = 100. As already mentioned, for the high mode numbers of the tangent-modulus model, initiation from deterministic forces is negligible compared to that from imperfections, and no curves are given for deterministic forces in this region.

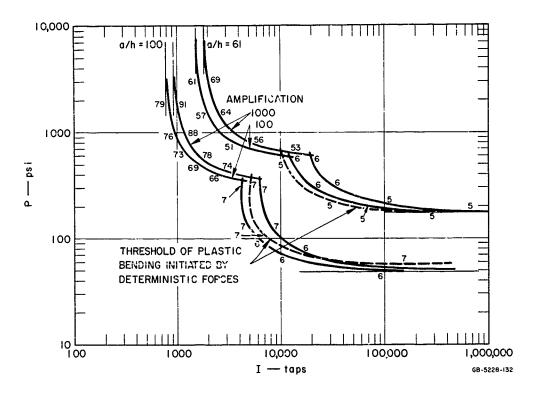


FIG. 8.13 COMPARISON OF CRITICAL PRESSURE-IMPULSE CURVES FOR CONSTANT AMPLIFICATION (Imperfection criterion) AND FOR PLASTIC BENDING THRESHOLD (from deterministic forces) (Exponential pulse, 6061-T6 aluminum shells, D = 6 inch, L/D = 1)

For quasi-impulsive loads on the elastic model at a/h = 100, the curve for deterministic forces falls between the curves for amplifications of 100 and 1000, while for a/h = 61 the curve for deterministic forces is below both the constant amplification curves. * In either case, however, the maximum difference between all the curves is about 60 percent, so that the differences in loads from the two buckling criteria are the same order of magnitude as differences caused by uncertainty in the magnitude of the imperfections. This supports the conclusion in Chapter 1 that details of the load distribution do not significantly affect failure loads.

3.5.4 Use of the Criteria in Determining Threshold Buckling Curves

The curves used in the discussion above are typical of the critical curves for buckling determined throughout the program. As mentioned, the upper branch of the curve comes from the tangent-modulus theory, and the lower branch from the elastic model. The curves are determined by numerical integration of the equations of motion given in Section 8.3, using buckling criteria given above.

For the tangent-modulus model, which is essentially impulse-sensitive, the computer input consisted of a pressure and two estimates of the impulse. The equations for the flexural modes were integrated using a Runge-Kutta approach and the maximum flexural growth was checked against the buckling criterion. If the criterion was not satisfied by one of the estimated values, a new value of the impulse was calculated based on the results of the previous two integrations, and the flexural motion was again calculated and checked.

The curves for a/h = 100 approach different asymptotes for large impulses because only odd modes are excited by a $\cos^2\theta$ distribution. In this region imperfections will dominate (because a very small pressure increment gives a very large increase in amplification) and the lower curves should be taken. For all of the examples to be given for $\cos^2\theta$ loading, the asymptote for imperfection buckling will be given in addition to the odd mode asymptote if there is a difference. This is not to be construed as suggesting that the dynamic buckling asymptote does not coincide with the static buckling pressure; it merely avoids the necessity of specifying when imperfections begin to dominate over deterministic forces.

This iterative procedure was repeated until the buckling criterion was satisfied to within an error of 5 percent. Usually one or two iterations were sufficient. The procedure used to calculate new values of the impulse in the iterative scheme was based on a semi-log interpolation of amplification factor versus impulse, which was found to be nearly linear over two or three decades of the amplification factor.

For the elastic model, the procedure was essentially the same except that input consisted of a pulse duration and two estimates of the critical pressure. The iterative scheme then varied the pressure at constant duration until the buckling criterion was satisfied. Pulse duration was held constant rather than pressure or impulse because the critical curves are pressure-sensitive for long durations and impulse-sensitive for short durations. Lines of constant pulse duration (at a slope of $+45^{\circ}$), however, in ersect the critical buckling curve at fairly large angles over the entired range of the elastic model.

8.6 <u>Critical Pressure-Impulso Curves for Buckling</u>

In this section the threshold buckling curves are described in more detail and the effects on these curves are given for variations in pulse shape, a/h, L/D, and material properties. Approximate formulas are given which can be used to generate curves for a wide range of parameters, and which make apparent the characteristic pulse durations for buckling.

8.6.1 General Description of Curves

The characteristic shape and regions of applicability of the tangent modulus and elastic models are indicated in Fig. 8.14.

This example is for a 6061-T6 aluminum shell with a/h = 100 subjected to a $\cos^2\theta$ load over one side with an exponential pulse shape. Unless otherwise noted, this example will be used as a basis of comparison throughout this section.

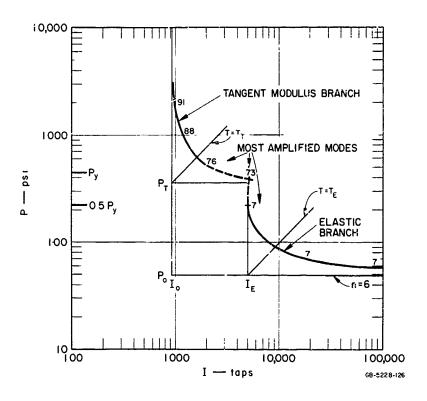


FIG. 8.14 TYPICAL THEORETICAL CRITICAL PRESSURE-IMPULSE CURVE FOR BUCKLING (Exponential pulse, $\cos^2\theta$ distribution, same shell as in Fig. 8.11)

The curve or branch from each model is hyperbolic in shape, with the tangent-modulus branch approaching asymptotes $I_{\rm o}$ and $P_{\rm T}$ and the elastic branch approaching asymptotes $I_{\rm E}$ and $P_{\rm o}$. The 45° lines labeled $T_{\rm T}$ and $T_{\rm E}$ define characteristic pulse durations for each branch. Approximate expressions for these quantities and the shape of the curves will be given after we have examined a few examples.

In the region of the cusp-like intersection between the two branches the assumptions used in each model are violated. This is indicated by using deshed curves near the cusp. For the tangent-modulus model, the assumption that buckling takes place during the initial inward motion is violated for impulses greater than about $2I_0$. For the elastic model the assumption of elastic response is violated for pressures larger than 0.5 Py because at these pressures the dynamic oversheat from the sude only applied load causes plastic hoop

strains. However, curves generated in this cusp region from the strain-reversal model, which overcomes these limitations, do not differ appreciably from the dashed curves shown. The strain-reversal model also gives a cusp shape and a discontinuity in mode number, but the mode numbers in the upper branch are about half those shown in Fig. 8.14 because strain reversal increases the effective modulus.

8.6.2 Effects of Parameter Variations

Effect of Pulse Shape. Figure 8.15 gives a comparison between critical curves calculated for exponential and triangular pulse shapes. The maximum difference between the curves (measured along a line at 45°) is 35 percent and occurs in the area of quasi-impulsive loads. This difference is not significant in many applications and we can conclude that changes in pulse shape are of secondary importance.

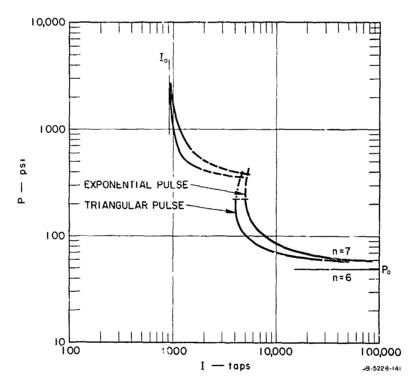


FIG. 8.15 EFFECT OF PULSE SHAPE ON CRITICAL CURVES FOR BUCKLING $(\cos^2\theta \text{ distribution, same shell as in Fig. 8.11})$

Effect of a/h. Figure 8.16 gives critical curves for L/D = 1 with a/h ranging from 24 to 250; each curve is normalized to I_o and P_o for the given a/h. The central effect of increasing a/h is an upward movement of the intersection between the tangent modulus and elastic branches, resulting in a broader range of quasi-impulsive response for the thinner (higher a/h) shells. These same curves are repeated in Fig. 8.17 without the normalization. In this plot the decrease in I_o as $(a/h)^{-3/2}$ and in P_o as $(a/h)^{-5/2}$, according to (8.50) and (8.53) given in the following discussion, is demonstrated.

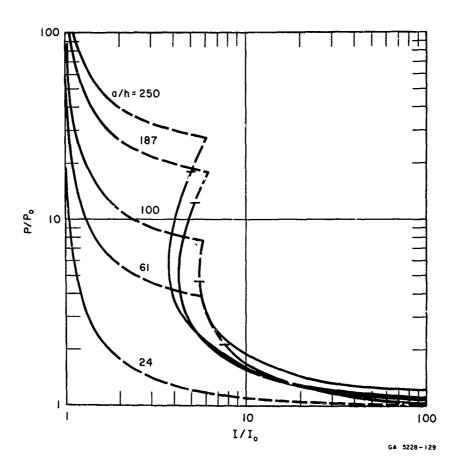


FIG. 8.16 EFFECT OF a/h ON CRITICAL CURVES FOR BUCKLING (Exponential pulse, $\cos^2\theta$ distribution; 6061—T6 aluminum, D = 6 inch, L/D = 1; curves normalized to P₀ and I₀ for each shell)

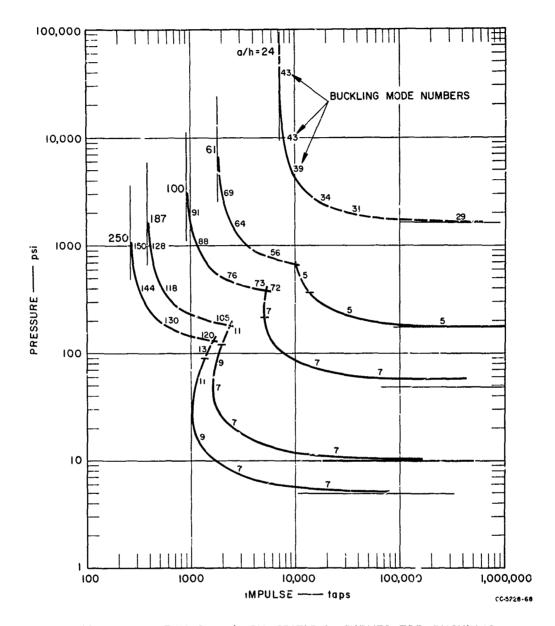
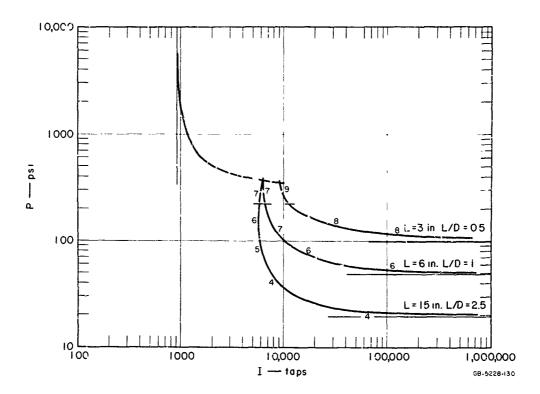


FIG. 8.17 EFFECT OF a/h ON CRITICAL CURVES FOR BUCKLING (Same as Fig. 8.16, but with no normalization)

Effect of L/D. Variations in L/D affect only the elastic branch, as shown in Fig. 8.18. Thus the main effect of increasing L/D is to lower the quasi-static pressure asymptote $P_{\rm o}$, giving a broader range of quasi-impulsive loads as for thin cylinders. The impulse "asymptote" $I_{\rm E}$ of the elastic branch does not change significantly because the mode numbers in this region are sufficiently high that end effects are secondary.



F.G. 8.18 EFFECT OF L/D ON CRITICAL CURVES FOR BUCKLING (Exponential pulse, uniform load, 6061-T6 aluminum shells, D = 6 inch, a/h = 100)

For these curves the load was taken as uniform around the circumference and the imperfection amplification buckling criterion was used to avoid questions of buckling criteria raised by the low mode numbers of the long cylinder.

Effect of Material Properties. A comparison among shells made from 2024-T8 aluminum, 6061-T6 aluminum, and AZ31B magnesium, all with L/D = 1 and a/h = 100, is given in Fig. 8.19. From the figure we see that the curves do not cross and are arranged in the order given above, with the 2024-T8 shell having buckling loads from 2 to 3 times the buckling loads for the AZ31B magnesium, depending on the duration of the load. A more meaningful comparison is given in Fig. 8.20; in this instance the wall thicknesses were adjusted to give equal weight shells. In this plot there is some crossing of the curves, but the overall result is that the AZ31B magnesium shell is strongest and the 6061-T6 shell is weakest. However, the maximum differences are only about 50 percent and would probably be masked by effects not considered here, such as postbuckling behavior and shear failure.

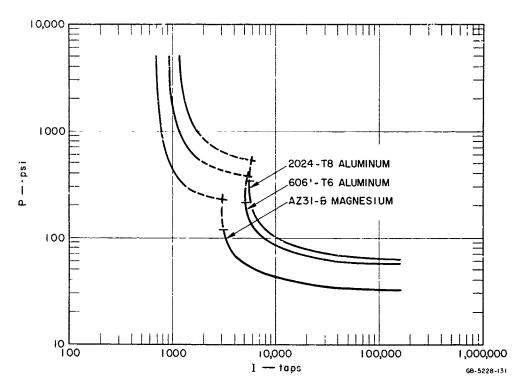


FIG. 8.19 EFFECT OF MATERIAL PROPERTIES ON CRITICAL CURVES FOR BUCKLING — SHELLS OF EQUAL SIZE (Exponential pulse, $\cos^2\theta$ distribution, D = 6 inch, a/h = 100, L/D = 1)

できています。 大い まくられ また またになる はなる またい こかけん はない あままり また 非常 はない ないない はない ないない ないない ないしゅうしゅう

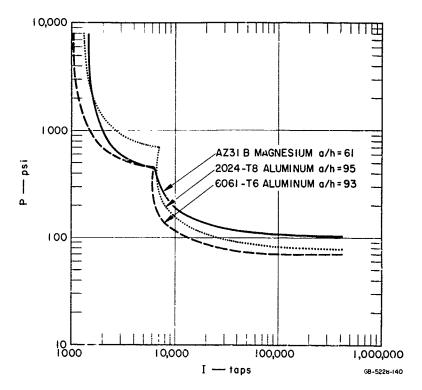


FIG. 3.20 EFFECT OF MATERIAL PROPERTIES ON CRITICAL CURVES FOR BUCKLING — SHELLS OF FQUAL WEIGHT (Same as Fig. 8.19, but a/h is adjusted to give shells of equal weight)

8.6.3 Approximate Formulas for Critical Curves for Buckling

In the tangent-modulus model, the vertical asymptote $I=I_{0}$ is the ideal impulse required to produce threshold buckling (i.e., an amplification of 1000). An approximate expression for I_{0} , derived in the next section, is

$$I_o = \left(\frac{95}{K}\right)^{1/4} \rho ca \epsilon_y^{1/2} \left(\frac{h}{a}\right)^{3/2}$$
 (8.50)

The extension of the tangent modulus curve beyond the cusp approaches a horizontal asymptote given approximately by

$$P_{T} = \frac{3}{4} P_{y}$$
 (8.51)

For the elastic model, the vertical asymptote (extended from the vertical tangent point) was found to be given approximately by

$$I_{\rm E} = 5 \, \rho \, {\rm ca} \, \left(\frac{h}{a}\right)^2$$
 (8.52)

The horizontal asymptote of the elastic model is given by the static uniform lateral buckling pressure P_o , which, from [21], is

$$P_o = 0.92 E \left(\frac{a}{L}\right) \left(\frac{h}{a}\right)^{5/2}$$
 (8.53)

For either the tangent modulus or elastic curves, to an accuracy consistent with the assumptions in the analysis, each branch may be represented by a simple hyperbolic-type curve of the form

$$(\frac{P}{P_A} - 1)(\frac{I}{I_A} - 1) = 1$$
 (8.54)

where P_A and I_A are the pressure and impulse asymptotes of each branch as given by the expressions above. For the examples studied, curves from these expressions lie within 20 percent of curves from numerical integration of the equations of motion.

8.6.4 Characteristic Pulse Durations

In addition to enabling one to quickly estimate critical curves for buckling of a wide variety of shells, the approximate formulas given here provide a convenient means for calculating characteristic load durations for buckling. Thus, one can quickly determine whether a given load on a given shell is impulsive, quasi-impulsive, or quasi-static.

This asymptote is not closely approached in Fig. 8.14 because only odd modes are excited by the $\cos^2\theta$ pressure in this example; imperfections would ultimately excite the even modes and give buckling at n = 6, but were unitted for simplicity (see Section 8.5).

The tangent modulus and elastic branches of the critical curves each have an associated characteristic time, as shown in Fig. 8.14 by the lines at 45° labeled T_{T} and T_{E} , respectively. These have been drawn assuming we are interested in exponential pulses for which T = I/P, where T is the time constant of the pulse as described in Section 8.1. Thus we define $T_{T} = I_{O}/P_{T}$ which, using (8.50) and (8.51), gives

$$T_T = \left(\frac{95}{K}\right)^{1/4} \frac{4a}{3c} \varepsilon_y^{-1/2} \left(\frac{h}{a}\right)^{1/2}$$
 (8.55a)

In the numerical examples it was found that variations in K moved the horizontal pressure asymptote slightly from the value given in (8.51) such that it compensates for the small variation of T_T with K as given in (8.55a). Thus, a better expression for T_T with K in the range 10 < K < 60 is simply

$$T_{T} = 2 \frac{a}{c} \epsilon_{y}^{-1/2} (\frac{h}{a})^{1/2}$$
 (8.55b)

Similarly, the characteristic time for the elastic model is defined as $T_E = I_E/P_O$ which using (8.52) and (8.53), gives

$$T_E = 5.5 \frac{a}{c} \left(\frac{L}{a}\right) \left(\frac{a}{h}\right)^{1/2}$$
 (8.56)

From Fig. 8.14 we see that if the time constant T of the applied pulse is much shorter than T_T , the load appears impulsive to the shell, and if T is much larger than T_E , the load appears quasi-static. Loads with durations near or between T_T and T_E are quasi-impulsive and both pressure and impulse are important to the response. As shells become longer and thinner T_T and T_E become more widely separated (see Figs. 8.16 - 8.18) and the range of quasi-impulsive loads increases. Conversely, for short, thick shells, the tangent modulus and elastic curves move closer together and only a small duration range is quasi-impulsive.

8.6.5 Shell Buckling Time

To assist in evaluating or simulating pressure pulses to be used in conjunction with the critical buckling curves, it is helpful to know the time at which the shell buckles. For the elastic model the numerical results showed that the maximum flexural growth occurred near the time when the pulse pressure had dropped to the static buckling pressure P_o , (i.e., t_e is found from $P(t_e) = P_o$).

The buckling time for the tangent-modulus model is taken as the duration of the initial inward motion of the hoop mode. For an ideal impulse this duration in real time is given approximately by

$$t_s = \frac{I_o a}{\sigma_y h}$$

in which for simplicity the material has been assumed to be rigid-plastic. Using the approximate formula (8.50) for I_0 , the buckling time is

$$t_s = (\frac{95}{K})^{1/4} (\frac{h}{\epsilon_v^a})^{1/2} \frac{a}{c}$$
 (8.57)

Numerical results show that for pulses of finite duration, the buckling time increases until at $I=2I_0$ it is about 1.8t_s. For longer loads the strain-reversal model must be used, but a rough estimate for buckling times in the region of the cusp can be made by interpolating between 1.8t_s and the elastic buckling time given above.

8.7 Derivation of an Approximate Expression for I

The estimate given for the impulse asymptote I_o of the tangent-modulus model is found by extending the arguments given in Section 8.4 on the character of the solution for impulsive loads. There it was shown that for impulsive loads the major part of the buckling takes place during plastic flow and that, if σ_θ and E_t are assumed constant,

the amplitude of the nth flexural mode is given by

$$u_{n}(\tau) = \dot{u}_{n}(0) \frac{\sinh q_{n} \tau}{q_{n}}$$
 (8.58)

This is the solution given in [11]. The most amplified mode is the one having the largest q_n which, using (8.43) and (8.44), gives

$$q_{n} = \frac{\sigma_{y}}{2E_{t}\alpha} \left(\frac{E_{t}}{E}\right)^{1/2}$$
 (8.59)

in which σ_θ has been replaced by σ_y in accordance with our original assumption, and ν^2 has been dropped compared to 1.

The magnitude of $u_n(\tau)$ depends mainly on the argument of the hyperbolic term since we are concerned with large amplifications in which exponential growth dominates. Thus, it is reasonable to assume that the buckling criterion of an amplification of 1000 corresponds closely to $q_n\tau$ reaching a critical value, i.e.,

$$q_{n} \int_{\text{max}} \tau_{s} = B$$
 (8.60)

where B is a constant to be determined and τ_s is the nondimensional duration of the inward membrane plastic flow. In real time, this duration is given by

$$t_{s} = \frac{I_{o}a}{\sigma_{v}h}$$
 (8.61)

in which the material has been assumed to be rigid-plastic. Using the definition $\tau = ct/a$ and combining (8.59), (8.60), and (8.61) results in the following expression for the critical impulse I

$$I_o = 2\alpha h (\rho \sigma_y)^{1/2} (\frac{E_t}{\sigma_y})^{1/2} B$$
 (8.62)

For a material in which E_t is nearly constant (8.62) suffices. However, for most materials E_t decreases significantly with increasing strain. As mentioned previously, measurements from post-yield tensile tests suggest that this decrease can be approximated by

$$\frac{\sigma}{\tilde{E}_{t}} = K(\varepsilon - \varepsilon_{y})$$
 (8.63)

where K is a material constant. This expression was used in the numerical integration, treating σ/E_t as a function of ε and hence of time τ . Since most of the amplification of u_n takes place near the end of the hoop mode motion (because σ/E_t is increasing) a reasonable approximation to the flexural motion can be found by assuming σ/E_t to be constant at its final value. With this assumption σ/E_t from (8.63) can be used in (8.62) to find I_o . To eliminate ε from the final expression for I_o , the relation between I_o and final strain ε_s must also be found. This is most easily done by equating the kinetic energy imparted by I_o to the strain energy absorbed in plastic work, which gives

$$I_o^2 = 2 \rho h^2 \int_0^{\varepsilon} \sigma(\varepsilon) d\varepsilon$$
 (8.64)

Taking the material to be elastic, perfectly plastic results in

$$I_o^2 = 2\rho h^2 \sigma_y (\varepsilon_s - \frac{\varepsilon_y}{2})$$
 (8.65)

To simplify the final expression for I_o we further assume that the final strain ε_s is large enough that we can take $\varepsilon_s - \varepsilon_y/2 \approx \varepsilon_s - \varepsilon_y$. With this approximation, (8.62), (8.63), and (8.65) yield the desired expression for critical impulse

$$I_o = \left(\frac{2}{3K}\right)^{1/4} B^{1/2} a(\rho \sigma_v)^{1/2} \left(\frac{h}{a}\right)^{3/2}$$
 (8.66)

TO SEE THE SECRETARY OF THE SECRETARY SECRETAR

Taking B = 7 gives Eq. (6.29) in [20]. To match the numerical integration to an amplification of 1000 here, we take B = 12 which gives

$$I_o = \left(\frac{95}{K}\right)^{1/4} a pc \epsilon_y^{1/2} \left(\frac{h}{a}\right)^{3/2}$$
 (8.67)

in which $(\rho\sigma_y)^{1/2}$ has been replaced by $\rho c\varepsilon_y^{1/2}$. Equation (8.67) agrees with the numerical integration of the complete equations of motion within 5 percent for 20 < a/h < 200 as shown in Fig. 5.1.

8.8 Strain-Reversal Model

8.8.1 General Remarks

The strain-reversal model to be described in this section predicts threshold buckling loads in the portion of the quasi-impulsive load region in which neither the tangent-modulus nor the elastic model is applicable (see Section 8.6). This is done by taking into account plastic strains beyond the valid range of the elastic model and allowing strain reversal and reloading which is beyond the valid range of the tangent-modulus model, which treats only the initial inward motion of the hoop mode. The central conclusion from the solutions using the strain-reversal model is that the curves established by the simpler models exhibit the essential characteristics found from the more complex theory.

The basic approach taken with the strain-reversa! model is to assume an infinite length cylinder under uniform load as was done with the tangent-modulus model, but instead of assuming that the flexural stresses are governed by the tangent modulus, the strain history

Results are also given for asymmetric loads using the procedures described for the elastic model, but for claring he analytical treatment described here is concentrated on symmetric loads.

throughout the cross-section is followed. The stresses are then evaluated from these strains, taking into account strain reversal, and the membrane force and flexural moment are determined. This procedure results in nonlinear equations which preclude superposition of flexural modes and also require that the magnitude of the imperfections be specified. These limitations require further comments on the buckling criteria discussed in Section 8.5. These comments are given in Section 8.8.3.

8.8.2 Equations of Motion

THE RESERVE TO SERVE
.

The equilibrium and kinematic relations for the tangent-modulus model (Eqs. 8.1 through 8.7) are also valid for the strain-reversal model, and the derivation of the equation of motion will proceed from this point. As mentioned, the main feature of the strain-reversal model is that the strain history is accounted for in determining the stress at a point, which allows us to follow elastic-plastic loading and unloading. To calculate the stress, the stress-strain relation for the material is assumed to follow a linear strain-hardening law and to behave the same in tension as in compression. Furthermore, unloading is assumed to occur with a modulus E until the unloading strain exceeds $2\varepsilon_y$, at which point it is associated with the modulus E_o . A typical loading-unloading-reloading cycle is shown by the arrows in Fig. 8.21.

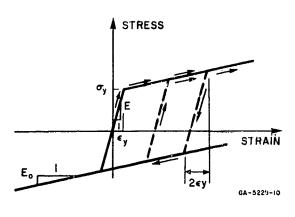


FIG. 8.21 IDEALIZED STRESS-STRAIN
RELATION FOR PLASTIC
LOADING AND UNLOADING

The strain-hardening modulus E_O is taken constant in order to examine the effects of strain reversal with a minimum of complication.

To completely describe the motion, including general elastic-plastic behavior as described, would require that the shell be broken up into small circumferential segments and that each segment in turn be decomposed into laminates in order to follow the

stress and strain history through the cross-section of the segment. This procedure has been used [34], but it requires very large computer storage and long computation times, particularly for the large number of segments required for the short wavelength buckling of interest here. Instead, it will be assumed that the motion of the shell consists of a uniform inward motion plus a flexural deformation in a single flexural mode. The variation in stress through the cross-section will be treated by dividing the shell thickness into laminates, but hoop force and bending moment will be characterized by their values at points of maximum curvature to avoid having to treat individual shell segments. This greatly reduces computational labor while still retaining the essential features of the elastic-plastic response.

The hoop force is treated as constant around the circumference, and the bending moment is assumed to vary sinusoidally, in phase with the sinusoidal flexural displacement. This allows the equation of motion to be separated into hoop and flexural equations containing only time derivatives.

The hoop force is assumed uniform since any deviation throughout a buckle wavelength is quickly adjusted by very small tangential displacements. Large plastic bending at the point of maximum curvature (interaction point) causes a reduction in normal force through the usual bending-normal force interaction, and results in unloading at sections away from the interaction point. Such unloading is elastic and can readily occur with a small strain increment, whereas loading at the interaction point could only occur with a large strain increment since it is governed mainly by the plastic modulus. Thus the magnitude of the hoop force is dictated by the value at the interaction point, and is calculated neglecting membrane strains caused by tangential displacements.

^{*}The method of selecting the flexural mode is discussed in Section 8.8.3.

The assumed sinusoidal variation of flexural displacement and bending moment, although not exact, is expected to give good
results because the displacements depend mainly on the moment at
maximum curvature; thus the exact distribution is of secondary importance. This assumption was confirmed in static plastic buckling of
columns, in which buckling loads from an assumed sinusoidal displacement and moment were in good agreement with a more exact analysis [28].

With these procedures in mind, the displacement from the unstressed position is expressed in dimensionless form by

$$u(\theta, \tau) = u_{\Omega}(\tau) + u_{n}(\tau) \cos n\theta \qquad (8.68)$$

Consistent with these displacements, the initial imporfections from the circular form are taken as

$$u_{i}(\theta) = \delta_{n} \cos n\theta$$
 (8.69)

the applied pressure is expressed by

CHARLES AND A COMPANY

$$p(\theta, \tau) = \frac{Eh}{(1 - v^2)a} [p_0(\tau) + p_n(\tau)\cos n\theta]$$
 (8.70)

and finally, the bending moment, under the preceding assumptions, is written

$$M(\theta, \tau) = M_n(\tau) \cos n\theta \qquad (8.71)$$

Using (8.68 - 8.71) in the equation of equilibrium (8.7), and remembering that we have assumed N_{θ} to be independent of θ , gives the following separated equations for u_0 and u_n :

gives the following separated equations for
$$u_0$$
 and u_n :
$$\ddot{u}_0 + \frac{N_\theta (1 - v^2)}{Eh} (1 + u_0) = p_0 \qquad (8.72)$$

$$\ddot{u}_{n} - \frac{(1 - v^{2})}{Eah} n^{2} M_{n} - \frac{N_{\theta}(1 - v^{2})}{Eh} (n^{2} - 1) u_{n} = p_{n} + \frac{N_{\theta}(1 - v^{2})}{Eh} (n^{2} - 1) \delta_{n}$$
(8.73)

To account for elastic-plastic loading and unloading, N_{θ} and M_{n} are calculated by dividing the cross-section into 2N

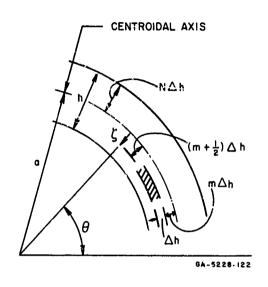


FIG. 8.22 NOTATION - LAMINATED SHELL

circular laminates as shown in Fig. 8.32, each of thickness Δh given by

$$\Delta h = \frac{h}{2N}$$
 (8.74)

Choosing m as the integer which locates the division lines, the center of each laminate is displaced from the shell midsurface by

$$\zeta = (m + \frac{1}{2}) \Delta h$$
 (8.75)

Denoting the circumferential stress in each laminate by

 $\sigma(m,\tau) = \sigma_{\theta}(\zeta,\tau)$, the resultant force and moment at the section are expressed by

$$N-1 \qquad N-1$$

$$N_{\theta}(\tau) = \sum_{m=-N} \sigma(m, \tau) \Delta h = \frac{h}{2N} \sum_{m=-N} \sigma(m, \tau) \qquad (8.76)$$

$$M_{n}(\tau) = \sum_{m=-N}^{N-1} \sigma(m, \tau) (m + \frac{1}{2}) \Delta h \cdot \Delta h = (\frac{h}{2N})^{2} \sum_{m=-N}^{N-1} \sigma(m, \tau) (m + \frac{1}{2}) (8.77)$$

The strain from the displacement given by (8.68), is

$$\varepsilon(\theta,\zeta,\tau) = u_0(\tau) - \frac{\zeta}{a} (n^2 - 1) u_n(\tau) \cos n\theta \qquad (8.78)$$

In calculating $\sigma(m, \tau)$, the strain is taken at the point of maximum curvature given by $\cos n\theta = 1$ which, with (8.75) yields

$$\varepsilon(m, \tau) = u_0(\tau) - \frac{1}{a}(m + \frac{1}{2}) \Delta h (n^2 - 1) u_n(\tau)$$
 (8.79)

and the stress-strain law is taken as described in Fig. 8.21.

The equations just described form a complete set which can be integrated numerically. Considering the shell initially at rest with no unstressed displacements other than those given by (8.69), the initial conditions are

$$u_{0}(0) = \dot{u}_{0}(0) = 0$$

$$u_{n}(0) = \dot{u}_{n}(0) = 0$$
(8.80)

At each time step the strain is determined from (8.79) for each laminate and is then compared with the strain at the previous time step to see if unloading or loading is taking place. Knowing the direction of loading and the previous stress, the current stress is calculated. The stress is then used in (8.76) and (8.77) to evaluate the hoop force and flexural moment, and these in turn are substituted into the differential equations (8.72) and (8.73). An Adams numerical integration scheme is then used to predict the values of u_0 and u_n at the next forward time step.

8.8.3 Buckling Criteria for Nonlinear Analysis

In the strain-reversal model the equations of motion are nonlinear and superposition of flexural modes must be abandoned. This requires that the buckling criteria as described in Section 8.5 must be interpreted in a slightly different manner. The implicit assumption throughout the linear theories (in both the tangent-modulus and elastic models) is that buckling is associated with the most amplified mode. In [33], this was demonstrated to be a reasonable procedure

by showing that, for a band of highly amplified modes such as those shown in Fig. 8.9, the mean wavelength resulting from superposition of random amplified harmonics is close to the most amplified wavelength. However, associating buckling with the most amplified mode can be interpreted in another manner which does not require superposition of flexural modes.

Rather than expressing the imperfections in a Fourier series taken over the whole circumference, it can be visualized that over each small segment of arc the imperfections can be associated with a discrete wavelength within the amplified band of the nonlinear theory. This wavelength will vary from segment to segment in a random manner, and with this interpretation the most amplified wavelength in the nonlinear amplification function determines which segments have the largest deformation; thus there is no requirement of superposition. This approach requires that there be many buckles around the circumference of varying wavelengths in the amplified band, both of which are observed experimentally (see Fig. 8.3). The net result for both the nonlinear and linear problems is similar, however, and the same buckling criterion is used in both cases. The essential difference in the two problems is that the amplification function in the nonlinear problem depends on the magnitude of the imperfections.

An alternate procedure in the nonlinear problem is to examine the amplified band during the early linear motion and then select only the most amplified mode at the time of first strain reversal to be used in the nonlinear theory. This alternate procedure has not been examined, but it is anticipated that it would give critical curves for buckling close to those from the procedure used here.

8.8.4 Numerical Results

Figure 8.23 gives critical curves for buckling from the strain-reversal model plotted together with corresponding curves from the tangent-modulus and elastic models. The strain-reversal model exhibits two branches, an upper branch close to the curve from the

tangent-modulus model and a lower branch close to the curve from the elastic model. Because of this behavior, the following discussion will be given in two parts, corresponding to the two branches. In both branches the curves are based on the buckling criteria described in Section 8.5. In the upper branch and in the lower branch labeled "axisymmetric load," the amplification criterion was used with assumed imperfections in each mode equal to 1/1000 of the wall thickness. In the lower branch labeled " $\cos^2\theta$ load" deterministic forces were used with no imperfections.

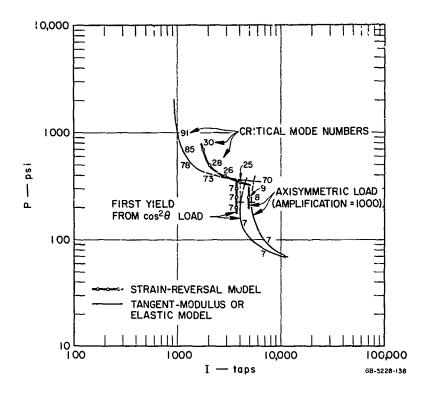


FIG. 8.23 THEORÉTICAL CRITICAL PRESSURE-IMPULSE CURVES FOR BUCKLING — COMPARISON OF STRAIN-REVERSAL MODEL WITH THE TANGENT-MODULUS AND ELASTIC MODELS (Triangular pulse, 6061-T6 aluminum shell, D = 6 inch, a/h = 100, L/D = 1)

The major conclusion from these results is that the location and shape of the critical curve in the region of the cusp is changed very little from that predicted by the simpler theories; a jump

in the critical mode number still exists, and associated with this jump is a cusp in the critical curve.

発表のできるからなることに、

Elastic-Type Response. For the deterministic load it is seen that at P = 200, which is in the valid region of the elastic model, there is a small difference between the critical load predicted by the two models. This difference is attributed to the neglect of end effects in the strain-reversal model, and the dotted curve represents the curve that would result if the support conditions were somehow accounted for. It is apparent that the error in neglecting the end conditions, although small, is larger than the error made by assuming only elastic action. This small change in load level (it is less than the variation between different buckling criteria) demonstrates that the buckling curve from the elastic theory is satisfactory even for loads with peak pressures somewhat larger than 0.5P_v.

Tangent-Modulus Type Response. As anticipated, the results of the numerical calculations for this type of response show that after strain reversal the bending resistance of the shell increases very significantly over that predicted by a tangent-modulus theory. This increase in bending resistance results in a decrease in critical mode numbers, and also accounts for the increase in the critical load at the higher pressures. Both effects are shown in Fig. 8.23.

Despite the increased bending resistance, at pressures below P = 400 psi the critical load falls below the tangent-modulus estimate. The load is lower for the strain-reversal model because at this pressure and pulse duration the maximum flexural motion occurred on the second inward movement of the hoop mode, not the first as is required for the tangent-modulus model. For pressures greater than 400 psi (impulses less than $2I_0$) buckling occurred during the first inward movement for either model, indicating that $I < 2I_0$ is the approximate range of validity of the tangent-modulus model.

As mentioned, these results are based on an initial imperfection of 1/1000 of the wall thickness for the strain-reversal model.

For this cylinder this corresponds to $\delta_n=10^{-5}$. To determine the influence of the magnitude of the initial imperfection on the critical load level, other values of δ_n (for P = 400 and n = 26) were used and the results are given in Fig. 8.24. The response is dependent on the magnitude of the imperfections, but, between initial imperfections of 1/100 and 1/1000 of the wall thickness ($\delta_n=10^{-4}$ and 10^{-5}), which are believed to be realistic values, the critical impulse varies by about 20 percent, which for many purposes is not significant.

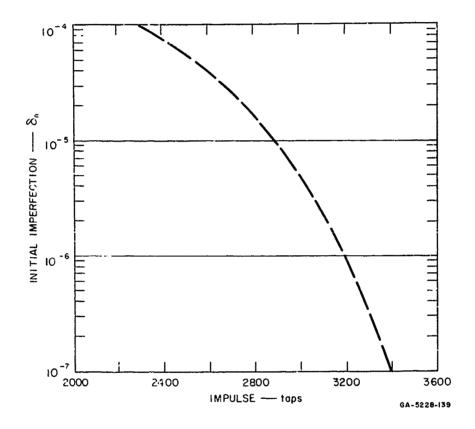


FIG. 8.24 EFFECT OF MAGNITUDE OF IMPERFECTION ON CRITICAL BUCKLING IMPULSE, P = 400 psi, CRITICAL MODE = 26 (same shell as in Fig. 8.23)

From these examples we can conclude that the main features of the critical buckling curves are not altered by the strain-reversal model, and that to within the accuracy of the buckling criteria the critical load levels are essentially unchanged. Also, since the

THE SERVICE OF THE SE

critical mode numbers are in better agreement with experiment than the tangent-modulus results, and since the theory better represents the actual stress conditions for large deformations, it may be profitable to investigate the strain-reversal model more fully.

9. TRANSIENT OBSERVATIONS OF SHELL RESPONSE FROM ELAST LOADS

Two special test series were conducted to provide data on shell response during the time of load application. In one series a Beckman-Whitley high-speed framing camera was used to photograph buckling shells, and in the other strain gages were used to observe details of the membrane and flexural response. The most significant observation from these experiments is that at load levels high enough to cause buckling, the dominant flexural motion is a continuous growth in one direction with no oscillations. The load level required to cause this buckling also agrees well with theory where comparison can be made.

9.1 Framing Camera Experiments

I

Photographs from three experiments are presented here, two on identical shells with a/h = 53 and one on a thinner shell with a/h = 250. For the thicker shells loads were produced with a small shock tube as shown in Fig. 9.1. The tube consisted of a 6-foot length of 1-foot diameter pipe, open at both ends and loaded with 2-foot lengths of primacord at one end. Since the primary purpose of the experiments was to observe the qualitative behavior of shell response, no pressure calibration of this system was made. However, pressures and impulses were estimated using data from the 2-foot shock tube.

The two shock tube experiments were at load levels that bracketed the response between just perceptible permanent deformation and a deformation sufficient to give a permanent buckling lobe typical

An attempt was made to photograph buckling from loads using HE spheres, which have been calibrated, but for these relatively thick shells the charge had to be placed so close to the model that smoke obscured the buckling.

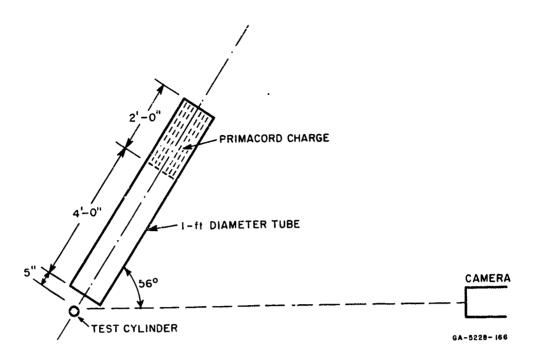


FIG. 9.1 SHOCK TUBE ARRANGEMENT FOR OBSERVING BUCKLING IN A SHELL WITH a/h = 53

of the photographs shown in Chapter 5. In both experiments the shells were made of 6061-T6 aluminum, 3 inches in diameter, with a/h = 53 and L/D = 1. Framing camera photographs are given in Figs. 9.2 and 9.3. The charge ratio in the shock tube in Fig. 9.2 was 0.5 and large elastic displacements resulted, as shown; however, terminal observation showed only a very small inward deformation under the peak load. In Fig. 9.3 the charge ratio was increased to 1.0 and the shell was permanently buckled, as shown in the last picture, which is a terminal photograph taken after the experiment. In both experiments the shell buckles monotonically inward with no oscillations.

To compare theory with experiment, pressures and impulses from the 6-foot shock tube were estimated using data from the 2-foot-diameter tube. Because of the shorter tube length, the pressure-impulse combinations available from the 6-foot tube fall to the left of those from the 2-foot-diameter tube at 10 feet (see Fig. 3.26). Also, since the tube is open at the driver end and the test model is located

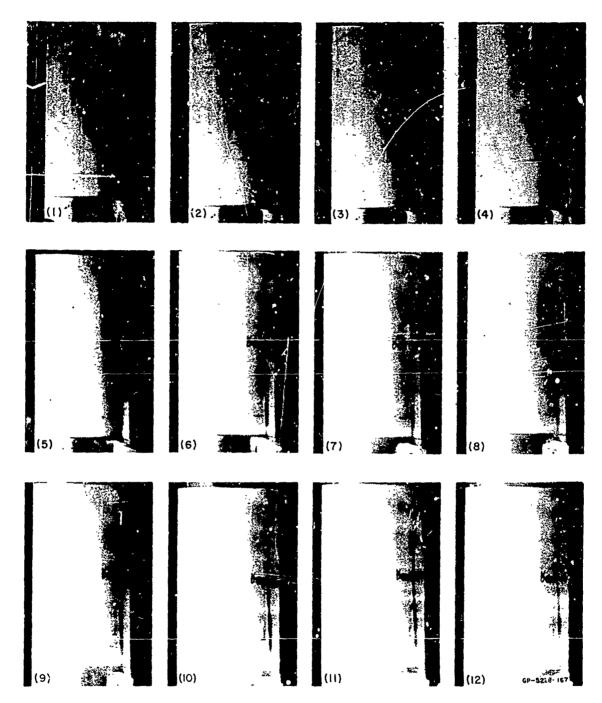
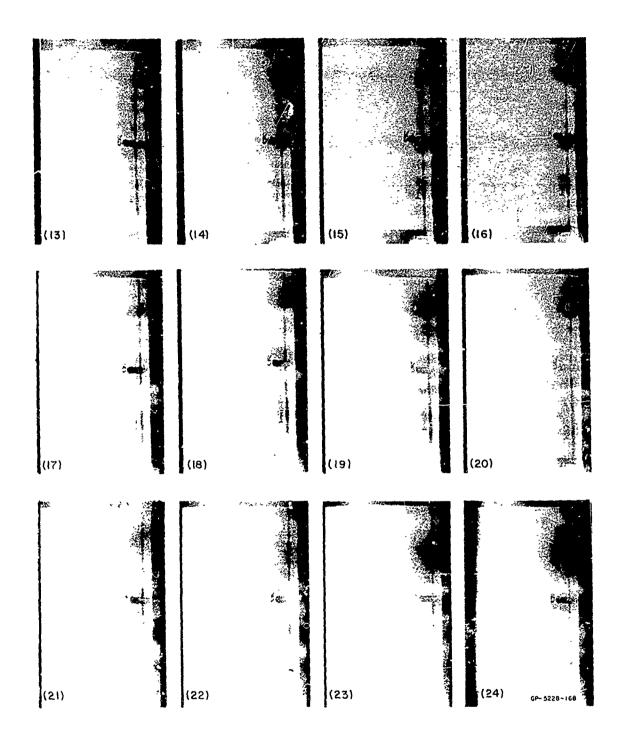


FIG. 9.2 FRAMING CAMERA PHOTOGRAPHS OF ELASTIC BUCKLING OF A SHELL WITH a/h = 53. (6061-T6 aluminum, D = 3 inc.h, L/D = 1; time between frames 41.7 μ sec, estimated load P = 350 psi, I = 14,000 taps)



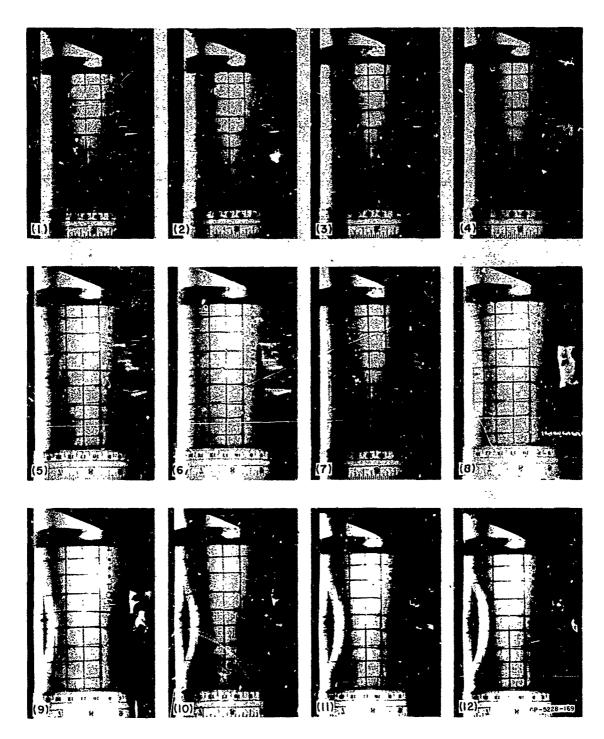
Souther as

The partitions

Streether, Cl

parameters a

FIG. 9.2 (Concluded)



神経の かんしゅう かんしゅう かんしゅう

FIG. 9.3 FRAMING CAMERA PHOTOGRAPHS OF ELASTIC-PLASTIC BUCKLING OF A SHELL WITH a/h=53. (same as in Fig. 9.2, except P ≈ 550 psi, I $\approx 21,000$ taps)

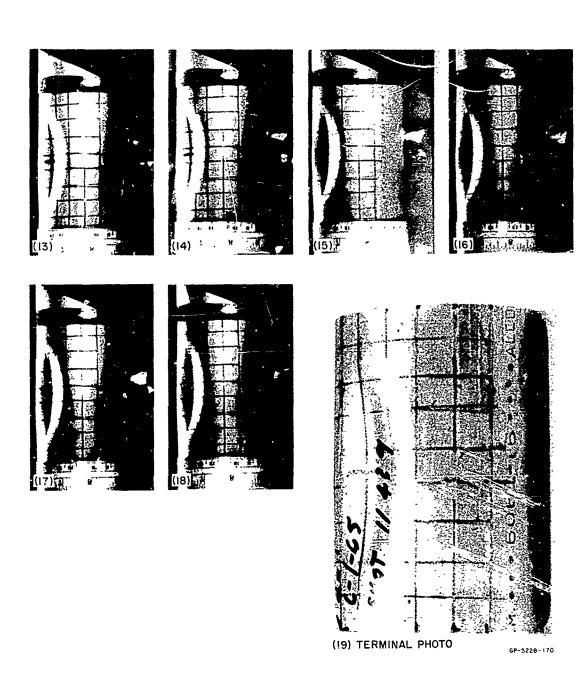


FIG. 9.3 (Concluded)

Annahama A

5 inches outside the end of the tube, the peak pressure for a given charge ratio will be less than in the other tubes. Using a linear variation in duration with tube length, the pressure-impulse combinations for the 6-foot tube were estimated by shifting the curve for the 2-foot-diameter tube at 10 feet to the left by 40 percent. From the shell response data of Table 4.1 it was concluded that permanent damage such as shown in Fig. 9.3 would be produced at a charge ratio of $\alpha = 0.6$ in the 2-foot-diameter tube at 10 feet. Since the charge ratio of the shot shown in Fig. 9.2 is one-half that of Fig. 9.3, it was assumed that a load giving similar deformation to that shown in Fig. 9.2 could be produced by $\alpha = 0.3$ in the 2-foot-diameter tube at 10 feet. The estimated pressure and impulse for the shot of Fig. 9.2 were then determined by starting at $\alpha = 0.3$ in the 2-foot-diameter tube at 10 feet, and paralleling the theoretical buckling curve for the small 40-percent shift to the P-I curve for the 6-foot tube. This gave P = 350 psi and I = 14,000 taps. For the shot of Fig. 9.3 the same procedure was used, starting at $\alpha = 0.6$ in the 2-foot-diameter tube and giving P = 550 psi and I = 2i,000 taps.

The response of the shell in Fig. 9.2 was calculated using the load of 350 psi and 14,000 taps and the theory in Chapter 8 for a $\cos^2\theta$ load over one side with an exponential pulse. These calculations gave a peak flexural deflection of 1.7 percent occurring 320 µsec after shock arrival. In Fig. 9.2 shock arrival is placed between frames 4 and 5 because in frame 4 there is no indication of movement and in frame 5 indication of smoke and movement of the rule can be seen. The maximum deflection occurs at frame 11, which at 47 µsec/frame gives a time increment of 280 µsec from shock arrival. This agrees within experimental accuracy with the calculated value of 320 µsec. The peak displacement in Fig. 9.2 is estimated to be about 5 percent of the radius, which is somewhat larger than the calculated value, but since the theoretical displacement grows exponentially with pressure, a slight increase in load level would bring the displacements into line. This agreement between theory and experiment demonstrates that the assumptions made in the theory are reasonable.

Color of the sales of the selection of t

In the more heavily loaded shell in Fig. 9.3, shock arrival is placed between frames 4 and 5 because some movement of the paper attached to the side of the shell can be seen in frame 6 (and taking into account the 40 μ sec for the shock front to traverse the shell radius). In this shell the growth of deformation is much more rapid, with large deformations appearing as early as frame 8, about 170 μ sec after shock arrival.

For the thinner shell it was possible to produce buckling with a blast wave from a spherical HE charge at a distance large enough that smoke did not obscure the experiment. A schematic of the shot arrangement is given in Fig. 9.4. The cylinder is 3 inches in diameter, made from 6061-T6 aluminum with a/h = 250 and L/D = 1, and it is

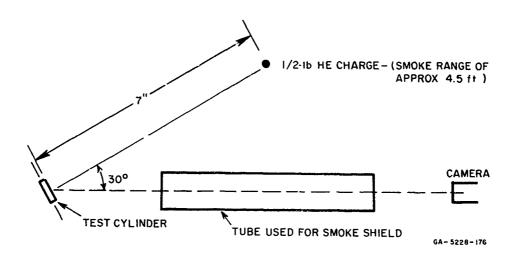
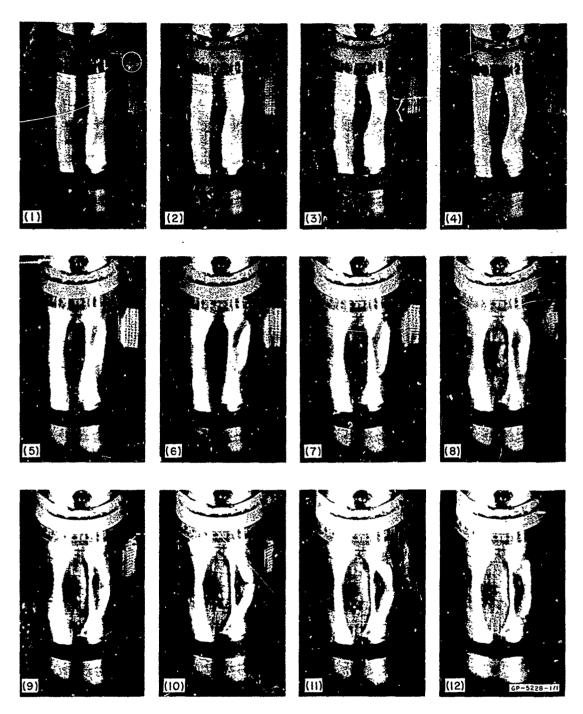


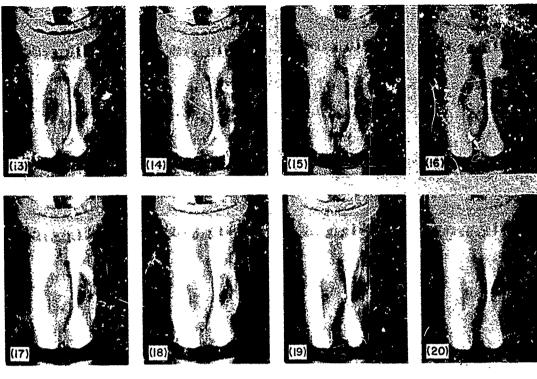
FIG. 9.4 EXPLOSIVE SPHERE ARRANGEMENT FOR OBSERVING BUCKLING IN A SHELL WITH a/h = 250

placed 7 feet from a 0.5-pound charge. The resulting load is in the lower portion of the quasi-impulsive range, and produced very large buckling displacements, as shown in Fig. 9.5. In the early part of the motion, in frames 3 and 4, relatively small wavelength buckles



一個ないのでは、このでは、これである。これに

FIG. 9.5 FRAMING CAMERA PHOTOGRAPHS OF ELASTIC-PLASTIC BUCKLING OF A SHELL WITH a/h=250 (6061-T6 aluminum, D = 3 inch, L/D = 1; time between frames 41.7 μ sec; P = 25 psi, I = 500 taps)



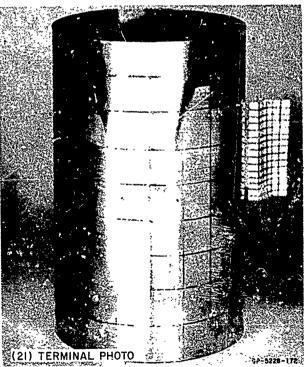


FIG. 9.5 (Concluded)

appear, having lengths of about 3/4 inch. ** Later, the wavelengths increase and by frame 6 are about 1 inch. These remain throughout the subsequent motion. A 1-inch wavelength corresponds to a mode number of 9, which is the critical mode number predicted by the theory for this shell and loading condition. The observed increase in wavelength with time is characteristic of this type of dynamic buckling and is predicted by the theory. It is caused by the decaying pressure which results in longer wavelengths being the most highly amplified as time increases.

This experiment also illustrates that very large deformations are necessary to produce permanent deformations in a thin shell. This is seen by comparing the large inward deformations in the transient motion to the final deformed shell, in which the only evidences of these deformations are axial creases at each outward buckle. This type of behavior may explain the large difference between theoretical threshold buckling loads and the loads that first produce permanent damage in the cylinders with a/h = 187 in Fig. 5.13.

9.2 Strain Gage Experiments

The strain gage experiments were performed to compare observed strains with those to be expected from the buckling theory in Chapter 8. The strain characteristics to be examined are: (1) the period of oscillation and decay of the hoop strain; (2) the period of oscillation, growth, and decay of elastic flexural motion; and (3) the growth of flexural strains in a buckling shell. The largest and most significant membrane and flexural strains are those under the peak load at the shell midspan; thus most of the records given here are from gages at this location. Gages at other axial and circumferential stations give little further information. In all, about 30 strain gage experiments were performed, all in the shock tubes as listed in the D series in Table 4.1. Here strains from 3 experiments are given

The cylinder is marked with 1/2-inch squares.

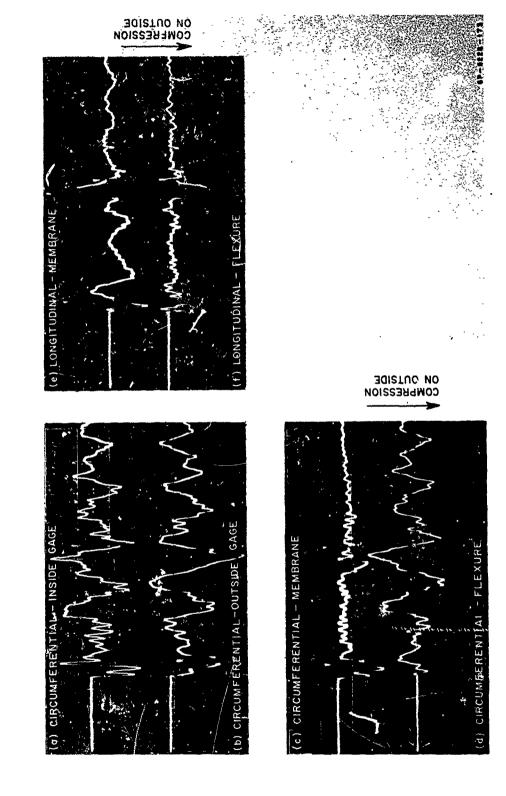
which show typical response in a relatively thin shell (a/h = 61) subjected to loads above and below the buckling load, and in a relatively thick shell (a/h = 24) subjected to a load just below the buckling soad. The shells are all 2024-T8 aluminum, 6 inches in diameter with L/D = 1.

For the thin shells (a/h = 61), the quasi-static buckling pressure, from group A412 in Table 4.1, is about 300 psi. The pressures used in the strain gage experiments here were 245 psi and 390 psi, which gave response with no buckling and with buckling into a central lobe as in Fig. 5.7(e).

The strain records are given in Fig. 9.6 for 245 psi and in Fig. 9.7 for 390 psi. In each figure, strains are given from longitudinal and circumferential gages on the inside and outside of the shells at the midspan location facing the oncoming shock. Figures 9.6(a) and (b) give records directly from the individual circumferential gages. In this form the records are very difficult to interpret. In order to separate the contributions to these strains from membrane and flexural motion, the outputs from the gages were added to give membrane strain (Fig. 9.6c) and subtracted to give flexural strain (Fig. 9.6d). Longitudinal membrane and flexural strains were recorded similarly, as in Fig. 9.6(e,f).

The circumferential membrane strain in Fig. 9.6(c) displays the essential characteristics assumed in the analysis of Chapter 8: the strain suddenly rises with the arrival of the shock, and then oscillates about a mean value which follows the decaying shock. The frequency of the oscillation is very close to the 11 kc calculated for the hoop mode. A similar response is shown in Fig. 9.8(a) for the experiment on the shell with a/h = 24. In each example, the membrane

The peak amplitude is not reached on the first overshoot, but this is of secondary importance and is probably caused by the finite time for the shock to envelop the front face of the shell (about 100 μ sec), and the very rapid dropoff of the initial pressure.



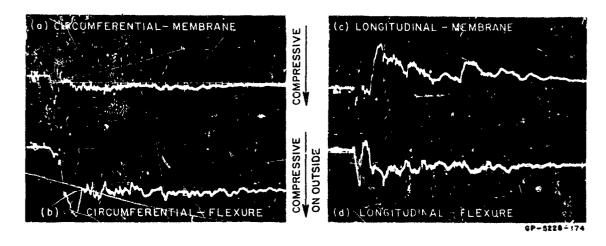
きぬ、これないないまで、

I

I

I

FIG. 9.6 STRAIN RECORDS FROM SUBCRITICAL RESPONSE OF A SHELL WITH a/h=61 (2024–T8 aluminum, D=6 inch, L/D=1; P=245 psi, I=32,000 taps; Sweep: $500~\mu sec/cm$, Gain: 0.0009 in./in./cm, compression positive downward)



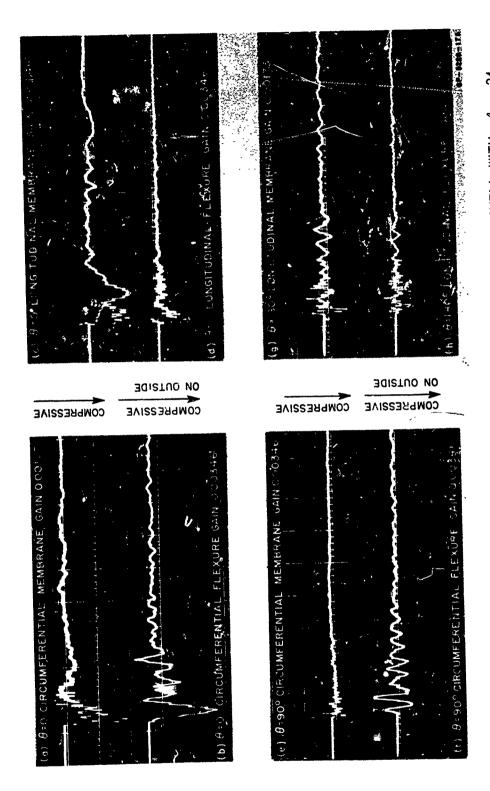
一番のでは、 できるのであることが、 こうこうしょうしょう

FIG. 9.7 STRAIN RECORDS FROM BUCKLING RESPONSE OF A SHELL WITH a/h=61 (same shell as in Fig. 9.6, but P=390 psi, $\Gamma=47,000$ taps; Sweep: 1 millisecond/cm, Gain: 0.0033 in./in./cm)

oscillations die out rather quickly by a mechanism not included in the theory and which might be associated with motion in higher order membrane modes. Nevertheless, for a buckling analysis, in which the mean value of membrane stress has the major influence, the assumption of membrane motion in only the n = 0 mode appears to be a good one. To account for the decaying membrane oscillations an artificial damping could be introduced, but calculations made in the theory of Chapter 8 show that the buckling is essentially the same with and without such damping.

The circumferential flexural strain in Fig. 9.6(d) has a very dominant oscillation with a period of approximately 750 μ sec. From Eq. (8.36), the flexural frequencies are given by

$$f_{n} = \frac{c}{2\pi a} w_{n} = \frac{c}{2\pi a} \left[\alpha^{2} (n^{2} + \frac{\pi^{2}}{\ell^{2}}) + \frac{(1-\nu^{2})(\frac{\pi}{\ell})^{4}}{(n^{2} + \frac{\pi^{2}}{\ell^{2}})^{2}} - n^{2} u_{o} \right]^{1/2}$$



STRAIN RECORD FROM THRESHOLD BUCKLING RESPONSE OF A SHELL WITH $\alpha/h=24$ (2024–T8 aluminum, D = 6 inch, L/D = 1; P = 1310 psi, I = 161,000 taps; Sweep: 1 millisecond/cm, Gain: as shown on individual records, in./in./cm) FIG. 9.8

TO THE TENED OF THE PROPERTY O

For the present shell the period of oscillation has been computed for no membrane force and for $u_0 = 0.0003$, which gives a membrane stress (in the theory on which Eq. (8.36) is based) corresponding to the strain from Fig. 9.6(c), taking into account the longitudinal strains of Fig. 9.6(e). The results of these calculations are

<u>n</u>	No-Load Period (µsec)	Loaded Period, u = .0003
4	560	660
5	570	700
6	460	560

In each case n = 5 gives the longest period and is the one closest to the observed dominant period. Thus we conclude that the shell is oscillating at a large amplitude in the 5th mode, which is the critical mode number predicted by the buckling theory.

The longitudinal membrane strain (Fig. 9.6e) is rather large in comparison to the circumferential membrane strain and oscillates at the flexural frequency observed in Fig. 9.6(d). The peak value, at about 500 µsec after shock arrival, gives an axial stress (taking into account the corresponding circumferential strain) of about 7000 psi. Although this is a sizable stress, its effect on buckling is small, since the classical elastic axial buckling stress is $\sigma = C.6Eh/a \approx 100,000$ psi (see discussion on buckling interaction, Section 5.3.4).

The strain records in Fig. 9.7 show the character of buckling motion in a similar shell subjected to a quasi-static load of 390 psi. The flexural strain (Fig. 9.7b) increases very rapidly and nearly monotonically to a peak value of 0.0066 at about 800 µsec after shock arrival, and then returns to a strain of 0.004 in the postbuckled state. The longitudinal membrane strain (Fig. 9.7c) follows this motion in tension, as expected.

The large spike at about 2000 µsec was probably caused by the gage opening.

Finally, Fig. 9.8 gives the strain records for the a/h = 24 shell subjected to a quasi-static load of 1310 psi, which is only slightly smaller than the buckling pressure for this shell (about 1400 psi, from experiment A17-12, Table 4.1). Figure 9.8(a) shows the circumferential membrane strain following the pressure pulse as discussed earlier. Figure 9.8(b) shows a very large growth in the flexural mode giving a peak strain of 0.007. It is evident that at a slightly greater pressure the shell would buckle as shown in Fig. 5.11(a). Consistent with the assumptions in the theory, the amplitude of the flexure at 90° (Fig. 9.8f) is much smaller than under the peak load (Fig. 9.8b), and the flexure at 180° is negligibly small. The only significant longitudinal strain (Fig. 9.8c) appears to be caused by the large circumferential flexure.

9.3 Concluding Remarks

These experiments demonstrate that the assumptions made in Chapter 8 concerning the behavior of the membrane strain and the rapid and monotonic growth of the buckling mode are both borne out in observed shell response. Details in the response not covered in the theory, such as the variation in membrane strain around the circumference and the exact nature of the membrane oscillations, do not appear to be significant.

APPENDIX A

INSTRUMENTATION FOR PRESSURE MEASUREMENTS

A.1 General Description

をないしまめいとでしていています

The blast pressures experienced by the structural test shells were measured using rigid instrumented models of the same outside dimensions and mounted in the same positions as the structural test shells. Pressure transducers installed in the walls of the rigid models measured the pressure distributions around them. Pressure distributions were measured over the entire range of application of the shock tubes, spherical HE charges, and oxyacetylene gas charges.

Three pressure-instrumented models were made, two cylinders 6 inches and 3 inches in diameter, and a 9° cone. All were made of steel with wall thicknesses as large as possible to minimize acceleration coupling to the pressure gages through mechanical vibration, which varies inversely with model wall thickness and density. The 6-inch cylinder (shown in Fig. A. 1) has a 1-inch-thick wall, with receptacles for 13 Kistler Mcdel 601M quartz pressure transducers, 11 around the circumference at midspan and 2 near one end to check the pressure distribution along the cylinder. The gage layout is shown in Fig. A. 3.

The gages on the 9° cone are similarly arranged, with one additional gage at the 0° location on the small end. The 3-inch-diameter cylinder has only 5 gages at midspan (because of space limitations) at 45° intervals from 0° to 180° .

The gage faces are set flush with the surface (Fig. A.2a) and the signal lines are brought out through rigid pipe and flexible armored conduit (Fig. A. la). The entire assembly is insulated by nylon bushings on the ends of the support shaft (Fig. A. lb) and by a plastic nipple in the signal line pipe. This "floating ground" arrangement was necessary to reduce electrical noise pickup.

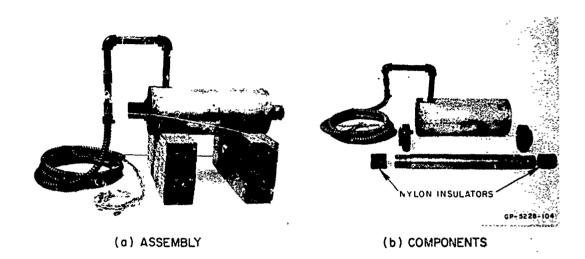


FIG. A.1 PRESSURE-INSTRUMENTED CYLiNDER (6-inch diameter)

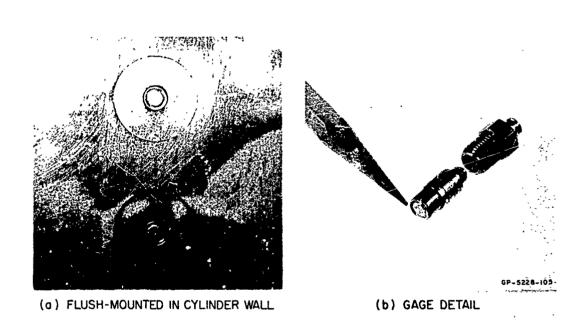


FIG. A.2 KISTLER MODEL 601H QUARTZ PRESSURE TRANSDUCERS

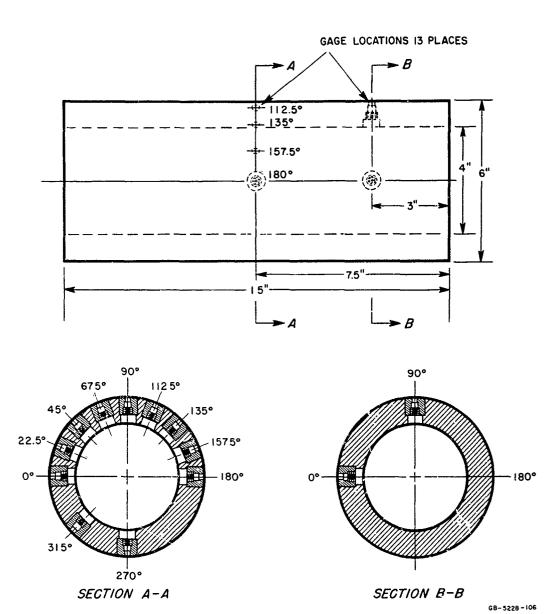


FIG. A.3 GAGE LOCATIONS IN 6-INCH PRESSURE CYLINDER

The piezoelectric crystal elements of the Kistler Model 601M transducers produce an electric charge that is proportional to the pressure applied to the gage face. The rise time is 3 microseconds and the natural frequency is 130,000 cycles per second (130 kc). Charge sensitivity is nominally 1 picocoulomb per psi (pcb/psi), and varies slightly depending upon the individual gage and the pressure range. The output sensitivity in terms of volts per psi is given by

$$volts/psi = (pcb/psi) \cdot \frac{1}{C}$$

where C is the total capacitance in picofarads of the gage and signal line. The output sensitivities of all channels were equalized to about 0.4 millivolts/psi (the input to the amplifier) by adjusting the capacitance.

The gage signals were fed to Endevco Model 2616B laboratory amplifiers, which provide gain levels of 1,3,or 10. The amplified signals were fed to a set of passive low-pass electronic filters to reduce oscillations in the recorded trace caused by the 130-kc mechanical resonance of the Kistler transducer elements, which were strongly excited by the fast-rise pressure pulses being measured. The filters provided selection of any one of eight cut-off frequencies between 13 and 120 kc. A 29-kc cut-off was generally used for the long, full-length shock tube pulses, and a 96-kc cut-off was used for spherical HE charges. The filter frequency response curve for the 29-kc cut-off position is given in Fig. A. 4. Figure A. 5 shows typical unfiltered records (upper traces) and typical filtered records (lower traces).

To eliminate excessive zero drift in the shock tube tests due to heating, a layer of 5-mil-thick Fiberglas tape was wrapped around the cylinder over the gages. Measurements with and without the tape showed that it did not affect pressure transmission to the gage face.

A CONTRACTOR OF THE PROPERTY OF THE PARTY OF

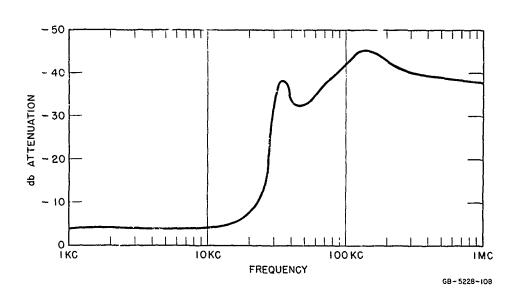
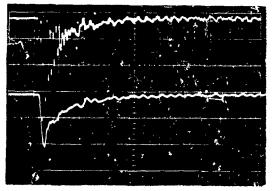
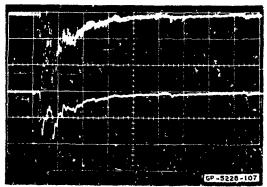


FIG. A.4 FILTER FREQUENCY RESPONSE IN 29 kc POSITION



(a) 0.5-1b HE CHARGE AT 2.3 ft, 0° GAGE, SWEEP = 50 μsec/cm, UPPER TRACE UNFILTERED, LOWER TRACE FILTERED AT 115 kc.



(b) 2-fi SHOCK TUBE, α=5 AT 5ff, 45° GAGE, SWEEP=500μsec/cm, UPPER TRACE UNFILTERED, LOWER TRACE FILTERED AT 29 kc.

FIG. A.5 PRESSURE RECORDS WITH AND WITHOUT FILTERING

Free-field pressures were measured with Atlantic Research Corporation Type LC-33 blast gages (Fig. A. 6). These have a cylindrical piezoelectric element of high output sensitivity and were connected directly to an oscilloscope.

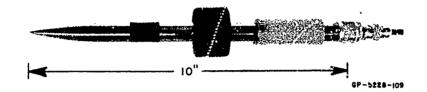


FIG. A.6 ATLANTIC RESEARCH TYPE LC-33 BLAST GAGE WITH MOUNTING COLLAR AND SLEEVE

Signals were recorded on film. with six dual-beam oscilloscopes. The oscilloscopes were synchronized with an electronic delay generator which was triggered by the detonator firing pulse. The delays were adjusted (depending on shock tube length and charge ratio, and spherical charge size and range) to minimize dead time on the scope records.

A.2 Calibration

《公司》的《公司》

The pressure transducers were calibrated with a standard dead-weight gage tester (Fig. A. 7) modified to apply a step pressure to the transducers. An initial, accurately measured hydrostatic pressure was applied and then suddenly released in a time comparable with the blast pulse durations.

The tester was equipped with a manifold to mount as many as eight Kistler transducers for simultaneous calibration. The desired initial static pressure in the system is established by pumping up the fluid against a floating piston loaded with calibration weights. The manifold has a valve at the bottom end so it can be isolated from the balance of the fluid in the tester to produce a minimum pressure

release time. A quick-opening valve at the top of the manifold opens it to the aimosphere when the valve lever is struck with a hammer. A piezoelectric sensor on the lever triggers the oscilloscopes.

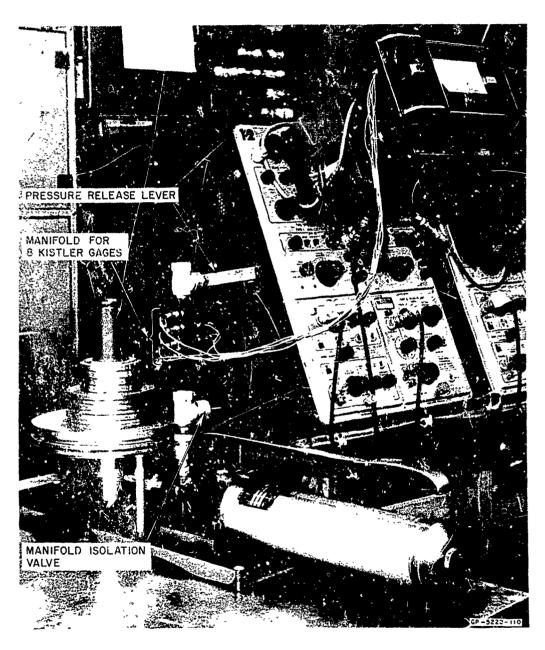


FIG. A.7 PRESSURE CALIBRATION ARRANGEMENT

Output signals from the pressure transducers are fed to the same Endevco amplifiers and displayed on the same oscilloscopes as used in the blast pressure tests. The low-pass filters were omitted; their characteristics were checked separately.

Figure A. 8 shows typical calibration records for two runs on two transducers. The horizontal baseline traces are for 250 psi static pressure. The pressure drop from 250 psi to zero (upwards in Fig. A. 8) takes about 10 milliseconds. The rate of the subsequent voltage decay from the peak back toward the baseline level is dependent upon the time constants of the amplifiers. The recorded voltage corresponding to 250 psi is the ordinate from the baseline to the extrapolation of the dynamic trace back to time zero. These values, and the transducer and signal line capacitance, are used to calculate the transducer charge sensitivity (pcb/psi), taking into account the amplifier gain. Since transducer and line capacities are as important as any other factor in the calibration procedure, these were accurately measured at 1 kc with a General Radio Type 1650-A impedance bridge.

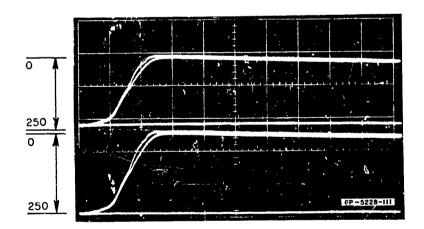


FIG. A.8 PRESSURE CALIBRATION RECORDS (2 runs on 2 gages, sweep 5 msec/cm)

The Kistler transducers were calibrated periodically during the test program at pressures ranging from 50 to 10,000 psi (the upper limit for the Model 601 H). Figure A.9 shows a representative calibration curve. Charge sensitivity varies with pressure below 1000 psi, but is relatively constant as pressure increases. In pressure data calculations this variation was taken into account.

経験をおから 多さしても

TO THE PROPERTY OF THE PROPERT

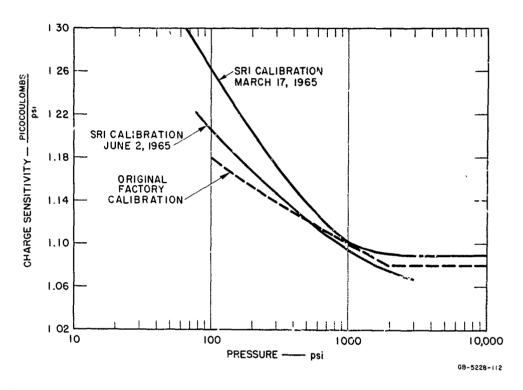


FIG. A.9 CHARGE SENSITIVITY vs. PRESSURE FOR TYPICAL KISTLER 601H GAGE

The Atlantic Penearch Company Type LC-33 blast gages were calibrated with the dead-weight tester in a similar manner.

APPENDIX B

MODEL SUPPORT FIXTURES

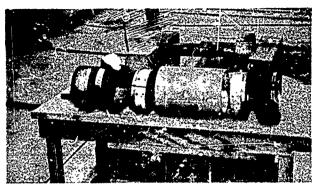
B. 1 Design Requirements

The cylindrical and conical shell structures were held in fixtures which provided clamped ends. This end condition was selected as being close to that provided by the heavy circumferential rings in actual re-entry vehicles, and also as giving a simple holding scheme that could be used for a wide variety of models. The fixtures were designed to meet the following requirements:

- 1. The end support conditions of the shells had to be secure and reproducible.
- 2. The fixtures had to accommodate several different shell wall thicknesses, shell lengths, and tolerance variations.
- 3. The assembled fixture mounts had to be compatible with the 2-foot shock tube, the 4-foot shock tube, and the field stands.
- 4. The fixtures had to withstand very high blast loads.
- 5. Mounting and demounting the shells on the fixtures and attaching the fixtures to the shock tubes and field test stands had to be simple and rapid so that these operations would retard the progress of the testing as little as possible.

B.2 Description of Support System

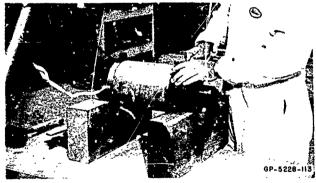
The model support fixture is shown in Figs. B. 1 and B. 2. The fixture shown is for 6-inch-diameter shells; 3-inch shells were supported in the same manner. The shell ends are clamped between internal expandable end plugs and external circumferential bands and the end plugs are supported by a central shaft. The cylindrical end-fairings extend the aerodynamic length of the cylindrical model.



(a) COMPONENTS

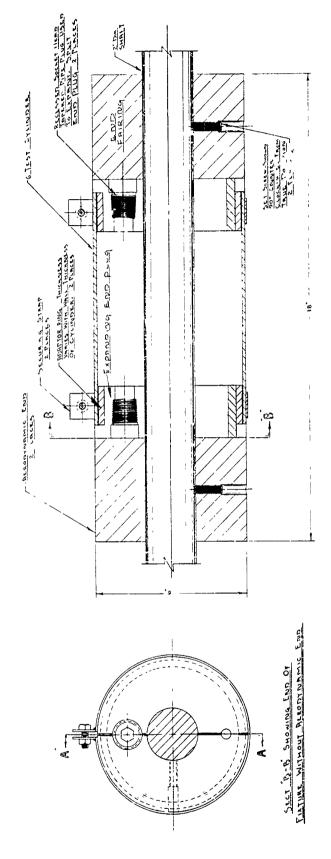


(b) CLAMPING BAND, ADAPTOR RING, EXPANDABLE END PLUG



(c) ASSEMBLY

FIG. B.1 CYLINDRICAL MODEL SUPPORT FIXTURE (6-inch diameter)



1

1

The same

T. Market

Transport .

*

issored.

1.11年18年

FIG. B.2 MODEL SUPPORT ASSEMBLY (6-inch diameter)

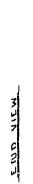
GD-5288-114

Almost all of the shell models were made from extruded tubing, which comes with a fixed outside diameter for any wall thickness. To accommodate shells of various wall thicknesses, the diameter of the end supports had to be adjustable. This was accomplished by using an end plug of a size to accommodate the thickest shells and by inserting adaptor rings between the end plug and shell model for the thinner shells. To take up manufacturing tolerances and insure a snug fit into the models, the end plugs were split along a diameter (leaving about 1/4 inch to serve as a hinge) and a taper-threaded bolt was used to expand the open end of the cut as shown in Fig. B. 1(b). The adaptor rings were knurled and external bands were clamped around the models to reduce axial slipping of the models. The end plugs and aerodynamic fairings were held in place on the shaft with set screws.

Two sets of fixtures were built for 6-inch-diameter cylinders, and three for 3-inch-diameter cylinders. One set of similar design was built for 9° conical shells but without the expanding end plug feature, since the cone end plugs had an inherent adjustment for diameter variations. A detailed drawing of the cone assembly is given in Fig. B.3.

The mounting shafts were 2-inch-diameter cold-rolled steel bars of different lengths to fit the two shock tubes and the field stands. At the highest charge levels in the 2-foot tube, the blast loads were sufficient to bend these shafts. Substitution of high-strength steel bars and/or addition of central strengthening sleeves minimized this problem. The mounting shafts for the 3-inch cylinder fixtures were 1-1/4-inch-diameter bars.

The model support fixtures were held in the test position in the shock tubes by heavy cross-frames bolted to lugs welded to the tops of the tubes. Both the frames and bars were made of 2×6 -inch steel bars and were designed to withstand aerodynamic drag loads up to 500,000 pounds. The shafts supporting the model shells are attached to the undersides of the cross-frames by simple bearing blocks and



SECT. A-A

. Basse (1.6

FIG. B.3 CONE SUPPORT ASSEMBLY

threaded studs. These attachments are made accessible by swinging the frames up and over to the sides of the tubes with an overhead electric hoist as shown in Fig. 3.18.

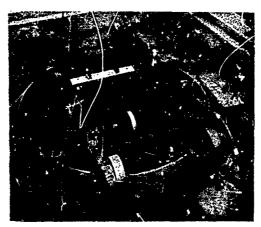
The cross-frames for the 4-foot shock tube allow two 6-inch or three 3-inch-diameter models to be tested at the same time (Fig. B. 4a). The 2-foot tube cross-frame can accommodate two 3-inch models (Fig. B. 4b). The 6-inch models were held in the 2-foot tube with end cradles which bolt directly into the tube walls (Fig. B. 4c).

B.3 Preload Fixture

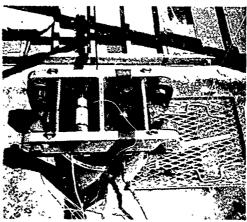
Some 6-inch shells were tested under axial preloads up to 5000 pounds in tension or compression. The basic support fixture design was modified to provide these preloads by incorporating a strain-gaged yoke at one end, through which the required thrust was transferred and monitored. Loads were applied to the shell by holding one end plug fixed on the mounting shaft and moving the other end out or in by turning a nut threaded on the shaft. Figures B. 5(a, b) show the components arranged for assembly in the tension mode, and Fig. B. 5(c) for the compression mode. Figure B. 6 is a detailed drawing of the assembly.

The shell is supported on expandable end plugs as before, with the addition of a circumferential row of bolts at each end to transfer the axial load from the end plugs to the shell. One plug is locked on the shaft and the other is free to slide but is bolted to the periphery of the strain-gaged yoke. Thrust is developed by screwing out the sleeve nut, which compresses two Belleville springs against the inner shoulder of the yoke. The deflection of the springs (0.15 inch) is sufficient to give about two full turns of the loading nut for the full 5000-pound thrust.

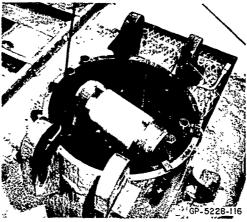
For compressive loading the Belleville springs are installed outside the yeke, and a hex-nut on the outside thread of the adjusting sleeve provides the thrust (Fig. B.5c).



(a) CROSS-FRAME IN 4-FOOT TUBE WITH 6-INCH MODELS

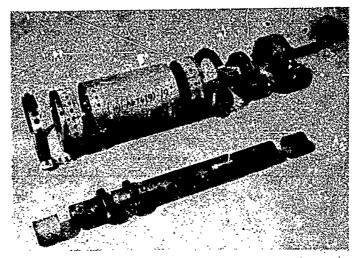


(b) CROSS-FRAME IN 2-FOOT TUBE WITH 3-INCH MODELS

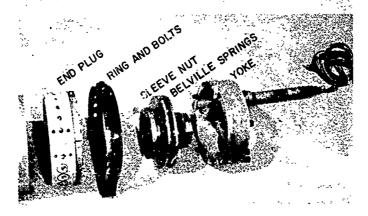


(c) CRADLE IN 2-FOOT TUBE FOR 6-INCH MODEL

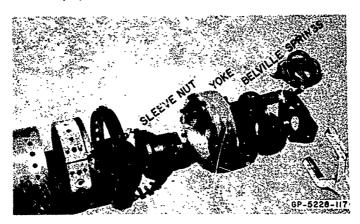
FIG. B.4 SHOCK TUBE MOUNTING ARRANGEMENTS



(a) COMPONENTS ARRANGED FOR TENSION



(b) YOKE ASSEMBLY FOR TENSION



(c) YOKE ASSEMBLY FOR COMPRESSION

FIG. B.5 PRELOAD FIXTURE

The state of the s

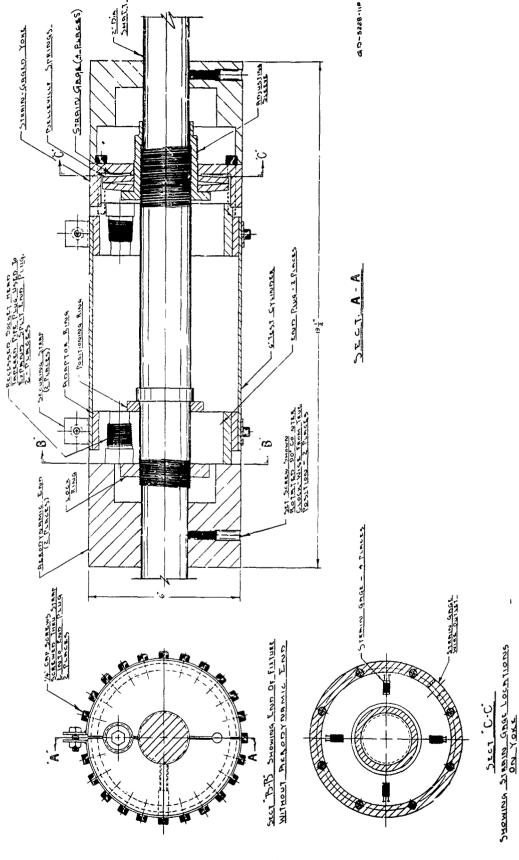


FIG. B.6 PRELOAD FIXTURE (assembly drawing, tension mode)

The forces acting on the end plate of the yoke result in combined bending and membrane stresses which were monitored as a measure of axial load. Four strain gages were mounted in the radial direction at 90° intervals and were connected so individual and combined outputs could be monitored. A BLH transducer indicator Model 352 was used. The yoke was calibrated in terms of voltage cutput versus load with an Instron testing machine.

Just prior to a blast load experiment, strain-gage outputs were recorded in the no-load condition; the preload was then applied. At the desired preload, outputs were again recorded and the shot was fired. A last reading was taken immediately after the shot to observe any change in load. Thermal drift of the gage outputs during this sequence was found to be small.

APPENDIX C

THEORY OF EXPLOSIVELY DRIVEN SHOCK TUBES

C. l Introduction

高さいでは、またいではないというできないという。

To estimate the pressures and durations obtainable with explosively driven shock tubes and to provide a basis for interpreting observed pressure pulses, a simplified analysis of shock tubes was carried out. The analysis is concerned primarily with free-field flow which, combined with data from flow past cylinders [18], is then used to make estimates of peak pressures and durations on cylindrical models. The analytical results agree reasonably well with test data.

The analysis is based on the theory for conventional shock tubes [17, 35], in which the high pressure gas in the driver section is separated from the lower pressure gas in the driven section by a diaphragm. For explosively driven shock tubes, the section containing the explosive is taken as the driver section. It is assumed that upon detonation of the explosive the pressure builds up to a uniform value in the driver section before an imaginary diaphragm is removed. This is a reasonable idealization since the detonation velocity of the explosive is several times greater than the highest shock velocity expected, and thus detonation is essentially instantaneous throughout the driver section.

A typical model pressure pulse to be analyzed is shown in Fig. C. l. This is drawn for a point on a cylindrical model directly facing the lateral bust. An analysis to determine the pulse completely would be an exceedingly complex task since it would require the transient solution for diffraction of a shock wave impinging on a cylinder.

See Section 3.4 for a general description of the operation of explosively driven shock tubes.

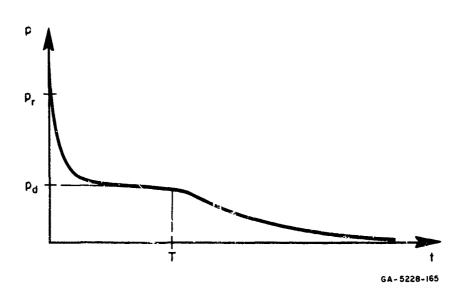


FIG. C.1 IDEALIZED PRESSURE PULSE ON CYLINDRICAL MODEL ($\theta = 0$)

However, it was felt that the peak pressure p_r would be given by the reflected pressure corresponding to the incident pressure of the driven air, and that as steady-state flow is established around the cylinder, the pressure would reduce quickly to the steady-drag pressure p_d . At time T the pressure again begins to decay because of rarefactions from the driver end of the shock tube. The primary results of the analysis to follow are estimates of p_r , p_d , and T.

The procedure for making these estimates is presented in four parts. First, empirical relations are taken from [15] to determine driver section pressures and gas properties for a given charge. Second, flow equations are presented to permit calculation of free-field shock and particle velocities, Mach numbers, and flow durations. Third, methods of calculating model pressures are given, based on shock relations and experimental observations of drag pressures given in [18]. Finally, a few example model pressures are calculated and compared with experimentally observed pressures.

C.2 Driver-Section Pressures and Gas Properties

The results of a previous theoretical and experimental study of explosively driven shock tubes [15] are used here to predict the driver-section pressures and gas properties. In the referenced study, theoretical predictions of the driver-section temperature T_4 and the pressure p_4 were lower than the experimental values. To circumvent this difficulty and provide correct driver conditions for the analysis of the subsequent expansion, the following empirical relation was determined in [15] for the driver-section pressure ratio

$$p_{41} = p_4/p_1 = 26.15 \alpha^{0.667}$$
 (C.1)

where the subscript 4 refers to conditions in the explosive gas-air mixture after detonation, and 1 to the ambient air conditions before detonation. The charge ratio α is the ratio of the weight of explosive to the weight of ambient air in the driver section. Regarding the explosive gas-air mixture as an ideal gas, the corresponding drivers section temperature is determined from

$$\frac{P_4}{P_1} = \frac{\rho_4 R_4 T_4}{\rho_1 R_1 T_1}$$

where R_1 and R_4 are gas constants, ρ_1 and ρ_4 are densities, and by definition $\rho_4 = \rho_1 (1 + \alpha)$. As shown in [35], for practical purposes $R_4 = R_1$ and thus

$$T_{41} = T_4/T_1 = \frac{P_{41}}{1+\alpha} = 26.15 \frac{\alpha}{1+\alpha}$$
 (C.2)

The remaining gas property required before the shock tube flow can be calculated is the ratio γ_4 of the specific heats of the explosive gas-air mixture. In [15] this is assumed as

$$\gamma_4 = \frac{\bar{C}_{pl} + \alpha \bar{C}_{pe}}{\bar{C}_{vl} + \alpha \bar{C}_{ve}}$$

[&]quot;PETN--see Section 3.4.

where the specific heats C_{pl} , C_{vl} , C_{pe} and C_{ve} are taken as average values over the temperature range T_l to T_4 , and the subscripts l and e refer to the ambient air and explosive gases respectively. Noting that C_{pe} - C_{ve} = R_e , the previous equation can be rearranged to give

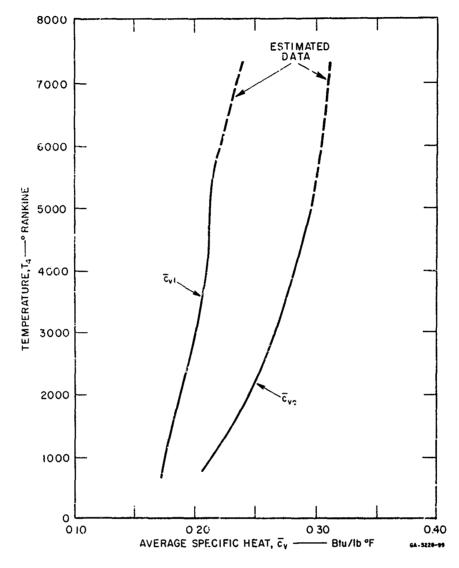
$$\gamma_{4} = \frac{\bar{\gamma}_{1} + \alpha \left(\frac{\bar{C}_{ve} + R_{e}}{\bar{C}_{vl}}\right)}{1 + \alpha \left(\frac{\bar{C}_{ve}}{\bar{C}_{vl}}\right)}$$
(C.3)

where $\bar{\gamma}_1 = \bar{C}_{p1}/\bar{C}_{v1}$. R_e is assumed constant at 51.6 ft-lb/lb°R and the values of \bar{C}_{ve} , \bar{C}_{v1} , and $\bar{\gamma}_1$ are given in Figs. C.2 and C.3, which are taken from [15].

Thus for a given charge ratio α , p_{41} and T_{41} can be determined from Eqs. (C.1) and (C.2). Knowing T_4 , the specific heats are found from Figs. C.3 and C.4 and used to calculate γ_4 . This then supplies enough data to calculate the shock tube flow and to estimate the loads developed on the cylindrical models.

C.3 Shock Tube Theory

Figure C. 4(a) shows an open-ended shock tube. The idealized pressure distribution immediately after detonation is shown in Fig. C. 4(b). Figure C. 4(c) shows the pressure distribution after expansion begins. As indicated, a shock wave moves into the expansion chamber at a velocity C_s , raising the pressure and accelerating the driven gas to the right, and a rarefaction wave moves into the driver section, lowering the pressure and accelerating the driver gas, also to the right. Figure C. 4(d) is a distance-time diagram showing the motion of the various waves. In the work that follows, gas properties in each region will be identified by subscripts corresponding to the circled numbers in Fig. C. 4(c).



To environ

FIG. C.2 AVERAGE SPECIFIC HEATS AT CONSTANT VOLUME vs. TEMPERATURE

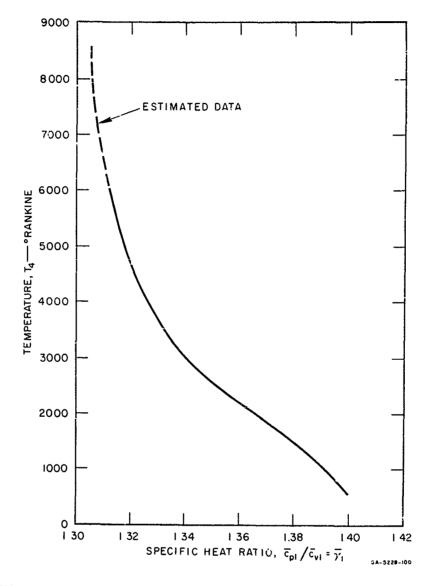


FIG. C.3 RATIO OF AVERAGE SPECIFIC HEATS vs. TEMPERATURE

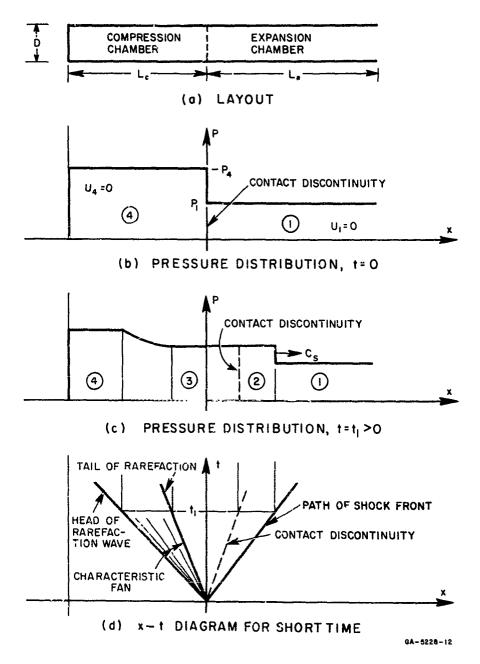


FIG. C.4 IDEALIZED SHOCK TUBE

C.3.1 Shock Conditions

We begin by determining the conditions behind the shock front. For $u_1 = 0$, the equations of conservation of mass, momentum and energy across a shock front are [17, 35]

$$\rho_1 C_s = \rho_2 (C_s - u_2) = m$$
 (C. 4)

$$p_2 - p_1 = \rho_2(C_s - u_2)u_2 = mu_2$$
 (C.5)

$$p_2 u_2 = -\rho_1 C_s e_1 + \rho_2 (C_s - u_2) e_2 + \frac{1}{2} \rho_2 (C_s - u_2) u_2^2$$

$$= m(e_2 + \frac{1}{2} u_2^2 - e_1)$$
(C. 6)

where p is pressure, ρ is density, u is particle velocity, and e is internal energy per unit mass.

For an ideal gas

$$p = \rho RT \tag{C.7}$$

where T is temperature and R is the gas constant. If the specific heats at constant pressure and constant volume, C_p and C_v , are constant, then

$$C_{p} - C_{v} = R \tag{C.8}$$

For an ideal gas the internal energy is

$$e = C_{v}T$$
 (C.9)

which can then be expressed as a function of pressure and density by

$$e = \frac{p}{(\gamma - 1)\rho}$$
 (C. 10)

where

CANAL STREET

$$\gamma = C_p/C_v$$
 (C.11)

If the shock strength is specified by one of the five unknowns $\,p_2^{}$, $\,\rho_2^{}$, $\,e_2^{}$, $\,u_2^{}$, $\,C_s^{}$, the other four can be determined from the four equations (C. 4, C. 5, C. 6, C. 10).

Sound speed in a gas is given by

$$a^2 = (\frac{\partial p}{\partial \rho})_s$$

where s is the entropy. For an ideal gas and an isentropic process

$$p = const. \cdot \rho^{\gamma}$$

therefore

The second secon

$$a^2 = \frac{\gamma p}{\rho} = \gamma RT \qquad (C. 12)$$

It is convenient to refer particle and shock velocities to the sound speed in the gas; this ratio is called the Mach number. Thus, the shock Mach number is

$$M_s = C_s/a_1$$
 (C. 13)

 $\label{thm:conditional} Shock \ strength \ is \ defined \ as \ the \ pressure \ ratio \ across \\ the \ shock$

$$p_{21} = p_2/p_1$$
 (C. 14)

In terms of shock strength the other unknowns become

$$M_s = \frac{C_s}{a_1} = \left(\frac{p_{21} + \mu_1}{1 + \mu_1}\right)^{1/2}$$
 (C. 15)

$$u_2 = \frac{a_1(p_{21}-1)(1-\mu_1)}{[(p_{21}+\mu_1)(1+\mu_1)]^{1/2}}$$
 (C. 16)

$$\frac{\rho_2}{\rho_1} = \rho_{21} = \frac{p_{21} + \mu_1}{1 + \mu_1 p_{21}} \tag{C.17}$$

$$\frac{T_2}{T_1} = T_{21} = p_{21} \frac{(1 + \mu_1 p_{21})}{\mu_1 + \mu_{21}} = (\frac{a_2}{a_1})^2$$
 (C. 18)

where $\mu = (\gamma - 1)/(\gamma + 1)$ and the temperature T is given in place of the internal energy, using (C. 9).

C.3.2 Rarefaction Waves

The flow in the rarefaction wave is taken to be isentropic. Denoting by c the absolute velocity of the characteristics (see Fig. C. 4d), the path of a characteristic is given by

$$x = -ct (C.19)$$

where

$$c = a - u$$
 (C.20)

and u is the particle velocity along the characteristic, positive to the right. In terms of the initial gas properties Eq. (C.20) becomes [35]

$$c = a_4 - \frac{\gamma_4 + 1}{2} u$$

$$= a_4 \left\{ 1 - \frac{\gamma_4 + 1}{\gamma_4 - 1} \left[\left(\frac{\rho}{\rho_4} \right)^{(\gamma_4 - 1)/2} - 1 \right] \right\}$$
 (C. 21)

Since $u_4 = 0$, the head of the rarefaction wave is given by

$$x = -a_4 t \qquad (C.22)$$

and the tail is given by

343

こうこうないのかないというないないのできる

$$x = -c_3 t$$

$$= (-a_4 + \frac{\gamma + 1}{2}u_3)t$$
(C.23)

The flow is uniform between the tail of the rarefaction wave and the contact discontinuity, with the pressure and density given by

$$\frac{p_3}{p_4} = p_{34} = \left(1 - \frac{(\gamma - 1)}{2} \frac{u_3}{a_4}\right)^{2\gamma/(\gamma - 1)}$$
 (C.24)

$$\frac{\rho_3}{\rho_4} = \rho_{34} = \left(1 - \frac{(\gamma - 1)}{2} \frac{u_3}{a_4}\right) \tag{C.25}$$

C.3.3 Continuity Condition

Across the contact discontinuity temperatures and densities may differ; however, the pressures and particle velocities must be the same. Hence

$$p_2 = p_3$$
 $u_2 = u_3$
(C. 26)

These two conditions determine the shock strength p_{21} and the rarefaction strength p_{34} in terms of the initial pressure ratio $p_{41} = p_4/p_1$. From [35] we obtain

$$p_{41} = p_{21} \left[1 - \frac{(\gamma_4 - 1)(a_1/a_4)(p_{21} - 1)}{2\gamma_1[2\gamma_1 + (\gamma_1 + 1)(p_{21} - 1)]} - \frac{2\gamma_4}{\gamma_4 - 1} \right]$$
 (C. 27)

Thus, for a known initial pressure ratio p_{41} , the shock strength p_{21} can be evaluated and the remaining flow quantities can be found from Eqs. (C.15-C.18, C.25, C.26).

C.3.4 Flow Conditions

The flow shown in Figs. C.4(c) and (d) continues until the head of the rarefaction wave reaches the closed end of the tube and a reflected rarefaction wave is generated. The head of this rarefaction is shown by the line CDE in Fig. C.5, where OC and OD represent the head and tail respectively of the incident rarefaction. From C to D the path is curved since the reflected rarefaction moves into gas of variable state; however, from D to E the path is straight since the flow is uniform in this region.

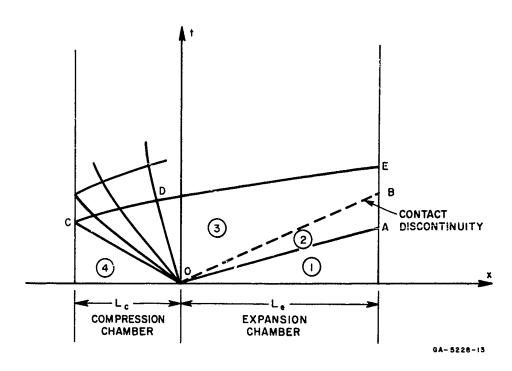


FIG. C.5 x-t DIAGRAM

With reference to Fig. C. 5, let u and <u>a</u> stand for the particle velocity and sound speed at points on CD. From Eqs. (C. 19) and (C. 20) we see that the equation for the characteristics of the first rarefaction is given by

$$x = -(a - u)t$$
 (C. 28)

Since the characteristic line of the second rarefaction is curving, the differential form of Eq. (C. 19) must be used, which is

$$dx = cdt = (a+u)dt (C.29)$$

where sign changes are made since the rarefaction is moving to the right. From Eqs. (C.20) and (C.21)

$$u = \frac{2}{\gamma_4 - 1} (a_4 - a)$$

which, with Eq. (C.28), is used to remove a and \underline{a} in Eq. (C.29), resulting in the following differential equation for the wave front

$$\frac{dx}{dt} = \left(\frac{3 - \gamma_4}{1 + \gamma_4}\right) \frac{x}{t} + \left(\frac{4}{1 + \gamma_4}\right) a_4 \tag{C.30}$$

The solution of Eq. (C.30) passing through the point C

is

$$2a_4 - (\gamma_4 - 1)\frac{x}{t} = (\gamma_4 + 1)a_4(\frac{a_4t}{L_c}) - \frac{2(\gamma_4 - 1)}{\gamma_4 + 1}$$
 (C.31)

The point D is then given by the simultaneous solution of Eqs. (C.31) and (C.23), which is the equation of the line OD. Denoting the coordinates of D by (x_D, t_D) , the intersection point is at

$$t_{D} = \frac{L_{c}}{a_{4}} \left[\frac{2a_{4} - (\gamma_{4} - 1) - (\gamma_{3} - a_{3})}{a_{4} (\gamma_{4} + 1)} \right]^{-\frac{(\gamma_{4} + 1)}{2(\gamma_{4} - 1)}}$$
 (C. 32)

The path DE is then given by

$$x - x_D = (a_3 + u_3) (t - t_D)$$
 (C. 33)

In the example in Fig. C. 5 the rarefaction wave does not intersect the contact discontinuity; however, this can occur and the x-t diagram for such a case is shown in Fig. C. 6. The equation for the

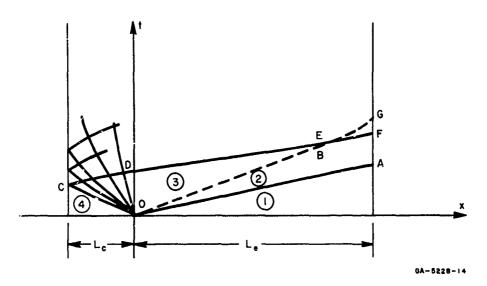


FIG. C.6 x-t DIAGRAM

line CDE is the same as in the previous case, but the line EF is given by

$$x - x_E = (a_2 + u_2) (t - t_E)$$
 (C. 34)

where (x_E, t_E) are the coordinates of the point E. The path BG of the contact discontinuity is curved since the gas particles behind the rarefaction front are slowing down.

C. 4 Theoretical Pressures on Cylindrical Models

the state of the second
The initial peak pressure p_r of the pulse is estimated by the normal reflected pressure of the initial shock striking a flat, rigid wall. This is given in [17] by

$$\frac{p_r}{p_2} = \frac{(2\mu_1 + 1)p_{21} - \mu_1}{\mu_1 p_{21} + 1}$$
 (C.35)

The experimental results agree quite well with this prediction, as will be shown.

The second pressure to be estimated is the steady-state drag pressure \mathbf{p}_d . For steady-state flow conditions in a wind tunnel, extensive experimental data are available [13], giving the pressure on cylindrical models for a wide range of Reynolds numbers and Mach numbers. For flow velocities greater than a Mach number of 0.5, these data show that the Reynolds number is of little, if any, significance, and that the Mach number is the important flow parameter. Following [18], the pressure \mathbf{p}_d on the model is given by

$$p_{d} = p_{i} + C_{p}p_{D}$$
 (C. 36)

where $p_i = p_2$ is the incident pressure, $p_D = 1/2 \rho u^2$ is the dynamic pressure, and C_p is the coefficient of pressure, determined experimentally in [18]. Values of C_p given in [18] vary with Mach number of the flow as well as with the location θ on the cylinder. In the following examples pressures are calculated for flow on both sides of the contact discontinuity.

C.5 Theoretical Results and Comparison with Experiment

C.5.1 Pressure vs. Charge Ratio

The shock strength $\,p_{21}$, which was used to calculate the gas properties behind the shock, has been taken from [15] where it was calculated using the same empirical results and relations given in Sections C.2 and C.3. An ambient temperature of $\,T_1=530^{\rm O}R$ was used in these calculations. To compute the gas properties required for the determination of the sound speed in the explosive air-gas mixture, an ambient temperature of $500^{\rm C}R$ was used; however, this will have little effect in the pressure calculations, and will only affect the pressures of the explosive gas-air mixture.

Figure C.7 shows the results of the calculations made to predict the various pressures. The incident pressure p_2 is based on an ambient pressure p_1 of 14.7 psi and values of p_2 ; from [15].

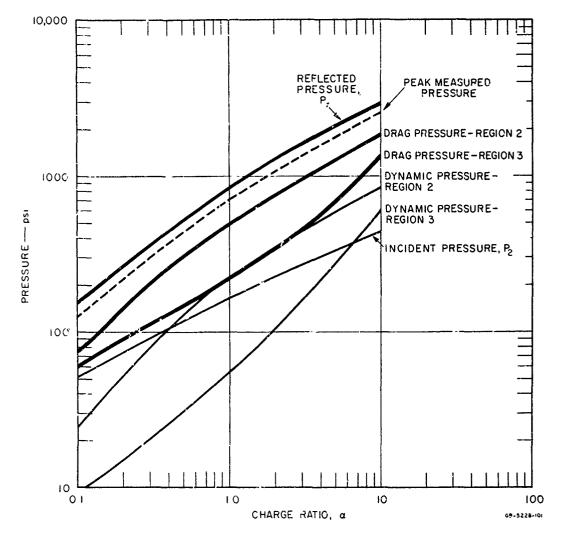


FIG. C.7 PRESIURE vs. CHARGE RATIO CURVES

The reflected pressure $\,p_{_T}\,$ is calculated directly from Eq.(C.35), for $\nu_{_1}$ = 1.40 ($\mu_{_1}$ = 1/6). The dynamic pressures 1/2 ρu^2 are given for the flow regions 2 and 3. Corresponding to these dynamic pressures, the model pressures at θ = 0 are also given, determined from Eq. (C.36) with $\,C_p$ taken from [18]. The large difference in the dynamic pressures between the two flow regions is due to the high temperature of the explosive gas-air mixture of region 3, which results in $\rho_3 < \rho_2$.

B. CALLES CONTRACTOR COMM.

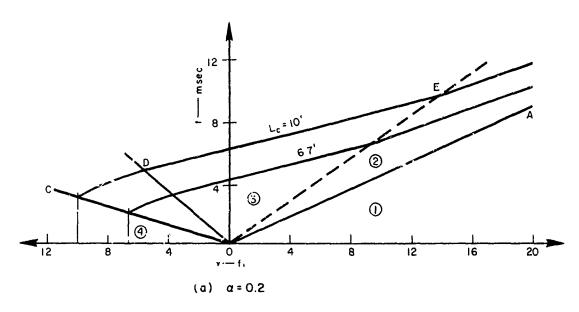
The peak pressures recorded on cylindrical models in the SRI tubes are given in Fig. 3.22. These results are replotted in Fig. C.7 as the dashed line. Aside from a fairly constant difference of about 35 percent in the charge ratio, the agreement is very good and indicates that the peak initial pressure is the reflected pressure. The low experimental pressures are attributed to two causes: First, the empirical relations used in determining the shock strength may be too high, as noted in [15], and second, the rise time of the gages may have been too long to record the short duration initial pressure peak.

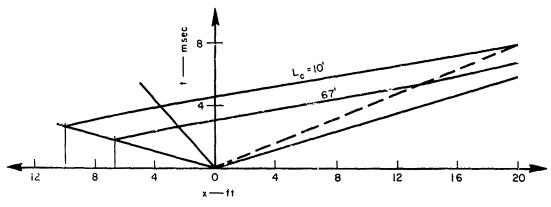
C.5.2 Flow Durations

The x-t plots for three charge ratios are given in Fig. C.8. The path of the rarefaction head for driver section lengths of 10 and 6.7 feet are given, since these are the lengths most commonly used in the two tubes. The path for other driver section lengths can be easily obtained since the length OD in Fig. C.8(a) is a linear function of L_c and DE has the same slope for all lengths. One of the main features to be seen from these figures is that the duration of flow of the shocked air, region 2, is reduced as the charge ratio is increased but that the total duration of region 2 plus region 3 is not changed appreciably. Also, for both driver section lengths the rarefaction head does not interact with the initial shock before it reaches the model location; therefore, the peak pressure should be the same for both lengths.

C.5.3 Pressure Pulses

Figure C. 9 shows three pressure pulses with differing flow conditions recorded at $\theta=0$. Superimposed on these traces are the pressures and durations predicted by the theory. Figures C. 9(a) and (b), which show the results for two different sized tubes at essentially the same charge ratio, show very good agreement with the theory in both pressure level and duration of flow (duration is taken as the time for the head of the rarefaction wave to reach the model). In these two examples the rarefaction wave overtakes the contact discontinuity





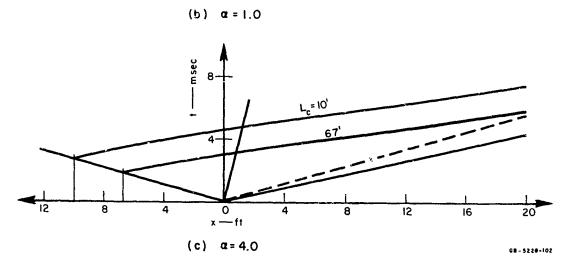
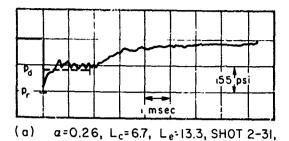
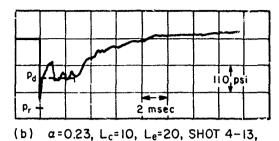
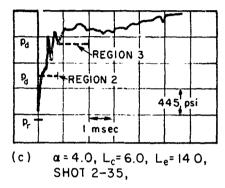


FIG. C.8 x-t DIAGRAMS







GA- 5226-103

FIG. C.9 PRESSURE PULSES ON CYLINDRICAL MODELS $(\theta = 0)$

before reaching the model. Figure C. 9(c) shows reasonable agreement with the peak pressure but is rather poor on the other counts. In this example the contact discontinuity reaches the model before the rarefaction wave, and so the model pressure based on both regions 2 and 3 is shown. The relatively short duration of the first region of flow may account for the poor agreement since it may be too short for steady-state conditions to become established.

These examples demonstrate that the simplified theory provides a good estimate of the pulses to be expected from an explosively driven shock tube. The initial peak pressure is close to the reflected pressure of the incident shock over the entire range of charge ratio. For charges or tube arrangements in which the flow duration of the shocked air (region 2) is of the order of 2 milliseconds or longer, it is seen that the drag pressure adequately describes the pressure plateau of the pulse, and that the beginning of decay is signaled by the arrival of the rarefaction head.

STATE OF MILITARY THE PROPERTY.

APPENDIX D

CHRONOLOGICAL SHOT LISTS

Table D. 1
HIGH EXPLOSIVE SPHERES

Date Cross Date Weight Cross Date Date Cross Date Date Date Cross Date D	**				ment*	Instrum	I	Charge			
14	Damage	I	Metal (% ·v/a)	Cylinder No.			Distance (ft)	Weight	Date	Group No.	Shot No.
14 A16 - 10 12-22 2. 2. 5.5 B82.55 3(53)1-A5T6(1)-10 37.4 No damage 15 B222-1 12-29 2. 1.50 B82.90 3(53)1-A5T6(1)-10 1.5 No damage 17 B222-2 12-29 2. 1.50 B83.00 3(53)1-A5T6(1)-10 1.5 No damage 18 B224-5 12-25 2. 1.50 B83.00 3(53)1-A5T6(1)-10 M	uckling.	No buc!	0. 75	3(53)1-4676(1)-9		i	3.50	2.	12-16	A16 -8	1,3
15 B222 1 12-22 2 2 5 B62.55 3(5)11-Act 6(1)-10 0 0 0 0 0 0 0 0 0						B@2.55					
16						B@2.55			12-22		
17 B222-2 12-29 2. 1.50 B892.00 3(5)1)-A5T6(1)-10P 15.7 No damage 15.00 B892.00 3(5)1)-A5T6(1)-10M 0.00 No damage 15.00 B892.00 B893.00 B393.00 B393.00 B893.00 B893.00 B893.00 B893.00 B893.00 B893.00 B393.00 B393			3.5		i						
19					1						
20 B224-7 12-31 2. 1.00 B83.00 36311-A676(1)-10M 4.4 M cracked 21 B24-7 12-31 2. 1.00 B83.00 B89.00 3(531)-A676(1)-10M 30.0 Severe, M 30.0 Sev	image.	No dam		3(53)1-A6T6(1)-10M		}	1	2.	12-29	B224-5	18
22					DG2 00						
22											
23											
24 A15 - 9											
25 A16 -13 1-13 4. 2.75 B82.27 6"82.00 3(33)1-A6T6(1)-18 >30.0 Severe. A15 -8 2.70 B84.00 6"84.00 G611-A6T6(1)-3 30.0 Beckled. A15 -7 3.50 B84.00 6"83.50 G6111-A6T6(1)-8 17.0 Buckled. A15 -7 3.50 B83.50 6"83.50 G6111-A6T6(1)-8 17.0 Buckled. A15 -6 A15 -6 3.50 B83.50 6"83.50 G6111-A6T6(1)-5 Z6.0 Buckled. A15 -6 A15 -6 4 5.0 B83.50 6"83.50 G6111-A6T6(1)-5 Z6.0 Buckled. A15 -6 A15 -6 C6111-A6T6(1)-6 Z6.0 Buckled. A15 -6 A17 -9 2.00 B84.50 5"83.00 G6111-A6T6(1)-1 M 30.0 M shattere G6111-A6T6(1)-7 M 30.0 M shattere G6111-A6T6(1)-1 M 30.0					6"@2.00						
A15 - 8	led.	Buckled	37. 0	6(61)1-A6T6(1)-1		ĺ	2.50			A15 -9	
26 A16 -12 1-15 4. 3.40 B@4.00 6"@4.00 (3(53)1-A676(1)-5 15.6 Buckled. 27 B224-15 1-15 4. 1.33 B@3.50 6"@3.50 (3(53)1-A676(1)-9M 30.0 Buckled. 28 B224-14 1-20 4. 1.50 B@3.50 6"@3.00 3(53)1-A676(1)-5 26.0 M shattere A15 -4 2.00 B@4.50 5"@3.00 3(53)1-A676(1)-1M 3.0 Buckled. A17 -9 2.00 B@4.50 5"@3.00 3(53)1-A676(1)-1M 3.0 M shattere No bucklin, A17 -9 2.00 B@4.50 6"@5.00 (6(4)1-A676(1)-1M 3.0 M shattere No bucklin, A17 -9 2.00 B@4.50 6"@5.00 (6(4)1-A676(1)-1M 0.0 M shattere No bucklin, A17 -8 1-22 4. 2.50 B@5.00 6"@2.50 (6(3)1-A676(1)-1M 0.0 M change No damage No damag					6"@2, 00	B@2.27		4.	1-13		25
A15 - 7					6"@4, 00	B@4.00		4.	1-15		26
27 B224-14 1-20 4. 1.50 B(3)					7 0	=0					-
28 B224-14	attered.	M shatt			6"@3.50	B@3.50		4.	1-15		27
A15 - 4	led.	Buckled	26.0				3.90			A15 -6	
2					6"@3. 00	B()3.00		4.	1-20		28
A17-9 B224-8 1-22 4. 3.00 B@4.50 6'@5.00 3(53)1-A6T6(1)-TM 0.0 0					5193.00	B@4.50		l 4.	1-20		20
30 B224-8 1-22 4. 3.00 B@4.50 6'@5.00 3(53)1-A6T6(1)-7M 0.0 No damage (624)1-A6T6(1)-7 0.0 No damage (7.2)					33	=====================================			20	A17 -9	, "
31 B224-9 1-22 4. 2.50 B@5.00 6''@2.50 3(53)1-A6T6(1)-2M 1.5 M cracked 6(1)1-A6T6(1)-7 1.5 No buckin No buckin No cracks					6"@5.00	B@4.50		4.	1-22		30
A15 - 5	amage.	No dam	0.6	6(24)1-A6T6(1)-F		i	2.20			A17 -8	
32					6"@2.50	B@5.00		4.	1-22		31
A17 - 7											
33 B224-11 1-27 4. 2.10 3"@3.00 3(53)1-A6T6(1)-8M 5.6 No bucklin, 34 B234-6 1-28 4. 1.40 3"@5.00 3(23)1-A6T6(1)-3M 30.0 Severe, M B222-4 2.20 3"@4.50 3(23)1-A6T6(1)-3M 30.0 Severe, M B222-3 2.250 3"@4.50 3(23)1-A6T6(1)-12M 10.0 M B222-4 2.50 3"@4.50 3(23)1-A6T6(1)-12M 10.0 M B224-12 2.50 3"@4.50 3(23)1-A6T6(1)-12M 10.0 M B224-12 2.50 3(23)1-A6T6(1)-11M 3.6 M B234-4 2.05 3(23)1-A6T6(1)-11M 8.4 M B234-4 1.80 3(23)1-A6T6(1)-1M 8.4 M B234-3 2-3 4. 2.00 (6100)1-A6T6(1)-7 2.86 A13 -6 3(23)1-A6T6(1)-18 3.6 M B232-5 2-4 4. 1.70 3(23)1-A6T6(1)-7 8.0 M A13 -5 7.00 3(23)1-A6T6(1)-18 3.6 A14 -7 5.70 3(23)1-A6T6(1)-18 3.6 A14 -8 4. 1.65 3(23)1-A6T6(1)-18 3.6 A14 -6 5.40 3(23)1-A6T6(1)-19 3.6 A14 -6 6.00 6.00 6(61)1-A6T6(3)-5M 3(23)1-A6T6(1)-19 3.8 A14 -6 6.00 6(61)1-A6T6(3)-5M 3(23)1-A6T6(1)-19 3.0 A14 -6 6.00 6(61)1-A6T6(3)-5M 3(23)1-A6T6(1)-11P 0.0 A14 -6 6.00 6(61)1-A6T6(1)-11P 0.0 0.0 A14 -6 6.00 6(61)1-A6T6(1)-11M 0.0 0.0 A14 -6					3"@4.00			4.	1-27		32
Al8 -8					31163 00			ا ا	1.27		22
B222-4					3 63.00			ļ "	1-21		, ,,
35 B234-5 1-26 4. 1.70 3''@4.50 3(23)1-A6T6(1)-2M 4.4 9 shattered	re, M shattered.	Severe,	>30.0	3(23)1-A6T6(1)-3M	3"@5.00			4.	1-28		34
B222-3						ł					
36					3"@4.50	1		4 .	1-28		35
B224-12					+	Į.		۱ .	2 2		34
B234-4 B234-5 Color						i		**	2-3]
B234-4	ling.	Bucklin	14.9	6(100)1-46T6(7)-6			5.10	4.	2-3	A13 -7	37
Ali							1.80	1			
B232-5					1			4.	2-3		38
A13 - S						ŧ		١.,			1
A14 - 7								4.	2-4		39
A14 -7 B232-7 2-4 4. 1.65	attered.	P shatt	54.5	3(23)1-A6T6 1)-6P	-		1.52	4.	2-4		40
A14 -8 B223-4 Z-11 4. Z.00 B@6.90 6(61)1-A6T6(1)-18 11.4 Buckled. No damage No buckling B223-5 1.6	uckling.	No buck	1.5	3(94)1-A6T6(1)-7			5,70	1			1
42 B223-4 2-11 4. 2.00 B@6.96 6(61)1-A6T6(3)-5M 3(94)1-A6T6(1)-9 1.8 No damage No buckling 43 B232-8 2-11 4. 1.60 B@7.00 3(23)1-A6T6(1)-5P 39.0 Buckled. P B223-5 1.60 6(61)1-A6T6(3)-5M 2.17 M cracked. P B223-6 1.40 1.68 B@8.00 3(23)1-A6T6(1)-13P 30.0 P shattered B223-6 1.49 6(61)1-A6T6(3)-4M 4.5 M cracked. P B232-1 2-17 4. 3.00 B@8.00 3(23)1-A6T6(1)-11P 0.0 No damage B212-8 2.30 B@8.50 3(23)1-A6T6(1)-11P 0.0 No damage G100)1-A6T6(2)-1M 0.0 No damage G100)1-A6T6(2)-1M 0.0 No damage G100)1-A6T6(1)-11P 1.3 P cracked.								į 4.	2-4		41
A14 -6 A14 -6 B232-8 B232-8 B232-5 A16 -6 A17 B232-6 B232-6 A18 A19 A19 A19 A19 A19 A19 A19						D66 06		1 4	2.11		42
B223-5						Bero. 48		3.	2-11		34
B223-5	led. P shattered.	Buckled	39. 0	3(23)1-A6T6(1)-5P'		B@7.00		4.	2-11		43
B223-6 B232-1 2-17 4. 3.00 B@8.00 3(23)1-A6T6(1)-11P 0.0 No damage 6(100)1-A6T6(2)-2M 3.7 M cracked. 46 B232-2 2-17 4. 2.70 B@8.50 3(23)1-A6T6(1)-11P 0.0 No damage 6(100)1-A6T6(2)-1M 0.0 No damage 6(100)1-A6T6(2)-1M 0.0 No damage 7(100)1-A6T6(1)-11P 0.0 No damage 8(100)1-A6T6(1)-11P 1.3 P cracked.	acked.	M crac		6(61)1-A6T6(3)-5M	İ	B@0 00			2 11		44
45 B232-1 2-17 4. 3.00 B@8.00 3(23)1-A6T6(1)-11P 0.0 No damage M cracked. 46 B232-2 2-17 4. 2.70 B@8.50 3(23)1-A6T6(1)-11P 0.0 1 cracked. B212-3 2.30 6(100)1-A6T6(2)-1M 0.0 No damage 6(100)1-A6T6(2)-1M 0.0 No damage 7 0.0 No damage 8 0.1 No damage 8 0.1 No damage 8 0.1 No damage 8 0.1 No damage 8 0.1 No damage 9 0.						Deg 6. 00		3.	2-11		""
B212-6					i	B@8.00		4.	2-17		45
B212-3											
47 B232-3 2-17 4. 2.50 B@9.00 3(23)1-A6T6(1)-11P 0.0 No damage B212-9 1.80 1.80 (6100)1-A6T6(2)-1M > 30.0 M shattere B232-4 2-18 4. 2.32 B@9.00 6''@5.50 3(23)1-A6T6(1)-11P 1.3 Peracked.						B@8.50		4.	2-17		46
B212-9 48 B232-4 2-18 4. 2.32 B@9.00 6'(00)1-A6T6(2)-1M > 30.0 M shattere 3(23)1-A6T6(1)-11P 1.3 P cracked.						B@9.00		4.	2-17		47
48 B232-4 2-18 4. 2.32 B@9.00 6'@5.50 3(23)1-A6T6(1)-11P 1.3 P cracked.	attered.	M shatt	> 30. 0	6(100)1-A6T6(2)-1M		1	1.80	1	١.	B212-9	I .
I I I I I I I I I I I I I I I I I I I	acked.	P crack		3(23)1-A6T6(1)-11P 6(100)1-A6T6(2)-3M	6"@5.50	B@9.00		4.	2-18	B232-4 B212-7	48
40 722 1 2 10 4 1 40 700 50 400 400 400 400 400 400 400 400 40					,,,,,,,,,	200 00]	,	٠		1
49 B233-1 2-18 4. 1.40 B@8.50 6''@6.00 6(24)1-A6T6(1)-2M 0.0 No damage 7.50 3(250)1-A6T6(1)-3 >30 0 Buckled.					o649* 00	De.50		7.	2-18		**
50 All -4 2-25 4. 10.73 B@7.50 2(250)1-A6T6(1)-10 16.0 Buckled.	led.	Buckled	16.0	2(250)1-A6T6(1)-10		B@7.50	10.50	4.	2-25	A11 -4	50
B233-2 1.30 6(24)1-A6T6(1)-2M 9.2 M cracked.			9.2	6(24)1-A6T6(1)-2M	ŀ	200 00		1	٠		1
51 All -3 2-25 4. 13.50 B@8.00 3(250)1-A6T6(1)-12 8.0 Buckled. Al2 -10 10.50 6(1871)-A6T6(1)-1 0.0 No damage					j	B@8.00		7.	4+45		"
A12 -10 10.50 6(187)1-A6T6(1)-1 0.0 No damage	mrege.	Mo delu	J. U	Aliaili-Vatalili1	-		1 .0.30	i	1	1	

B = blast gage, R = rod gage, 3" = 3.5-inch-diameter instrumented cylinder, 6' = 6-inc..-diameter instrumented cylinder.

**P = Flexiglas, M = Micarta, R = rubber.

Table D. 1 (Continued)

Shot No.	Group No.	Date	Gnarge Weight (lbs)	Distance (ft)	Instrument and Distance (ft)	Cylinder No.	Metal (% w/a)	Damage
52	≠425-2	2-25	4.	3, 00	B@8.00	6(24)1-M31B(1)-8	8.5	No buckling.
53	A12 -12 A425-1	2-26	4.	8.30 3.80	B@8.50	6(187)1-A6T6(1)-1 6(24)1-M31B(1)-7	21.8 1.08	Euckled. No buckling.
	A12 -11			9.30		6(187)1-A6T6(1)-2	0.3	Wrinkling.
54	A12 -13 A423-2	2-26	4.	8.20 5.60	B@8.50	6(187)1-A6T6(1)-3 6(61)1-M31B(1)-1	12.0 3.3	Buckled. No buckling.
55	A423-1 A422-2	2-26	4.	6. 10 7. 50	B @7. 50	((61)1-M31B(1)-2 6(100)1-M31B(1)-1	2.8 4.3	No buckling. Buckled.
56	B235-6	2-26	4.	1.80	3€9.00	3(23)1-A6T6(1)-1R	12.0	Buckled.
57	A422-1 A425-3 A423-5	3-4	4.	8.30 2.50 4.80	B@4.50	6(100)1-M31B(1)-2 6(24)1-M31B(1)-1 6(61)1-M31B(1)-3	6. 7 10. 2 20. 0	Buckled. Buckled. Buckled.
58	A423-4	3-4	4.	5, 20	B@5.00	6(61)1-M31B(1)-4	>30.0	Severe
59	A422-3			6.80	- u	6(100)1-M31B(1)-3	13.1	Buckling.
59	A423-3 Bi `5-5	3-4	4,	5.20 2.20	B@5.50 6'95.50	6(61)1-M31B(1)-5 3(23)1-A6T6(1)-4R	·.0	No buckling. No buckling.
60	Ale -5	3-5	0, 5	0.70	B-@2.00 6"@2.00	3(23)1-A6T6(1)-11	31.0	Buckling,
	A13 -3			2.20	ł	6(100)1-A6T6(7)-1	9.4	Buckling.
61	A18 -4 A13 -2	3-5	0,5	0.95 2.60	B@2,00 6-22.00 Filtered	3(23)1-A6T6(1)-13 6(100)1-A6T6(7)-3	19. 0 3. 4	Buckling. Buckling.
62	A18 -1	3-5	0,5	1.30	B@2.00 6"@2.50	3(23)1-A6T6(1)-12	0.3	No buckling.
63	A13 -1	3-11		2.90	DB2 00	6(100)1-A6T6(3)-7	1.8	Buckling,
(0)	A18 -2 A15 -3	3-11	0,5	1. 10 1. 50	₿ ₿ ₿3.00	3(23)1-A6T6(1)-12 6(61)1-A6T6(4)-11	0.9 11.2	No buckling. Buckling.
64	A14 -4	3-11	0.5	2.50	B@2.06 6"@3.00	3(94)1-A6T6(1)-8	4,2	Buckling.
65	A15 -2 A14 -5	3-11	0.6	1.70	303.50 6'63.50	6(61)1-A6T6(4)-12	2.5 13.0	No buckling.
65	A15 -1	3-11	0.5	2.35 1.85		3(94)1-A6T6(1)-3 6(61)1-A6T6(4)-13	13.0	Buckling. No buckling.
66	A14 -3 A17 -4	3-12	0.5	2.70 0.75	3€ 1.50 6'€1.50	3(94)1-A6T6(1)-12 6(24)1-A6T6(3)-2	7.0 8.2	Buckling. Buckling.
67	A14 -1	3-12	0,5	3.40	B@1,30 6"@1,50	3(94)1-A6T6(1)-30	0.0	No damage.
68	A17 -3 A14 -2	3-12	0.5	0. 85 3. 05	B@1.00 Ø'@1.00	6(24)1-A6T6(3)-3 3(94)1-A6T6(1)-30	4.0 0.08	No buckling. No buckling
69	A17 -1 A16 -4	3-18	0.5	0. 95 1. 50	B@1.80	6(24)1-A6T6(3)-3 3(53)1-A6T6(1)-21	10.8	Buckling No buckling.
0,	A17 -2	J	U. 3	0. 95		6(24)1-A6T6(3)-6	1.3	No buckling.
70	A16 -3 A17 -5	3-18	0.5	1.70 0.70	36 1.60	3(53)1-A6T6(1)-22 6(24)1-A6T6(3)-6	1.6 13.6	No buckling. Buckling.
71	A16 -1 A12 -2	3-18	0.5	1.00 4.10	B@1.40	3(53)1-A5T6(1)-23	5.2	No buckling.
72	A16 -6	3-19	0.5	1.40	B@1.40 6'@1.00	6(187)1-A6T6(2)-2 3(53)1-A6T6(1)-23	5.1 40.0	Buckling. Buckling.
	A12 -1			4.80	1	6(187)1-A6T6(2)-3	0.03	No damage.
73	A16 -2 A12 -4	3-17	0.5	2.00 3.40	B@1.86 \$'@1.00	3(53;1-A6T6(1)-24 6(187)1-A6T6(2)-4	0.0 1.74	No damage. Buckling.
74	A15 -7	3-19	0.5	1.40	201.80 6'01.20	3(53)1-A6T6(1)-24	18,0	Buckling.
75	B212-3	3-25	9.5	1.00		6(100)1-A6T6(2)-13M 3(23)1-A6T6(2)-20	6.2	M cracked. Buckled.
	A12 -3			3, 80	•	6(187)1-A6T6(2)-6	6. 15	Buckled.
76	B224-4 A12 -8	3-25	0.5	0.75 3.20		3(53)1-A6T6(1)-4M 6(187)1-A: T6(1)-2	21.6 5.7	Cracked. Buckled, sheared.
77	A12 -9 B224-1	3-25	0.5	3.20 1.00		6(187)1-A6T6(2)-5 3(53)1-A6T6(1)-6M	27. 0 2. 45	Bucklud. No cracks.
78	B224-2	3-25	0.5	0, 90	6" 24.0 0	3(53)1-A6T6(1)-6M	10.5	M cracked.
79	B212-4 B224-3 B212-1	3-26	0.5	0.90 0.86 1.20	<i>U</i> + @ 3.00	6(100)1-A6T6(2)-4M 3(53)1-A6T6(1)-16M 6(100)1-A6T6(2)-9M	9. 2 7. 0 0. 0	M cracked. M cracked. No damage.
80	A11 -2	3-26	0.5	5.20	<i>6</i> ા @ 1. 8 3	3(250)1-A6T6(1)-1	10.0	Buckled.
81	B212-2 A11 -1	3-26	0.5	1.05 7.09	6"●1.30	6(190)1-A6T6(2)-9M 3(250)1-A6T6(1)-2	2. 6Z 1. 3	lio cracks. Buckling.
82	B212-0 A16 -5	4-1	0.5	0.85 1.45	N.G. B@2.50 R\$1.00	6(100)1-A6T6(2)-9M 3(53)1-A6T6(1)-25	1.0	No buckling. Buckling.
-2	A12 -6	4.		3.60	200 40 2004 40	6(187)1-A6T6(1)-10	6.7	Buckling.
83	B234-1 B211-4	4-1	0.5	0.70 0.95	364.00 3164.00	3(23)1-A6T6(1)-12M 6(100)1-A6T6(6)-6P	4.7	M cracked. P cracked.
84	B235~1	4-1	0.5	1.00	3"₩ 3.50	3(23)1-A6T6(1)-2R	3.7	No buckling.
85	B211-1 B235-2	4-2	0.5	1, 10 0, 90	R@3.00 5"@3.00	6(100)1-A6T6(6)-4P 3(23)1-A6T5(1)-5R	0.7	No cracks. No damage.
	B211-3	-		1,00		6(100)1-7.6T6(6)-4P	8.6	P shattered.

Table D. 1 (Continued)

Shot No.	Group No.	Date	Charge Weight (lbs)	Distance (ft)	Instru an Distan	d	Cylinder No.	Metal (% w/a)	Damage
86	B235-3	4-2	0.5	0.80	R@2.50	3"@2.50	3(23)1-A6T6(1)-6R	4.7	No buckling.
00	B211-2	7-2] " !	1.05	Kes. 30	3 62.50	6(100)1-A6T6(6)-1P	5.1	P cracked.
87	B235-4	4-2	0.5	0.75	R@2.00	3"@2.00	3(23)1-A6T6(1)-7R	19.0	Buckled.
	B231-1			1.00			6(24)1-A6T6(2)-10P	0.0	No damage
88	B226-2 B231-2	4-15	0.5	1.10 0.70		3''@1.50	3(53)1-A6T6(1)-9R 6(24)1-A6T6(2)-10P	13.6 0.17	Buckled. P shattered.
89	B226-1	4-15	0.5	1, 30		3''@1.00	3(53)1-A6T6(1)-6R	0.86	No buckling.
	A12 -7			3.50			6(187)1-A6T6(1)-5	19.5	Buckled.
90	R234-2 R223-1	4-15	0.5	0.65 0.85		3"91.51	3(23)1-A6T6(2)-17M 6(o!)1-A6T6(9)-12M	15.6 5.7	M cracked. M cracked.
91	A12 -5	4-16	2,5	3.63		3"@1.80	6(167)1-A6T6(1)-6	8.8	Buckled.
	B223-2			0.80			6(61)1-A6T6(9)-12M	1.0	No cracks.
92	B223-3	4-16	0.5	0.75		3"@2.30	6(61)1-A6T6(9)-13M	5.2	M cracked.
93	B221-1 B221-2	4-16	0.5	1.60 1.50	R@1.00	3"@2.60	6(61)1-A6T6(5)-9P 6(61)1-A6T6(5)-9P	0.0 0.17	No damage. No cracks.
94	B221-3	4-23	0.5	1.40	R@	3"@1.00	6(61)1-A6T6(5)-6P	0.0	No damage.
95	A16 -11	4-23	4.	3.80	R@2.00	3"@2.00	3(53)1-A6[6(1)-27	12.5	Buckled.
	B212-8			1.80			6(100)1-A6T6(3)-16M	16.0	M cracked.
96 97	B221-4 6725-1	4-29 4-29	0.5	1, 10 1, 70	R@2.00 R@2.00	3"@2.00 3"@2.00	6(61)1-A6T6(5)-7P	1.9 0.97	P shattered.
98	B3Z3-1	4-29	0.5 0.5	1.70	R@2.00 R@3.50	3"@2.00	6(61)1-A6T6(4)-10F 6(61)1-A2T8(1)-5R	0.97	No buckling. No buckling.
99	B275-2	4-30	0.5	1.40	R94.00	3"@4.00	6(61)1-A6T6(4)-8R	1. 17	No buckling.
100	B225-3	4-30	0.5	1.20	R@3.25	3"@3.25	6(61)1-A6T6(4)-3R	8.3	No buckling.
101	B213-1	4-30	0.5	2.00		- 1	6(100)1-A6T6(8)-7R	0.67	No buckling.
102	A414-1	5-6	4.	2.20		3"@4.00	3(23)1-A2T8(1)-2	0.0	No damage.
	A412-1			3.80		21101 22	6(61)1-A2T8(1)-4	0.67	No buckling.
103	A414-2 A412-2	5-6	4.	1.80 3.40	İ	3"@6.00	3(23)1-A2T8(1)-2 6(61)1-A2T8(1)-4	2.5 3.8	No buckling. No buckling.
104	A-14-7	5-6	4.	1.55		3"€8.00	3(23)1-A2T8(1)-10	_30.0	Severe.
	A412-3			2.70			6(61)1-A2T8(1)-9	10.8	Buckled.
105	A414-6	5-7	4.	1.65		3"@8.00	3(23)1-A2T8(1)-3	27.0	Sheared.
106	B421-1 A414-5	5-7	4.	4.40 1.73		3"@8.00	6(61)1-M31B(1)-4P	0.0 30.0	No damage.
100	B421-2	3-1	*	4. 15		3 60.00	3(23)1-A2T8(1)-5 6(61)1-M31B(1)-4P	0.0	Buckled. No damage.
107	A414-4	5-7	4.	1.76		3"@10, 00	3(23)1-A2T8(1)-4	47.0	Sheared.
	B421-3			4.00		-	6(61)1-M31B(1)-4P	0,0	Cracked.
108	B213-2	5-7	0.5	1.50		3"@6.00	6(100)1-A6T6(8)-13R	4.6	Buckled.
109	A414-3	5-12	4.	1.79		6"@10.00	3(23)1-A2T8(1)-7	15.0	Buckled.
110	C112-1 C112-2	5 12	4.	4.50 3.80		6"@8.00	6(50)1-2Rib(060)-(1)-7 6(50)1-2Rib(060)-(1)-7	0.33 1.0	No buckling. No buckling.
	Clii-i	, . .	"	6.00		0 60.00	6(100)1-5Rib(030)-(4)-12	0.43	No buckling.
111	C111-2	5-12	4.	4.80			6(100)1-5Rib(030)-(4)-12	3.2	No buckling,
112	C112-6	5-13	4.	3.00	i	6"@6.00	6(50)1-2Rib(060)-(11-5	20.0	Buckled.
113 114	C111-3 C112-3	5-13 5-13	4.	4.30 3.30		6''@6.00 6''@4.00	6(100)1-5Rib(030)-(3)-5	8.3 5.4	No buckling.
115	C112-4	5-13	4.	3. 15		6"@3.00	6(50)1-2Rib(060)-(3)-15 6(50)1-2Rib(060)-(3)-15	4.3	No buckling. No buckling.
116	C112-5	5~13	4.	3.04		6"@3.00	6(50)1-2R1b(060)-(1)-4	4.8	No buckling.
117	C112-7		4.	2.70		1	6(50)1-2Rib(060)-(1)-3	12.0	Buckled.
119	C121-4		4.	1.50		j	6(50)1-2Rib(250)-(3)-10P	>30.0	P shattered.
119 120	C121-1 C121-2		4. 4.	3.00 2.50			6(50)1-2R1b(250)-(3)-3P 6(50)1-2R1b(250)-(3)-3P	0.5	No cracks. No cracks.
121	C121-3		4.	2.20			6(50)1-2Rib(250)-(3)-3P	3.5	P shattered.
122	C122-5	5-27	4.	1.55	' 	ĺ	6(50)1-2Rib(250)-(-)-2M	3.06	M cracked.
123	C122-4	5-27	4.	1.65	1	-	6(50)1-2Rib(250)-(-)-3M	5.7	M cracked.
124 125	C122-3	5-27	4.	1.80		1	6(50)1-2Rib(250)-(-)-4M	2.2	M cracked.
126	C122-2 C122-1	5-28 5-28	4. 4.	2.00 2.20		ļ	6(50)1-2Rib(250)-(-)-4M 6(50)1-2Rib(250)-(-)-5M	6, 7 2, 5	M cracked. M cracked.
127	B612-1	5-28	4.	2.20		1	6(100)1-A6T6(L)-CP5	0,73	CP delaminated.
128	B612-2	5-28	4.	2.00		ļ	6(100)1-A6T6(L)-CP5	2.6	CP delaminated.
129	B621-2	5-28	4.	1.84		ļ	6(50)1-A6T6(L)-RL3	2,4	RL delaminated.
130 131	B621-1 B612-3	5-28 6-4	4.	2.0G 1.70		į	6(50)1-A6T6(L)-RL5	1,6	RL delaminated.
132	B621-3	6-4	1.	1.70		ļ	6(100)1-A6T6(L)-CP4 6(50)1-A6T6(L)-RL1	3.0 1.07	CP delaminated. RL delaminated.
133	A34 -1	6-4	4.	2.40		ì	C(24)90-A6T6(1)-1	0,4	No buckling.
134	A34 -2	6-4	4.	2.05			C(24)90-A6T6(1)-1	13.9	Buckled.

Table D. 1 (Concluded)

136 137 138 139 140 141 142 143 144 145	A33 -1 A33 -2 A32 -2 A31 -2 A31 -3 A31 -1 C223-6 C223-1 C223-2 C223-3	6-10 6-10 6-10 6-10 6-11 6-11	4.4444	4.80 3.90 6.15 5.15 9.30		C(60)9°-A6T6(1)-1 C(60)9°-A6T6(1)-6	0 75	Y buckling.
136 137 138 139 140 141 142 143 144 145	A33 -2 A32 -1 A32 -2 A31 -2 A31 -3 A31 -1 C223-6 C223-1 C223-2 C223-3	6-10 6-10 6-10 6-11 6-11	۸. 4. 4.	3.90 6.15 5.15 9.30				
137 138 139 140 141 142 143 144 145	A32 -1 A32 -2 A31 -2 A31 -3 A31 -1 C223-6 C223-1 C223-2 C223-3	6-10 6-10 6-11 6-11 6-11	4. 4. 4.	6. 15 5. 15 9. 30			8.4	No bu kling.
138 139 140 141 142 143 144 145	A32 -2 A31 -2 A31 -3 A31 -1 C223-6 C223-1 C223-2 C223-3	6-11 6-11 6-11	4.	9.30		C(94)90-A6T6(1)-4	0.45	No buckling.
139 140 141 142 143 144 145	A31 -2 A31 -3 A31 -1 C223-6 C223-1 C223-2 C223-3	6-11 6-11			i	C/94)90-A6T6(1)-7	10.4	Buckled.
141 142 143 144 145	A31 -1 C223-6 C223-1 C223-2 C223-3	6-11	4.			C(187)90-A6T6(1)-1	6. 8	Buckled.
142 143 144 145	C223-6 C223-1 C223-2 C223-3			8.90		C(187)90-A6T6(1)-5	8.0	Buckled.
142 143 144 145	C223-1 C223-2 C223-3	1	4.	12.00		C(187)90-A6T6(1)-4 6(61)1-A6T6(10)-17#F-3	0.4 25.0	No buckling.
143 144 145	C223-2 C223-3		4.	1.60 3.90		6(61)1-A6T6(10)-17#F-5	0.0	Pushed in. No damage,
144 145	C223-3	6-24	4.	3.00		6(61)1-A6T6(10)-18#F-5	0.63	No buckling.
145		6-24	4.	2.20		6(61)1-A6T6(10)-18#F-5	5, 15	Pushed in.
146	C223-4	6-24	4.	2.00		6(61)1-A6T6(10)-20#F-1	7.0	Buckling.
	C223-5	6-24	4.	1,84		6(61)1-A6T6(10)-20#F-1	9.2	Buckling.
	C213-1	6-25	4.	4.20		6(100)1-A6T6(5)-18#F-2	0.0	No damage.
	C213-2	6-25	4.	2.60		6(100)1-A5T6(4)-20#F-4	0,84	No buckling.
	C221-1			3.90		6(61)1-A6T6(10)-8#F-2	1.0	No buckling.
	C221-3 C213-3	6-25	4.	2.40 1.84		6(61)1-A6T6(10)-8#F-2 6(100)1-A6T6(5)-18#F-2	20.0 12.0	Pushed in. Buckling.
	-			2 20		6(61)1-A6T6(11)-8#F-4	8.5	Buckled.
	C221-2 C211-3	5-25	4.	4.20		6(100)1-A6T6(4)-E#F'-3	6.6	Buckled.
	C211-2	7-1	4.	4.80		6(100)1-A6T6(4)-8#F-3	5.3	Buckled.
	C222-1	'	l ••	3, 33		6(61)1-A6T6(10)-10#F-3	2.0	No buckling.
	C211-1	7-1	4.	5.40		6(100)1-A6T6(7)-8#F-4	0.0	No damage.
	C212-1			4,00		6(100)1-A6T6(4)-12#F-4	1.0	No buckling.
153	C211-5	7-1	4.	3.90		6(100)1-A6T5(7)-8#F-4	2.7	No buckling.
1	C212-2		i	3, 00		6(100)1-A6T6(4)-12#F-4	12.5	Buckled.
154	C211-6	7-1	4.	3.90		6(10')1-A6T6(7)-80F-4	i.2	No buckling.
1	C222-4			2, 15		6(61)1-A6T6(10)-12#F-2	22.0	Buckling.
155	C211-4 C314-1	7-2	4.	4.10 3.90		6(100)1-A6T6(9)-9#F-1 6(49/30)1-A6T6-23#F-2	0.0/ 0.0	Buckling. No damage.
156	C211-?	7-2	4.	3.20		G(100)1-AcT6(9)-9#F-1	9,0	Puckling.
.30	C314-2		} "	3,30	1	6(49/30)1-A6T6-23#F-2	6.0/ 0.0	No damage.
157	C314-3	7-2	4.	3.10	{	6(49/30)1-A6T6-23#F-2	0.33/0.0	No buckling.
	C312-2			4.00		6(30/30)1-A6T6-23#F-2 6(61)1-A6T6(11)-11#F-4	21.5/ 0.97	Buckling.
158	C222-2	7-8	4.	2.50 2.35		6(61)1-A6T6(11)-11#F-4	4.9 8.4	Pushed in. Buckling.
157	C222-3	' -•	•	l			ł	Ducking.
160	C312-1	7-8	4.	4.00	1	6(30/30)1-A6T6-23#F-2	1.3/ 0.0	No buckling.
161	C314-4	7-3	4.	2.50	ł	6(49/30)1-A6T6-23#F-2	6.9/ 2.3	Buckling.
162	C314-0	7-8	4.	2.90	1	6(49/30)1-A6T6-24#F-4	13.4/ 8.4	Buckling.
163	C314-5	7-8	4.	2.30	ł	6(49/30)1-A6T6-21#F-3 6(49/49)1-A6T6-26#F-4	0.8/ 0.1	Buckling. No buckling.
165	C315-1 C315-2	7-9	4.	2.35		6(49/49)1-A6T6-26#F-4	3.6/ 0.2	No buckling.
166	G3/5-3	7-9	4.	2.10		6(49/49)1-A6T6-24#F-2	8.7/ 2.14	Buckling.
167	C322-1	7-9	4.	1.70	1	6(49/30)1-A6T6-25#F-3M		No cracks.
158	C32.1-2	7-9	4.	1.43]	6(49/30)1-A6T6-25#F-3M		Cracked.
169	C322 -3	7-9	4.	1.35	1	6(49/30)1-A6T6-24#F-2M		Cracked.
176	C321 -2 C311-1	7-15	4.	2.00 3.10		6(30/30)1-A6T6-25#F-2M 6(49/30)1*-A6T6-25#F-1	0.3/3.0 1.37/0.12	Cracked. No buckling.
		1		1	}	1		-
171	C311-2 C321-1	7-15	4.	2.30	1	6(49/30)1*-A6T6-25#F-1 6(30/30)1-A6T6-24/F-3M	8.7/ 2.8 0.3/ 0.0	No buckling. No cracks.
172	C317-3	7-15	4.	2.25		6(49/30)1*-A6T6-25#;"-2	19.3/15.5	Sheared.
[C32 1 - 3	l		1.50		6(30/30)1-A6T6-74#7-3M		M cracked.
173	B622-1 B11-1	7-15	4.	2.2ú 2.50		6(50)1-A6T6-1 CD 6.5(26)1-Mica.re 5	0.0 0.17	No damage. No cracks.
		1	١.	1	1		1	
174	B/22-7, B11 -2	7-16	4.	1.90 2.30		6(50)1-A6T6-1GF 6.5(26)1-Micaria-5	0.37 0.07	Delamination. No cracks.
175	B11 -3 E611-2	7-16	4.	2. 10 2. 40		6.5(26)1-Micarta-5 6(100)1-A6T6-5RL	> 30, 0 0, 48	M cracked. Cracked.
176	3611-2	7-16	4.	2.70]	6(100)1-A6T6-5RL	0.0	No damage.
177	B613-3	7-21	4.	2.00		6(100)1-A6T6-IRL	0.3	Cracked.
- 1	C37/1-4]]	1.44	1	6(30/30)1-A6T6-24#F-3M	4.5/10.5	Cracked.
178	B511-4 7622-3	7-21	4.	1.60	[6(100)1-A6T6-1RL 6(50)1-A6T6-2CP	9.7	RL cracked. CP delaminated.
179	B622-4	8-4	4.	1.40	(6(90)1-A6T6-2CP	10.4	CP delaminated.
	C322-4	1	1	1.23	I	6(49/30)1-A6T6-24#F-6M		Cracked.

^{*1/4&}quot; foam wall.

A TOTAL TO THE TOTAL TO THE TOTAL

Table D. 2
2-FOOT-DIAMETER SHOCK TUPE

Shot No.	Group No.	Date	Charge Ratio Q	Tube Length	Instrument	Cylinder No.	Metal (% w/a)	Damage
2-1	B222-11	١-4	2.00	20.		3(53)1-A6T6(1)-7P		Buckled. P off.
2-2	A18 -21 B224-23	2-3	2.00 4.00	20. 20.		3(23)1-A6T6(1)- 3(53)1-A6T6(1)- M	0.0	No damage. Blew off.
2-3	A)8 -24 A16 -24	2-3	4.00 0.50	20. 20.	3	3(23)1-A6T6(1)- 3(53)1-A6T6(10)-10	29.	Sheared both ends. Buckled.
2-4	A213-2 B222-8	2-4	1.00	20.	3	3(53)1-A6T6(1)-11P	2.	Cracks.
2-5	A16 -25	2-4	1.00	20.	3	3(53)1-A6T6(1)-19		Blew off.
2-6	B222-7	2-4	1.00	20.	3	3(53)1-A6T6(1)-8P	2.	No cracks.
2-7	B224-17 B224-19	2-5 2-5	2.00ª 1.00	20. 20.	3	3(53)1-A6T6(1)-24M 3(53)1-A6T6(1)-23M	0.0	No cracks. No cracks.
2-9	B234-13	2 ~5	4.00	20.	3	3(23)1-A6T6(1)-10M	3,	No cracks.
2-10	B234-16	2-8	8, 00 ^b	20.	3	3(23)1-A6T6(1)-5M	 -	Buckled. M off.
2-11	B234-18	2-8	8.00a	20.	3	3(23)1-A6T6(1)-9M	2.	No crache
2-12	B234-19 B224-20	2-9	8. 00 ^b 2. 00	20. 20.	3 B	3(23)1-A6T6(1)-4M 3(53)1-A6T6(1)-13M	1.	Buckled. A oif.
	B232-12	2-7	2.00	20.	•	3(23)1-A6T6(1)-1P	Ö. 0	No cracks.
2-14	B222-10	2-10	1.50	27.	В	3(53)1-A6T6(1)-3P	3.	Cracks.
2-15	A14 -12 A424-3	2-10	0.062	20.	₿	3/94)1-A6T6(1-25	17.	Buckled.
1			0, 062	20.		3(50)1-M314(-)-10	0.0	No damage.
2-16	A14 -13	2-10	0. 125	20.	В	3(94)1-A6T6(1,-23		Sheared ends.
2-17	A424-6 B234-20	2-10	0.135 4.00°	20. 20.	3	3(50)1-M31B(-)-10 3(23)1-A6T6(1)-7M	1.0	Sheared and torn. No cracks.
2-18	B232-11	2-11	8.002	20.	3	3(23)1-A676(1)-9P	5.	Cracks.
2-19	B234-15	2-11	6.00	20,	3	3(23)1-A6T6(1)-8M	5.	Crack.
2-20	A424-4	2-16	0.094	20.	3	3(50)!-M31B(-)-	0.0	No damage.
2-21	A424-5	2-16	0.103	20.	3	3(50)1-M3iB(-)-	0.0	No damage.
2-22	A14 -11 B224-21	2-16 2-16	0.050 3.00	20. 20.	3, B B	3(94)1-A6T6(1)-11 3(53)1-A6T6(1)-25M	-0.5 3.5	No buckling. No cracks.
· · ·	A18 -22		3 00	20.	_	3(23)1-A6T6(1)-7	2.	No buckling.
2-24	A223-1 A14 -9	2-17	062	10.	3	3(94)1-A6T6(1)-26	0.0	No damage.
2-25	A140	2-17	0.10	10.	3	3(94)1-A6Tb(1)-26	20.	Buckled.
2-26	A16 -20	2-17	0.50	10.	3	3(53)1-A6T6(1)-4	1.	No buckling.
2-27	A18 -20 A13 -9	2-17 2-18	4.00 0.050	39. 20.	3	3(23)1-A6T6(1)-3 6(160)1-A6T6(7)-10	25. 0.0	Buckled.
- 1	A511-1	2-10		20.		0(100)1-A010(1)-10	0.0	No damage.
2-29 2-30	A17 -11 A15 -12 A512-1	2-18 2-18	3.00 0.25	20. 20.		6(24)1-A6T6(3)-9 6(61)1-A6T6(1)-10	2. 0.5	No buckling. No buckling.
2-31		2-19	0.26	20.	6			
2-32		2-19	0.52	20.	6			
2-34		2-19 2-23	ì.00 2.00	20. 20.	6	6" cylinder pressure		
2-35		2-23	4.00	20.	6	calibration series		
2-36		2-23	8.00 0.125	20. 20.	6			
2-38	B226-4	2-26		20.		2/5211 1/5/111 15	•	
2-39	B224-32	2-26	1.00 3.50	20. 20.	1	3(53)1-A6T6(1)-2R 3(53)1-A6T6(1)-22M	30. 4.	Buckled. Grack.
	B235-9		3 50	20.		3(23)1-A676(1)-3P	17.	Buckled.
2-40	A17 -12	2-26	3.50	20.		6(24)1-A6T6(3)-1	22.	Buckled.
2-41	B223-12	3-1	3.50	20.		6(61)1-A6T6(3)-1M		Blew off.
2-42	B223-11 A521-1	3-1	2.50	20.		6(61)1-A6T6(3)-7M	5.	Cracks.
2-43	B233-3	3-1	6.00	20.		6(24)1-A6T6(1)-5M		Cracks. No valid %.
2-44	B212-11	3-2	2.00	20.		6(100)1-A6T6(2)-8M	3.47	Cracks. C-ridge.
2-45 2-46	B237-15 B235-7	3-2 3-2	6.00 3.00	₹0. 30.		3(23)1-A6T6(1)-12P 3(23)1-A6T6(1)-9R	25, 4.	P Off. No buckling.
2-47	B226-3	3-3	0.50	20.	3	3(53)1-A6T6(1)-IR	1	
2-48	B2343	3-3	4.00	20.	,	3(23)1-A6T6(11-10P	1.	No buckling. No cracks.
2-49	3222-9	3-3	1.50	20.		3(53)1-A6T6(1)-2P	3,	Grack,
2-50	A18 -23 A223-2	3-3	3,50	20.		3(23)1-A6T6(11-16	³9.	Buckled.

a3-foot charge length.

b4.5-foot charge length

c9-foot charge length,

Table D. 2 (Continued)

Shot No.	Group No.	Date	Charge Ratio G	Tube Length	Instrument	Cylinder No.	Metal (% w/a)	Damage
2-5) 2-52 2-53 2-54 2-55 3-56	A16 -31 A16 -21 A14 -15 A16 -32 B222-6 B224-18	3-4 3-4 3-5 3-5 3-5 3-5	0,28F [†] 1,00 0,28F 0,50F 2,00 4,00	20. 10. 20. 20. 10.	3 3 3, B 3, B 3, B	3(53)1-A6T6(1)-12 3(53)1-A6T6(1)-12 3(53)1-A6T6(1)-16 3(53)1-A6T6(1)-20 3(53)1-A6T6(1)-1P 3(53)1-A6T6(1)-20M	0. 0 3. 22.	No desge Ends sheared. Buckled to mandrel. Sheared one end. Crack. Cracks; delaminations
2-57 2-58 2-59 2-60 2-61 2-62	A18 -15 A18 -19 A18 -16 A18 -18 A18 -17	3-5 3-8 3-8 3-8 3-8 3-9	0.52F 3.50 0.65F 3.00 4.00	5. 10. 5. 10. 5.	3 3 3 3	3(23)1-A6T6(1)-15 3(23)1-A6T6(1)-14 3(23)1-A6T6(1)-18 3(23)1-A6T6(1)-19 3(23)1-A6T6(1)-17	1. 23. 42. <1. 13.	No buckling. Buckled. Buckled. No buckling. Buckled.
2-63 2-64 2-65 2-66 2-67 2-68	B224-16 A16 -18 B222-5 B232-10 A16 -19 B222-12	3-9 3-9 3-9 3-10 3-10	5.00 0.50 2.50 8.00 0.43 5.00	5, 5, 5, 10, 20,	3 3 3 3, B 3, B	3(53)1-A6T6(1)-17M 3(53)1-A6T6(1)-13 3(53)1-A6T6(1)-5P 3(23)1-A6T6(1)-2P 3(53)1-A6T6(1)-11 3(53)1-A6T6(1)-4P	15. 4. 4. 4. 0.0	Gracks. Duckled. Grack. Cracks. No damage. Blew off.
2-69 2-70 2-71 2-72 2-73 2-74	A18 -12 B232-14 A18 -11 B234-10 B234-7 B234-11	3-10 3-11 3-11 3-12 3-12 3-12	0.17F 5.00 0.14F 9.00 0.29F 7.00	1. 20. 1. 5. 1.	3, B 3 3 3 3	3(23)1-A6T6(1)-2 3(23)1-A6T6(1)-1P 3(23)1-A6T6(1)-19 3(23)1-A6T6(1)-15M 3(23)1-A6T6(1)-13M 3(23)1-A6T6(1)-14M	4. < 0. 5 5. 6. 7.	Sheared one end. Cracked. No buckling. Cracks. Cracks.
2-75 2-76 2-77 2-78 2-79 2-80	A16 -14 A16 -15 A425-11 A423-10 A423-9 A425-10	3-15 3-15 3-15 3-15 3-16 3-16	0.02f 0.03f 1.00 0.10 0.075 0.75	1. 20. 20. 20. 20.	3, B 3, B	3(53)1-A6T6(1)-11 3(53)1-A6T6(1)-11 6(24)1-M31B(1)-2 6(61)1-M31B(1)-7 6(61)1-M31B(1)-8 6(24)1-M31B(1)-8	0. 0 6. 0. 0 10.	No damage. Buckloć. Shearee both ends. Sheared, blew off. No damage. Bucklod.
2-81 2-82 2-83 2-84 2-85 2-86	B422-5 B422-6 B422-8 B422-7 P432-7 B432-6	3-16 3-16 3-16 3-16 3-17 3-17	0.62 0.87 2.25 1.50 3.50 2.50	20. 20. 20. 20. 20. 20.		6(61)1-M31B(1)-1M :1)1-M31B(1)-1M o(61)1-M31B(1)-1M 6(61)1-M31B(1)-2M 6(24)1-M31B(1)-1M 6(24)1-M31B(1)-5M	0. 0 0. 0 2. 22 4. 02 2. 52	No cracks. No cracks. Blew off. Cracks. Cracks. Cracks.
2-87 2-88 2-89 2-90	B11 -6 B11 -4 B11 -5 A422-9	3-17 3-17 3-17 3-17	2.00 1.00 1.50 0.20	20. 20. 20. 20.		6.5(26)1-Micarta-1 6.5(26)1-Micarta-3 6.5(26)1-Micarta-3 6(100)1-M31B(1)-4	0, 0 1, 0	Blew off, No damage, Cracks, Blew off,
2-91 2-92 2-93 2-94 2-95 2-96		3-22 3-22 3-22 3-22 3-22 3-23	0.50 1.00 2.00 4.00 6.00 0.125	20. 20. 20. 20. 20. 20.	6, B 6, B 6 6 6 6	6" cylinder pressure calibration series		
2-97 2-96 2-99 2-100	Ai13-2 A412-8 A412-10 A414-8	3-23 3-23 3-23 3-23	3.25 0.28 0.33 3.25	29. 20. 20. 20.		6(24)1-A2T8(1)-4 6(61)1-A2T8(1)-1 6(61)1-A2T8(1)-2 3(23)1-A2T8(1)-1	11. 3. 9. <0.5	Buckled. Incipient buckling. Buckled, No buckling.
2-101 2-102 2-103 2-104 2-105 2-106 2-107 2-108		3-24 3-24 3-24 3-24 3-25 3-25 3-25	0.50 1.00 2.00 4.00 8.00 0.125 0.025 2.00	10. 10. 10. 10. 10. 10. 10.	6 6 6 6 6 6	6" cylinder pressure calibration series	•	
2-109 2-110 2-111 2-112 2-113	A15 -13 A512-2 A423-7 A423-8 A425-7	3-25 3-25 3-25 3-26	0.33 0.10 0.15 1.00 5.00	20. 10. 10. 10. 10.		6(61)1-A6T6(1)-2 6(61)1-M31B(1)-6 6(61)1-M31B(1)-6 6(61)1-M31B(1)-4 6(24)1-M31B(1)-3M	27. 0.0 22. 9.	Buckled. No damage. Buckled. Buckled.

[†]F = flet charge (see Fig. 3.17)

b . 100 b . 10

THE COLUMN THE COLUMN

Table D. 2 (Continued)

Shot No.	Group No.	Dece	Charge Ratio a	Tube Length	Instrument	Cylinder No.	Metal (% w/a)	Damage
2-114 2-115 2-116 2-117 2-118 2-119 2-120	B432-3 B422-3 B422-4 A422-4 A422-5 A421-2 A421-1	3-26 3-26 3-26 3-26 3-26 3-26 3-29	3.50 1.50 1.75 0.050 0.075 0.050 0.037	10. 10. 10. 10. 10. 10.		6(24)1-M31B(1)-4M 6(61)1-M31B(1)-3M 6(61)1-M31B(1)-3M 6(100)1-M31B(1)-7 6(100)1-M31B(1)-7 6(187)1-M31B(1)-2 6(187)1-M31B(·)-3	4. 05 1. 07 3. 56 0. 0 11 14. 2.	Cracks. No cracks. Crack. No damage. Buckled. Buckled. Incipient buckling.
2-121 2-122 2-123 2-134 2-125 2-126 2-127		3-29 3-29 3-30 3-30 3-30 3-30	0.06F 0.06F 0.03F 0.12F 0.20F 0.55F 0.83F	2. 2. 2. 2. 2.	6 6 6 6	6" cylinder pressure calibration series		
2-128 2-129 2-130 2-131 2-132 2-133	D14 -1 A15 -10 B223-9 A12 -15 A12 -14 B221-8	4-1 4-2 4-2 4-2 4-2 4-2	3,00 0,44 3,25 0,050 0,038 1,15	20. 10. 10. 10. 20.	s.g.†	3(23)1-A6T6(2)-21 6(61)1-A6T6(4)-13 (61)1-A6T6(3)-5M 5(187)1-A6T6(1)-8 6(187)1-A6T6(1)-9 6(61)1-A6T6(5)-10P	2. 21. 4.85 9. 0.0 1.48	No buckling. Buckled. Cracks. Buckled. No damage. No cracks.
2-134 2-135 2-136 2-137 2-138 2-139	B221-7 B211-5 b211-6 B211-7 B211-8 B421-8	4-2 4-2 4-5 4-5 4-5 4-5	1. 75 0. 50 0. 69 1. 00 1. 25 0. 69	10. 20. 20. 20. 20. 20.		6(61)1-A6T6(5)-5P 6(100)1-A6T6(7)-15P 6(100)1-A6T6(7)-15P 6(100)1-A6T6(6)-7P 6(100)1-A6T6(7)-15P 6(61)1-M31B(1)-5P	1.68 0.5 1.0 3.00	Cracks. No cracks. No cracks. No cracks, C-ridge. Blew off. No cracks.
2-140 2-141 2-142 2-143 2-144 2-145	B421-9 A13 -8 B23:-6 B231-5 A411-1 A411-2	4-5 4-5 4-6 4-6 4-6	1.00 0.10 5.50 4.75 0.062 0.075	20. 10. 10. 20. 20.		6(61)1-M31B(1)-5P 6(100)1-A6T6(7)-9 6(24)1-A6T6(2)-4P 6(24)1-A6T6(2)-5P 6(100)1-A2T8(1)-4 6(100)1-A2T8(1)-4	11. 3.82 1.93 0.0 0.0	Blew off. Buckled. F off. Cracked. No damage. No damage.
2-146 2-147 2-148 2-149 2-150 2-151	A411-3 B431-7 B431-6 B431-4 B431-3	4-6 4-6 4-6 4-6 4-6	0.100 2.50 1.75 2.00 2.00 1.50	20. 20. 20. 10. 20.	В	6(100)1-A2T8(1)-4 6(24)1-M31B(1)-1P 6(24)1-M31B(1)-3P 6(24)1-M31B(1)-4P 6(24)1-M31B(1)-5P	16. 3.33 2.80 2.56	Buckled. Sheared and torn. P off. Cracks. Cracks. No cracks.
2-152 2-153 2-154 2-155 2-156	B421-6 B421-7 B322-2 B423-3 B423-2	4-7 4-7 4-7 4-7 4-7	0.81 1.00 2.50 0.15 0.10	10. 10. 20. 20. 20.		6(61)1-M31B(1)-1P 6(61)1-M31B(1)-1P 6(61)1-A2T8(1)-1M 6(61)1-M31B(1)-1R 6(61)1-M31B(1)-3R	1,36 2,94 0,83	No cracks. Cracks. Cwacks. Sheared and torn. R OK. No buckling.
2-157 2-158 2-159 2-160 2-161	D14 -2 D14 -3 D14 -4 B234-12 D21 -1 B234-14	4-8 4-8 4-8 4-8	2.00 1.00 3.30 2.00	20. 20. 20. 20.	s. g. s. g. s. g. s. g.	3(23)1-A6T6(2)-21 3(23)1-A6T6(2)-21 3(23)1-A6T6(2)-21 3(23)1-A6T6(1)-16M 3(23)1-A6T6(1)-16M	3. 3. 50. 0. 0	No buckling. No further deformation. Buckled to mandrel. No cracks. No cracks.
2-162	D21 -2 A16 -22	4-9	0.25	20.	s. G.		0.0	
2-163	D12 -1 A16 -23 D12 -2 A213-1	4-9	0.37	20.	s. G.	3(53)1-A6T6(1)-28 3(53)1-A6T6(1)-28	0. 0	No damage. No damage.
2-164 2-165 2-166 2-167 2-168 2-169 2-170 2-171	A16 -17 A16 -16 A17 -10 B223-8	4-15 4-15 4-15 4-15 4-15 4-16 4-16	0.16F 0.05F 0.03F 0.27F 0.21F 0.11F 0.21F 0.16F	2. 2. 2. 2. 2. 2.	В	3(53)1-A6T6(1)-26 3(53)1-A6T6(1)-29 6(24)1-A6T6(3)-13 6(61)1-A6T6(3)-2M 6(61)1-A6T6(9)-11M 3(23)1-A6T6(2)-18M 3(23)1-A6T6(2)-19M	25. <1. 1.57 17. 4.	Buckled. No buckling. Ends sheared. Sheared. M off. No cracks. Cracks. No cracks.
2-172 2-173 2-174 2-175 2-176 2-177	A18 -14 A18 -13 A424-1 A424-2 A425-5	4-16 4-16 4-16 4-16 4-16 4-19	0.13F 0.11F 0.01F 0.03F 0.07F 0.12F	2. 2. 2. 2. 2. 2.	6	3(23)1-A6T6(2)-24 3(23)1-A6T6(2)-23 3(50)1-M31B(-)-9 3(50)1-M31B(-)-9 6(24)1-M31B(1)-6	35. < 1. 0.0 25. 15.	Buckled. No buckling. No damage. Buckled. Buckled. Water at 10 feet.

VON BU

The state of the s

THE RESIDENCE TO SERVICE sup>†</sup> S ú. = strain-gaged shell

Table D. 2 (Continued)

Shot No.	Group No.	Date	Charge Ratio	Tube Length	Instrument	Cylinder No.	Metal (% w/a)	Damage
2-178 2-179 2-180 2-181 2-182 2-183	A425-6 A425-4 B221-5 B221-6 B231-4 B231-3	4-19 4-19 4-19 4-19 4-19 4-19	0.08F 0.05F 0.05F 0.07F 0.16F 0.12F	2. 2. 2. 2. 2.		6(24)1-M31B(1)-9 6(24)1-M31B(1)-10 6(61)1-A6T6(5)-4P 6(6)1-A6T6(5)-4P 6(24)1-A6T6(2)-9P 0(24)1-A6T6(2)-6P	35. 3. 1.00 8. 10. 0.88	Buckled, wheared. Suckled. No cracks. P off one side. P off. No cracks.
2-184 2-185 2-186 2-187 2-188 2-189	B422-1 B422-2 B421-5 B421-4 B431-2 B431-1	4-19 4-19 4-20 4-20 4-20 4-20	0.07F 0.09F 0.05F 0.03F 0.12F 0.09F	2. 2. 2. 2. 2. 2.		6(61)1-M31B(1)-5M 6(61)1-M31B(1)-4M 6(61)1-M31B(1)-2P 6(61)1-M31B(1)-3P 6(24)1-M31B(1)-2P 6(24)1-M31B(1)-5P	0.82 2.20 2.44 0.20 10. 3.50	Crack. Cracks. Cracks. No cracks. P shattered. Cracks.
2-190 2-191 2-192 2-193 2-194 2-195	B432-2 B432-1 B225-5 B225-4 B423-1 A423-6	4-21 4-21 4-22 4-22 4-22 4-22	0.12F 0.09F 0.05F 0.04F 0.03F 0.03F	2. 2. 2. 2. 2. 2.		6(24)1-M31B(1)-2M 6(24)1-M31B(1)-2M 6(61)1-A6T6(4)-9R 6(61)1-A6T6(4)-6R 6(61)1-M31B(1)-2R 6(61)1-M31B(1)-9	1.45 0.88 3. 1.5 2.	Cracks. No cracks. Incipient buckling. No buckling. Lucipient buckling. Buckled.
2-196 2-197 2-198 2-199 2-200 2-201	A412-4 A412-5 A412-6 B323-2 B323-3 A212-1	4-22 4-22 4-22 4-23 4-23 4-23	0.03F 0.04F 0.05F 0.06F 0.08F 0.17	2. 2. 2. 2. 2. 20.		6(61)1-A2T8(1)-7 6(61)1-A2T8(1)-7 6(61)1-A2T8(1)-8 6(61)1-A2T8(1)-2R 6(61)1-A2T8(1)-4R 3(53)1.5-A6T6(2)-2	<1. 1. 6. <1. 2.5 0.0	At one end. No buckling. Buckled. No buckling. Wrinkling. No damage.
2-202 2-203 2-204 2-205 2-206 2-207	A212-2 A212-3 A214-1 A214-2 A214-3 A214-4	4-23 4-26 4-26 4-26 4-26 4-26	0.21 0.25 0.46 0.57 0.75 1.00	20. 20. 20. 20. 20. 20.		" 3(53)2/3-A6T6(1)-1 " 3(53)2/3-A6T6(1)-2	< 0.5 43. 0.0 0.0 ≤ 0.5 16.	No buckling Buckled. No damage. No damage. No buckling. Buckled.
2-208 2-209 2-210 2-211 2-212 2-213	A222-3 A222-2 A222-1 A222-0 D11 -1 D11 -2	4-26 4-26 4-26 4-26 4-27 4-27	2.50 2.00 1.50 1.50 0.15 0.22	20. 20. 20. 20. 20. 20.	s. G. s. G.	3(23)1.5-A6T6(2)-1 3(23)1.5-A6T6(2)-2 3(23)1.5-A6T6(2)-3 " 6(61)1-A2T8(1)-5	50. 2. 2. 0.0 0.0	Buckled to mandrel. Buckled. No buckling. No buckling. No damage. No damage.
2-214 2-215 2-216	D11 -3 A412-7 D11 -4 A414 0	4-27 4-27 4-27	0.28 0.28 0.33	20. 20. 20.	S. G. S. G. S. G.	n n	0. c 0. 0	No damage No damage.
2-217 2-218	D11 -5 A211-1 A211-3	4-28 4-28	0. 125 0. 187	20. 20. 20.	5. 0.	3(53)2-A6T6(2)-1	2. <1.0	No buckling. No buckling. Buckled to mandrel.
2-219 2-220 2-221 2-222 2-223 2-224	A211-2 C111-7 C111-4 C111-6 C112-10 C112-9	4-28 4-28 4-28 4-28 4-28 4-28	0.150 0.50 0.15 0.31 1.00 0.82	20. 20. 20. 20. 20. 20.		3(53)2-A6T6(2)-2 6(100)1-5Rib(030)(4)-11 6(100)1-5Rib(030)(4)-8 "6(50)1-2Rib(060)(1)-12 6(50)1-2Rib(060)(1)-14	<1.0 <0.5 6. 2.	No buckling. Blev off. No buckling. Shear buckle one end. No buckling. No buckling.
2-225 2-226 2-227 2-228 2-229 2-230	C112-8 C112-11 A221-2 A221-3 B51 -1 B51 -2	4-28 4-28 4-29 4-29 4-29 4-29	9.62 1.33 1.00 1.12 1.00	20. 20. 20. 20. 20. 20.		6(50)1-2Rib(060)(1)-8 3(23)2-A6T6(2)-1 3(23)2-A6T6(2)-2 3(53)2-A6T6(2)-3M 3(53)2-A6T6(2)-1M	< 1. 22. 3. 5. 2. 0	No buckling. Buckled. No buckling. Incipient buckling. Gracks. Buckled to mandrel.
2-231 2-232 2-233 2-234 2-235 2-236 2-237	A221-1 B52 -1 B52 -2 B52 -3 B611-5 B611-6 B611-7	4-29 4-29 4-30 4-30 4-30 4-30	0.80 1.50 2.00 3.00 1.00 2.00 2.50	20. 20. 20. 20. 20. 20. 20.		3(23)2-A6T6(2)-3 3(23)2-A6T6(2)-1M " 3(23)2-A6T6(2)-3M 6(100)1-A6T6-RL3	<1.0 1.5 4. 0.0 0.28 0.39	No buckling. No cracks. No cracks. Buckled. M off. No damage. Delamination at ends. Delamination over length.
2-238 2-239 2-240 2-241 2-242 2-243	B611-8 B612-6 B612-5 B612-4 C111-5 B622-6	4-30 5-3 5-4 5-4 5-4 5-4	4.00 3.00 2.00 1.50 0.22 4.00	20. 20. 20. 20. 20. 20.		6(100)1-A6T5-RL2 6(100)1-A5T6-CP2 6(100)1-A6T6-CP3 6(100)1-AbT6-CP4 6(100)1-5RiN(030)(3)-4 6(50)1-A6T6-CP3	20. 2. <1. 1. 2.35	Sheared one end. C-ridge. Severe delamination. Delamination. No cracks. No buckling. C-ridge. Severe delamination.

Table D. 2 (Continued)

Shot No.	Group No.	Date	Charge Ratio a	Tube Length	Instrument	Cylinder No.	Metal (% w/a)	Damage
2-244 2-245 2-246 2-247 2-248	B622-5 A425-9 A511-7 A511-10 A511-8	5-5 5-6 5-6 5-6 5-7	2.50 0.55 0.050 0.100 0.075	20. 20. 20. 20. 20. 20.	PL ^t PL PL	6(50)1-A6T5-CP4 6(24)1-M31B(1)-4X ² 6(100)1-A6T6(5)-14 " 6(100)1-A6T6(5)-15	0.43 6. 0.0 23. 0.0	Light delaminations. Buckted. No damage. Buckled. No damage.
2-249 2-250 2-251 2-252	A511-11 A511-6 A511-5	5-7 5-7 5-7 5-10	0.087 0.075 0.062 0.050	20. 20. 20. 20.	PL PL PL 6	6(100)1-A6T6(5)-16 Pressure calibration	21. 12. 11.	Buckled. Buckled. Buckled.
2-253 2-254 2-255	A511-4 D11 -6	5-10 5-11 5-11	0.025 0.050 0.22	20. 20. 20.	6 PL S.G.	" 6(100)1-A6T6(5)-16 6(61)1-A2T8(1)-5	0. 0 0. 0	No damage. No damage.
2-256 2-257 2-258 2-259 2-260 2-261	A511-9 A511-12 B311-2 C122-7 C122-6 C132-8	5-12 5-12 5-12 5-13 5-13 5-13	0.087 0.025 0.50 2.00 1.50 2.50	20. 20. 20. 20. 20. 20.	PL PL	6(100)1-A6T6(5)-17 6(100)1-A6T6(9)-18 6(100)1-A2T8(1)-2R 6(50)1-2Rib(250)(-)-10M 6(50)1-2Rib(250)(-)-7M 6(50)1-2Rib(250)(-)-9M	17. 0.0 2. 0.5 2.5	Buckled. No damage. Rupture. R off. No cracks. No cracks. Crack.
2-262 2-263 2-264 2-265 2-266 2-267	C121-6 C121-7 C122-9 A511-13 A511-14 A511-15	5-13 5-13 5-13 5-14 5-14 5-14	1.50 2.00 3.50 0.025 0.050 0.075	20. 20. 20. 20. 20. 20.	PL PL FL	6(50)1-2Rib(250)(3)-8P 6(50)1-2Rib(250)(3)-4P 6(50)1-2Rib(250)(-)-6M 6(100)1-A6T6(9)-18	2. 7. 5. 0.0 0.0	No cracks. P off, Cracks. No damage. No damage. Buckled.
2-268 2-269 2-270 2-271	B621-5 B621-4 D11 -7 A412-11	5-14 5-14 5-17 5-17	5.00 3.00 0.28 0.33	20. 20. 20. 20.	£.G. s.G.	6(50)1-AUT6-RL4 6(50)1-A6T6-RL1 6(61)1-A2T8(1)-5	12. 0.5 1.	C-ridge. Severe delamination. No delamination. No buckling. Blew off.
2-272 2-273	D11 -8 B321-1 B321-2	5-17 5-17	1.50 2.00	20. 20.		6(61)1-A2T8(1)-4P	0.37 1.18	No cracks. Crack. C-ridge.
2-274 2-275 2-276 2-277 2-278 2-279	B322-3 B322+1 B223-10 B221-9 B212-10 A413-1	5-18 5-18 5-18 5-18 5-18 5-18	3.50 2.00 2.00 1.50 1.50 3.00	20. 20. 20. 20. 20. 20.		6(61)1-A2T8(1)-2M 6(61)1-A2T8(1)-3M 6(61)1-A6T6(3)-6M 6(61)1-A6T6(5)-8P 6(100)1-A6T6(1)-15M 6(24)1-A2T8(1)-9	8. 0.23 2.12 27. 2.18 <0.5	Cracks and delamination. No cracks. No cracks. Buckled. P off one side. No cracks. C-ridge. No buckling.
2-280 2-281 2-282 2-283 2-284 2-285	A425-8 B431-5 B432-5 B323-4 B333-2 B331-1	5-18 5-19 5-19 5-19 5-19 5-19	0.37 1.37 1.75 0.37 6.00 5.00	20. 20. 20. 20. 20. 20.		6(24)1-M31B(1)-2 6(24)1-M31B(1)-3P 6(24)1-M31B(1)-5M 6(61)1-A2T8(1)-2R 6(24)1-A2T8(1)-2M 6(24)1-A2T8(1)-1P	1.0 1.63 1.50 0.0 0.5 0.54	No buckling. No cracks. No cracks. No buckling. No cracks. No cracks.
2-286 2-287 2-288*	B335-1 B335-2	5-20 5-21	3.00 3.50	20. 26.		6(24)1-A2T8(1)-2R 6(24)1-A2T8(1)-4R	0.5 1.0	No buckling. No buckling.
2-289	B331-3 B334-1 B332-1	5-21 5-21 5-21	8.00 8.00 8.00	20. 20. 20.		6(24)1-A2T8(1)-3P 3(23)1-A2T8(1)-2M 3(23)1-A2T8(1)-4P	<2.	Blew off. No cracks. Blew off.
2-291 2-292 2-293 2-294 2-295 2-296	A521-2 A512-7 A512-6 A512-5 A512-3 A512-4	5-24 5-24 5-25 5-25 5-25 5-25	2,50 0,31 0,25 0,19 0,19 0,25	20. 20. 20. 20. 20. 20.	PL PL PL PL PL PL	6(61)1-A6T6(3)-8M 6(61)1-A6T6(1)-18 6(61)1-A6T6(1)-19 6(61)1-A6T6(1)-17	2. 21. 20. 0.0 0.0	Crack. Buckled. Buckled. No damage. No damage. No damage.
2-297 2-298 2-299 2-300 2-301 2-302	C122-10 C122-11 B622-7 A33 -5 A33 -3 A32 -4	5-25 5-26 5-26 5-27 5-27 5-27	4.50 6.00 5.50 0.25 0.187 0.062	20. 20. 20. 20. 20. 20.		6(50)1-2Rib(250)(-)-1M 6(50)1-2Rib(250)(-)-8M 6(50)1-A6T5-CP5 C(60)9°-A6T6(1)-3 C(60)9°-A6T6(1)-5 C(94)9°-A6T6(1)-8	7. 15. 2.25 29. <0.5 0.0	Cracks. Cracks. C-ridge. Severe delamination. Buckled. No buckling. No buckling.
2-303 2-304 2-305 2-306 2-307 2-308	A32 -6 A32 -5 A34 -4 A34 -3 A31 -4 A31 -5	5-28 5-28 5-28 5-28 5-28 5-28	0, 125 0, 075 3, 00 2, 00 0, 025 0, 037	20. 20. 20. 20. 20. 20.		C(94)9°-A6T6(1)-10 C(54)9°-A6T6(1)-9 C(24)9°-A6T6(1)-3 C(24)9°-A6T6(1)-2 C(187)9°-A6T6(1)-2 C(187)9°-A6T6(1)-3	50, 10, 22, 2, 1, 25,	Buckled. Buckled. Buckled. No buckling. Incipient buckling. Buckled.

^{*} No shot.

a Uncovered shell, originally with rubber.

bPL=preforded shelf

Table D. 2 (Continued)

Shot No.	Group	Date	Charge Ratio Q	Tube Length	Instrument	Cylinder No.	Metal (% w/a)	Damage
2-309 2-310 2-311 2-312 2-313 2-314	A32 -3 A33 -4 B331-2 C223-7 C223-8 C223-11	6-1 6-1 6-1 6-4 5-4	0.050 0.22 6.50 0.50 1.00 2.00	20. 20. 20. 20. 20. 20.		C(94)9°-A6T6(1)-1 C(60)9°-A6T6(1)-7 6(24)1-A2T8(1)-2P 6(61)1-A6T6(10)-17#F-1 " (rev.)	0.0 12. 0.95 0.0 0.0 4.0	No buckling. Buckled. Cracked. No damage. No damage. No buckling.
2-315 2-316 2-317	C223-12 C213-6 C213-5	6-7 6-7 6-7	4.00 2.50 1.75	20. 20. 20.		6(61)1-A6T6(10)-17#F-2 6(100)1-A6T6(4)-20#F-1 6(100)1-A6T6(4)-20#F-2	33. 6. 4.	Sheared one end. Wrinkles. Wrinkles.
2-318 2-319 2-320 2-321 2-322		6-8 6-8 6-8 6-8	0.050 0.125 0.50 2.00 6.00	20. 20. 20. 20. 20.	00000	Pressure cone calibration series		
2-323 2-324 2-325 2-326 2-327 2-328	C222-7 C222-6 C212-4 C212-5 C222-5 C211-10	6-9 6-9 6-9 6-9 6-9 6-14	2.00 1.00 0.75 1.50 0.80 0.43	20. 20. 20. 20. 20. 20.		6(61)1-A6T6(10)-12#F-1 6(61)1-A6T6(10)-12#F-2 6(100)1-A6T6(4)-12;F-1 6(100)1-A6T6(4)-12;F-2 6(61)1-A6T6(10)-12#F-3 6(100)1-A6T6(10)-8#F-2	29. 1.5 3. 27. 0.5	Sheared. Wrinkled. No buckling. No buckling. Wrinkled. Dished. No buckling. Wrinkles.
2-329 2-330 2-331 2-332 2-333 2-334	C211-9 C221-6 C221-5 C221-7 C213-7 C313-2	6-15 6-15 6-15 6-16 6-16 6-17	0.25 0.80 0.50 1.25 3.00 3.00	20. 29. 20. 20. 20. 20.		6(100)1-A6T6(4)-8#F-1 6(61)1-A6T6(10)-8#F-1 6(61)1-A6T6(9)-8#F-4 "6(100)1-A6T6(4)-18#F-1 6(49/30)1-A6T6-12#F-1	2. 6. 3. 29. 30.	Wrinkles. Buckled. No buckling. Buckled. Dished. Sheared. Wrinkled. Blew off.
2-335 2-336 2-337 2-338 2-339 2-340	C313-1 D11 -9 D11 -10 C221-4 C223-10 C213-4	6-17 6-18 6-18 6-21 6-21 6-21	0.50 0.22 0.22 0.37 1.75 1.25	20. 20. 20. 20. 20. 20.	s.G. s.G.	6(49/30)1-A6T6-12#F-2 (;61)1-A2T8(1)-10 " 6(61)1-A6T6(9)-8#F-3 6(61)1-A6T6(10)-17#F-4 6(100)1-A6T6(5)-18#F-2	17. 0/10. 0 ² 0. 0 0. 0 0. 0 <1. <0, 5	Buckled. No damage. No damage. No damage. No buckling. No buckling.
2-341 2-342 2-343 2-344 2-345	C212-3 C211-8 C223-9 C121-5 C315-6	6-22 6-22 6-22 6-23 6-23	0.56 0.15 1.50 1.20 ^b 2.70	20. 20. 20. 20. 20.		6(100)1-A6T6(4)-12#F-1 6(100)1-A6T6(4)-8#F-1 6(61)1-A6T6(10)-17#F-4 6(50)1-2Rh(250)(3)-6P 6(49/49)1-A6T6-28#F-1	1, 0,0 0,5 2,	No buckling. No damage. No buckling. No cracks. Sheared both ends.
2-346 2-347 2-348 2-349 2-350	Dil -11 Dil -12 Dil -13 Dil -14 Dil -15	6-23 6-24 6-24 6-24 6-24	0.19 0.22 0.25 0.31 0.41	20. 20. 20. 20. 20.	s. c. s. c. s. c. s. c. s. c.	6(61)1-A2T8(1)-10 '' '' ''	0.0 0.0 0.0 <1. 11.	No damage. No damage. No damage. No buckling. Buckled.
2-351 2-352		6-25 6-25	0.33 1.33	20. 20.	3 3	Compare Kistler 601H vs. Atlantic Research		ł
2-353 2-354 2-355 2-356 2-357 2-358	C312-4 C312-5 C312-6 C312-7 C314-6 C314-7	6-28 6-28 6-28 6-28 6-28 6-28	0.25 0.33 0.41 0.67 0.33 0.67	20. 20. 20. 20. 20. 20.		6(30/30)1-A6T6-25#F-1 " " 6(49/30)1-A6T6-24#F-1	0.5 3. 1. 6.*/ 5.5 0.6	No buckling. Wrinkling, outer skin. No buckling. Buckled. No damage. No buckling.
2-359 2-360 2-361 2-362 2-363 2-364	C314-8 C315-5 C315-4 C322-5 C322-6 C321-5	6-28 6-29 6-29 6-29 6-29 6-30	1.00 1.00 0.67 2.00 3.00 2.70	20. 20. 20. 20. 20. 20.		6(49/49)1-A6T6-24#F-1 6(49/30)1-A6T6-23#F-1M 0(30/30)1-A6T6-26#F-1M	13. 0/16. 0 14. 0/12. 0 < 0. 5 2. 11. 8.	Buckled. Buckled. No buckling. No cracks. C-ridge. M cracks. C-ridge. M cracks.
2-365 2-366 2-367 2-368 2-369 2-370	B333-3 B333-1 C311-4 D13 -1 D13 -2 C311-5	7-1 7-1 7-7 7-7 7-7 7-7	6.00 12.00 0.67 0.67 0.67 1.00	20. 10. 20. 20. 20. 20.	s.g. s.g.	6(24)1-A2T8(1)-5M 6(24)1-A2T8(1)-4M 6(49/30)1*-A6T6-25#F-3 6(24)1-A2T8(1)-2 6(49/30)1*-A6T6-25#F-3	2.30 2.28 0.5 0.0 0.0 1.5/ 4.0	Crack. No cracks. No buckling. No damage. No damage. C-ridge one end.

^{*1/4&}quot; foam wall.

a Outside/inside deformations respectively

Charge ratios for Shots 2-344 onward have been multiplied by 2/3 because of tube end failure in driver section which increased driver volume.

Table D.2 (Concluded)

						(
Shot No.	Group No.	Date	Charge Ratio a	Tube Length	Instrument	Cylinder No.	Metal (% w/a)	Damage
2-371 2-372 2-373 2-374 2-375 2-376	D13 -3 D15 -4 D13 -5 D13 -6 D13 -7	7-8 7-8 7-8 7-9 7-9 7-12	1.17 2.00 2.34 3.00 4.00 1.33	20. 20. 20. 20. 20. 20.	s. g. s. g. s. g. s. g. s. g. B	6(24)1-A2T8(1)-Z "" "" "" ""	0.0 0.0 <0.5 2.	No damage. No damage. No buckling. No buckling. Blew off.
2-377 2-378 2-379 3-380 2-381 2-382 2-383	C311-6 C322-7 C322-8 B613-1 B613-2 B613-4 B613-3	7-19 7-19 7-19 7-29 7-29 7-29 7-29	1.17 4.00 5.30 1.00 2.00 3.00 2.34	20. 20. 20. 20. 20. 20. 20.		6(49/30)1*-A6T6-25#F-4 6(49/30)1-A6T6-24#F-4M 6(49/30)1-A6T6-26#F-5M 6(100)1-A6T6-NX-2 6(100)1-A6T6-NX-3 6(100)1-A6T6-NX-2 6(100)1-A6T6-NX-4	17. 0.0 2. 21. 8.	Sheared one end. C-ridges. M cracks. Sheared; blew off. No damage. Delaminations both ends. C-ridge, cover sheared. C-ridge; severe delaminations.
2-384 2-385 2-386 2-387 2-388		8-12 8-12 8-13 8-13	0,33 0,67 0,08 1,23 2,67	20. 20. 20. 20. 20.	6 6 6 6	6" cylinder pressure callbration checks; tube bottom dry, corrected a indicated.		
2-389 2-390 2-391		8-27 8-27 8-27	1.00 1.00 4.00	20. 20. 20.	6 6	6" cylinder pressure calibration checks; water at 19'6".		
:								
					<u> </u>			
								1

^{*1/4&}quot; foam wall.

THE WASHINGTON THE PROPERTY OF

Table D. 3
4-FOOT-DIAMETER SHOCK TUBE

CONTRACTOR OF THE PROPERTY OF

The state of the s

Shot No.	Group No.	Date	Charge Ratio a	Tube Length	Instrument	Cylinder No.	Metal (% w/a)	Damage
4-1		12-3	0.057	30.				
4-2		12-3	0.012	30.	В	·		
4-3		12-3	0.023	30.]	
4-4		12-3	0.023	30.	В			
4-5		12-5	Gas	30.	В		i	
4-6		12-21	0.057	30.	3			
4-7		12-21	0.114	30.	3		1	:
4-8	A16 -26	12-22	0.114	30.		3(53)1-A6T6(1)-15	C. 0	No damage.
4-9	A16 -27	12-23	0.23	30.		3(53)1-A6T6(1)-16	0.0	No damage.
4-10	A16 -30	12-23	0.46	30.		3(53)1-A6T6(1)-17	25.	Buckled.
4-11	A18 -25	12-28	0.91	30.		3(23)1-A6T6(1)-3	0.0	No damage.
4-14	A15 -15	1-27	0.46	30.	6	6(61)1-A6T6(1)-6		Buckled to mandrel.
4-13	A15 -14	1-28	0.23	30.	6	6(61)1-A6T6(1)-9	22.	Buckled.
4-14	A13 -13	1-28	0.114	30.	6, B	6(100)1-A6T6(7)-2	46.	Buckled.
4-15	A13 -12	1-30	0.063	30.	6, B	6(100)1-A6T6(7)-4	30.	Buckled.
4-16	A511-3	1-30	0.029	20		(11001) . ((
4-17	A13 -10 A15 -11	1-30	0.029	30. 15,	6, B 6, B	6(100)1-A6T6(7)-5 6(61)1-A6T6(1)-2	0, 0 0, 0	No damage. No damage.
			1		·	0(0-)1-11010(1)-11		no demago.
4-18	A17 -13	1-30	1.37	30.	6, B	6(24)1-A6T6(3)-4	0.0	No damage.
4-19	A12 -16	3-10	0.023	31.	6	6(187)1-A6T6(2)-1	0,0	No damage.
4-20	A12 -18	3-11	0.034	30.	6, 3	"	24.	Buckled.
4-21	A422-6	3-18	0.017	30.		6(100)1-M31B(1)-5	0,0	No damage.
4-22	A422-7	3-18	0.023	30.	В	"	0.5	No buckling.
4-23	A422-8	3-18	0.034	30.	В	1)	7.	Buckled.
4-24	A421-4	318	0.020	30.	В	6(187)1-M31B(1)-1	3.	Incipient buckling.
4-25	B213-3	3-18	0.057	30.	В	6(100)1-A6T6(8)-2R	0.0	No damage.
4-26	B213-4	3-18	0.086	30.	В	n ' n ' ' ' ' ' ' ' ' ' ' ' ' '	0.0	No damage.
4-27	B213-5	3-19	0.114	30.	В	"	40.	Buckled.
4-28	All -6	3-19	0.017	30.	В	3(250)1-A6T6(1)-7	6.	Buckling creases.
	A421-3		0.017	30.		6(187)1-M31B(1)-5	0.0	No damage.
4-29	A14 -14	3-19	9.057	30.	в	3(94)1-A6T6(1)-1	0.0	No damage.
	A13 -11		0.057	30.		6(100)1-A6T6(7)-10	0.0	No damage.
	A511-2			-		., .,		•••
4-30	A12 -17	3-19	0.029	30.	В	6(187)1-A6T6(1)-4	22.	Buckled.
4-31	A16 -28	4-12	0.40	30.	S.G.	3(53)1-A6T5(1)-28	0.0	No damage.
	D12 -3							
4-32	A16 -29	4-12	0.46	30.	s.c.	u	19.	Buckled.
	D12 -4							
4-33	B411-2	4-12	0.057	30.	1	6(100)1-M31B(1)-1R	23.	Buckled.
4-34	B411-1	4-13	0.043	30.	6, B	6(100)1-M31B(1)-2R	0.5	No buckling.
4-35 4-36	B433-1 B433-2	4-13 4-13	0.46 9.57	30. 30.	6, B	6(24)1-M31B(1)-3R	1.	No buckling.
4-30	B323-6	4-12	0.57	30.		6(24)1-M31B(1)-1R	5.	No buckling.
			5 .51	٠٠٠.		6(61)1-A2T8(1)-1R	1	Ends sheared. R OK.
4-37	B225-6	4-14	0.46	30.		6(61)1-A6T6(4)-5R	29.	Buckled.
	B323-5		0.46	30.		6(61)1-A2T8(1)-3R	16.	Buckle
4-38	B311-1	4-14	0.114	30.	6, B	6(100)1-A2T8(1)-1R	1.	Incipies buckling.
4-39	A425-12	4-14	0.57	30.	6, B	6(24)1-M31B(1)-5	30.	Buckled, sheared ends.
4-40 4-41	A412-12	4-14 4-21	0.023 0.34	30. 30.	6, B	6(61)1-AZT8(1)-6	18.	Buckled. Fastax pictures.
1	· · · · · · · · · · · · · · · · · · ·		1			-,,		manuscae Lunder hierari 3:
4-42		5-5 5-5	0.020	30. j	6, B		ļ	
4-44		5-5	0.020	30.	6, B		1	
4-45		5-10		30. 30.	6, B	i i	Į	.
4-46		5-10	0.15	30. 30.	6, B		1	Fastax pictures.
4-47		7-15			6, B		}	Fastax pictures.
7-2/		1-13	0.25	30.	į			Fastax pictures.

REFERENCES

- 1. Abrahamson, G. R. and H. E. Lindberg, "Explosive Simulation for Structural Response of Re-Entry Vehicles and Satellites (U)," Paper presented at Tenth Symposium on Space and Ballistic Missile Technology, 4-6 August 1965 (to be published in the Proceedings) (SRD).
- 2. Abrahamson, G. R., "Structural Response of Re-Entry Vehicles to Impulsive Loads (U)," Part 2, Vol. 1, Mark 3 Tests, Part 2, Vol. 2, Mark 4 Tests, Stanford Research Institute, AFSWC-TR-61-44, Contract AF 29(601)-2791, 9 June 1961 (SRD).
- 3. Lindberg, H. E., "Impulse Response of an Early A3X Polaris Re-Entry Structure (U)," Stanford Research Institute Final Report, Contract LMSC P.O. 18-103338 under NOrd-17017, November 1, 1962 (SRD).
- 4. Florence, A. L., "Structural Response of the Mark 6 Re-Entry Vehicle to Impulsive Loads (U)," Stanford Research Institute Final Report, TDR-63-3117, Contract AF 29(601)-5858, November 29, 1963 (SRD).
- 5. Firth, R. D., "Structural Response of Agena B Satellite to Impulsive Loading (U)," Stanford Research Institute Supplementary Report, TR-64-18, Contract AF 29(601)-4329, April 1965 (S).
- 6. Mayerhofer, R. D. and E. Rosicky, "Blast Damage to Missiles in Non-Flight Configurations," Ballistic Research Laboratories Memorandum Report No. 1603, October 1964 (C).
- 7. Johnson, O. T., R. D. Mayerhofer, and W. J. Schuman, Jr., "Effects of Blast upon Simulated and Actual Missiles (Project 1.4, Operation Snowball)," Ballistic Research Laboratories Memorandum Report No. 1655, May 1965 (C).
- 8. Rosendorf, L., "Operation Snowball ~ Project 1.5, Effects of Impulsive Loading on Reentry Vehicles," Picatinny Arsenal Technical Report 3227, June 1965.
- 9. Schuman, W. J., Jr., "The Response of Cylindrical Shells to External Blast Loading," Ballistic Research Laboratories Memorandum Report No. 1461, March 1963.

- 10. Schuman, W. J., Cr., "The Response of Cylindrical Shells to External Blast Loading," Part II, Ballistic Research Laboratories Report No. 1560, May 1964.
- 11. Abrahamson, G. R. and J. N. Goodier, "Dynamic Plastic Flow Buckling of a Cylindrical Shell from Uniform Radial Impulse,"

 Proceedings of the Fourth U.S. National Congress on Applied Mechanics, U. of California, Berkeley, California, June 18, 1962.
- 12. Lindberg, H. E., "Buckling of a Very Thin Cylindrical due to an Impulsive Pressure," J. Appl. Mech 31, p. 267, June 1964.
- 13. Lindberg, H. E., Dynamic Plastic Buckling of a Thin Cylindrical Shell Containing an Elastic Core," J. Appl. Mech. Paper No. 65-APMW-18 (to be published in J. Appl. Mech.
- 14. Goodman, H. J., "Compiled Free-Air Blast Data on Bare Spherical Pentolite, Ballistic Research Laboratories Report No. 1092, February 1960.
- 15. Holt, R. E. and R. A. Crist, "Calibration of a Six-Foot- and a Two-Foot-Diameter Shock Tube," U. of New Mexico Report under Contract AF 29(601)-4520, Report No. AFSWC-TDR-63-5, April 1963.
- 16. Korobeinikov, V. P., "Approximate Formulas for Calculation of the Characteristics of a Shock Wave Front in the Case of a Point Explosion in a Gas," Doklady Akad. Nauk SSSR 3, 3, 557-559 (1956), Translated Associated Tech. Services, Inc., Glen Ridge, N. J.
- 17. Wright, J. K., Shock Tubes, Metheun and Co., Ltd., London, John Wiley & Sons, Inc., N.Y., 1961.
- 18. Gowen, F. E. and E. W. Perkins, "Drag of Circula: Cylinders for a Wide Range of Reynolds Numbers and Mach Numbers," NACA-TN-2960, June 1953.
- 19. Hodge, P. G., Jr., Limit Analysis of Rotationally Symmetric Plates and Shells, Prentice-Hall, Inc., Englewood Cliffs, N.J.
- 20. Lindberg, H. E. and L. V. Parker, "Impulse Response of Stiffened Shell Structures (U)," Stanford Research Institute Final Report, AEC Project Agreement 41 under AT(04-3)-115, November 15, 1964 (S-FRD).
- 21. Windenburg, D. F. and C. Trilling, "Collapse by Instability of Thin Cylindrical Shells under External Pressure," <u>Transactions</u> of ASME, Vol. 56, 1934, pp. 819-825.